Advanced Flamelet Modelling of Turbulent Nonpremixed and Partially Premixed Combustion

Satyanarayana Murthy
Ravikanti Veera Venkata

A Doctoral Thesis

Submitted in partial fulfilment of the requirements for the award of
Doctor of Philosophy of Loughborough University

January 2008

Dedicated
To
My Parents

Abstract

Current work focuses on the development and performance evaluation of advanced flamelet models for turbulent non-premixed and partially premixed combustion in RANS and large eddy simulation (LES) based modelling. A RANS based combustion modelling strategy which has the ability to capture the detailed structure of turbulent non-premixed flames, including the pollutant NO, and account for the effects of radiation heat loss and transient evolution of NO, has been developed and incorporated into the in-house RANS code. The strategy employs an 'enthalpy-defect' based non-adiabatic flamelet model in conjunction with steady or unsteady non-adiabatic flamelets based NO submodels.

The performance of the non-adiabatic model and its NO submodels has been assessed against experimental measurements and steady flamelet model predictions for turbulent CH_4/H_2 bluff-body stabilized and CH_4-air piloted jet flames. Appreciable improvements in the mean thermal structure predictions have been observed in the piloted jet flames by consideration of radiation heat loss through the non-adiabatic flamelet model. Since transient effects were weaker in the piloted jet flame, both unsteady and steady non-adiabatic NO submodels provided similar level of improvement in the pollutant NO predictions in comparison to their adiabatic counterparts. Transient effects were, however, dominant in the bluff-body flame. The unsteady non-adiabatic NO submodel provided excellent agreement with measured NO distribution in comparison to the appreciably overpredicted distribution by its steady counterpart. The strategy of non-adiabatic flamelet model in conjunction with unsteady non-adiabatic NO submodel seems to provide an accurate and robust alternative to the conventional strategy of steady flamelet model with steady NO submodel.

While addressing the limitations of steady flamelet model in regard to radiation and slow chemistry of NO is one objective of this research, extending the applicability of the model to partially premixed combustion has been pursued as the second objective.

Flamelet/progress variable (FPV) approach based combustion models, which have the potential to describe both non-premixed and partially premixed combustion, have been incorporated in the in-house RANS and LES codes. Based on the form of the PDF for reaction progress variable, two different formulations, FPV-δ function model and FPV-β function model, have been derived. The performance of these models in predicting the thermal structure of a partially premixed lifted turbulent jet flame in vitiated co-flow has been evaluated with both RANS and LES. Both the FPV models have been found to successfully predict the flame lift-off even with RANS, while employing SLFM resulted in a false attached flame. The mean lift-off height is however underpredicted by FPV-δ function model by ~50% while the FPV-β function model which accounts for the fluctuations in the reaction progress variable overpredicted the height by 27%. The form of the PDF for reaction progress variable thus seems to have a strong influence on predictions of gross characteristics of the flame.

Adopting LES based modelling has been found to greatly improve the performance of the FPV models. While the deviation in mean lift-off height with FPV-δ function has been reduced to 30%, the mean lift-off height with FPV-β function model was predicted remarkably close to the measured value (predicted normalized lift off height=35.4 while measured height=35.0). LES has been found to also help in realizing the ability of the FPV models to predict to a fair degree, the local extinction and re-ignition phenomena associated with the fluctuation of the lifted flame base. The β function model in particular has been found to predict the lifted flame base characteristics remarkably well. However, the extinction and re-ignition observed with the models has been found to be limited to the conditions on the fuel rich side of stoichiometric mixture fraction and hence the measured level of fluctuation in the flame base is not yet captured. Nevertheless, the FPV models provide major advantage over SLFM in that the models are able to capture the gross characteristics of partially premixed flames. The FPV-β function model in conjunction with LES presents an excellent prospect for further research.

Acknowledgements

I wish to express my heartfelt thanks to my research supervisor, Professor W. Malalasekera, for providing me the opportunity to pursue Ph.D degree. Throughout the course of this research work, he has been immensely supportive and has made every effort to carefully consider my ideas and interests and keep me on track. The freedom and encouragement he rendered to explore varied areas of research in computational combustion helped me gain the necessary skills and self belief to take up large eddy simulation work in the final phase of this research.

I am grateful to a number of people who have helped me in meeting the challenges I encountered during the course of this research. Dr. Tariq Mahmud from University of Leeds, helped a great deal with Reynolds stress transport modelling. Dr. Matthias Ihme, Stanford University, provided valuable insight into the Flamelet/Progress variable approach. Dr. Stefano Piffaretti, ETH Zurich, has been instrumental in the success behind the implementation of look-up-table concept. Dr. Alexander Telangator, University of California SanDiego, and Dr. Perrine Pepiot, Stanford University, helped me with chemical mechanisms. Professor Heinz Pitsch, Stanford University, provided access and support to the FlameMaster code for flamelet calculations. My large eddy simulation work has greatly benefited from the support of Dr. Michael Kirkpatrick, University of Tasmania.

I am also quite thankful to my colleagues in the CFD research lab who have been ever helpful. Dr. Ranga Dinesh provided excellent support on large eddy simulation. The collaborative work I carried out with Dr. Mamdud Hossain and Mr.Anand Odedra on flamelet modelling proved vital to the progress of this research.

My sincere thanks to Professor Colin Garner, Thermo-Fluids lab, for all the help and encouragement he rendered during the course of this research work.

Finally, this work was funded with a research studentship from Loughborough University and is gratefully acknowledged.

Contents

Chapter 1: Introduction ..... - 1 -

1.1 Motivation ..... - 1 -

1.2 Objectives ..... - 6 -

1.3 Thesis outline ..... - 7 -

Chapter 2: Literature Survey ..... - 9 -

2.1 Flamelet models for turbulent non-premixed combustion ..... - 9 -

2.1.1 SLFM based modelling in RANS ..... - 10 -

2.1.2 Transient flamelet modelling in RANS ..... - 12 -

2.1.3 Non-adiabatic flamelet modelling in RANS ..... - 14 -

2.1.4 SLFM based modelling in LES ..... - 17 -

2.2 Flamelet models for turbulent partially-premixed combustion ..... - 19 -

2.3 Flamelet/progress variable (FPV) approach ..... - 24 -

Chapter 3: Governing Equations for Turbulent Combusting Flows ..... - 26 -

3.1 Instantaneous governing equations ..... - 26 -

3.1.1 Conservation of mass ..... - 26 -

3.1.2 Conservation of momentum ..... - 27 -

3.1.3 Conservation of species ..... - 27 -

3.1.4 Conservation of energy ..... - 29 -

3.2 Overview of turbulence simulation methods ..... - 30 -

3.2.1 Direct Numerical Simulation ..... - 30 -

3.2.2 Large Eddy Simulation ..... - 31 -

3.2.3 Reynolds Averaged Navier Stokes (RANS) modelling ..... - 32 -

Chapter 4: Turbulence Modelling ..... - 34 -

4.1 Reynolds-averaged Navier-Stokes formulation ..... - 34 -

4.1.1 Reynolds and Favre averaging ..... - 34 -

4.1.2 Favre averaged governing equations ..... - 35 -

4.1.3 Standard k-ε model ..... - 38 -
4.1.4 Reynolds stress transport model ..... - 40 -
4.2 Large Eddy Simulation formulation ..... - 45 -
4.2.1 Spatial filtering ..... - 45 -
4.2.2 Modelling of subgrid scale stresses ..... - 47 -
4.2.3 Modelling of subgrid scalar fluxes ..... - 50 -

Chapter 5: Combustion Models ..... - 51 -
5.1 Conserved scalar mixture fraction approach ..... - 52 -
5.1.1 Models for system chemistry ..... - 53 -
5.2 Steady laminar flamelet model ..... - 54 -
5.2.1 Flamelet equations ..... - 55 -
5.2.2 Statistics of mixture fraction and scalar dissipation rate ..... - 57 -
5.2.3 Flamelet quenching ..... - 59 -
5.2.4 Application of SLFM to LES ..... - 60 -
5.2.5 Limitations of steady laminar flamelet model ..... - 61 -
5.3 Non adiabatic flamelet model ..... - 62 -
5.4 Flamelet based NO sub models ..... - 65 -
5.4.1 Steady adiabatic NO submodel ..... - 66 -
5.4.2 Steady non-adiabatic NO submodel ..... - 67 -
5.4.3 Unsteady adiabatic NO submodel ..... - 68 -
5.4.4 Unsteady non-Adiabatic NO submodel ..... - 70 -
5.5 Flamelet/Progress Variable Approach ..... - 71 -
5.5.1 Motivation for FPV ..... - 71 -
5.5.2 FPV formulation ..... - 74 -

Chapter 6: Numerical Approach ..... - 85 -
6.1 Finite-Volume Method ..... - 86 -
6.2 Spatial discretisation in LES ..... - 89 -
6.2.1 Unsteady term ..... - 89 -
6.2.2 Convection term ..... - 89 -
6.2.3 Diffusion term ..... - 92 -
6.2.4 Source term ..... - 93 -
6.2.5 Complete discretised equation ..... - 94 -

6.3 Time advancement in LES ..... - 95 -
6.3.1 Time integration of scalar equations ..... - 95 -
6.3.2 Time integration of momentum equations ..... - 96 -
6.4 Pressure correction in LES ..... - 98 -
6.5 Solution of LES equations ..... - 99 -
6.5.1 Overall solution procedure for reacting flows ..... - 99 -
6.5.2 Procedure for steady flamelet model ..... - 101 -
6.5.3 Procedure for FPV-δ function model ..... - 102 -
6.5.4 Procedure for FPV-β function model ..... - 103 -
6.6 Boundary conditions in LES ..... - 106 -
6.6.1 Solid boundaries ..... - 107 -
6.6.2 Inflow boundary condition ..... - 107 -
6.6.3 Outflow boundary condition ..... - 109 -
6.7 Steady RANS numerical framework ..... - 110 -
6.7.1 Arrangement of Reynolds stresses on staggered grid ..... - 111 -
6.7.2 Spatial discretisation ..... - 112 -
6.7.3 Pressure correction ..... - 114 -
6.7.4 Solution of RANS equations ..... - 116 -
6.7.5 RANS procedure for steady flamelet model ..... - 118 -
6.7.6 RANS procedure for non-adiabatic flamelet models ..... - 120 -
6.7.7 RANS procedure for FPV-δ function model ..... - 122 -
6.7.8 RANS procedure for FPV-β function model ..... - 123 -
6.7.9 Boundary Conditions ..... - 126 -
6.8 Unsteady RANS procedure ..... - 129 -

Chapter 7: Pre-processing for RANS & LES based Calculations of Turbulent Flames ..... - 131 -
7.1 Generation of flamelets ..... - 132 -
7.1.1 Steady adiabatic flamelets ..... - 133 -
7.1.2 Steady non-adiabatic flamelets ..... - 138 -
7.2 Look-up-tables for SLFM ..... - 143 -
7.3 Look-up-tables for NADM ..... - 150 -
7.4 Look-up-tables for FPV models ..... - 152 -
7.4.1 Pre-PDF FPV δ ..... - 153 -

7.4.2 Pre-PDF FPV β ..... - 158 -

Chapter 8: Modelling of Turbulent Non-premixed Bluff-body and Jet flames ..... - 163 -

8.1 Experimental study of bluff-body stabilized flames ..... - 164 -

8.1.1 Experimentally observed flame structure ..... - 165 -

8.2 RANS modelling of HM1e & HM1 flames ..... - 167 -

8.2.1 Computational domain & boundary conditions ..... - 169 -

8.2.2 Computational grid ..... - 171 -

8.2.3 Adiabatic flamelet Modelling: Results & Discussion ..... - 174 -

8.2.4 Influence of chemical mechanism ..... - 189 -

8.2.5 Non-adiabatic flamelet modelling: Results & Discussion ..... - 194 -

8.2.6 Influence of transient effects on NO ..... - 205 -

8.3 Experimental study of Sandia D jet flame ..... - 208 -

8.4 RANS modelling of Sandia D jet flame ..... - 209 -

8.4.1 Computational set up ..... - 211 -

8.4.2 Non-adiabatic flamelet modelling : Results & Discussion ..... - 212 -

Chapter 9: Modelling of Turbulent Partially-premixed Lifted Jet Flame ..... - 218 -

9.1 Experimental study of Berkeley lifted jet flame in vitiated co-flow ..... - 219 -

9.2 Computational set up for RANS ..... - 221 -

9.3 Computational set up for LES ..... - 222 -

9.4 Results and Discussion ..... - 225 -

9.4.1 Performance of SLFM & FPV models in RANS ..... - 225 -

9.4.2 Performance of SLFM & FPV models in LES ..... - 234 -

Chapter 10: Conclusions and Future Recommendations ..... - 247 -

10.1 Conclusions ..... - 249 -

10.2 Recommendations for future work ..... - 253 -

10.3 Present contribution ..... - 254 -

Appendix I ..... - 255 -

References

List of Figures

5.1: Surface of stoichiometric mixture in a turbulent jet diffusion flame.....55

5.2: Locus of Stoichiometric temperature for all the solutions of the steady flamelet equations. Generated for the Berkeley lifted flame (section 9.1) conditions: Fuel CH_4-Air (25%-75%) at 323 K and Oxidizer (vitiated co-flow) at 1355 K..... ...72

5.3: Variation in parameterization of flamelets (a) along the entire solution space and (b) close to the equilibrium state with two different definitions of flamelet parameter. Generated for the Berkeley lifted flame (section 9.1) conditions.....75

5.4: Reaction progress variable distribution within a flamelet and the definition of flamelet parameter. Generated for the Berkeley lifted flame (Section 9.1) conditions.....76

6.1 Staggered grid and node placement in two dimensions. Circles indicate scalar nodes, horizontal arrows indicate nodes of the *u* velocity component and vertical arrows indicate the *v* velocity component. Examples of a u, v and scalar cell are highlighted.....87

6.2: A finite volume cell and its neighbours in three dimensions.....89

6.3: Staggered storage arrangement for the Reynolds shear stresses.....111

6.4: Schematic of a 2D grid for a bluff-body flow problem.....117

6.5: *u* velocity cell at wall boundary.....128

7.1: Steady flamelet solutions for fully burning and fully extinguished states. Generated for conditions corresponding to (a) HM1 flame and (b) Sandia D flame. These solutions are used for SLFM based turbulent flame calculations.....135

7.2: NO source term profiles corresponding to fully burning and fully extinguished steady state solutions. Generated for the HM1 flame conditions. These solutions are required in NO modelling with SLFM-NO-TRE.....137

7.3: Steady flamelet solutions for fully burning, partially extinguished and fully extinguished states. Generated for the Berkeley CH_4-Air lifted jet flame conditions. These solutions are used for FPV based turbulent flame calculations. (——) fully burning and fully extinguished states; (-------) partially extinguished state.....138

7.4: Imposing enthalpy defect on a steady adiabatic flamelet generated for HM1 flame conditions.....140

7.5: Variation of NO source term with enthalpy defect for HM1 flame conditions. The profiles correspond to a stoichiometric scalar dissipation rate of $2.0s^{-1}$.....142

7.6: Variation of extinction limit with enthalpy defect for HM1 and SANDIA D flame conditions.....142

7.7: Steady adiabatic flamelet solution for equilibrium condition. Generated for HM1 flame conditions. Dots show alternative grid points along Z space.....145

7.8: The distribution of points along $\widetilde{Z''^2_{norm}}$ and $\tilde{\chi}$ axes of the look-up-table for SLFM based calculations.....145

7.9: Structure of 3D look-up-tables for integrated temperature (K) for SLFM calculations. Generated for HM1flame (top) and Sandia D (bottom) flame conditions.....149

7.10: The 3D look-up-tables in λ space generated for Berkeley flame conditions. Structures of mean progress variable (top) and temperature (bottom) colored by the mean flamelet parameter.....156

7.11 Extracted scalar data as a function of $\tilde{\lambda}$ for $\tilde{Z}=0.6$ and $\widetilde{Z''^2_{norm}}=0.4$.....157

7.12: 2D array of data extracted for each variable from their respective look-up-tables in λ space for a given $\tilde{Z}$ and $\widetilde{Z''^2_{norm}}$. Scalars represented by $\tilde{\phi}=\left(\bar{\rho},\tilde{T},\tilde{Y}_i,\tilde{\dot{\omega}}_c,\widetilde{C''\dot{\omega}''_c}\right)$.....162

7.13: Steps involved in obtaining a unique combination of values for $\tilde{\lambda}$ and $\widetilde{\lambda''^2_{norm}}$ corresponding to every combination of $\tilde{C}$ and $\widetilde{C''^2_{norm}}$ 162

8.1: Schematic of bluff-body burner, and stabilized flame with measurement locations. (Bottom figure : www.aeromech.usyd.edu.au/thermofluids).....166

8.2: Computational domain for RANS modelling of HM1e & HM1 flames.....171

8.3: Computational grid for RANS modelling of HM1e & HM1 flames. Grid consists of 162 axial nodes and 111 radial nodes.....172

8.4: HM1e radial profiles of mean and rms fluctuations of axial (U) and radial (V) velocities. Comparison for grid independence test.....173

8.5: HM1e flame (a) axial velocity (m/s) and (b) temperature (k) contours superimposed with streamlines. RANS predictions from SLFM in conjunction with RST model for turbulence closure.....175

8.6: Radial profiles of mean axial velocity (a) and mean radial velocity (b) for at various axial locations in the HM1e flame. Predictions obtained from RANS calculations with SLFM.....177

8.7: Radial profiles of rms fluctuations of axial (a) and radial (b) components of velocities at various axial locations in the HM1e flame. Predictions obtained from RANS calculations with SLFM.....178

8.8: Radial profiles of mean mixture fraction at various axial lengths of HM1 flame. Predictions obtained from RANS calculations with SLFM.....181

8.9: Radial profiles of rms of mixture fraction fluctuations at various axial lengths of HM1 flame. Predictions obtained from RANS calculations with SLFM.....182

8.10: Comparison of the in-house RANS code's RST model prediction capability with that of commercial code CFX 4.4 (Dally *et al.*, 1998b) and full second moment closure (Li *et al.*, 2003). All predictions pertain to HM1flame conditions.....182

8.11: Radial profiles of mean temperature at various axial lengths of HM1 flame. Predictions obtained from RANS calculations with SLFM.....185

8.12: Radial profiles of mean CO_2 mass fraction at various axial lengths of HM1 flame. Predictions obtained from RANS calculations with SLFM.....185

8.13: Radial profiles of mean H_2O mass fraction at various axial lengths of HM1flame. Predictions obtained from RANS calculations with SLFM.....186

8.14: Radial profiles of mean CO mass fraction at various axial lengths of HM1 flame. Predictions obtained from RANS calculations with SLFM.....186

8.15: Radial profiles of mean OH mass fraction at various axial lengths of HM1flame. Predictions obtained from RANS calculations with SLFM.....187

8.16: Radial profiles of mean NO mass fraction at various axial lengths of HM1 flame. Dots indicate measurements; (——) SLFM-NO-TRE + RST model, (----) SLMF-NO-TRE + mod. k-ε model; (– • – • – •) SLFM Direct+ RST model ; (.....) SLFM Direct + mod. k-ε model.....188

8.17: Radial profiles of mean temperature : comparison of different mechanisms for hydrocarbon chemistry. Predictions obtained from RANS calculations of SLFM in conjunction with RST model.....192

8.18: Radial profiles of mean CO_2 (top) and CO (bottom) mass fractions. Sensitivity of predictions to mechanisms for hydrocarbon chemistry. Predictions obtained from RANS calculations of SLFM in conjunction with RST model 193

8.19: Radial profiles of mean NO mass fraction: comparison of different mechanisms for nitrogen chemistry. Predictions obtained from RANS calculations with RST model and SLFM-NO-TRE.....194

8.20: Radial profiles of mean mixture fraction along various axial stations in HM1 flame. Predictions obtained from adiabatic and non-adiabatic RANS simulations using RST model for turbulence closure.....196

8.21: Radial profiles of rms of mixture fraction fluctuations along various axial stations in HM1 flame. Predictions obtained from adiabatic and non-adiabatic RANS simulations using RST model for turbulence closure.....196

8.22: Radial profiles of mean temperature (K) along various axial stations in HM1 flame. Predictions obtained from adiabatic and non-adiabatic RANS simulations using RST model for turbulence closure.....197

8.23: Contours of mean enthalpy defect (kJ/kg) in HM1 flame. Predictions obtained from simulation with NADM model using RST model for turbulence closure.....197

8.24: Radial profiles of mean CO_2 mass fraction along various axial stations in HM1 flame. Predictions obtained from adiabatic and non-adiabatic simulations using RST model for turbulence closure.....199

Figure 8.25: Flamelet CO_2 structure at various enthalpy defects. Generated for HM1 flame conditions using GRI 2.11 mechanism.....199

8.26: Radial profiles of mean CO mass fraction along various axial stations in HM1 flame. Predictions obtained from adiabatic and non-adiabatic simulations using RST model for turbulence closure.....200

8.27: Radial profiles of mean NO mass fraction along various axial stations in HM1 flame. Predictions obtained from adiabatic and non-adiabatic simulations using RST model for turbulence closure.....200

8.28: Predicted 'High Enthalpy Defect' zone and its sub-zone within HM1 flame from RANS simulation carried out with NADM model in conjunction with RST model for turbulence closure.....203

8.29: The β PDF shapes extracted from the entire HED zone (a) and within each HED sub-zone (b)-(f) in HM1 flame. RANS Simulation carried out with NADM model in conjunction with RST model for turbulence closure.....204

8.30: Time evolution of domain averaged conditional scalar dissipation rate (a) and the corresponding evolution of flamelet NO distribution (b).....206

8.31: Steady vs. Unsteady NO submodels in RANS calculations of HM1flame with RST model for turbulence closure.....207

8.32: Experimentally observed image of Flame D (left) and close-up of the pilot flame (right). (Courtesy: Barlow and Frank (2007)).....209

8.33: Computational domain (top) and grid (bottom) used for RANS based modelling of Sandia D flame. Grid consists of 141 axial nodes by 104 radial nodes.....212

8.34: Mean temperature (K) (top) and enthalpy defect (kJ/kg) (bottom) contours of Sandia D flame predicted by RANS simulation with NADM model.....213

8.35: Radial profiles of mean and variance of mixture fraction at various axial locations in the Sandia D flame. Predictions from adiabatic and non-adiabatic RANS simulations with RST model for turbulent closure.....214

8.36: Radial profiles of mean temperature (K) at various axial locations in the Sandia D flame. Predictions from adiabatic and non-adiabatic RANS simulations with RST model for turbulent closure.....215

8.37: Radial profiles of mean CO_2 mass fraction at various axial locations in the Sandia D flame. Predictions from adiabatic and non-adiabatic RANS simulations with RST model for turbulent closure.....216

8.38: Radial profiles of mean NO mass fraction at various axial locations in the Sandia D flame. Predictions from adiabatic and non-adiabatic RANS simulations with RST model for turbulent closure.....216

9.1: (a) Burner schematic and (b) measured image of a turbulent CH4/air lifted jet flame in vitiated coflow. (Cabra *et al.* 2005).....220

9.2: Computational domain and grid for RANS based simulations of Berkeley CH_4/air lifted flame. The grid consists of 198x110 nodes.....221

9.3: (a) Computational domain and (b) grid used for LES based modelling of Berkeley CH_4/air lifted jet flame.....224

9.4: Predictions of mean mixture fraction contours from RANS simulations of Berkeley CH_4/air lifted jet flame at baseline conditions.....227

9.5: Predictions of mean temperature contours from RANS simulations of Berkeley CH_4/air lifted jet flame at baseline conditions.....227

9.6: Predicted distribution of mean chemical source term from RANS simulations of Berkeley CH_4/air lifted jet flame at baseline conditions.....229

9.7: Radial profiles of mean and rms fluctuations of mixture fraction at various axial locations in Berkeley CH_4/air lifted jet flame. Predictions correspond to RANS calculations at baseline conditions.....232

9.8: Radial profiles of mean temperature (K) at various axial locations in the Berkeley CH_4/air lifted jet flame. Predictions correspond to RANS calculations at baseline conditions.....233

9.9: LES predictions of mean temperature (K) contours for Berkeley CH_4/air lifted jet flame at baseline conditions. Contours plotted along the mid-plane (X=0) of the LES computational domain.....235

9.10: Variation in the instantaneous filtered temperature (K) distribution with respect to time. LES FPV-β function model predictions of Berkeley CH_4/air lifted flame at baseline conditions. All contours plotted along the mid-plane (X=0) of the LES computational domain.....238

9.11: Predicted and measured distributions (scattered data) of instantaneous temperature (K) at four axial stations in the Berkeley CH4/air lifted jet flame at baseline conditions.....241

9.12: Radial profiles of mean temperature at various axial locations in Berkeley CH_4/air lifted jet flame at baseline conditions.....244

I.1: Scenario of 4^{th} order interpolation in 3D space.....255

List of Tables

4.1: Standard k-ε model constants.....39

5.1: RANS based NO sub-models for SLFM and non-adiabatic flamelet modelling.....66

6.1: Co-efficients in the complete discretised equation with hybrid scheme.....114

8.1: Investigated Bluff-body flames and their conditions.....165

8.2: List of RANS Simulations carried for bluff-body stabilized flames using a grid of 162x111 (axial x radial) nodes.....170

Nomenclature

Roman Letters

C	Progress variable
C_p	Specific heat at constant pressure
h	Mixture enthalpy
k	Turbulent kinetic energy
l	Turbulent length scale
p	Pressure
$P( )$	Probability density function
Pe	Peclet number
Ro	Universal gas constant
Re	Reynolds number
u_k	Cartesian velocity components
W_i	Molecular weight of species
x_k	Cartesian direction components
Y_i	Mass fraction of species
Ze	Mass fraction of element
C_s	Smagorinsky co-efficient
Pr	Prandtl number
Sc	Schmidt number
T	Temperature
t	Time
Z	Mixture fraction
Z_{st}	Stoichiometric mixture fraction
NO	Nitric Oxide
Cou	Courant number

Greek Letters

Γ	Diffusive transport coefficient
$\Gamma( )$	Gamma function
δ	Delta function
γ	Time scale ratio

τ	Stress tensor
β	Beta function
λ	Flamelet parameter
δ_{ij}	Kronecker delta
ε	Rate of dissipation of turbulent kinetic energy
κ	Von karman constant
μ	Dynamic viscosity
μ_T	Dynamic eddy viscosity
ρ	Density
ζ	Enthalpy defect
ν	Kinematic viscosity
ϕ	Scalar variable
χ_c	Reactive scalar (progress variable) dissipation rate
χ	Scalar (mixture fraction) dissipation rate
$\overline{\Delta}$	Grid filter width

Diacritical marks

$\overline{\phi}$	Reynolds averaged mean of ϕ
$\widetilde{\phi}$	Favre filtered or Favre averaged value of ϕ
ϕ''	Fluctuations about the Favre filtered or averaged value of ϕ

Subscripts and superscripts

f, fu	Fuel
e	Element
in	Inlet
k	Cartesian directions
o, ox	Oxidizer
pr	Product
st	Stoichiometric
norm	Normalized
eq l	Equilibrium

q	Quenching limit
sfe	Steady flamelet equations

Abbreviations

CFD	Computational Fluid Dynamics
CMC	Conditional Moment Closure
RANS	Reynolds Averaged Navier Stokes
DNS	Direct Numerical Simulation
EPFM	Eulerian Particle Flamelet model
PDF	Probability density function
RIF	Representative interactive flamelets
rms	Root mean square
SIMPLE	Semi-implicit method for pressure linked equations
SLFM	Steady laminar flamelet model
TDMA	Tri-diagonal matrix algorithm
FPV	Flamelet/progress variable
LES	Large eddy simulation
SGS	Subgrid scale
FPDF	Filtered probability density function
HED	High enthalpy defect zone
NADM	Non adiabatic flamelet model with multiple flamelets
NADS	Non adiabatic flamelet model with single flamelet
RST	Reynolds stress transport model
NADM-NO-TRE	Non-adiabatic NO submodel based on steady transport equation
SLFM-NO-TRE	Adiabatic NO submodel based on steady transport equation
NADM-EPFM	Non-adiabatic NO submodel based on unsteady flamelets
SLFM-EPFM	Adiabatic NO submodel based on unsteady flamelets
DTRM	Discrete Transfer Method

Chapter 1

Introduction

1.1 Motivation

With the environmental regulations on combustion generated pollutants becoming stringent, optimum design of combustors, mainly those pertaining to automobile, aircraft, marine and industrial engines, is now of greater necessity than ever before. Modern day advanced combustors involve rapid mixing and short combustion times with complicated flow patterns to ensure proper flame stabilization. Design optimisation of the combustors thus demands a significant amount of testing, and industry is increasingly adopting numerical modelling to assist experimentation in this regard. Numerical modelling facilitates studying a wide range of coupled, interacting physical and chemical phenomena within the turbulent combusting flows, more closely and with greater flexibility compared to experiments. However, it is important that the predictive capability of numerical modelling is of sufficient engineering accuracy for the predictions to provide the right guidance to designers and consequently help in reducing the extent of experimentation and thereby the design cycle time and cost.

Amongst the available numerical modelling techniques, Direct Numerical Simulation (DNS) provides the highest accuracy as all the time scales and length scales involved in a turbulent combusting flow are completely resolved. However, the process of calculating a time dependent solution of the exact Navier Stokes equations and the equations pertaining to the transport of chemical species requires high end computational resources. Despite the significant advancements in computer technology, application of DNS has only reached as far as flows with Reynolds numbers of the order of 3000 in very simple geometries. Reynolds numbers for flows in practical combustors are several orders of magnitude higher and hence application of DNS to practical combustor flows cannot be envisaged in the foreseeable future.

Two alternative methods which avoid resolving the small scales by resorting to some form of averaging of the governing equations are the Reynolds Averaged Navier Stokes (RANS) and Large Eddy Simulation (LES) technique. RANS technique, in stark contrast to DNS, involves modelling all the scales and solves only for mean quantities in the flow. The result is a significant reduction in computational time which makes RANS best suitable for practical applications. Currently, RANS based simulation of complex combusting flows in large and intricate combustor geometries with nearly exact representation of the actual geometry has become an established practice in the gas turbine industry (Mongia, 2002). However, in RANS, significant amount of modelling of the governing equations is necessitated due to averaging of the equations. Consequently, it is critical for the adopted mathematical models, viz. for turbulence and combustion, to be of sufficient accuracy for RANS to provide reliable predictions. While the k-ε based models and the Reynolds Stress model have been more or less accepted as the preferred models for turbulence closure, there is an ever growing demand to increase the level of sophistication of the combustion models.

Over the past two decades, significant amount of research in numerical combustion has focussed on the development of RANS based combustion models which account for non-premixed and premixed combustion. The models which are developed on infinitely fast chemistry assumption are the simplest of all and are associated with quick turn around times. The most popular of these models include the Conserved Scalar Equilibrium Model which is valid for non-premixed combustion and the Bray Moss Libby Model (Bray and Moss, 1977; Libby and Bray, 1981) valid for premixed combustion. The models based on infinitely fast chemistry have significant limitations in regard to predictions of emissions.

Models which have been developed to account for finite-rate chemistry include, the PDF Transport Equation Model of Pope (1985) and Linear Eddy Model (LEM) of Kerstein (1992), Laminar Flamelet Model based on mixture fraction (Peters, 1984), Laminar Flamelet Model based on G-equation (Peters, 1986) and the Conditional Moment Closure Method (CMC) independently derived by Klimenko (1990) and Bilger (1993). The PDF and LEM models are applicable to both non-premixed and premixed combustion and are currently the most advanced combustion modelling

methods. However, their use in practical applications is as yet scant as the computational expense associated with these models is significantly high especially when elaborate chemical reaction mechanisms need to be considered in the analysis. The CMC Method and the Laminar Flamelet Model based on mixture fraction are formulated for non-premixed combustion while the Laminar Flamelet Model based on G-equation is formulated for premixed combustion. The CMC method is closely related to the flamelet model for nonpremixed combustion. However, the computational time needed for chemistry calculations with CMC is much higher than the flamelet model for nonpremixed combustion.

Most of the numerical modelling work using detailed chemistry in turbulent combustion is currently being done using flamelet models. The flamelet concept allows for numerical separation of turbulence and chemistry calculations leading to economic computational times whilst offering sufficient engineering accuracy in predicting low to moderate finite rate chemistry effects. The Laminar Flamelet Model, particularly for non-premixed combustion, is being extensively used in the gas turbine combustor industry (Held and Mongia, 1998a, 1998b; Held *et al.*, 2001) where CFD driven design of combustors essentially working in non-premixed mode is progressing at a rapid pace.

Consequently, there is also a growing demand to advance the predictive capability of the model especially in regard to capturing slow chemical phenomena such as NO_x formation, physical phenomena such as radiation and extreme finite rate effects like extinction and re-ignition which influence pollutant formation. Also, with the new generation low NO_x emission/low fuel consumption combustion systems using both the non-premixed and premixed modes of combustion, there is an interest in extending the applicability of the flamelet models, originally developed for non-premixed combustion, to partially premixed combustion.

Research aimed at advanced flamelet based models is thus of practical interest, as the advanced models are expected to enhance the utility of RANS based modelling which, is currently the main predictive tool for carrying out design iterations in the industry. While there is little doubt that RANS based modelling will continue to thrive as a design tool for at least the next decade or so, LES of turbulent combustion has started

establishing itself as an accurate and sophisticated alternative to RANS. Although LES of turbulent combustion has emerged as a science only in the 1990's and hence it is relatively new field, it has already been applied to a variety of combustion problems of technical interest including aircraft engine combustion (Moin 2002, Di Mare *et al*, 2004), blow-off in gas turbine combustors (Stone and Menon, 2003) and combustion generated instabilities (Pitsch, 2006). The relentless advancement in computer technology has been the main factor behind the rapid emergence of LES. However, much of the necessary theory for combustion LES has yet to be developed and the performance of the incorporated mathematical models stills needs to be corroborated for the large variety of combusting problems which exist in practice.

LES is motivated by the limitations of RANS and DNS and lies in between each of the two approaches in terms of computational expense. Unlike RANS, where all the scales are modeled, LES resolves the large scale turbulent motions which contain the majority of turbulent kinetic energy and control the dynamics of turbulence while modelling is restricted only to the small scales or the subgrid scales. Additionally, the model co-efficients for the sub-grid scale models can be determined as part of the solution by employing dynamic modelling (Germano *et al.* 1991). Thus, LES is expected to provide a more accurate and reliable representation of turbulence as compared to RANS, especially in flows where large-scale unsteadiness is significant. Typical examples include, the reciprocating engine flows and combustion generated instabilities in gas turbine engines.

The advantage with resolving the large scale motion is however not applicable to chemical source term as chemical reactions in turbulent flows occur essentially on the smallest scales. Thus, as with RANS, the chemical source term is entirely modelled. Despite this, LES still provides a substantial advantage because the scalar mixing process which is of paramount importance in chemical conversion can be predicted with a considerably improved accuracy as compared to RANS in complex flows (Pitsch, 2006).

The fact that combustion needs to be entirely modelled in LES means that the combustion models originally developed for RANS could be extended to LES. The flamelet models stand as a popular choice for subgrid scale combustion modeling as

detailed chemistry can be incorporated with the least penalty in computational cost which is as such an order of magnitude higher with LES as compared to RANS. Extension of flamelet models to LES of non-premixed combustion and their performance evaluation has drawn significant research in the past (Cook and Riley, 1998; Pitsch and Steiner, 2000; Pitsch, 2002; Mahesh *et al.*, 2004; Raman and Pitsch, 2005) and it is ever growing due to the increasing interest shown by industry to adopt LES as an advanced numerical tool.

A recent breakthrough in flamelet based modelling of turbulent non-premixed combustion is the Flamelet/Progress Variable (FPV) approach of Pierce and Moin (2004). Using LES, this flamelet based approach has been shown to exceed the accuracy of the flamelet model of Peters (1984) for non-premixed combustion. An interesting advantage that has been claimed (Pierce and Moin, 2004) with this approach is its ability to simultaneously account for partially premixed combustion. Such versatility is indeed of great advantage in practical applications. Hence, research work that can further explore the strengths and weaknesses of this approach and contribute to its development is not only of academic interest but also of practical interest. The predictive capability of the FPV approach in LES of turbulent partially premixed combustion and the extent to which RANS based modelling could benefit from the approach are questions yet to be answered and hence attract research attention.

Motivated by the current and future needs of the industry, in particular the gas turbine industry, present research work focuses on advancements in flamelet models for RANS and LES based modelling of turbulent gaseous non-premixed and partially premixed combustion.

1.2 Objectives

The specific objectives of the current research are:

1. Develop and evaluate the predictive capability of a RANS turbulent non-premixed combustion modelling strategy which is based on a steady non-adiabatic flamelet model integrated with steady or unsteady non-adiabatic flamelets based pollutant NO submodels.

2. Conduct the first ever investigation into the predictive capability of Flamelet/Progress Variable approach based combustion models in turbulent partially premixed combustion using RANS and LES based modelling approaches.

It was proposed to conduct the current research by incorporation of the advanced flamelet models into the in-house FORTRAN based RANS and LES numerical codes. Thus, by achieving the aforementioned objectives, it is expected that this research would not only contribute to the knowledge in the predictive capability of the advanced models but would also enhance the sophistication of the in-house RANS and LES combustion modelling facility.

In order to achieve the ultimate objectives of this research the following tasks have been laid out to be accomplished:

1.1 Incorporation of a Reynolds stress transport model based turbulence closure in the in-house RANS code

1.2 Incorporation of steady laminar flamelet model, non-adiabatic flamelet model and flamelet/progress variable approach based models in the in-house RANS code with the capability of conducting calculations through a computationally efficient look-up-table strategy.

1.3 Development of pollutant NO post-processing tools based on steady and unsteady flamelets based NO submodels.

1.4 Development of pre-processing tools for generating pre-integrated look-up-tables specific to a combustion model for RANS and LES combustion calculations.

1.5 Incorporation of a steady laminar flamelet model and flamelet/progress variable approach based models in the in-house LES code with the capability of conducting calculations through look-up-table strategy.

1.6 RANS based modelling of turbulent non-premixed bluff-body stabilized flames and piloted jet flames with steady flamelet model and non-adiabatic flamelet model in conjunction with pollutant NO submodels and RST model for turbulence closure.

1.7 LES and RANS based modelling of turbulent partially premixed lifted jet flames using flamelet/progress variable approach based models as well as the steady laminar flamelet model.

1.3 Thesis outline

In this chapter the motivation behind this research and the specific objectives have been discussed. The remainder of the thesis has been organized as follows:

Chapter 2: Literature in the area of flamelet based modelling of turbulent non-premixed and partially premixed combustion has been reviewed. Works carried out in the context of both RANS and LES has been presented.

Chapter 3: The governing equations for turbulent combusting flows in their instantaneous form have been presented along with an overview of the different simulation methods, DNS, LES and RANS.

Chapter 4: The RANS and LES approaches of modelling turbulence have been presented. With respect to the RANS approach, the k-ε model and the Reynolds stress transport model based turbulence closures adopted in the presented study have been presented. The LES formulation has been discussed in detail through the description of filtering technique, models employed for the closure of subgrid stress and models employed for closure of subgrid scalar fluxes.

Chapter 5: Combustion models incorporated into the in-house RANS and LES codes have been presented. The formulations of the steady flamelet model, the non-adiabatic flamelet models and the different NO submodels used by the RANS calculations have been presented first. Subsequently, the extension of steady flamelet model to LES has been presented. Finally, the motivation for the development of flamelet/progress variable approach has been explained and its formulation in LES and RANS based modelling has been presented.

Chapter 6: The numerical approach adopted by the in-house RANS and LES codes has been presented. A detailed description of the working procedures of the RANS and LES combustion calculations with the different combustion models and NO submodels has been presented.

Chapter 7: The pre-processing calculations required to generate the inputs for the RANS and LES combustion calculations has been presented. The process of generating the different types of flamelets for the different flames modelled in the present study has been discussed first. Subsequently, processing of these flamelets to obtain pre-integrated look-up-table has been discussed. A detailed working procedure has been presented for the pre-processing tools developed for the steady flamelet model, non-adiabatic flamelet model and the FPV approach based models.

Chapter 8: Results from the RANS based modelling of turbulent non-premixed bluff-body stabilized and piloted jet flames using the steady flamelet model and non-adiabatic flamelet model in conjunction with pollutant NO submodels have been presented and the relative performances of the models has been discussed.

Chapter 9: Results pertaining to the RANS and LES based modelling of turbulent partially premixed lifted jet flames with steady flamelet model and the flamelet/progress variable approach based models have been presented and the relative strengths and limitations of the models has been discussed.

Chapter 10: Conclusions from the modelling study, directions for future work and key contributions from the current research work have been presented.

Chapter 2

Literature Survey

In this chapter, research works which have contributed to the development of flamelet models for RANS and LES based modelling of turbulent non-premixed and partially premixed flames have been reviewed. Works employing flamelet models for turbulent non-premixed flames have been discussed in section 2.1 followed by the works on flamelet models specifically developed for partially premixed flames in section 2.2. Since the flamelet/progress variable approach has been originally developed for turbulent non-premixed combustion but the current interest is to apply it to partially premixed combustion, works carried out on this approach have been dealt separately in section 2.3.

2.1 Flamelet models for turbulent non-premixed combustion

In the process of turbulent non-premixed combustion, fuel and oxidizer enter separately into the combustion chamber where they mix and burn during continuous interdiffusion (Example, industrial furnaces, diesel engines, and traditional gas turbine combustors). Turbulent nonpremixed combustion is often referred to as turbulent diffusive combustion or combustion in diffusion flames since diffusion is the rate-controlling process. The laminar flamelet model of Peters (1984) also known by steady or stretched laminar flamelet model (SLFM) is based on the proposed view of Williams (1975) that a turbulent diffusion flame consists of an ensemble of 'flamelets' which are stretched in a turbulent reacting flow. The theory of existence of laminar flamelets in turbulent flows has been validated analytically (Peters 1983; 1984) as well as experimentally (Roberts and Moss, 1981; Drake, 1986). The 'flamelets' represent thin one dimensional laminar diffusion flames and a parameter in the form of scalar dissipation rate quantifies the extent of stretch experienced by the

flamelets. For a fixed level of stretching, all the thermo-chemical properties of a flamelet are expressed as a function of conserved scalar, the mixture fraction which quantifies the extent of mixing of the reactants. Hence, according to the flamelet model, the thermo-chemical structure of a turbulent non-premixed flame is dependent only on mixture fraction and scalar dissipation rate which are statistically distributed in a turbulent flow. To predict non-equilibrium effects in turbulent non-premixed flames, introduction of these flamelets into turbulent flow is performed by considering their joint probability density function. The evaluation of joint PDF is simplified by assuming statistical independence and presuming the shape of the PDF for mixture fraction to follow a β function and that of scalar dissipation to follow log-normal distribution. By numerically separating the turbulent flow calculations from those of chemistry, the laminar flamelet model drastically simplifies the effort required in turbulent flow calculations and facilitates accounting of detailed chemical kinetics.

2.1.1 SLFM based modelling in RANS

Liew *et al.* (1984) were the first to apply SLFM for modelling turbulent methane-air jet diffusion flames. Employing experimentally obtained flamelet profiles, they showed that the model is successful in predicting the observed oxygen penetration through burning zone due to local quenching. However, both O_2 and CO concentrations were overpredicted thereby leading to the conclusion that amendments are required in the model to account for the post flamelet process where probable partial mixing of reactants occurs. Haworth *et al.* (1988a) and Lentini (1994) applied SLFM to $CO/H_2/N_2$ (Syngas) turbulent jet diffusion flame and found that model's prediction capability with respect to super equilibrium concentration of OH radical is superior to that of equilibrium model. However, both works showed that SLFM predicts an overly rapid approach to chemical equilibrium. Haworth *et al.* (1988a) stated that this could possibly be tackled by considering the time variation of scalar dissipation rate. Lentini (1994) also applied SLFM to methane-air jet flame test cases previously studied by Liew *et al.* (1984). His work showed that inclusion of a range of flamelets representing burning states (ranging from close to equilibrium to extinction condition) plus an additional flamelet representing extinguished state improves the accuracy of the reactive scalars particularly CO which was overpredicted by Liew *et*

al. (1984). Lentini and Puri (1995) further corroborated this strategy of flamelet library with SLFM by studying a chloromethane-air turbulent jet diffusion flame.

Application of SLFM to relatively complicated reacting flame structures in the form of bluff-body stabilized flames has been carried out by Hossain (1999) who used the steady laminar flamelet model with a range of flamelets similar to that advocated by Lentini (1994). He studied the model's performance in $CO/H_2/N_2$ and CH_4/H_2 bluff-body stabilized flames of Correa and Gulati (1992), and Dally *et al.* (1998a) respectively. These flames operate at different blow-off limits thereby allowing for an investigation into the model's ability to capture extreme finite rate effects. The SLFM was found to result in good agreement with data for flames operating far from blow-off. However, the model failed to predict experimentally observed localized extinction in flames which are 70% and 90% close to blow-off. This showed that in SLFM, the approach of considering extinction on criterion of mean scalar dissipation rate exceeding the quenching limit is not adequate and use of transient flamelets have been suggested. The inadequacy of SLFM to predict the experimentally observed local extinction and re-ignition has also been reported by Ferreira (1996, 2001) who studied methane-air jet diffusion flames of Masri *et al.* (1988).

Additional insight into the predictive capability of SLFM has been provided through works on flamelet based NO modelling. Vranos *et al.* (1992) were the first to use flamelet concept for prediction of NO in turbulent methane-hydrogen jet flame. They showed large discrepancies between the flamelet model results and the measured NO levels. Overprediction of differential diffusion effects of hydrogen and hydrocarbon species, transient effects and flame interactions were speculated as causes for the discrepancy. Similar findings were obtained from the works of Sanders *et al.* (1997) and Schlatter *et al.* (1996). The above speculated causes for NO overprediction and in addition the effect of radiative heat loss on NO formation were tested by Chen and Chang (1996) using SLFM as well as joint scalar PDF approach. Their study showed that radiative heat loss plays an important role in the predicted NO levels especially at downstream portion of the jet flame where the residence time of the flamelet is high enough for effects of radiation to become significant. Work of Heyl *et al.* (2001) showed that NO mass fraction predictions have strong dependence on the form of the PDF for scalar dissipation rate. Hossain and Malalasekera (2003) conducted SLFM

based NO modelling of bluff body stabilized CH_4/H_2 flame through a mean NO transport equation based approach. Contrary to the findings of earlier modelling works on NO, their results showed large underprediction. This was attributed to the simplified NO chemistry which accounted for only thermal NO and therefore the need for accounting for all possible NO production pathways was highlighted.

With the insight provided by these and several other modelling works with SLFM, developments to SLFM have been made to account for transient effects on reactive scalar structure including NO, radiation heat loss and partial premixing.

2.1.2 Transient flamelet modelling in RANS

In SLFM, the flamelets are generated from the steady form of flamelet equations of Peters (1984) and the flamelet library is typically parameterized in terms of values of the scalar dissipation rate at the stoichiometric mixture fraction. Because of the omission of the time dependent term, the underlying assumption is that the imposed value of the scalar dissipation rate varies slowly enough. If the scalar dissipation varies rapidly, however, the unsteady term in the flamelet equations must be retained leading to a slow relaxation of the profiles. The importance of time dependent flame structures in laminar flamelet models for turbulent jet diffusion flames was first shown by Haworth *et al.* (1988b). They introduced an ad-hoc modification to the laminar flamelet model through an equivalent strain analysis and obtained improved agreement with data for $CO/H_2/N_2$ jet flame.

Unsteady flamelets were first employed by Mauss *et al.* (1990) to simulate flamelet extinction and re-ignition in a steady turbulent jet diffusion flame. A Lagrangian time was introduced to account for history effects in the flamelet structure. Unsteady effects caused by localized extinction in steady jet diffusion flames was studied by Ferreira (1996, 2001) who developed a transient laminar flamelet model (TLFM) which uses a transient flamelet library parameterized by mixture fraction, scalar dissipation rate, reaction progress variable and flamelet residence time similar to the Lagrangian time. TLFM was shown to reproduce to a reasonable extent the local extinction and re-ignition behaviour observed in the jet diffusion flames experimentally studied by Masri *et al.* (1988).

The importance of transient effects in modelling steady jet diffusion flames has also been discussed by Pitsch *et al.* (1998) who developed an unsteady model called the Lagrangian flamelet model. They observed that the modelling of unsteady and radiation effects hardly influenced the temperature and major species distribution in the studied nitrogen diluted hydrogen flame. However, significant improvement was found for the mean NO distribution in the flame. An important observation from their work is that consideration of radiation through a radiation source term in steady flamelet equations leads to deterioration in predictions since the omission of time dependent term leads to inaccurate capturing of the effect of radiation heat loss which is a slow physical phenomenon. However, the same when considered with unsteady flamelet equations improves the predictions for NO. Hence, their work suggests that transient flamelet modelling is essential both from the perspective of slow chemistry of NO as well as consideration of effect of radiation heat loss on NO. Later, Pitsch (2000) extended the Lagrangian Flamelet Model to account for differential diffusion effects in steady turbulent $CH_4/H_2/N_2$-air diffusion flame of Bergmann *et al.* (1998) and found reasonably good agreement with data.

Unsteady flamelet models have also been applied to turbulent unsteady flows, like those in diesel engines. Pitsch *et al.* (1996) proposed a new concept called "Representative Interactive flamelet" (RIF) where unsteady 1D flamelet calculations are interactively coupled with the CFD code. The flamelet parameters that govern the unsteady evolution of the flamelets are extracted from the solution of the CFD code by statistically averaging over a representative domain. This model was applied to an n-heptane fueled diesel engine and was found to be capable of describing auto-ignition, the following burnout of the partially premixed phase, and the transition to diffusive burning. A very good agreement with data for NO_x and slight under-prediction of soot has been reported. In the RIF model of Pitsch *et al.* (1996), only one interactive flamelet was considered representative of entire domain and the spatial variation of scalar dissipation rate was ignored. Barths *et al.* (1998b) extended the RIF model to multiple flamelets which account for the spatial dependence of scalar dissipation rate. Numerical tracer particles each representing a flamelet history is introduced into the turbulent flow field. An unsteady convection-diffusion equation is solved in CFD code for each tracer particle to find the probability of local occurrence of flamelet. The current flamelet solution is then weighted with these local

probabilities to obtain scalar concentrations. This approach has been named as Eulerian Particle flamelet model (EPFM). This model was applied to turbulent non-premixed DI diesel engine combustion by Barths *et al.* (1998b) and Barths *et al.* (2000). They found a significant improvement in the prediction of partially premixed burning phase and subsequent pollutant formation, NO_x and Soot.

The EPFM has also been applied to steady turbulent non-premixed combustion in a gas turbine combustor by Barths *et al* (1998a). One of the main advantages of EPFM over Lagrangian model is it's applicability to both parabolic as well as elliptical flows. In the Lagrangian flamelet model the flamelet time is computed by integration of the inverse of the streamwise velocity at the stoichiometric radial position along the streamwise direction which limits its application to strictly parabolic flows. For thorough validation of EPFM, Coelho and Peters (2001a) simulated the piloted methane/air jet flame of Barlow and Frank (1998). Unsteady calculations were performed in the post processing stage using Eulerian transport equations for passive scalars to describe temporal evolution of the scalar dissipation rate. Predictions with EPFM were shown to have significantly better agreement for NO compared to those with SLFM. Coelho and Peters (2001b) applied EPFM to a combustor with high air preheating and strong internal exhaust gas recirculation. Good agreement to data for NO_x emissions was achieved. In a recent work of Riesmeier *et al.* (2004), the EPFM was applied to kerosene fueled diffusion flame gas turbine combustor and encouraging predictions for exhaust emissions, NO_x and soot were achieved.

This review on works on transient flamelet modelling shows the importance of unsteady flamelets for accurate prediction of NO. Unsteady flamelet modelling is also a necessity if the effect of radiation heat loss on NO is to be considered through a radiation source term in the flamelet equations.

2.1.3 Non-adiabatic flamelet modelling in RANS

While, accounting for the effect of radiation heat loss on the thermo-chemical structure of the flame through a radiation source term in the flamelet equations is a simple method, Bray and Peters (1994) suggested that it is more appropriate to consider the effect of emission and absorption over a wide range of length scales

present in a turbulent flame. They introduced a parameter called 'enthalpy defect' (difference between the adiabatic and actual enthalpy) to provide the coupling between the non-adiabatic turbulent flow and the flamelet structure. The flamelet library is then parameterized by mixture fraction, scalar dissipation rate and additionally the enthalpy defect. Based on this concept, Marracino and Lentini (1997) developed a non-adiabatic flamelet model to study the effects of radiation in turbulent methane/air jet flames. Considering an optically thin medium assumption for the gas phase radiation, they obtained marked improvement in mean temperature predictions. This non-adiabatic flame model was extended by Giordano and Lentini (2001) to account for turbulence-radiation interaction. Hossain *et al.* (2001) extended SLFM to a non-adiabatic model using the enthalpy defect concept and the methodology of Marracino and Lentini (1997). The Discrete Transfer Method has been used for radiation source term calculations. They validated the model for turbulent CH_4/H_2 bluff-body flames and found marked improvements in OH radical concentrations. However, no notable improvement in temperature or major species was reported. Enthalpy defect based non-adiabatic flamelet modelling has also been reported by Ma *et al.* (2002) who extended the premixed flamelets based mixedness-reactedness flamelet model of Bradley *et al.* (1990) to account for thermal radiation in laboratory scale and large scale natural gas flames. Reasonable improvements in the mean temperature have been reported with the non-adiabatic model.

Use of non-adiabatic flamelet models different to the enthalpy defect concept has also been reported. Young and Moss (1995) presented an approach which is rather arbitrary. According to their approach, the enthalpy and mixture fraction relationship derived from detailed laminar flamelet calculations is first linearly approximated and then a series of radiatively perturbed flamelets are generated from this by systematic variation of a heat loss parameter which prescribes the fraction of the sensible enthalpy, relative to ambient, lost from the adiabatic profile. Solution procedure in CFD then involves identifying locally most appropriate "heat loss" flamelet. Radiation source term in CFD adopt an optically thin limit approximation. This approach was used in modelling sooting turbulent jet flames by Young and Moss (1995) while Carpentier *et al.* (2005) applied the same to model NO in turbulent natural gas flames in industrial furnaces.

Coelho *et al.* (2003) developed a non-adiabatic approach based on steady flamelet model for studying the spectral radiative effects and turbulence/radiation interaction in turbulent jet diffusion flames. This approach employs steady flamelet equations and ignores the effect of radiative heat transfer on flamelet chemical composition. Effect of radiation heat loss on flamelet temperature is however accounted through an implicit equation which is a function of temperature, conditional averaged scalar dissipation rate and radiation heat loss factor which is obtained from calculations based on Discrete Ordinates Method. Later Coelho (2004) employed this approach to study the different methods of accounting for turbulence-radiation interaction in turbulent jet diffusion flames. This approach however, is not suitable for modelling NO. Recently Xu *et al.* (2006) developed a non-adiabatic form of Lagrangian flamelet model. In this model, the effects of thermal radiation on thermo-chemical structure of the flame are accounted through a radiation source term in unsteady flamelet equations which is obtained from CFD using detailed radiation calculations based on finite volume correlated *k* method. They applied this model to methane/air Sandia D jet flame and showed promising improvements for temperature, major species as well as NO.

Current Work: The non-adiabatic flamelet modelling carried out in the current work, extends the work carried by Hossain *et al.* (2001). The non-adiabatic flamelet model has been integrated with non-adiabatic NO submodels to facilitate NO modelling with the consideration of radiation heat loss effects on NO production. Both steady and unsteady (EPFM) non-adiabatic flamelets based NO submodels have been developed for integration with the non-adiabatic flamelet model. The steady NO submodel involves solving a transport equation for the mean NO mass fraction with its production term derived from enthalpy defect imposed non-adiabatic flamelets. In the unsteady (EPFM) non-adiabatic NO submodel, the mixing field is first obtained from the non-adiabatic flamelet model calculations in CFD. Subsequently, time history of scalar dissipation rate is extracted from post-processing calculations using EPFM. The time history is then used to generate the unsteady NO evolution from unsteady flamelet equations with radiation accounted through an optically thin limit approximation. Thus, the unsteady non-adiabatic NO submodel takes into account both the effects of radiation heat loss and the transient evolution of laminar structure

of NO. The non-adiabatic model employs a detailed chemical kinetic mechanism in the form of GRI 2.11 thereby accounting for all possible NO formation pathways. Development has also been made in regard to the computational efficiency of the model in that CFD calculations with the non-adiabatic model now run on a look-up-table strategy. Further details on the non-adiabatic model are given in section 5.3.

2.1.4 SLFM based modelling in LES

Flamelet models have been extended to LES as subgrid scale combustion models by taking guidance from closure procedures that have been successful on the RANS level. Cook and Riley (1997) were the first to extend steady laminar flamelet model to LES. They employed a presumed shape beta PDF formulation called the Large Eddy Probability Density Function (LEPDF), for the mixture fraction and the flamelet profiles were obtained from a single step reaction. The LEPDF was proposed in their previous work (Cook and Riley, 1994) by the filtered mixture fraction and its subgrid variance which is obtained from an algebraic model equation based on scale similarity assumption. This model was found to be reasonably accurate compared to DNS data of homogeneous, isotropic decaying turbulence. Cook and Riley (1998) performed further a priori testing of this model by varying the activation energy of the one-step model and obtained better agreement with DNS data than models using equilibrium chemistry. The LEPDF model of Cook and Riley (1994) has been tested by Jiménez *et al.* (1997) together with a lognormal PDF for scalar dissipation rate and the scale similarity assumption. De Bryun kops *et al.* (1998) performed a full LES calculation with steady flamelet model by solving the balance equations for filtered mixture fraction and its variance. The model was found to accurately reproduce the spatial average of the filtered species obtained from DNS data.

While the above works were restricted to a priori studies, LES of large scale turbulent non-premixed flames with steady flamelet model was first conducted by Pierce and Moin (1998). They proposed a dynamic model for the calculation of subgrid scale variance of mixture fraction and scalar dissipation rate. Using the dynamic model, they conducted LES of a swirling, confined, coaxial jet flame and obtained convincing comparisons with experimental data. Branley and Jones (1999) employed the dynamic model of Pierce and Moin (1998) and conducted LES of swirling

methane flame with a single flamelet profile. The results showed good qualitative agreement with the measurements.

Raman and Pitsch (2005) developed a new strategy for LES grid generation, namely the Recursive filter refinement procedure which generates optimized clustering of grid for variable density simulations. This procedure was used along with the steady flamelet model for subgrid scale combustion and the dynamic model of Pierce and Moin (1998) in the simulation of turbulent CH_4/H_2 bluff-body stabilized flames and excellent match with experimental data was obtained. Kempf (2005) conducted LES of piloted methane/air jet flame using a steady flamelet model with a library of multiple flamelets obtained from detailed chemistry. The subgrid mixture fraction variance was modelled using the approach of Forkel (1999) while the filtered scalar dissipation rate was obtained from the model suggested by Girimaji and Zhou (1996) and De Bruyn Kops *et al.* (1998). Their calculations showed that for the selected partially premixed fuel, steady flamelet approach sufficiently describes the major species except for CO which is overpredicted in the fuel rich region. Using the same LES strategy, Kempf (2006) conducted LES of CH_4/H_2 bluff-body stabilized flames of Dally *et al.*(1998a) and obtained encouraging results for temperature and major species but they reported significant errors in the computed NO concentration. Recently, Ranga-Dinesh *et al.* (2006) employed a single flamelet based steady flamelet model to study LES of turbulent CH_4/H_2 unconfined swirling flames. They adopted the scale similarity model of Cook and Riley (1994) to model the subgrid variance of mixture fraction and employed the localized dynamic procedure of Piomelli and Liu (1995) to calculate the turbulent eddy viscosity. Their results showed reasonably good results for temperature and major species. However, the predictions failed to capture the downstream vortex breakdown in the flame.

Application of unsteady flamelet models to LES was first taken up by Pitsch and Steiner (2000). They employed the Lagrangian flamelet model (Pitsch *et al.*, 1998) along with the dynamic model of Pierce and Moin (1998) for the subgrid variance of mixture fraction. The unsteady flamelet equations were coupled with the LES solution to provide the filtered density and other filtered reactive scalar quantities. The scalar dissipation rate required to solve flamelet equations was determined from a method proposed by Bushe and Steiner (1999). They employed the model to a piloted

methane/air diffusion flame and found promising results especially for NO. This study was also the first demonstration of combustion LES of a realistic configuration using a detailed description of chemistry. A more advanced subgrid scale flamelet combustion model has been developed by Pitsch (2002) wherein flamelet equations are rewritten in Eulerian form which leads to a full coupling with the LES solver and thereby enables the consideration of the resolved fluctuations of the scalar dissipation rate. This model was used in LES of piloted methane/air jet diffusion flames and significant improvements in the CO formation have been achieved in comparison to the Lagrangian flamelet model based calculations of Pitsch and Steiner (2000) and steady flamelet model calculations of Kempf (2005).

Current Work: In the current work, LES with steady flamelet model has been conducted on a turbulent lifted methane-air jet flame using a look-up-table strategy which allows for consideration of variation in thermo-chemical structure of the flame with respect to the filtered scalar dissipation rate. The presumed filtered PDF for filtered mixture fraction assumes a β function while that for filtered scalar dissipation rate assumes a log-normal distribution. The subgrid scale variance of mixture fraction and the filtered scalar dissipation rate have been modelled based on the suggestions of Cook and Riley (1994) and Cook and Riley (1998), respectively. The turbulent eddy viscosity has been evaluated using the local dynamic procedure of Piomelli and Liu (1995). Current work on LES, extends the work carried by Ranga-Dinesh *et al.* (2006) in that the sophistication of the steady flamelet model in the in-house LES code has been enhanced by relaxing the assumption of a single representative filtered scalar dissipation rate. Further details are presented in section 5.2.4.

2.2 Flamelet models for turbulent partially - premixed combustion

If fuel and oxidizer enter separately, but partially mix by turbulence, combustion occurs in a stratified medium upon ignition. Such a mode of combustion has been traditionally referred to as partially premixed combustion. However, such a situation can be created as well when a premixed fuel and an oxidizer enter in separate streams.

Partially premixed combustion profits from the advantageous features of both the extreme modes of combustion, the non-premixed and premixed, while avoiding their adverse effects. Non-premixed combustion is faced with the concerns of excessive NO_x formation at the stoichiometric mixture fraction where temperatures are conducive for thermal NO. While lean premixed combustion which is adopted in low NO_x lean-burn gas turbine engines is a solution to this problem, it poses the challenge of handling combustion generated instabilities.

Examples of partially premixed combustion range from aircraft gas turbine engines to large scalar industrial boilers. In aircraft engine combustors, flame propagation through a stratified mixture occurs when the hot gases from pilot burner come into contact with the inhomogeneous mixture formed at the main injector inlet. Another practical example results from the molecular mixing of species after local flamelet extinction in a turbulent flame. If conditions in the turbulent flame are favorable after molecular mixing, then the mixed reactants can ignite and burn in a premixed fashion. Direct injection gasoline engines are another example where partially premixed combustion can be observed.

Another important manifestation of partially premixed combustion is the lift-off and the stabilization at the lift-off height in turbulent jet diffusion flames. Lift-off occurs commonly in large industrial boilers where lifting the flame base off the burner prevents erosion of the burner rim although at the risk of increasing the susceptibility of the flame to blowoff. Explanations of the stabilization mechanism for lifted jet diffusion flames have however been quite controversial. Vanquickenborne and Van Tigglen (1966), Eickhoff *et al.* (1984) and Kalghatgi (1984) have shown from measurements that the stabilization of a lifted diffusion flame is governed by premixed turbulent flame propagation. On the other hand, Janicka and Peters (1982) and Peters and Williams (1983) proposed diffusion flamelet extinction as the responsible mechanism for flame stabilization. The idea that large scale turbulent structures control flame stabilization has also been discussed by Broadwell *et al.* (1984). In the recent years, triple flames have attracted much interest, because it is believed that they may play a significant role in many partially premixed combustion situations including the stabilization of lifted jet flames. Liñán (1994) and Veynante *et al.* (1994) have shown theoretically that in a laminar flow lifted flames are stabilized

by a triple flame configuration. The leading edge of a triple flame, called the triple point, propagates along a surface that is in the vicinity of stoichiometric mixture fraction. On the lean side of that surface there is a lean premixed flame branch while on the rich side there is a rich premixed flame branch, both propagating with a lower burning velocity. Domingo and Vervisch (1996) showed that the triple flame, also called as tribrachial flame or edge flame is more robust than a diffusion flame. In view of the many different aspects that are potentially important for a physically correct description of flame stabilization at the lift-off height, formulation of a turbulent combustion model is rather difficult.

Bradley *et al.* (1990) proposed a flamelet model called the mixedness-reactedness model in which combustion proceeds essentially as premixed turbulent flame propagation. This model employs premixed laminar flamelets rather than the conventional diffusion flamelets in the flamelet model for nonpremixed combustion, and allows for a degree of premixing before combustion occurs. The volumetric heat release rates are computed for a range of equivalence ratios or mixture fraction or the mixedness parameter from premixed laminar flamelet structure which is provided as a function of reaction progress variable or the reactedness parameter. It is assumed that the premixed flamelet structure remains unaltered as long as the instantaneous strain rate is less than a critical quenching value beyond which flamelet extinguishes. The mean heat release rates are then calculated from the marginal PDFs of mixture fraction, reaction progress variable defined on the basis of dimensionless increase in temperature due to reaction and strain rate. The marginal PDF for flame straining is assumed to follow a quasi-Gaussian shape and both the PDF for mixture fraction and that of reaction progress variable is assumed to follow beta function distribution. The lift-off height is determined as the location of onset of heat release rate. The predicted lift-off heights compared favorably with the experimental data of Kalghatgi (1984). This model was later improved by Bradley *et al.* (1998a, 1998b) by allowing for flame extinction at both positive and negative strain rate. The model was found to not only predict the lift-off heights of Donnerhack and Peters (1984) but also the blow-off velocity as a function of nozzle diameter as reported by Kalghatgi (1981).

Sanders and Lamers (1994) formulated a model based on diffusion flamelet extinction. The stretch on the flame was accounted by a strain rate rather than scalar

dissipation rate. In addition, to model the influence of large scale structures, they used a PDF of spatial fluctuations to determine the mean reactive scalars. This model reproduced approximately the correct slope of linear dependence of lift-off heights on exit velocities in turbulent natural gas lifted diffusion flames.

Müller *et al.* (1994) developed a model for partial premixed turbulent combustion using the G-equation approach similar to that adopted by the premixed laminar flamelet model of Peters (1986). Their model is based on two scalar fields, the mixture fraction and the scalar G which determines the location of the flame front. The mixture fraction determines the local equivalence ratio and thereby the value of the laminar burning velocity as a function of mixture fraction. Both the scalars are then subjected to turbulent modelling. The G-equation formulation used for flame propagation differs from the level-set approach of Peters (1986) in that the laminar burning velocity is now a function of scalar dissipation rate as well as mixture fraction. For the turbulent burning velocity, Müller *et al.* (1994) proposed a model containing three terms: a term for premixed flame propagation, a term accounting for partial premixing, and a flamelet quenching term. By including the three terms, they claimed to have accounted for both the premixed flame propagation and diffusion flamelet extinction theories. This model was applied to turbulent methane diffusion flames and was shown to be successful in predicting the upstream propagation within a partially premixed jet and the stabilization of the turbulent flame at the lift-off height. Müller *et al.* (1994) claimed that the premixed flame propagation term controls the upstream flamelet propagation while the modelling of the flamelet quenching term controls the lift-off height. However, it was later concluded that the diffusion flamelet extinction was not the mechanism that has been modelled. Henceforth, Peters (1999) modified the formulation and based it entirely on the premixed flame propagation mechanism.

The partially premixed flamelet model of Peters (1999) combines the flamelet models for non-premixed and premixed combustion. The level-set, G equation, approach is used to calculate the location and geometry of the premixed flame front while mixing is accounted by mixture fraction. The dependence of scalar field on mixture fraction is accounted by a diffusion flamelet structure. The turbulent partially premixed burning velocity is based on the premixed flame propagation but takes into account the partial premixing via a conditional turbulent burning velocity based on mixture fraction. This

model has been successfully applied to turbulent methane and propane jet flames by Chen *et al.* (2000) and it was shown that the mean structure of the lifted flame is similar to that of a laminar triple flame and the lift-off heights were found to be in good agreement with measurements.

Extension of the partially premixed flamelet model of Peters (1999) to LES has been carried out by Duchamp de Lageneste and Pitsch (2001). Validations have been carried through LES of turbulent bunsen burner flames as well as turbulent partially premixed combustion in a dump combustor. The predictions have been shown to be good agreement with experimental measurements thereby showing the ability of the approach to handle both premixed as well as partially premixed combustion. Pitsch and Duchamp de Lageneste (2001) also reported the successful application of this model in LES of turbulent lifted methane/air flames.

Current Work: Current work differs from the reviewed works in that the partially premixed combustion has been modelled using a turbulent combustion model, namely the Flamelet/progress variable (FPV) approach, which was primarily developed (Pierce and Moin, 2004) for turbulent non-premixed combustion but uses a two scalar, mixture fraction and reaction progress variable, formulation. Also, the test case chosen for the simulation of partially premixed combustion is that of a turbulent lifted methane-air jet flame where the fuel is premixed (Cabra *et al.*, 2005). Hence, the numerical simulations employ partially premixed flamelets. These flames have an additional feature of interest in that the fuel jet is surrounded by high temperature vitiated coflow and this introduces a new flame stabilization mechanism in the form of auto-ignition in addition to the premixed flame front propagation. However, the extent of numerical investigation undertaken in the present work does not attempt to draw definitive conclusions about the exact mechanism responsible for the model's ability to capture the flame lift-off. Instead, the investigations are limited to the extent of studying the ability of the models based on the FPV approach to capture the gross characteristics of the lifted flame when employed in LES as well as RANS.

2.3 Flamelet/Progress Variable (FPV) approach

A model that was developed specifically for LES is the flamelet/progress variable (FPV) model of Pierce (2001) and Pierce and Moin (2004). This model uses steady state flamelets but is substantially different from the typical SLFM used by the aforementioned works. The FPV approach uses a reaction progress variable instead of a scalar dissipation rate to parameterize the flamelet library. The advantage of this different way of parameterizing is that it potentially gives a better description of local extinction and re-ignition phenomena and flame lift-off. With scalar dissipation rate as a parameter, typically only the steady state solutions lying below the extinction limit and those on fully extinguished state are considered in the flamelet library. Consideration of partially extinguished states is not possible since they result in a non-unique parameterization of the flamelets. Adopting reaction progress variable addresses this problem and the full range of steady state solutions can be considered in the library. In LES, the model requires solving a transport equation for the filtered reaction progress variable which can be defined as the sum of product mass fractions. The challenge in using the reaction progress variable is that, in order to close the model, the joint PDF of mixture fraction and reaction progress variable needs to be provided. Pierce and Moin (2004) in their study on confined coaxial jet swirling non-premixed flame, employed a delta (δ) function for the filtered PDF of reaction progress variable. They showed significant improvement with the FPV approach in comparison to SLFM especially in the accuracy with which the flame stabilization region was captured. The FPV model can be interpreted as a two variable intrinsically low dimensional manifold (ILDM) model (Maas and Pope, 1992), where the ILDM library tabulation is generated with a flamelet model.

Potential areas for the improvement of this approach have been identified by Ihme *et al.* (2005) in *a priori* tests using DNS data of turbulent non-premixed combustion in isotropic turbulence. The model for the presumed filtered PDF for reaction progress variable was considered important. The beta (β) function was proposed as a possible improvement for the FPDF of reaction progress variable and a closure model for the reactive scalar variance has been provided. They also showed that the steady state assumption of the flamelet solutions especially during re-ignition at low scalar

dissipation rates is inaccurate. Extension of the FPV model to an unsteady flamelet formulation has been carried out by Pitsch and Ihme (2005). They employed the unsteady FPV model in LES of turbulent confined swirling flames previously studied by Pierce (2001) and obtained notable improvement in the distribution of CO mass fraction. Recent developments to the FPV model include the evaluation and application of the statistically most like distribution as a new model for reactive scalar FPDF (Ihme and Pitsch, 2005).

Current Work: It is one of the goals of the present research to contribute to the know-how in the predictive capability of FPV approach based combustion models when employed in LES as well as RANS. Although, the beta function based FPDF for reaction progress variable has been shown as a possible advancement to the FPV δ function model of Pierce and Moin (2004), no simulations of have been conducted on experimental configurations to further validate the findings. Also, since, the model's potential to predict local extinction and re-ignition phenomena and especially the flame lift-off have been identified, it is of dual interest to investigate the predictive capability of FPV models (based on δ and β function based FPDF for reaction progress variable) in partially premixed combustion typically observed in lifted flames. In the current work, FPV models have also been employed in RANS framework to study the accuracy with which they can describe partially premixed combustion without the benefits of resolution of large scale motion, provided by LES. The FPV approach and its different formulations used in the present study are presented in section 5.5.

Chapter 3

Governing Equations for Turbulent Combusting Flows

The starting point for numerical modelling of turbulent reacting flows resides in the mathematical description through a set of governing equations. For turbulent reacting flows, the conservation equations of fluid mechanics are supplemented by those for conservation of chemical species to form the governing equations. In addition, variation in density with respect to pressure, temperature and composition of chemical species needs to be accounted and the relationship is established through an equation-of-state. These equations along with the enforced assumptions relevant to the flows of current interest are presented in section 3.1 of the present chapter. A brief overview of the turbulence simulation methods is then presented in section 3.2.

3.1 Instantaneous governing equations

The governing equations can be derived by applying conservation laws of physics viz. for mass, momentum and energy, to a situation of fluid flow through an infinitesimal control volume fixed in space. The equations are presented here in a Cartesian tensor notation with summation implied through indices k and l.

3.1.1 Conservation of mass

Though chemical reaction may result in production and destruction of individual species, overall, mass is neither created nor destroyed. Application of this physical law and furthermore that the net mass across a control surface can be transported only through convection, results in the so called continuity equation:

$$\frac{\partial \rho}{\partial t} + \frac{\partial}{\partial x_k}(\rho u_k) = 0 \tag{3.1}$$

Where ρ denotes the mixture density, t the time and u_k is the velocity in the direction x_k.

3.1.2 Conservation of momentum

The conservation of momentum is based on the Newton' second law of motion and is expressed by the Navier-Stokes equations:

$$\frac{\partial}{\partial t}(\rho u_i)+\frac{\partial}{\partial x_k}(\rho u_k u_i)=-\frac{\partial p}{\partial x_i}+\frac{\partial \tau_{ik}}{\partial x_i}+F_i \tag{3.2}$$

Where, τ_{ij} is the shear stress in the i^{th} coordinate direction on a surface whose outward normal is in the j^{th} direction, P is the static pressure and F_i is the body force in the i^{th} coordinate direction. Fluid in turbulent reacting flows is often considered as Newtonian and hence the shear stress can be related to velocity gradient.

$$\tau_{ij}=\mu\left(\frac{\partial u_j}{\partial x_k}+\frac{\partial u_j}{\partial x_k}-\frac{2}{3}\delta_{ij}\frac{\partial u_k}{\partial x_k}\right) \tag{3.3}$$

where, μ is the dynamic viscosity and δ_{ij} is the kronecker delta.

3.1.3 Conservation of species

Similar to overall mass conservation, mass continuity for individual species (Y_i) can be derived and is given by:

$$\frac{\partial}{\partial t}(\rho Y_i)+\frac{\partial}{\partial x_k}(\rho u_k Y_i)=-\frac{\partial J_{ik}}{\partial x_k}+\dot{\omega}_i \tag{3.4}$$

where J_{ij} is the mass molecular flux of the i^{th} specie in the j^{th} coordinate direction and $\dot{\omega}_i$ is the rate of formation of specie i per unit volume. In combusting flows involving multiple species with varied molecular weights, complete treatment of molecular fluxes requires full array of diffusion coefficients characterizing diffusion of species i in a mixture involving species j, j=1,2,3,...N. However, in turbulent flows of practical interest, turbulence Reynolds number is sufficiently high so that molecular transport is of secondary importance and Fick's law of diffusion can be employed (Libby and Williams, 1994).

Hence,

$$J_{ij} = -\rho D_i \frac{\partial Y_i}{\partial x_j} \tag{3.5}$$

Introducing Eq.3.5 in Eq.3.4 leads to:

$$\frac{\partial}{\partial t}(\rho Y_i) + \frac{\partial}{\partial x_k}(\rho u_k Y_i) = \frac{\partial}{\partial x_k}\left(\rho D_i \frac{\partial Y_i}{\partial x_k}\right) + \dot{\omega}_i \tag{3.6}$$

The above equation applies to each species and thus, in the presence of N species, N-1 equations are to be solved considering the fact that

$$\sum_{i=1}^{N} Y_i = 1$$

However, it is highly desirable as is shown in steps to follow, to utilize element mass fractions denoted by Z_e for an element e and defined by

$$Z_e = \sum_{i=1}^{N} m_{ie} Y_i \tag{3.7}$$

where m_{ie} is the number of kilograms of element e in a kilogram of species i. This implies that for M number of elements,

$$\sum_{e=1}^{M} Z_e = 1 \tag{3.8}$$

Since in chemical reactions elements are conserved unlike the species, we have for each element,

$$\sum_{e=1}^{M} m_{ie} \dot{\omega}_i = 0 \tag{3.9}$$

Conducting operations on Eq. 3.6, conservation equation for element mass fraction can be written as

$$\frac{\partial}{\partial t}(\rho Z_e) + \frac{\partial}{\partial x_k}(\rho u_k Z_e) = \frac{\partial}{\partial x_k}\left(\sum_{i=1}^{N} \rho m_{ie} D_i \frac{\partial Y_i}{\partial x_k}\right) \tag{3.10}$$

Complexity in the right hand term of the above equation is often dealt by assuming a single diffusion coefficient, $D_i = D$, leading to

$$\frac{\partial}{\partial t}(\rho Z_e) + \frac{\partial}{\partial x_k}(\rho u_k Z_e) = \frac{\partial}{\partial x_k}\left(\rho D \frac{\partial Z_e}{\partial x_k}\right) \tag{3.11}$$

Equations 3.10 and 3.11 are quite useful in turbulent reacting flows as they eliminate the need to evaluate the chemical source term which introduces great complexity. Furthermore, by introducing a conserved scalar mixture fraction Z which is based on linear combination of elemental mass fractions, the computational effort is brought down to solving for just one equation.

$$\frac{\partial}{\partial t}(\rho Z)+\frac{\partial}{\partial x_k}(\rho u_k Z)=\frac{\partial}{\partial x_k}\left(\rho D\frac{\partial Z}{\partial x_k}\right) \tag{3.12}$$

3.1.4 Conservation of energy

Conservation of energy can be derived from first law of thermodynamics and it is customary with low-mach number flows to adopt enthalpy as the energy variable.

$$\frac{\partial}{\partial t}(\rho h)+\frac{\partial}{\partial x_k}(\rho u_k h)=\frac{\partial p}{\partial t}+\frac{\partial}{\partial x_k}\left[\frac{\mu}{Pr}\frac{\partial h}{\partial x_k}+\mu\sum_{i=1}^{N}\left(\frac{1}{Sc_i}-\frac{1}{Pr}\right)h_i\frac{\partial Y_i}{\partial x_k}\right]+\nabla.Q_{rad} \tag{3.13}$$

Where h is the specific enthalpy of mixture, h_i is that of species i, $Sc_i=\mu/\rho D_i$ is the Schmidt number pertaining to species i, and Pr is the mixture Prandtl number. The final term represents radiative heat loss which requires calculation through a separate radiative heat transfer equation in a radiation submodel such as the Discrete Transfer Method discussed in section 5.3. Assuming the characteristic Mach number of the turbulent flow to be smaller than unity, kinetic energy of mixture and viscous dissipation rate are neglected. Additionally considering,

1. Equal diffusivities for all the species, same as needed for Eq. (3.11), $D_i=D$, and, $Sc_i=Sc$.
2. Lewis number $(Sc/Pr) = 1$, and
3. $\frac{\partial p}{\partial t}$ negligible in case of low Mach number flows, Eq. (3.13) is simplified to

$$\frac{\partial}{\partial t}(\rho h)+\frac{\partial}{\partial x_k}(\rho u_k h)=\frac{\partial}{\partial x_k}\left[\frac{\mu}{Pr}\frac{\partial h}{\partial x_k}\right]+\nabla.Q_{rad} \tag{3.14}$$

In case of adiabatic flows, Eq. (3.14) is further simplified to:

$$\frac{\partial}{\partial t}(\rho h)+\frac{\partial}{\partial x_k}(\rho u_k h)=\frac{\partial}{\partial x_k}\left[\frac{\mu}{Pr}\frac{\partial h}{\partial x_k}\right] \tag{3.15}$$

From observation of Equation 3.12 and Equation 3.15 it is clear that they are identical. Hence under the above considered assumptions, complexity of the problem in turbulent reacting flows is further reduced as solving only for the mixture fraction and introducing an appropriate functional relationship between enthalpy and mixture fraction would suffice.

In reacting flows, combustion influences fluid dynamics through density (assuming low Mach number flows where pressure fluctuations are negligible). The equation of state is used to calculate density. For ideal gases,

$$\rho = \frac{p}{R_o T \sum_{i=1}^{N} \frac{Y_i}{W_i}} \tag{3.16}$$

where R_o is the universal gas constant and W_i is the molecular weight of species i.

3.2 Overview of turbulence simulation methods

3.2.1 Direct Numerical Simulation

The above set of instantaneous governing equations with appropriate initial and boundary conditions could be solved numerically without further approximation other than numerical discretisation resulting in a direct numerical simulation (DNS). Thus, in DNS, all the motions in the flow are resolved. This approach is the simplest from a conceptual point of view and results in the most accurate predictions. For Reynolds numbers which are sufficiently low such that the flow can be considered to be laminar and if the geometry is simple, then flows with complex transport and chemical kinetic characteristics could be solved with DNS to a high degree of accuracy (Smooke *et al.*, 1990).

However, at high Reynolds numbers the flow is fully turbulent and is characterized by a wide range of length scales and time scales. Resolution of all these scales is prohibitively expensive. For DNS of turbulent flows, inorder to ensure that all the significant structures of turbulence are captured, each linear dimension of the computational domain must be at least a few times the size of the largest turbulent eddy or the integral length scale (L). At the same time, it is equally important to

capture all of the dissipation of kinetic energy which occurs on the smallest scales or the Kolmogorov length scale, η. Thus the size of the grid should be a small multiple of η. Considering the simplest case of homogeneous isotropic turbulence, the number of grid points in each direction must be atleast L/η. It turns out that this ratio is proportional to $R_t^{3/4}$ (Tennekes and Lumley, 1972). Where the turbulent Reynolds number R_t is based on the integral length scale. Since turbulence is a three dimensional phenomenon, the computations are necessarily 3D and hence the number of grid points is proportional to $(L/\eta)^3$. In effect, the number of grid points and subsequently the cost of a simulation scale as $R_t^{9/4}$. Thus, limiting the application of DNS to flows with turbulence Reynolds numbers considerably smaller than those of practical interest. Application of DNS to turbulent flows of practical interest is presently beyond the capability of the available computational power and is expected to remain so for the indefinite future.

However, DNS can be of valuable use as a research tool for understanding the mechanisms of turbulence production, dissipation, energy transfer, interaction between combustion and turbulence. Two alternative techniques which facilitate applicability to turbulent flows of practical interest are the large eddy simulation (LES) and Reynolds averaged Navier Stokes (RANS).

3.2.2 Large Eddy Simulation

A significant portion of the computational effort in DNS is expended in resolving the small scales while it is the large scales which are more energetic and effective transporters of conserved properties. The large scales are dependent on the particular flow geometry and Reynolds number, while the small scales tend to be universal. Large eddy simulation is built around the idea of exploiting this relative difference in the roles played by the large and small scales. In LES, the scales of turbulence are conveniently separated into large scales and small scales or sub-grid scales (SGS). The large scales are completely resolved and hence directly computed while the influence of small scales on the large scales is modelled with appropriate SGS mathematical models. Thus, LES employs '*filtering*' of the instantaneous governing equations such that they provide description of the space and time dependence of the resolved large scales. Since chemical reactions occur at the smallest scales, there is no

resolved portion of chemical source term in LES and the entire combustion needs to be modelled just as in RANS. Thus, combustion models are introduced into LES as SGS models. However, since LES can predict the turbulent mixing which is key to chemical conversion, more accurately than RANS, it is capable of bringing improvements to predictions of turbulent reacting flows.

Resolving only the large scales allows for the use of much coarser mesh and larger time step sizes in LES as compared to DNS. Thus, the computational times for turbulent reacting flow of practical interest are made tractable. However, LES still requires substantially finer meshes than in RANS to resolve a majority of the turbulent kinetic energy and has to be run for a sufficiently long flow-time to facilitate stable statistics of the flow being modelled. As a result, the computational cost involved with LES is orders of magnitude higher than those associated with RANS calculations thereby necessitating high performance computing for engineering applications.

3.2.3 Reynolds Averaged Navier Stokes (RANS) modelling

For complex practical flow configurations currently the most feasible numerical simulation technique is the Reynolds Averaged Navier Stokes (RANS). The RANS approach is based on '*averaging*' of the governing equations over time (if the flow is statistically steady) or over an ensemble of realizations (for a statistically unsteady flow). Hence, the numerical effort is reduced to the description of only mean flow field while all the scales of turbulence are modelled. If the mean flow is steady, the governing equations will be devoid of time derivative and hence a steady state solution can be obtained quite economically. Even if the mean flow is unsteady, RANS provides computational advantage since the size of time step is dictated by global unsteadiness rather than turbulence time scales. Commonly two types of averaging procedures are in use:

(1) Conventional time averaging (Reynolds averaging) and

(2) Density weighted averaging (Favre averaging)

Favre averaging procedures are highly recommended Bilger (1976; 1980) for all turbulent flows with significant density variations. In combusting flows with large

density variations, Reynolds averaging leads to additional terms with density fluctuations. Modelling these terms involves considerable complexity. Favre averaging, being a mass weighted average approach avoids terms involving density fluctuations leading to simpler forms of the governing equations. However, the Favre averaged equations still contain unclosed terms which necessitate the introduction of approximations in the form of turbulence and combustion models.

Chapter 4

Turbulence Modelling

In the previous chapter, it has been pointed out that large eddy simulation (LES) and RANS, which are currently the feasible numerical simulation techniques for flows of practical interest, require models to approximate the unclosed terms in the set of governing equations. In this chapter, the governing equations in RANS form and the RANS turbulence models adopted in the current work are presented in section 4.1. In section 4.2, the details of the filtered governing equations in LES and the models employed for closure of subgrid scale stresses and scalar fluxes are presented.

4.1 Reynolds-averaged Navier-Stokes formulation

4.1.1 Reynolds and Favre averaging

In the Reynolds decomposition, any flow variable ϕ can be written as the sum of a mean $\bar{\phi}$ and a ϕ' fluctuation about the mean:

$$\phi(x_i,t)=\bar{\phi}(x_i)+\phi'(x_i,t) \text{ with } \overline{\phi'}(x_i,t)=0 \tag{4.1}$$

The mean can be obtained from time averaging (in case of statistically steady flows)

$$\bar{\phi}(x_i)=\lim_{T\to\infty}\frac{1}{T}\int_0^T\phi(x_i,t)dt \tag{4.2}$$

or by a more general ensemble averaging

$$\bar{\phi}(x_i,t)=\lim_{N\to\infty}\frac{1}{N}\sum_{n=1}^{N}\phi(x_i,t)dt \tag{4.3}$$

In the above equations, t denotes time, T the time interval and N represents the number of samples of the ensemble. Substitution of the above decomposition into the continuous form of the governing equations with subsequent ensemble averaging results in the governing equations for mean flow variable. While averaging of any linear term simply gives the identical term for the averaged quantity, a quadratic

nonlinear term results in the product of the average and an additional covariance term which needs to be modeled.

$$\overline{u\phi} = \bar{u}\,\bar{\phi} + \overline{u'\phi'} \tag{4.4}$$

In turbulent reacting flows, density is subjected to fluctuation due to thermal heat release and Reynolds averaging induces additional difficulties. For example, Reynolds averaging the mass conservation equation yields:

$$\frac{\partial \bar{\rho}}{\partial t} + \frac{\partial}{\partial x_k}(\bar{\rho}\bar{u}_k + \overline{\rho' u_k'}) = 0 \tag{4.5}$$

The velocity-density correlation is an additional complexity involving significant uncertainty in its explicit modelling. Hence, it is more desirable to avoid its introduction by adopting mass weighted or Favre averaging. In Favre averaging, all the instantaneous values of velocity and scalars (ϕ) except for pressure and density are decomposed into a steady and fluctuating part as:

$$u_i = \frac{\overline{\rho u_i}}{\bar{\rho}} + u_i'' = \tilde{u}_i + u_i'' \;,\quad \phi_i = \tilde{\phi}_i + \phi_i'' \tag{4.6}$$

Favre mean is denoted by a tilde while the fluctuation about the Favre mean is given by double prime. Additionally, $\overline{\rho u_i''} = 0$, and $\overline{\rho\phi''} = 0$ while $\overline{\phi''} \neq 0$ and $\overline{u_i''} \neq 0$. Insertion of this decomposition into the continuous form of the governing equations with subsequent ensemble averaging results in Favre averaged equations for the mean flow quantities.

4.1.2 Favre averaged governing equations

- Conservation of Mass:

$$\frac{\partial \bar{\rho}}{\partial t} + \frac{\partial}{\partial x_k}(\bar{\rho}\tilde{u}_k) = 0 \tag{4.7}$$

  This equation is devoid of terms involving density fluctuations and hence is formally identical to the Reynolds averaged continuity equation for constant density flows and the results holds good for other conservation equations as well.

- Conservation of Momentum:

$$\frac{\partial}{\partial t}(\bar{\rho}\tilde{u}_i) + \frac{\partial}{\partial x_k}(\bar{\rho}\tilde{u}_k\tilde{u}_i) = -\frac{\partial \bar{p}}{\partial x_i} + \frac{\partial}{\partial x_k}(\tilde{\tau}_{ik}^{vis}) + \tilde{F}_i - \frac{\partial}{\partial x_k}(\overline{\rho u_i'' u_k''}) \tag{4.8}$$

Where the viscous stress tensor $\tilde{\tau}^{vis}$ for a Newtonian fluid and incompressible flow is given by

$$\tilde{\tau}_{ij}^{vis} = 2\frac{\mu}{\bar{\rho}}S_{ij} \tag{4.9}$$

where μ is the laminar dynamic viscosity, and S_{ij} is the strain rate tensor

$$S_{ij} = \frac{1}{2}\left(\frac{\partial \tilde{u}_i}{\partial x_j} + \frac{\partial \tilde{u}_j}{\partial x_i}\right) \tag{4.10}$$

- Conservation of Species

$$\frac{\partial}{\partial t}\left(\bar{\rho}\tilde{Y}_i\right) + \frac{\partial}{\partial x_k}\left(\bar{\rho}\tilde{u}_k\tilde{Y}_i\right) = \frac{\partial}{\partial x_k}\left(\tilde{D}_k^i\right) + \widetilde{\dot{\omega}_i} - \frac{\partial}{\partial x_k}\left(\widetilde{\rho u_k'' Y_i''}\right) \tag{4.11}$$

where $i = 1, 2,..N$ species.

- Conservation of Energy

$$\frac{\partial}{\partial t}\left(\bar{\rho}\tilde{h}\right) + \frac{\partial}{\partial x_k}\left(\bar{\rho}\tilde{u}_k\tilde{h}\right) = \frac{\partial}{\partial x_k}\left(\tilde{D}_k^h\right) + \nabla.\tilde{Q}_{rad} - \frac{\partial}{\partial x_k}\left(\widetilde{\rho u_k'' h''}\right) \tag{4.12}$$

- Any Conserved scalar (example: mixture fraction)

$$\frac{\partial}{\partial t}\left(\bar{\rho}\tilde{Z}\right) + \frac{\partial}{\partial x_k}\left(\bar{\rho}\tilde{u}_k\tilde{Z}\right) = \frac{\partial}{\partial x_k}\left(\tilde{D}^z\right) - \frac{\partial}{\partial x_k}\left(\widetilde{\rho u_k'' Z''}\right) \tag{4.13}$$

In the above Favre averaged equations the following unknown quantities need to be closed:

- Reynolds Stresses: $\widetilde{\rho u_i'' u_k''}$

  These terms represent turbulent transport and their closure is approximated through a turbulence model. Common approaches of modelling the Reynolds stresses range from simple linear eddy viscosity based k-ε model to complex second moment closures where transport equations are solved for individual components of the Reynolds stresses and the modelling is shifted to higher order terms. The k-ε model is quite popular for practical application owing to its quick turn around times and reasonably good accuracy. However, it is incapable of accurately reproducing the augmentation or suppression of individual components of the turbulent stresses occurring due to a range of phenomena in turbulent

combustion. Currently, second moment closures represent about the simplest level at which a more detailed and accurate description of turbulent transport can be achieved in RANS.

One of the tasks undertaken in the current research work was to enhance the turbulence modelling capability of the in-house RANS code which is equipped with a standard k-ε model. To this end, a Reynolds stress transport model has been implemented in the in-house RANS code and it has been employed for turbulence closure in all the RANS based calculations in the current work. The relative performances of the Reynolds stress transport model and k-ε model have been studied in turbulent bluff-body stabilized flames and the results are presented in section 8.2.3.

- Turbulent scalar fluxes: $\widetilde{\rho u_k'' Y_i''}$, $\widetilde{\rho u_k'' h''}$ and $\widetilde{\rho u_k'' Z''}$

These terms represent turbulent transport of a scalar and are usually modelled based on the gradient diffusion and turbulent viscosity hypothesis and are expressed as:

$$\widetilde{\rho u_k'' Y_i''} = -\frac{\mu_T}{Pr_i}\frac{\partial \tilde{Y}_i}{\partial x_k}\ ;\ \widetilde{\rho u_k'' h''} = -\frac{\mu_T}{Pr_h}\frac{\partial \tilde{h}}{\partial x_k}\ ;\ \widetilde{\rho u_k'' Z''} = -\frac{\mu_T}{Sc_Z}\frac{\partial \tilde{Z}}{\partial x_k} \qquad (4.14)$$

Where μ_T is the turbulent eddy viscosity and is estimated from the turbulence model, Pr_i is the turbulent Prandtl number corresponding for the species i, Pr_h is the turbulent Prandtl number corresponding to enthalpy and Sc_Z is the turbulent Schmidt number corresponding to mixture fraction. This approach is computationally effective and hence was adopted in the current work. An alternative but computational expensive approach of handling the turbulent fluxes is by employing a second moment closure wherein transport equation for individual components of turbulent fluxes for each scalar are solved and the higher order moments are modelled.

In high Reynolds number flows, the Reynolds stresses are considerably larger than the mean viscous stress $\tilde{\tau}_{ik}^{vis}$ and hence can be neglected. Analogous to Reynolds stresses,

the turbulent scalar fluxes represent the dominant mode of transport in high Reynolds numbers and hence the laminar diffusive fluxes $\tilde{D}_k^l$, $\tilde{D}_k^h$ and $\tilde{D}^z$ can be neglected.

- Chemical source term, $\tilde{\dot{\omega}}_i$

The determination of mean chemical source term is one of the central problems of turbulent combustion modelling and is the main motivation behind the development of turbulent combustion models. The turbulent combustion models adopted in the present study are discussed in detail in Chapter 5.

4.1.3 Standard k-ε model

The two equation k-ε model has been originally developed by Jones and Launder (1972) for constant density recirculating flows. However, its use can be made in reacting flows with variable density by simply recasting the model in terms of Favre averaged quantities with the inherent presumption that density fluctuations are accounted for by the averaging. This approach has been discussed in detail by Jones and Whitelaw (1982), Jones (1994) and Kuo (1986). In this model, the Reynolds stresses are assumed to be linearly related to rate of strain, hence

$$\widetilde{\rho u_i'' u_j''} = -\mu_T \left(\frac{\partial \tilde{u}_i}{\partial x_j} + \frac{\partial \tilde{u}_j}{\partial x_i} \right) + \frac{2}{3} \delta_{ij} \bar{\rho} \tilde{k} \tag{4.15}$$

Where $\delta_{ij} = 1$, for $i=j$ and $\delta_{ij} = 0$ for $i \neq j$ and $\tilde{k}$ is the turbulent kinetic energy:

$$\tilde{k} = \frac{1}{2} \left(\widetilde{u_k'' u_k''} \right) \tag{4.16}$$

Dimensional analysis considerations dictate that the eddy viscosity μ_T be given by the product of a turbulent velocity scale given by $\sqrt{\tilde{k}}$ and a turbulent length scale given by $\tilde{k}^{3/2} / \tilde{\varepsilon}$:

$$\mu_T = C_\mu \bar{\rho} \frac{\tilde{k}^2}{\tilde{\varepsilon}} \tag{4.17}$$

Where C_μ is the turbulence constant and $\tilde{\varepsilon}$ is the rate at which the turbulent kinetic energy is dissipated. Both $\tilde{k}$ and $\tilde{\varepsilon}$ are computed from their respective transport equations.

$$\frac{\partial}{\partial t}\left(\bar{\rho}\tilde{k}\right)+\frac{\partial}{\partial x_k}\left(\bar{\rho}\tilde{u}_i\tilde{k}\right)=\frac{\partial}{\partial x_k}\left(\frac{\mu_T}{Pr_k}\frac{\partial\tilde{k}}{\partial x_k}\right)+G-\bar{\rho}\tilde{\varepsilon} \tag{4.18}$$

$$\frac{\partial}{\partial t}\left(\bar{\rho}\tilde{\varepsilon}\right)+\frac{\partial}{\partial x_k}\left(\bar{\rho}\tilde{u}_i\tilde{\varepsilon}\right)=\frac{\partial}{\partial x_j}\left(\frac{\mu_T}{Pr_\varepsilon}\frac{\partial\tilde{\varepsilon}}{\partial x_k}\right)+C_{\varepsilon 1}\frac{\tilde{\varepsilon}}{\tilde{k}}G-C_{\varepsilon 2}\bar{\rho}\frac{\tilde{\varepsilon}^2}{\tilde{k}} \tag{4.19}$$

In the above equations, Pr_k and Pr_ε are the turbulent Prandtl numbers for turbulent kinetic energy and dissipation rate respectively. The term G represents the rate of production of turbulent kinetic energy and is expressed as:

$$G=\mu_T\left(\frac{\partial\tilde{u}_j}{\partial x_i}+\frac{\partial\tilde{u}_i}{\partial x_j}\right)\frac{\partial\tilde{u}_i}{\partial x_i} \tag{4.20}$$

The standard values of modelling constants in Eqs. 4.17 and 4.19 are given in Table 4.1. These modelling constants are obtained from analysis of simple constant density flows and are optimized to handle wide variety of flows.

C_μ	$C_{\varepsilon 1}$	$C_{\varepsilon 2}$	Pr_k	Pr_ε
0.09	1.44	1.92	1.0	1.30

Table 4.1: Standard k-ε model constants.

Modified k-ε model

In the present work, a modified form of the standard k-ε has been employed. The modification comes in the form of using $C_{\varepsilon 1}=1.6$ instead of the standard value. This modification has been found by Dally *et al.* (1998b) to improve the spreading rate of the fuel jet in bluff-body stabilized flames.

4.1.4 Reynolds stress transport model

The Reynolds stress transport (RST) model involves solving a differential transport equation for each component of Reynolds stresses and scalar fluxes. Hence, instead of modelling directly the second moments, as is done with the $k-\varepsilon$ model, the modelling effort is shifted to unknown higher-order correlations appearing in differential transport equations. Also, the turbulence production terms are now subjected to exact treatment. This is expected to facilitate accurate prediction of turbulent stress field and its anisotropy. Further, capturing stress anisotropy also enables a more realistic modelling of turbulence dissipation rate (Hanjalic and Jakirlic, 2002). In the present work, the Reynolds stress model proposed by Launder, Reece and Rodi (1975) has been implemented in the in-house RANS code with few modifications which are discussed below. The generalized form of transport equation for Reynolds stresses for an incompressible flow is given in the Cartesian tensor notation as:

$$\frac{\partial}{\partial t}\left(\bar{\rho}\widetilde{u_i''u_j''}\right)+\frac{\partial}{\partial x_k}\left(\bar{\rho}\tilde{u}_k\widetilde{u_i''u_j''}\right)=D_{ij}^{\nu}+D_{ij}^{T}+D_{ij}^{P}+P_{ij}+G_{ij}+R_{ij}+\Phi_{ij}-\bar{\rho}\tilde{\varepsilon}_{ij} \qquad (4.21)$$

Where the first and second terms on the left hand side represent the time derivative and convective transport of the Reynolds stresses. The first three terms (D_{ij}) on the right hand side represent molecular, turbulent and pressure diffusion; P_{ij} is the production by mean flow deformation; G_{ij} is the production by body force; R_{ij} is the production by rotation force; Φ_{ij} is the stress re-distribution due to fluctuating pressure and $\tilde{\varepsilon}_{ij}$ is the stress dissipation. These terms have been discussed below:

Molecular diffusion

The molecular diffusion can be treated exactly as:

$$D_{ij}^{\nu}=\frac{\partial}{\partial x_k}\left(\mu\frac{\partial\overline{u_i''u_j''}}{\partial x_k}\right) \qquad (4.22)$$

However, for high Reynolds number flows which, are of interest in the present study, molecular diffusion is negligible and hence can be neglected. The remaining two terms turbulent and pressure diffusion need to be modelled.

Turbulent diffusion

The most popular model for turbulent diffusion is the generalized gradient diffusion (GGD), also known as Daly-Harlow (1970) model:

$$D_{ij}^{T} = -\frac{\partial}{\partial x_k}\left(\overline{\rho}.\widetilde{u_i''u_j''u_k''}\right) = \frac{\partial}{\partial x_k}\left(C_T \frac{\tilde{k}}{\tilde{\varepsilon}} \widetilde{u_k''u_l''} \frac{\partial}{\partial x_l}\left(\widetilde{u_i''u_j''}\right)\right), \; C_T=0.22 \qquad (4.23)$$

However, this tensorial form when expanded gives rise to cross-diffusion terms that result in severe numerical instabilities. Hence, the present study employs a numerically stable and simpler gradient diffusion model proposed by Lien and Leschziner (1994):

$$D_{ij}^{T} = -\frac{\partial}{\partial x_k}\left(\mu_T \frac{\partial \widetilde{u_i''u_j''}}{\partial x_k}\right) \qquad (4.24)$$

Pressure diffusion

Diffusion by pressure fluctuations has a different nature in that the propagation is through disturbances and none of the gradient transport forms is applicable for modelling this term.

$$D_{ij}^{P} = -\frac{\partial}{\partial x_k}\left(\widetilde{p''u_i''}\delta_{jk} + \widetilde{p''u_j''}\delta_{ik}\right) \qquad (4.25)$$

However, in many flows the pressure transport is much smaller than velocity transport and hence pressure diffusion has been neglected in the present study.

Production by shear

Production by deformation or shear is subjected to exact treatment and is given by:

$$P_{ij} = -\left(\overline{\rho}\widetilde{u_j''u_k''}\frac{\partial \tilde{u}_i}{\partial x_k} + \overline{\rho}\widetilde{u_i''u_k''}\frac{\partial \tilde{u}_j}{\partial x_k}\right) \qquad (4.26)$$

Pressure –strain rate term

The effect of pressure fluctuations is redistribution of the turbulent stress among components thereby making turbulence more isotropic. The pressure strain interaction term is usually split into the following parts:

$$\Phi_{ij} = \overline{\frac{p''}{\rho}\left(\frac{\partial u_i''}{\partial x_j} + \frac{\partial u_j''}{\partial x_i}\right)} = \Phi_{ij,1} + \Phi_{ij,2} + \Phi_{ij,3} + \Phi^{w}_{ij,1} + \Phi^{w}_{ij,2} + \Phi^{w}_{ij,3} \qquad (4.27)$$

The first term $\Phi_{ij,1}$ is the return to isotropy of non-isotropic turbulence or 'slow term'. The second term $\Phi_{ij,2}$ is the 'isotropization' of the process of stress production due to mean rate of strain. The third term $\Phi_{ij,3}$ is the 'isotropization' of stress production due to a body force. The last three terms correspond to wall blockage and pressure reflection effects associated with Φ_{ij1}, Φ_{ij2} and Φ_{ij3}. The wall blockage effect acts against the isotropizing action of the pressure fluctuations while the pressure reflection effect augments the isotropizing action due to enhanced eddy scrambling. All the terms need to be modelled and different modelling approaches have been proposed in the literature. The models adopted in the present study are discussed below:

Model for Slow Term Φ_{ij1}: Rotta (1951) proposed a simple linear model by which Φ_{ij1} is proportional to stress anisotropy tensor.

$$\Phi_{ij1} = -C_1\overline{\rho}\frac{\tilde{\varepsilon}}{\tilde{k}}a_{ij} = -C_1\overline{\rho}\frac{\tilde{\varepsilon}}{\tilde{k}}\left(\widetilde{u_i''u_j''} - \frac{2}{3}\delta_{ij}\tilde{k}\right) \qquad (4.28)$$

Where a_{ij} is the stress anisotropy tensor.

Models for Rapid Terms Φ_{ij2} and Φ_{ij3} : The term Φ_{ij2} is associated with mean strain rate which is usually the major source of turbulence production. Hence pressure fluctuations can be expected to modify the very process of stress production. Following this concept, Naot *et al.* (1970) proposed a model analogous to Rotta's model for the slow term and is known as the 'isotropization of production' IP model.

According to this model:

$$\Phi_{ij2} = -C_2\left(P_{ij} - \frac{1}{3}\delta_{ij}P_{kk}\right) \tag{4.29}$$

Where the constant C_2 is correlated to the constant C_1 by:

$$C_1 \approx 4.5(1 - C_2) \tag{4.30}$$

The values adopted in the present work for these constants are: C_1=1.8 and C_2=0.6

An analogous approach can be adopted for the pressure effect on the stress production due to body force. For the flows modelled in the present work, body forces are negligible and hence Φ_{ij3} is neglected. Since the modelled flames are unconfined, wall reflection and wall blockage effects, if any, are not expected to influence the regions of interest in the studied flames. Hence the last three terms in Eq (4.27) have been neglected.

Dissipation rate term

This has been modelled using the local isotropy hypothesis of Kolmogorov which is pertinent to high Reynolds number flows.

$$\tilde{\varepsilon}_{ij} = \frac{2}{3}\bar{\rho}\tilde{\varepsilon}\delta_{ij} \tag{4.31}$$

The mean energy dissipation rate $\tilde{\varepsilon}$ is obtained by solving its transport equation. The basic form of the model equation is same as in the *k-ε* model, except that now the production term is treated in exact form:

$$\frac{\partial}{\partial t}(\bar{\rho}\tilde{\varepsilon}) + \frac{\partial}{\partial x_k}(\bar{\rho}\tilde{u}_i\tilde{\varepsilon}) = \frac{\partial}{\partial x_k}\left(\frac{\mu_T}{Pr_\varepsilon}\frac{\partial\tilde{\varepsilon}}{\partial x_k}\right) + C_{\varepsilon 1}\frac{\tilde{\varepsilon}}{\tilde{k}}P_{kk} - C_{\varepsilon 2}\bar{\rho}\frac{\tilde{\varepsilon}^2}{\tilde{k}} \tag{4.32}$$

The model constants used in the present study are $C_{\varepsilon 1}$=1.60 (same as in the modified k-ε model), $C_{\varepsilon 2}$=1.92 and Pr_ε=1.0 (from Lien and Leschziner, 1994).

Turbulent kinetic energy

Since, the Reynolds stresses are solved in the RST model, the mean turbulent kinetic energy can be directly obtained from the normal stresses. However, presence of walls requires special treatment to bridge the viscous sub-layer. The log-law-based wall

function treatment used with k-ε model can be extended to RST model but it is less straightforward. The main problem associated with RST model is the need to calculate additional pressure-strain terms in the Reynolds stress transport equations. The pressure-strain terms contain products of stresses and strains, and the variation of the former across the sublayer is uncertain (Leschziner and Lien, 2002). To overcome this problem, an equation for $\tilde{k}$ is solved at the near wall cells rather than the equations for Reynolds stress components. However, for computational ease, the equation for $\tilde{k}$ has been solved in the entire domain rather than just at the near wall cells.

$$\frac{\partial}{\partial t}\left(\bar{\rho}\tilde{k}\right)+\frac{\partial}{\partial x_k}\left(\bar{\rho}\tilde{u}_i\tilde{k}\right)=\frac{\partial}{\partial x_k}\left(\frac{\mu_T}{Pr_k}\frac{\partial \tilde{k}}{\partial x_j}\right)+P_k-\bar{\rho}\tilde{\varepsilon} \tag{4.33}$$

Where $Pr_k = 0.82$ (Lien and Leschziner, 1994).

Near wall components of stresses are then derived from the mean turbulence kinetic energy from a closed set of algebraic equations (Eq. 4.34). These equations are obtained by considering local equilibrium forms of the Reynolds stress equations from which the convective and diffusive transport terms are omitted and the log-law is used to approximate the shear strain which is assumed to be the only strain (Leschziner and Lien, 2002).

$$\left(\widetilde{u''u''}\right)_p^w = 1.098\tilde{k}_p, \left(\widetilde{v''v''}\right)_p^w = 0.247\tilde{k}_p,$$

$$\left(\widetilde{w''w''}\right)_p^w = 0.655\tilde{k}_p, \left(\widetilde{u''v''}\right)_p^w = -0.255\tilde{k}_p \tag{4.34}$$

Where $\tilde{k}_p$ is the turbulent kinetic energy at the near wall node p.

Turbulent scalar flux modelling

Turbulent scalar fluxes could be modelled using the same approach as adopted for the closure of Reynolds stresses. However, this would lead to enormous increase in computational time due to the need to solve for additional transport equations for each conserved scalar. Hence in the present study the simple gradient diffusion hypothesis (Eq. 4.14) has been adopted to model the turbulent scalar fluxes.

4.2 Large Eddy Simulation formulation

4.2.1 Spatial filtering

In LES, the governing equations are subjected to spatial filtering to partition the solution space into resolved and unresolved scales. According to Leonard (1974) spatial filtering of a function f can be defined as:

$$\bar{f}(x) = \int_D G(x - x'; \overline{\Delta}(x)) f(x') dx' \tag{4.35}$$

In the above equation, G represents a filter function and the integral is extended to the entire computational domain. The most commonly used filter functions are the sharp Fourier cut-off filter, the Gaussian filter and the box filter. Each filter has a length scale $\overline{\Delta}$ associated with it and is taken to be intermediate between the Kolmogorov length scale and the integral length scale. Eddies of size larger than $\overline{\Delta}$ are classified as large eddies while the ones smaller than $\overline{\Delta}$ are classified as the small eddies which need to be modelled. In the present LES, a box filter has been adopted, as this filter fits naturally into a finite volume discretisation. The process of finite volume discretisation of the continuous governing equations is equivalent to applying a box filter of width:

$$\overline{\Delta} = 2(\Delta x \, \Delta y \, \Delta z)^{1/3} \tag{4.36}$$

where Δx , Δy and Δz denote the width of a computational cell in the three co-ordinates. The box filter is defined as

$$\begin{aligned} G(x - x') &= 1 \quad |x - x'| < \overline{\Delta} \\ &= 0 \quad |x - x'| > \overline{\Delta} \end{aligned} \tag{4.37}$$

As already discussed in the context of RANS, for turbulent reacting flows where the density fluctuations are appreciable, it is more convenient to adopt a density weighted form of the governing equations. Hence in the context of LES, a Favre 'filtered' form of the governing equations is adopted. These equations are very similar in form to the Favre averaged equations in RANS.

Favre filtered continuity equation

$$\frac{\partial \overline{\rho}}{\partial t} + \frac{\partial}{\partial x_k}(\overline{\rho}\widetilde{u}_k) = 0 \tag{4.38}$$

Favre filtered Navier Stokes equations

$$\frac{\partial}{\partial t}(\overline{\rho}\tilde{u}_i) + \frac{\partial}{\partial x_k}(\overline{\rho}\tilde{u}_k\tilde{u}_i) = -\frac{\partial \overline{P}}{\partial x_i} + \frac{\partial}{\partial x_k}\left[2\mu\left(\tilde{S}_{ik} - \frac{1}{3}\delta_{ik}\tilde{S}_{kk}\right)\right] - \frac{\partial \tau_{ik}}{\partial x_k} + \tilde{F}_i \tag{4.39}$$

where the strain rate tensor, $\tilde{S}_{ij} = \frac{1}{2}\left(\frac{\partial u_i}{\partial x_j} + \frac{\partial u_j}{\partial x_x}\right)$ (4.40)

In the context of LES, the term τ_{ij} is the subgrid scale (SGS) stress tensor and it represents the impact of the unresolved velocity components on the resolved ones.

$$\tau_{ij} = \overline{\rho}\left(\widetilde{u_i u_j} - \tilde{u}_i\tilde{u}_j\right) \tag{4.41}$$

This is introduced from the nonlinearity of the convection term, which does not commute with the linear filtering operation. In much similarity to the closure problem encountered in RANS, the SGS stresses need to be closed with a suitable SGS model.

Favre filtered scalar conservation equation

Applying Favre filtering to the continuous form of conserved scalar such as mixture fraction (Eq. 3.12) yields:

$$\frac{\partial}{\partial t}\left(\overline{\rho}\tilde{Z}\right) + \frac{\partial}{\partial x_k}\left(\overline{\rho}\tilde{u}_k\tilde{Z}\right) = \frac{\partial}{\partial x_k}\left(\Gamma\frac{\partial \tilde{Z}}{\partial x_k}\right) + Z_k^{SGS} \tag{4.42}$$

The additional term Z_k^{SGS} is manifested due to the non-linearity of the convection term and represents the unresolved or subgrid scale portion of the turbulent scalar flux and needs to be closed through a subgrid scale model.

4.2.2 Modelling of subgrid scale stresses

The primary requirement of SGS model is to ensure that the energy cascade (from large scales to small scales) in the LES is same as that obtained with the cascade fully resolved, as in DNS. The cascading is however an average process. Locally and instantaneously the transfer of energy can be much larger or much smaller than the average and in flows, such as transitional flows, energy cascade can also occur in the opposite direction (i.e. from smaller scales to larger scales) known as 'backscatter' (Piomelli *et al.*, 1996). Hence ideally, the SGS model should also account for this local instantaneous transfer.

Smagorinsky model

The Smagorinsky model (Smagorinsky 1963) was the first model to be proposed for SGS stress tensor and is still widely employed. It employs the eddy viscosity concept thereby relating the anisotropic part of the SGS stresses to the rate of strain $\tilde{S}_{ik}$ of resolved velocity field.

$$\tau_{ij} - \frac{1}{3}\delta_{ij}\tau_{kk} = -2\mu_{SGS}\tilde{S}_{ij} \tag{4.43}$$

The eddy viscosity μ_{SGS} is determined by considering it to be proportional to the product of the length scale of the unresolved motion and its velocity scale. Relating the length scale to filter width $\overline{\Delta}$ and velocity scale to the strain rate tensor $\tilde{S}_{ik}$, the eddy viscosity μ_{SGS} can be expressed as:

$$\mu_{SGS} = \bar{\rho}\left(C_s\overline{\Delta}\right)^2\left|\tilde{S}\right| \tag{4.44}$$

Where $\left|\tilde{S}\right| = \sqrt{2\tilde{S}_{ij}\tilde{S}_{ij}}$ and C_s is a dimensionless co-efficient called the Smagorinsky co-efficient. The widespread use of this classical Smagorinsky model is mainly due to its simplicity. However, the model suffers from significant drawbacks. The Smagorinsky co-efficient is flow dependent and hence has to be calibrated for each variety of flow. Lilly (1966) determined the value of $C_s \approx 0.23$, for homogeneous isotropic turbulence with a filter cutoff in the inertial subrange and $\overline{\Delta}$ equal to the grid size. However, in the presence of mean shear, this value resulted in excessive

damping of the resolved large scale fluctuations, and in his simulation of turbulent channel flow, Deardorff (1970) used $C_s = 0.1$. For the same type of flow, Piomelli *et al.* (1988) found the value of $C_s = 0.065$ to be optimal. The optimal value is changed for other types of flows such as transitional flows. Another drawback stems from the fact that the classical model does not account for the reduction in eddy viscosity close to the walls. To overcome this problem, use of Van Driest style damping functions is advocated (Moin and Kim, 1982).

$$\mu_{SGS} = \bar{\rho}\left(C_s\bar{\Delta}\right)^2\left|\tilde{S}\right|.\left(1-e^{-\left(y^+/A^+\right)^3}\right) \tag{4.45}$$

However, this ad hoc approach is restricted to simple flows and is far from desirable. In addition, the assumption of eddy viscosity makes the Smagorinsky model strictly dissipative and hence is not capable of reproducing 'backscatter'.

Dynamic procedure

Motivated by the limitations of the classical Smagorinsky model, Germano *et al.* (1991) developed dynamic procedure wherein the co-efficient C_s is computed dynamically as the calculation progresses rather than input *a priori*. In this procedure, an additional filter known as the test filter (^) which is larger than the grid filter is applied to the velocity field and information is extracted from the smallest resolved scales (i.e larger scales close to the cut-off). This information is then used in calculating the Smagorinsky co-efficient. Application of the test filter to the filtered Navier-Stokes equations results in sub-test-scale stress tensor analogous to sub-grid-scale stress tensor.

$$T_{ij} = \bar{\rho}\left(\widehat{\tilde{u}_i\tilde{u}_j} - \hat{\tilde{u}}_i\hat{\tilde{u}}_j\right) \tag{4.46}$$

The test filtered velocities $\hat{\tilde{u}}_i$ can be computed from known resolved velocities $\tilde{u}_i$ by applying the test filter using an appropriate function $\hat{G}$. Similarly, the resolved part L_{ik} of the sub-test-scale stress T_{ij} on the grid $\bar{\Delta}$ can be evaluated.

$$L_{ij} = \bar{\rho}\left(\widehat{\tilde{u}_i\tilde{u}_j} - \hat{\tilde{u}}_i\hat{\tilde{u}}_j\right) \tag{4.47}$$

These resolved turbulent stresses are also known as Leonard stresses and are representative of the contribution of the Reynolds stresses by the scales whose length

is intermediate between the test filter width and the grid filter width. Germano *et al.* (1991) related L_{ij} to the subgrid test scale stresses at the test level and grid level by the identity:

$$L_{ij} = T_{ij} - \hat{\tau}_{ij} \tag{4.48}$$

Thus, on one hand L_{ij} can be directly computed while on the other hand a model expression can be obtained with the application of Smagorinsky model to the anisotropic parts of T_{ij} and τ_{ij}.

$$\tau_{ij} - \frac{1}{3}\delta_{ij}\tau_{jj} = -2\left(C_s\bar{\Delta}\right)^2 \left|\tilde{S}\right| \tilde{S}_{ij} \tag{4.49}$$

$$T_{ij} - \frac{1}{3}\delta_{ij}T_{kk} = -2C_s^2\hat{\bar{\Delta}}^2 \left|\hat{\tilde{S}}\right| \hat{\tilde{S}}_{ij} \tag{4.50}$$

where

$$\hat{\tilde{S}}_{ij} = \frac{1}{2}\left(\frac{\partial \hat{\tilde{u}}_i}{\partial x_j} + \frac{\partial \hat{\tilde{u}}_j}{\partial x_i}\right) \text{ and } \left|\hat{\tilde{S}}\right| = \sqrt{2\hat{\tilde{S}}_{ij}\hat{\tilde{S}}_{ij}} \tag{4.51}$$

Substitution of Eq. 4.49 and 4.50 in 4.48 leads the model expression:

$$L_{ij}^{mod} = -2C^2{}_s\hat{\bar{\Delta}}^2 \left|\hat{\tilde{S}}\right| \hat{\tilde{S}}_{ij} + \widehat{2C^2{}_s\bar{\Delta}^2 \left|\tilde{S}\right| \tilde{S}_{ij}} \tag{4.52}$$

Ideally, C_s can be chosen such that

$$L_{ij} - L_{ij}^{mod} = 0 \tag{4.53}$$

But since the Eq.4.53 is a tensor equation, it can only be satisfied in some average sense. Lilly (1991) proposed the minimization of the root mean square of the left-hand-side which yields:

$$C_s^2(x,y,z,t) = -\frac{L_{ij}M_{ij} - 1/3L_{kk}M_{ll}}{2\bar{\Delta}^2\left(M_{ij}M_{ij} - 1/3M_{kk}M_{ll}\right)} \tag{4.54}$$

Where $M_{ij} = \alpha^2\hat{\bar{\rho}}\left|\hat{\tilde{S}}\right|\hat{\tilde{S}}_{ij} - \overline{\rho\left|\tilde{S}\right|\tilde{S}_{ij}}$ and $\alpha = \frac{\hat{\bar{\Delta}}}{\bar{\Delta}}$ is the ratio of test filter to grid filter.

For an incompressible flow, Eq. 4.54 simplifies to

$$C_s^2(x,y,z,t) = -\frac{L_{ij}M_{ij}}{2\bar{\Delta}^2 M_{ij}M_{ij}} \tag{4.55}$$

Thus, with the dynamic procedure, the Smagorinsky co-efficient can be dynamically calculated at every spatial grid point and time step with only α as the only input to the model. The dynamic procedure ensures correct behaviour near wall without any ad

hoc damping functions by automatically reducing the value of the co-efficient near to the wall.

However, the values of model co-efficient tend to fluctuate considerably in space and time thus requiring some form of averaging to maintain stability of the numerical simulation. Typically, L_{ij} and M_{ij} are averaged in spatially homogeneous directions in space. However, this requires the flow to have at least one homogeneous direction. A number of alternative approaches which give better stability than the standard dynamic procedure have been proposed. Breur and Rodi (1994) proposed to relax the value in time using the co-efficient from previous time step. Piomelli and Liu (1995) proposed to use the known value of the co-efficient from previous timestep in the rightmost term of Eq. (4.52) rather than extracting it from the test filter. This method offers the advantage of smoothing in space without any homogeneous direction required and hence is adopted in the present LES.

4.2.3 Modelling of subgrid scalar fluxes

Analogous to the eddy viscosity based strategy adopted for SGS stresses, a simple gradient diffusion model with eddy diffusivity is employed to model the SGS scalar fluxes. For a conserved scalar mixture fraction Z:

$$Z_k^{SGS} = \Gamma_t \frac{\partial \tilde{Z}}{\partial x_k} \tag{4.56}$$

Where the eddy diffusivity Γ_t can be obtained from the knowledge of eddy viscosity by scaling with a turbulent Schmidt number.

$$\Gamma_t = \frac{\mu_T / \bar{\rho}}{Sc_T} \tag{4.57}$$

Substituting the Eqs. 4.56 and 4.57 in 4.42 yields the Favre filtered mixture fraction transport equation in its closed form:

$$\frac{\partial}{\partial t}\left(\bar{\rho}\tilde{Z}\right) + \frac{\partial}{\partial x_k}\left(\bar{\rho}\tilde{u}_k\tilde{Z}\right) = \frac{\partial}{\partial x_k}\left(\left(\Gamma + \Gamma_T\right)\frac{\partial \tilde{Z}}{\partial x_k}\right) \tag{4.58}$$

The laminar and turbulent Schmidt numbers take values of 0.7 and 0.4 respectively in the present work.

Chapter 5

Combustion Models

The direct approach of handling combustion is to find a suitable chemical kinetic mechanism for the fuel under investigation, solve the transport equations for all the species in the mechanism and attempt to model the mean chemical source term. However, a realistic chemical mechanism can involve tens of species and several hundreds of elementary reactions even for a simple hydrocarbon fuel like methane. In addition, if one is interested in accurate prediction of pollutant NO_x, accounting for all the possible reaction pathways becomes a necessity and the overall mechanism could be reduced only to a limited extent. Solving for a large number of transport equations, even with RANS, is not tractable let alone for LES. Another concern is that of finding a suitable model for the mean or filtered chemical source term which is, in principle, an arbitrary nonlinear function of the scalar variables. Thus, it is required of a combustion model to address both the issues with an accurate, yet computationally efficient method.

For non-premixed combustion, conserved scalar mixture fraction based models appear to offer the most effective description of the chemistry. When used in conjunction with a non-conserved reaction progress variable, they are as well capable of handling partially premixed combustion. One of the main objectives of this work is to develop and implement advanced flamelet based combustion models all of which are mixture fraction based. In this chapter, the role of mixture fraction in non-premixed combustion has been discussed section 5.1 as a prelude to the classical steady laminar flamelet model which is discussed in section 5.2. An advanced formulation for non-premixed combustion, the non-adiabatic flamelet model which accounts for radiation heat loss effects is discussed in section 5.3. For NO modelling, both the steady laminar flamelet model and non adiabatic flamelet model require the use of NO submodels and these submodels are presented in section 5.4. Finally, the flamelet/progress variable approach has been discussed in section 5.5.

5.1 Conserved scalar mixture fraction approach

It has been shown in section 3.1, that in a chemical reaction the element mass fractions are conserved and their equations are devoid of chemical source term. And under the assumption of unity Lewis number, equal diffusivity and adiabatic conditions, the enthalpy too is conserved and its equation (Eq. 3.15) takes a form identical to that of element mass fraction (Eq. 3.11). These conserved scalars in the chemical reaction can be represented by a single normalized scalar, namely the mixture fraction, Z. For a two feed fuel-oxidizer non-premixed combustion, the mixture fraction is simply the local fuel stream mass fraction taking a value of unity in the fuel stream and zero in the oxidizer stream. A relationship between mixture fraction and reactive scalar variables (species mass fractions, temperature etc.) could then be specified through thermo-chemical models and complete information on chemical state can be obtained at a significantly reduced computational expense. This forms the basis of conserved scalar mixture fraction approach.

The mixture fraction which is by itself a conserved scalar, assumes the vital roles of tracking the mixing of inflow streams, transport of all the conserved scalars (element mass fraction, enthalpy etc.), and the advection of reactive scalars. Mixture fraction can be related to any of the conserved element mass fractions. However, in the presence of differential diffusion, the mixture fraction values become sensitive to the particular element on which the definition is based. The element mass fraction no longer has a linear dependence with flame position (Drake and Blint, 1988). To overcome this problem, Bilger (1988) suggested a definition for mixture fraction which is based on a linear combination of elemental mass fractions of C, H and O:

$$Z = \frac{2(Z_c - Z_{c,2})/W_c + (Z_H - Z_{H,2})/2W_H - (Z_o - Z_{o,2})/W_o}{2(Z_{c,1} - Z_{c,2})/W_c + (Z_{H,1} - Z_{H,2})/2W_H - (Z_{o,1} - Z_{o,2})/W_o} \tag{5.1}$$

where subscripts 1 and 2 denote fuel and air streams and W represents the molecular weight. This formulation preserves the stoichiometric value of the mixture fraction, independent of the effects of differential molecular diffusion. This definition of mixture fraction has been widely adopted (Dally, 1998a; Pitsch and Peters, 1998;

Hossain, 1999; Barlow *et al.*, 2000; Liu *et al.*, 2005) and is employed in present study as well.

5.1.1 Models for system chemistry

The models used to establish relationship between chemical state and mixture fraction are based on the general assumption of 'fast' chemistry, the condition that chemical kinetics are infinitely fast in comparison to other processes in the flow. Simplest of the models is the Flame Sheet (also known as Burke-Schumann limit) model wherein chemistry is described by a single step irreversible reaction and the reactive scalar variables are determined directly from the given reaction stoichiometry, with no reaction rate or chemical equilibrium information required. The Flame Sheet model requires minimal calculation effort but is limited to the prediction of only major species of the single step reaction. It provides no information on intermediate species or dissociation effects thereby often resulting in an overprediction in flame temperatures. Equilibrium chemistry model as the name indicates, assumes that the chemistry is fast enough for the chemical equilibrium to always exist at molecular level. The reactive scalar variables are expressed as a function of mixture fraction using the minimization of Gibbs free energy. This model offers the advantage of predicting intermediate species even without the knowledge of detailed chemical kinetic rate data. In each of these models, the reactive scalar variables are expressed only as function of mixture fraction:

$$\phi = \phi(Z), \phi = \rho, T, Y_i \tag{5.2}$$

In turbulent reacting flows, the instantaneous relationship between the mixture fraction and the reactive scalars is non-linear due to fluctuations. Hence the mean scalar variables cannot be obtained by the above relations by simple substitution of a mean mixture fraction $\tilde{Z}$ instead of Z. To overcome this problem, a presumed shape probability density function $P(Z)$ is introduced and the mean reactive scalar variables in the turbulent field are obtained from:

$$\tilde{\phi} = \int_0^1 \phi(Z) P(Z) dZ \tag{5.3}$$

The Flame Sheet and Equilibrium chemistry models are limited to first cut estimations or situations where chemical kinetics do not play significant role. However, they provide basis for the development of more capable models which can account for the

effect of turbulence on chemistry, ignition and extinction phenomena which occur, for example, in the region upstream of a lifted flame.

5.2 Steady laminar flamelet model

This model is considered (Peters, 1984) as a non-equilibrium version of the classical Burke-Schumann limit. The steady laminar flamelet model (SLFM) approaches this limit asymptotically in the limit of one-step irreversible reaction with a large Damköhler number (kolmogorov time scale to chemical time scale). The SLFM is similar to the models discussed before in that it relies on a single scalar transport equation for the mixture fraction and employs chemical state relationships to relate the reactive scalar variables to the mixture fraction. However, the critical difference is that the equilibrium chemical states which are solely obtained from thermochemistry are replaced in SLFM by solutions of one-dimensional, steady, diffusion-reaction equations termed as the flamelet equations. These solutions represent laminar diffusion flamelets.

The SLFM is based on the concept that a turbulent diffusion flame can be treated as an ensemble of locally one-dimensional laminar diffusion flamelets. Presence of laminar flamelets in turbulent flame requires that the chemical time scales and length scales are smaller than those of turbulence. Bray and Peters (1994) presented the limits of flamelet regime in turbulent non-premixed combustion. According to them, flamelet regime in non-premixed combustion is observed when the Damköhler number is greater than unity and the flame thickness, based on mixture fraction coordinate, is lesser than mixture fraction variance. Flamelets in turbulent flow are subjected to aero-dynamic strain resulting in departure from chemical equilibrium. In order to account for the effect of turbulence on flamelets, scalar dissipation rate χ which is representative of turbulent mixing is introduced as an additional parameter. Hence in SLFM, the thermo-chemical structure of the flame is a function of mixture fraction and its dissipation rate.

Turbulent mean reactive scalar variables can be computed by integrating the laminar flamelets with the joint PDF of mixture fraction and scalar dissipation rate. The laminar flamelet concept thus, eliminates the need to resolve small chemical time and

length scales in turbulent flow calculations making the numerical effort quite economic. Furthermore, it allows for detailed chemical kinetics since the flamelet calculations are decoupled from the turbulent flow calculations.

5.2.1 Flamelet equations

The flamelet equations have been derived by Peters (1984) for describing the reactive-diffusive structure in the vicinity of flame surface as a function of mixture fraction. The derivation is based on two steps. In the first step, a co-ordinate transformation, applied at the flame surface is introduced. This is illustrated in Fig. 5.1 for a two feed turbulent jet diffusion flame.

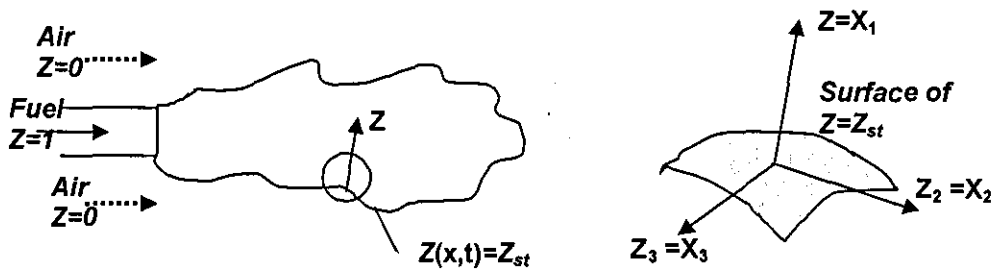

Figure 5.1: Surface of stoichiometric mixture in a turbulent jet diffusion flame

The field equation for the mixture fraction that determines the location of the flame surface is given (under the assumption of equal diffusivity and unity Lewis number) by:

$$\frac{\partial}{\partial t}(\rho Z)+\frac{\partial}{\partial x_k}(\rho u_k Z)=\frac{\partial}{\partial x_k}\left[\rho D\frac{\partial Z}{\partial x_k}\right] \tag{5.4}$$

Solution of balance equation for mixture fraction provides knowledge about its distribution as a function of space (x) and time (t) and henceforth the flame surface defined as the surface of stoichiometric mixture fraction can be obtained by setting:

$$Z(x,t)=Z_{st} \tag{5.5}$$

Combustion essentially takes place in the vicinity of this surface and this thin layer with the surrounding inert mixing region is termed as laminar diffusion flamelet. An orthogonal coordinate system is attached to this stoichiometric surface (Fig. 5.1) such that Z is normal to the surface while the two tangential coordinates lie within the

surface. Coordinate transformation (x_1, x_2, x_3, t) to (Z, Z_2, Z_3, τ) is then implemented in the instantaneous balance equations for species and temperature. The coordinate x_1 which is defined as being locally normal to the flame surface is replaced by a new independent variable Z, whereas the tangential coordinates x_2 and x_3 are the same as the new coordinates Z_2 and Z_3, respectively.

In the second step, simplifications to the equations are made by considering the derivates of the reactive scalars in the tangential directions to be negligible in comparison to those in the normal or Z direction. This is based on the classical boundary layer argument for thin layers. Since the temperature, for instance, is nearly constant along the flame surface, $Z(x,t)=Z_{st}$, gradients along the surface are expected to be small compared to those normal to it. Similar argument is put forward for the chemical species concentrations as well. For unity Lewis number, the flamelet equations are then expressed as:

$$\begin{aligned} &\rho\frac{\partial Y_i}{\partial t}=\rho\frac{\chi}{2}\left(\frac{\partial^2 Y_i}{\partial Z^2}\right)+\dot{\omega}_i \\ &\rho\frac{\partial T}{\partial t}-\rho\frac{\chi}{2}\left(\frac{\partial^2 T}{\partial Z^2}\right)-\rho\frac{\chi}{2C_p}\left(\frac{\partial T}{\partial Z}\frac{\partial C_p}{\partial Z}\right) \\ &-\sum_{i=1}^{N}\rho\frac{\chi}{2}\frac{C_{pi}}{C_p}\left(\frac{\partial Y_i}{\partial Z}\frac{\partial T}{\partial Z}\right)+\frac{1}{C_p}\sum_{i=1}^{N}h_i\dot{\omega}_i+\frac{Q_{rad}}{C_p}=0 \end{aligned} \tag{5.6}$$

where ρ is the density, T is the temperature, C_p is the specific heat at constant pressure, $\dot{\omega}$ is the reaction rate, h is the enthalpy, Q_{rad} is the radiative source per unit volume, and the subscript i refers to the i^{th} chemical species. The symbol χ represents the instantaneous scalar dissipation rate and it is defined as:

$$\chi=2D\left(\frac{\partial Z}{\partial x_k}\right)^2 \tag{5.7}$$

The scalar dissipation rate plays an important role in flamelet models for non-premixed combustion. It can be interpreted as an inverse diffusion time scale and it represents the influence of flow field on local flame structure. It incorporates implicitly the influence of convection and diffusion normal to the surface of stoichiometric mixture. In order to solve the above equations, the functional dependence of scalar dissipation rate on mixture fraction is modelled according to Peters (1984) by considering laminar counter flow diffusion flame configuration.

$$\chi = \frac{a}{\pi} exp\left\{-2\left[erfc^{-1}(2Z)\right]^2\right\} \tag{5.8}$$

where a is the velocity gradient at the stagnation point of a counter flow diffusion flame and $erfc^{-1}$ is the inverse of the complementary error function. In consistence with the flamelet concept, this functional dependence is parameterized by the scalar dissipation rate at stoichiometric mixture fraction $\chi_{st} = \chi(Z_{st})$.

In steady flamelet modelling, a quasi-steady burning is assumed and hence time derivatives are neglected in the flamelet equations. However, they play important role (Mauss *et al.*, 1990) during rapid transitions between fully burning and extinguished states which occur during extinction and re-ignition and are retained in case of unsteady flamelet modelling.

In the present study, flamelet calculations have been carried out in the mixture fraction space using the FlameMaster code of Pitsch (1998).

5.2.2 Statistics of mixture fraction and scalar dissipation rate

Solutions of flamelet equations provide the thermo-chemical structure of a flame as a function of mixture fraction and scalar dissipation rate. In principle, both the mixture fraction and the scalar dissipation rate are fluctuating quantities and their statistical distribution needs to be considered for evaluation of statistical moments of the reactive scalars in the turbulent flow. Provided the joint Favre PDF $\tilde{P}(Z,\chi_{st})$ is known and the steady flamelet equations are solved to obtain reactive scalars ϕ as a function of Z and χ_{st}, the Favre averaged values of ϕ can be obtained from:

$$\tilde{\phi} = \int_0^1 \int_0^\infty \phi(Z;\chi_{st}) \tilde{P}(Z,\chi_{st};x,t)\, d\chi_{st} dZ \tag{5.9}$$

In the present study, the joint PDF is modelled by assuming statistical independence between Z and χ_{st} and presuming the shape of their marginal PDFs:

$$\tilde{P}(Z,\chi_{st}) = \tilde{P}(Z)\tilde{P}(\chi_{st}) \tag{5.10}$$

The most widely used shape for the marginal PDF of mixture fraction $\tilde{P}(Z)$ is the β-function distribution (Peters, 1984; Bray and Peters, 1994). It has the advantage that

its parameters can be related algebraically to the first two moments of mixture fraction which are obtained as part of the solution in CFD. The PDF for mixture fraction is given by:

$$\tilde{P}(Z)=\frac{Z^{a-1}(1-Z)^{b-1}}{\int_0^1 Z^{a-1}(1-Z)^{b-1}}=\frac{\Gamma(a+b)Z^{a-1}(1-Z)^{b-1}}{\Gamma(a)\Gamma(b)} \tag{5.11}$$

where the coefficients a and b are given by:

$$a=\tilde{Z}\left[\frac{\tilde{Z}(1-\tilde{Z})}{\widetilde{Z''^2}}-1\right] \tag{5.12}$$

$$b=(1-\tilde{Z})\left[\frac{\tilde{Z}(1-\tilde{Z})}{\widetilde{Z''^2}}-1\right] \tag{5.13}$$

The mean mixture fraction $\tilde{Z}$ and its variance $\widetilde{Z''^2}$ are obtained from their respective transport equations

$$\frac{\partial}{\partial t}(\rho\tilde{Z})+\frac{\partial}{\partial x_k}(\rho u_k\tilde{Z})=\frac{\partial}{\partial x_k}\left[\frac{\mu_t}{Sc_{\tilde{z}t}}\frac{\partial\tilde{Z}}{\partial x_k}\right] \tag{5.14}$$

$$\frac{\partial}{\partial t}(\rho\widetilde{Z''^2})+\frac{\partial}{\partial x_k}(\rho u_k\widetilde{Z''^2})=\frac{\partial}{\partial x_k}\left(\frac{\mu_t}{Sc_{\widetilde{z''^2}t}}\frac{\partial\widetilde{Z''^2}}{\partial x_k}\right)+2\frac{\mu_t}{Sc_{\widetilde{z''^2}t}}\left(\frac{\partial\widetilde{Z''^2}}{\partial x_k}\right)^2-\overline{\rho\chi} \tag{5.15}$$

Where the turbulent Schmidt numbers for both mixture fraction and its variance take the value of 0.9 in the present RANS work. The mean scalar dissipation rate $\tilde{\chi}$ is obtained by relating it to the mean scalar fluctuations $\widetilde{Z''^2}$ and the mean turbulent time scale $\tilde{\varepsilon}/\tilde{k}$ (Jones, 1982).

$$\tilde{\chi}=C_\chi\frac{\tilde{\varepsilon}}{\tilde{k}}\widetilde{Z''^2} \quad \text{where} \quad C_\chi=2.0 \tag{5.16}$$

The marginal PDF for scalar dissipation rate is assumed to follow a log-normal distribution. The presumption of log-normal distribution for scalar dissipation rate has been has been experimentally found valid by Effelsberg and Peters (1988).

$$\tilde{P}(\chi_{st})=\frac{1}{\chi_{st}\sigma\sqrt{2\pi}}exp\left[-\frac{1}{2\sigma^2}(ln\chi_{st}-\mu)^2\right] \tag{5.17}$$

where the parameters μ and σ are related to the first and second moments of χ by

$$\tilde{\chi} = exp\left(\mu + \frac{\sigma^2}{2}\right) \tag{5.18}$$

$$\widetilde{\chi^{n2}} = \tilde{\chi}^2 exp\left(\sigma^2 - 1\right)$$

Therefore, $\tilde{P}(\chi_{st})$ can be evaluated from the knowledge of $\tilde{\chi}$ and σ. For the present study a value of σ=2.0 has been chosen after experimental results by Sreenivasan *et al.* (1977).

5.2.3 Flamelet quenching

The scalar dissipation rate is used to describe local extinction according to the flamelet concept. As the scalar dissipation rate is increased, the stretch on the flamelet is increased and at a particular limit the heat loss from the reaction zone balances the heat generation from chemical reaction. This is the quenching limit, χ_q and is obtained from the flamelet calculations. Beyond this limit, the flamelet extinguishes. The fraction of burnable flamelets in the turbulent flame may then be calculated as probability of $\chi < \chi_q$:

$$P_b = \frac{1}{2} + \frac{1}{2}\left(erf\left(\frac{\ln \chi_q / \tilde{\chi} + 1/2\sigma^2}{\sqrt{2}\sigma}\right)\right) \tag{5.19}$$

The value of P_b lies between zero and unity depending on the extent of non-equilibrium in the turbulent flame. For a zero mean scalar dissipation rate corresponding to equilibrium condition P_b is unity. As the scalar dissipation rate increases the chemistry shifts away from equilibrium, probability of occurrence of flamelets decreases and P_b becomes less than unity. Flamelet after quenching is assumed to follow pure mixing state.

As the extinction process from fully burnt to pure mixing is very rapid, it is assumed that a turbulent flame is composed of an ensemble of fully burning flamelets and completely extinguished flamelets. Such a method of accounting for local extinction is reasonable if there is sufficient residence time for the flame to approach the steady

state, being either a fully burning state or pure mixing state (Ferreira, 1996). However in turbulent flows with rapid changes in scalar dissipation rate, the steady state flame structure approximation is shown to be incapable of handling local extinction (Ferreira, 1996; Hossain, 1999) and a transient modelling has been recommended. (Haworth *et al.*, 1988a; Mauss *et al.*, 1990; Ferreira, 1996).

5.2.4 Application of SLFM to LES

The formulation for SLFM discussed thus far in the context of RANS is equally valid for LES. However, in LES, the integrated values of the scalars represent Favre filtered values and the PDF for mixture fraction and scalar dissipation rate are Favre filtered PDFs. Similar to the mean mixture fraction equation in RANS, a transport equation (Eq. 4.58) for filtered mixture fraction is solved in LES. However, the subgrid variance is modelled in LES. Such an approach has been established for LES after significant testing carried out by several works in the past (Cook and Riley, 1994; Branley and Jones, 2001; Pierce and Moin, 1998). Cook and Riley (1994) suggested the following model based on a scale similarity hypothesis.

$$\widetilde{Z''^2} = C_z\left(\widehat{\tilde{Z}^2} - \hat{\tilde{Z}}^2\right) \tag{5.20}$$

The hat in the above equation indicates the test filtering operator in dynamic procedure. The value of the constant C_z = 1.0 has been found to be a reasonable assumption. The hypothesis behind scale similarity is that the largest unresolved scales have a structure similar to the smallest resolved scalars. The above model has been used in the present LES computations.

In RANS, the mean scalar dissipation rate is obtained from the knowledge of mean turbulent kinetic energy and dissipation rate which are obtained from the solution of their respective transport equations. However, in LES, a different approach is adopted. Cook and Riley (1998) suggested that filtered scalar dissipation rate can be derived using the effective viscosity and filtered mixture fraction gradient. The model equation is given as:

$$\tilde{\chi} = 2\left(\frac{\nu}{Sc} + \frac{\nu_T}{Sc_T}\right)\left(\frac{\partial \tilde{Z}}{\partial x_k}\frac{\partial \tilde{Z}}{\partial x_k}\right) \tag{5.21}$$

The effective viscosity is obtained from the localized dynamic procedure while the laminar and turbulent Schmidt numbers take the values of 0.7 and 0.4 respectively. Current LES calculations adopt the above model for filtered scalar dissipation rate calculations. Since a look-up-table strategy is employed, all the PDF integrations for filtered scalars are carried out in pre-processing stage in Pre-PDF SLFM (discussed in section 7.1.3) and read into the LES calculations. From the knowledge of filtered, mixture fraction, its subgrid variance and filtered scalar dissipation rate, 3D interpolation (Appendix I) is performed to obtain the filtered values of the reactive scalars and hence the filtered distribution of the flame.

5.2.5 Limitations of steady laminar flamelet model

In addition to the inability of SLFM to handle local extinction, the predictive capability of the model with respect to NO_x and radiation is as well of equal concern. The assumption of considering steady-state solutions of the flamelet equations has been advocated by Peters (1984) with the view that away from extinction, the changes in scalar dissipation rate are slow enough for the flamelet structure to be considered as in steady state. However, this assumption becomes invalid for the slow chemistry of NO_x and the slow physical phenomena of radiation. Pitsch *et al.* (1998) have shown that considering the radiation heat loss through the source term in the steady flamelet equations results in large discrepancies in the reactive scalars. Considering solutions of unsteady flamelet equations and therefore resorting to a transient flamelet modelling has been advocated by them to resolve the issues with both radiation and NO_x. However, from a practical application perspective, employing a transient flamelet modelling is significantly expensive than the steady flamelet modelling especially when CFD calculations are coupled with flamelet calculations.

Hence in the present work, attempts have been made to extend the steady flamelet model to a RANS based non-adiabatic formulation which while using steady flamelets, is able to consider the effect of radiation heat loss and when integrated with steady or unsteady flamelets based NO submodels, is able to account for the slow chemistry of NO.

5.3 Non adiabatic flamelet model

The flamelet model allows for specification of radiation heat loss in the flamelet equations through a radiation source term. The assumption here is that radiation is effective essentially as a thin gas radiative emission to the surroundings only within the thin region of high temperature. However, radiative heat exchanges in realistic combustion systems involve emission and absorption taking place over much larger length scales. Present non-adiabatic model attempts to account for the effect of global radiation heat loss on flamelet structure through an 'enthalpy defect' concept proposed by Bray and Peters (1994). Enthalpy defect ζ is defined as the difference between the actual enthalpy $\tilde{h}$ and adiabatic enthalpy $\tilde{h}_{ad}$ which can be directly related to the mean mixture fraction:

$$\zeta = \tilde{h} - \tilde{h}_{ad} = \tilde{h} - \left(h_2 - \tilde{Z}\left(h_2 - h_1\right)\right) \tag{5.22}$$

Where h_2 and h_1 are enthalpy of the fuel and air streams. The enthalpy defect thus, provides a measure of the local non-adiabatic conditions in the turbulent flame. By imposing enthalpy defect as an additional parameter on to the flamelet, coupling between the non-adiabatic conditions in the turbulent flame and the thermo-chemical structure of the flamelet are achieved. The method of imposing enthalpy defect on the flamelet has been discussed in detail in Chapter 7, section 7.1.2.

Since the effect of radiation on flamelet structure is not handled through a source term, steady flamelet equations can be used to obtain the thermo-chemical structure of the flame. Any scalar variable (ϕ) in the non-adiabatic flamelet model is a function three parameters, the mixture fraction Z, stoichiometric scalar dissipation rate χ_{st} and additionally the enthalpy defect ζ.

$$\phi = \phi\left(Z; \chi_{st}; \zeta\right) \tag{5.23}$$

Turbulent mean value of a scalar ϕ can then be obtained by integrating the instantaneous values with joint PDF of the three parameters Z, χ_{st} and ζ.

$$\tilde{\phi} = \int_0^1 \int_0^\infty \int_{\zeta_{min}}^{\zeta_{max}} \phi\left(Z; \chi_{st}; \zeta\right) \tilde{P}\left(Z, \chi_{st}, \zeta; x, t\right) d\zeta \, d\chi_{st} dZ \tag{5.24}$$

Following a strategy similar to that used for adiabatic version of the steady flamelet model, statistical independence between the three parameters has been assumed and a presumed PDF approach has been adopted. The PDF for mixture fraction is assumed to follow β function distribution, PDF for scalar dissipation rate assumed to follow log-normal distribution and a δ function has been assumed for enthalpy defect. Assumption of δ function gains support from the argument (Bray and Peters 1994) that the fluctuations of enthalpy are mainly due to mixture fraction fluctuations and hence are accounted by the latter. Upon imposing the simplifications, the integration for mean value of the scalars is given by:

$$\tilde{\phi} = \int_0^\infty \int_0^1 \phi(Z;\chi_{st};\zeta)\tilde{P}(Z)\tilde{P}(\chi_{st})\delta\left(\zeta-\tilde{\zeta}\right)dZd\chi_{st} \tag{5.25}$$

This non-adiabatic version of SLFM has been referred as NADM (non-adiabatic model with multiple scalar dissipation rates) in the present thesis. In this model, the variation in non-adiabatic structure with respect to scalar dissipation rate is considered for each enthalpy defect. Thus, the effort of generating flamelets in SLFM is multiplied by the number of enthalpy defects. In order to simplify the pre-processing effort, Hossain *et al.* (2001) who previously contributed to the development of this model considered only a single flamelet per enthalpy defect. Such a simplification drastically reduces the flamelet generation effort as well as pre-integration effort since Eq (5.25) will be reduced to:

$$\tilde{\phi} = \int_0^1 \phi(Z;\zeta)\tilde{P}(Z)\delta\left(\zeta-\tilde{\zeta}\right)dZ \tag{5.26}$$

This simplified non-adiabatic model with single flamelet or scalar dissipation rate per enthalpy defect is referred as NADS in the current thesis. In the present work, simulations have been carried out with both the models to verify the impact of omitting the effects of scalar dissipation rate on the predictions especially the pollutant NO which was not studied by Hossain *et al.* (2001).

With both the non-adiabatic models, enthalpy is no longer a conserved scalar and a transport equation for the mean enthalpy has to be solved in addition to the mean mixture fraction and its variance equations.

The balance equation for mean enthalpy follows:

$$\frac{\partial}{\partial t}\left(\bar{\rho}\tilde{h}\right)+\frac{\partial}{\partial x_k}\left(\bar{\rho}\tilde{u}_k\tilde{h}\right)=\frac{\partial}{\partial x_k}\left(\frac{\mu_t}{Pr_h}\frac{\partial \tilde{h}}{\partial x_k}\right)+\tilde{Q}_{rad} \qquad (5.27)$$

Where the turbulent Prandtl number Pr_h takes a value of 0.9. The radiative source term Q_{rad} requires elaborate calculations in the CFD and it has been obtained from the Discrete Transfer Method (DTRM) of Lockwood and Shah (1981).

Discrete Transfer Method

In this method representative rays are fired from the domain boundaries. For each boundary element, a radiating hemisphere is divided into finite number of solid angles and the intensity through a particular solid angle is represented by a single ray which is infact the main assumption of the model. The direction of each ray is specified in terms of the zenith (theta) and azimuthal (phi) angles. In the current work each quadrant is divided into 64 parts in theta and 64 parts in phi directions thereby giving 64 x 64 rays in one quadrant. The radiative transfer equation or the recurrence equation is solved along each ray and this tracks the change in radiation intensity along the path of the ray from one boundary element to the other. In the present model the surfaces are assumed to be diffuse and gray. i.e, the emissivities are independent of direction and wavelength respectively.

The recurrence equation is employed successively from boundary to boundary and the net radiation heat flux from each boundary element is calculated. The sum of the intensity changes of all the rays that traverse a control volume in the domain provides the radiation source term which goes into the mean enthalpy equation (Eq. 5.27). In solving the recurrence equation, the total intensity at the beginning of the path for a ray in a particular element is required. This is a sum of reflected part of incoming intensity and directly emitted intensity. In the current work, the directly emitted intensity is calculated from the knowledge of wall temperature and wall emissivity (set as 0.8). The incoming intensity is a summation of the incident intensities for all rays. This is not known prior to radiation calculations and hence the solution process is iterative. In the current work, the value is initialised by calculating incident radiation from near wall gas temperature.

The DTRM handles radiation in participating media. In the present model, only CO_2 and water vapour H_2O have been considered as the participating gases, which absorb and emit radiation depending on local mixture temperatures. The emissivities of the gases are calculated using the weighted sum of gray gases model (WSGGM).

5.4 Flamelet based NO sub models

Oxides of Nitrogen (NO_x) are chemical components which are present in low concentrations in turbulent non-premixed flames and are considered to be trace species in comparison to other major products of combustion. Trace species which maintain chemical equilibrium pose no special issues in that their instantaneous concentrations can be directly parameterized by mixture fraction, scalar dissipation rate and enthalpy defect (in non-adiabatic model). However, the slow and kinetically controlled chemistry of NO results in concentrations which are almost always away from equilibrium and adopting the classical steady flamelet approach results in significant overprediction in the concentrations. Hence, separate treatment has been adopted through NO sub-models. The sub-models that have been implemented in the in-house RANS code are classified into:

(a) Steady flamelets (adiabatic and non-adiabatic) based NO submodels

(b) Unsteady flamelets (adiabatic and non-adiabatic) based NO submodels

The low concentration of NO means that its influence on the mixing field, temperature and major species is negligible and hence it could be post-processed with RANS calculations. Thus, in the present study, CFD calculations of turbulent flow and mixing field are performed until convergence and subsequently the mean NO is post-processed by invoking an appropriate submodel. A noteworthy point here is that, even the unsteady flamelets based NO calculation uses the turbulent flow and mixing field obtained from steady flamelets. Such an approach is computationally efficient and of great practical interest. It avoids the need for expensive interactive flamelet modelling wherein unsteady flamelet equations are solved during the turbulent flow and mixing field calculations. The validity of this approach has been demonstrated by Pitsch *et al.*(2000) who showed that heat release and major species concentration predictions are unaffected by transient effects.

The different NO_x submodels that have been employed with adiabatic and non-adiabatic flamelet modelling in the current work are shown in Table 5.1 and the submodels are discussed in the subsections to follow.

	Adiabatic flamelet modelling (SLFM) with RANS		**Non-adiabatic flamelet modelling (NADM & NADS) with RANS**	
Flow, mixing field, Temp & Major Species	Steady adiabatic flamelets		Steady non-adiabatic flamelets	
NO (Post-processing)	**Steady adiabatic submodel**	**Unsteady adiabatic submodel**	**Steady non-adiabatic submodel**	**Unsteady non-adiabatic submodel**
	Steady adiabatic flamelets	Unsteady adiabatic flamelets	Steady non-adiabatic flamelets	Unsteady non-adiabatic flamelets

Table 5.1: RANS based NO sub-models for SLFM and non-adiabatic flamelet modelling.

5.4.1 Steady adiabatic NO submodel

This submodel (referred by SLFM-NO-TRE) is used in conjunction with SLFM to model NO. It follows a simple technique of addressing the slow and kinetically controlled chemistry of NO_x. In the post-processing phase, the mean NO mass fraction is calculated from the solution of its steady transport equation (Eq. 5.28) which contains the mean NO production rate as a source term. This model requires as input, the converged solution of turbulent flow and mixing fields from steady flamelet modelling.

$$\frac{\partial}{\partial t}\left(\bar{\rho}\tilde{y}_{NO}\right)+\frac{\partial}{\partial x_k}\left(\bar{\rho}\tilde{u}_k\tilde{y}_{NO}\right)=\frac{\partial}{\partial x_k}\left(\frac{\mu_t}{Sc_{NO}}\frac{\partial\tilde{y}_{NO}}{\partial x_k}\right)+\bar{\rho}\tilde{\dot{\omega}}_{NO} \qquad (5.28)$$

Where the turbulent Schmidt number Sc_{NO} has been considered to be 0.7.

Consistent with the approach adopted for mean temperature and major species, the closure of the mean chemical source term is achieved by presumed PDF approach. The PDF for mixture fraction is assumed to follow β function while the PDF for scalar dissipation rate follows log-normal distribution.

$$\tilde{\dot{\omega}}_{NO} = \int_0^\infty \int_0^1 \dot{\omega}_{NO}(Z;\chi_{st})\tilde{P}(Z)\tilde{P}(\chi_{st})dZd\chi_{st} \tag{5.29}$$

Where $\dot{\omega}_{NO}$ the instantaneous production is rate of NO and is obtained from the solution of steady adiabatic flamelet equations.

5.4.2 Steady non-adiabatic NO submodel

Two versions of this submodel (referred by NADM-NO-TRE and NADS-NO-TRE) have been employed in the present study and both follow exactly the same strategy as the steady adiabatic NO_x submodel except that they work within the framework of non-adiabatic flamelet modelling. The turbulent flow and mixing field necessary for post-processing are obtained from the steady non-adiabatic flamelet model which uses enthalpy defect imposed non-adiabatic flamelets. The transport equation for mean mass fraction of NO is same as in the Eq (5.28). However, the mean source term is now derived from an instantaneous source term which is obtained from enthalpy defect imposed non-adiabatic flamelets. For the NADM-NO-TRE submodel which is used in conjunction with the NADM model for non-adiabatic turbulent flame calculations, the mean source term is evaluated as:

$$\tilde{\dot{\omega}}_{NO} = \int_0^\infty \int_0^1 \dot{\omega}_{NO}(Z;\chi_{st};\zeta)\tilde{P}(Z)\tilde{P}(\chi_{st})\delta(\zeta-\tilde{\zeta})dZd\chi_{st} \tag{5.30}$$

For NADS-NO-TRE submodel which is used in conjunction with NADS model, the scalar structure is independent of the variations in scalar dissipation rate and hence the required integration for the mean source term is given by:

$$\tilde{\dot{\omega}}_{NO} = \int_0^1 \dot{\omega}_{NO}(Z;\zeta)\tilde{P}(Z)\delta(\zeta-\tilde{\zeta})dZ \tag{5.31}$$

Here again, the PDF for mixture fraction is assumed to follow β function while the PDF for scalar dissipation rate follows log-normal distribution. The PDF for enthalpy defect is assumed to follow a δ function.

5.4.3 Unsteady adiabatic NO submodel

The unsteady modelling follows a radically different approach to the steady submodels. The Lagrangian flamelet model (LFM) of Pitsch *et al.* (1998) and the Eulerian particle flamelet model (EPFM) of Barths *et al.* (1998a) are the popular approaches to unsteady modelling. While LFM is restricted to parabolic flows, EPFM is a more sophisticated approach and is applicable to both parabolic and elliptical flows. In the present study both the parabolic jet flames and elliptic bluff-body stabilized flames have been investigated and hence EPFM has been implemented as the standard unsteady NO submodel. This submodel as with the steady submodels is invoked in the post-processing stage. However, the post-processing calculations are more involved since time varying calculations have to be performed at both CFD and flamelet levels.

EPFM is motivated by the theoretical and experimental evidence that flamelet structure cannot respond instantaneously to changes in scalar dissipation rate. To account for these transient effects present in globally steady flames, it is necessary that unsteady terms in the flamelet equations are retained and the transient evolution of scalar dissipation rate is accounted. Hence, in EPFM, marker particles which represent flamelets are introduced into the turbulent flow field and transported throughout the domain. These particles follow the paths along which the scalar dissipation rate is changing and thus they can be viewed as carrying the unsteady flamelets. The spatial distribution of a particle of type n can be obtained from an Eulerian unsteady passive scalar transport equation for the mean number of particles per unit volume $\tilde{I}_n$ at a particular position in space (Barths *et al.*, 1998a).

$$\frac{\partial}{\partial t}\left(\bar{\rho}\tilde{I}_n\right)+\frac{\partial}{\partial x_k}\left(\bar{\rho}\tilde{u}_k\tilde{I}_n\right)=\frac{\partial}{\partial x_k}\left(\frac{\mu_t}{Sc_{I_n}}\frac{\partial\tilde{I}_n}{\partial x_k}\right) \tag{5.32}$$

The number of particles I (x,t) per unit volume represents the probability of finding a marker particle at a particular location x and time t. This is set equal to unity at t =0 within an initialization region and zero outside the region. The initialization region is close to the fuel inlet and is defined as $Z > Z_{st}$. This definition ensures that the particles are initialized in a fuel rich region where the temperature is low enough for NO formation to be negligible. If only one particle is considered, the initial

probability $\tilde{I}_1$ is set to unity in the initialization region and zero outside the region. If more than one particle and hence more than one flamelet history is considered, the initialization region remains unchanged but it is divided into number of sub-regions corresponding to the different types of marker particles and each sub-region is attached to one particle. The initial probability of finding a marker particle is then equal to unity in its own sub-region and zero elsewhere. The time dependent CFD calculations are run long enough to allow for all the particles to exit from the domain. From the solution of the time dependent calculations, distribution of $\tilde{I}_n$ within the domain can be stored as a function of flow time. For a type n marker particle, a domain averaged scalar dissipation rate conditioned on stoichiometric mixture fraction can then be calculated for each time step as:

$$\hat{\chi}_{st,n} = \frac{\int_V \tilde{I}_n \bar{\rho} \tilde{\chi}_{st}^{3/2} \tilde{P}(Z_{st}) dV'}{\int_V \tilde{I}_n \bar{\rho} \tilde{\chi}_{st}^{1/2} \tilde{P}(Z_{st}) dV'} \tag{5.33}$$

Where V denotes the volume of the computational domain. The average conditional scalar dissipation rate $\tilde{\chi}_{st}$ is related to the unconditional scalar dissipation rate $\tilde{\chi}$ by:

$$\tilde{\chi}_{st} = \frac{\tilde{\chi} f(Z_{st})}{\int_0^1 f(Z) \tilde{P}(Z) dZ} \tag{5.34}$$

This has been derived from the functional dependence of scalar dissipation rate and on mixture fraction presented previously in Eq 5.8:

$$\chi = \frac{a}{\pi} exp\left\{-2\left[erfc^{-1}(2Z)\right]^2\right\} = \frac{a}{\pi} f(Z)$$

$$\therefore \chi / \chi_{st} = f(Z) / f(Z_{st}) \tag{5.35}$$

For turbulent flows, the function $f(Z)$ can be integrated with a presumed PDF for Z in the form of β function distribution thereby leading to Eq. 5.33.

Thus, for a marker particle of type n, by computing $\hat{\chi}_{st,n}$ for each time interval and for the entire length of the flow time, transient evolution of scalar dissipation rate is obtained. Unsteady flamelet equations are then solved for each time interval by setting $\hat{\chi}_{st,n}$ equal to χ in Eq.5.6. Solutions of the unsteady flamelet equations provide the

flamelet history or the transient evolution of thermo-chemical structure. Calculations of the unsteady flamelet equations require initial solution. In the present study, solution of the steady flamelet equations for $\hat{\chi}_{st,n}$ at t =0 is prescribed as the initial solution after resetting all the mass fractions of species associated with the NO reaction mechanism to zero.

Upon obtaining the solutions of unsteady flamelet equations for every type of marker particles, the mean NO mass fractions at every spatial location in the computational domain can be computed from:

$$\tilde{Y}_{NO}(\vec{x}) = \frac{\sum_n \int_0^t \tilde{I}_n(t') \tilde{Y}_{NO,n}(\vec{x},t') dt'}{\sum_n \int_0^t \tilde{I}_n(t') dt'} \tag{5.36}$$

Where $\tilde{Y}_{i,n}(\vec{x},t')$ is the Favre averaged NO mass fraction at location $\vec{x}$ and time t' and is calculated through integration of the unsteady flamelet solution weighted by the PDF of mixture fraction.

$$\tilde{Y}_{NO,n}(\vec{x},t') = \int_0^1 Y_{NO,n}(\vec{x},t') \tilde{P}(Z) dZ \tag{5.37}$$

Present study uses only a single marker particle and hence CFD calculations involve solving for a single time dependent passive scalar transport equation and the flamelet calculations involve solving for a single flamelet history. The current unsteady adiabatic NO submodel is referred by SLFM-EPFM.

5.4.4 Unsteady non-adiabatic NO submodel

The unsteady non-adiabatic submodel (NADM-EPFM) is in most respects similar to the EPFM model discussed in the previous section and follows the same mathematical procedure. However, there are a few but key differences. The converged turbulent flow and mixing field required for time dependent passive scalar calculations is obtained from the solution of non-adiabatic flamelet model with steady enthalpy defect imposed non-adiabatic flamelets.

While the procedure for generating steady non-adiabatic flamelets with enthalpy defect imposed as additional parameter is well in place, it is not so with generating unsteady non-adiabatic flamelets.

Enthalpy defect varies spatially and even with a high degree of automation, it is extremely tedious and time consuming to generate transient flamelets for the multitude of enthalpy defects encountered in the domain. One could contemplate on leveraging the procedure of domain averaging of scalar dissipation rate to enthalpy defect. However, it is still ambiguous as to whether or not such an averaging is justifiable. Hence, in the present study, the transient evolution of flamelet structure is calculated by solving the unsteady flamelet equations with radiation heat loss incorporated through a radiation source term instead of enthalpy defect. While this approach, as discussed before, is not advisable for steady flamelets, it could be well utilized for unsteady flamelets. An accurate yet feasible procedure for enthalpy defect imposed transient flamelet calculations is still an open problem and future works should try addressing it.

5.5 Flamelet/progress variable approach

The Flamelet/Progress Variable (FPV) Approach has been developed specifically for LES by Pierce (2001) and Pierce and Moin (2004). In the present work, the FPV approach has been implemented in both the in-house LES and RANS codes.

5.5.1 Motivation for FPV

The FPV approach derives motivation from some of the fundamental problems with the steady flamelet model for non-premixed combustion (SLFM). As previously mentioned, one of limitations of the steady flamelet model is its inability to account for local extinction and re-ignition phenomena. Causes other than the assumption of steady state structure can be understood by studying the Fig. 5.2 where the complete locus of solutions of steady flamelet equations is shown. The shape of the curve, which is often referred to as "S–shaped curve" (mirrored "S" in Fig.5.2) in

combustion literature is determined primarily by the chemical kinetics. With Arrhenius kinetics, there are typically three solution branches:

1. stable burning branch
2. unstable branch of partially extinguished states, and
3. the completely extinguished states

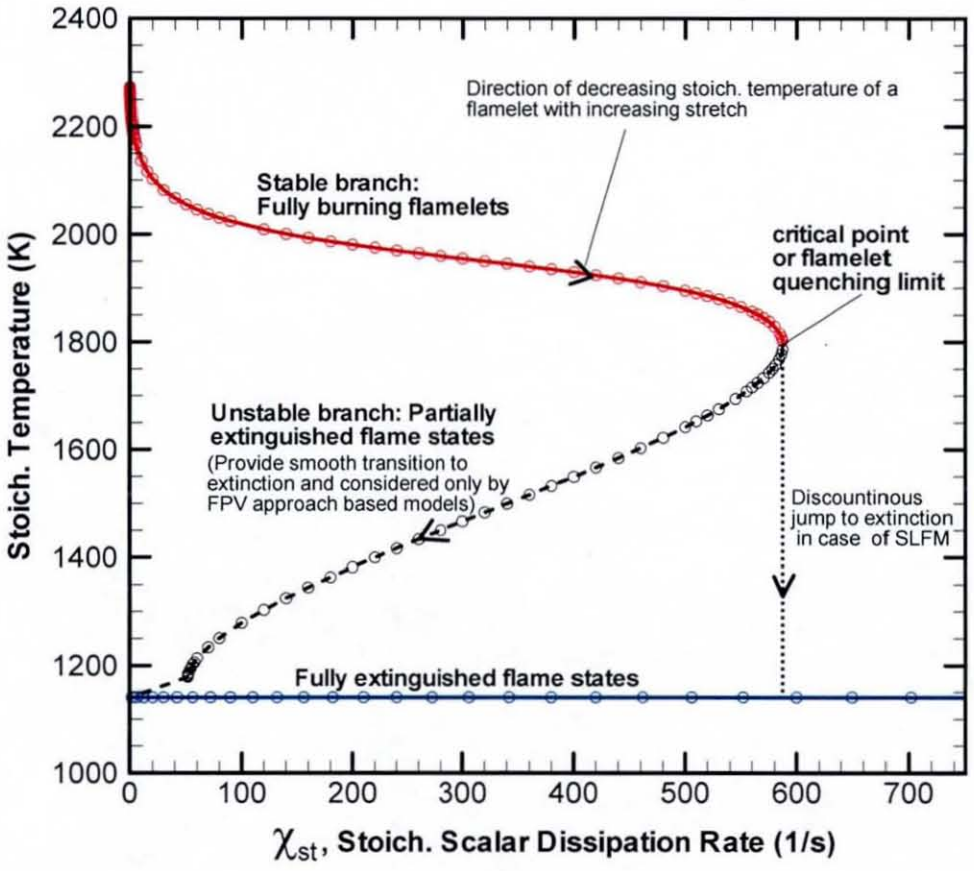

Figure 5.2: Locus of Stoichiometric temperature for all the solutions of the steady flamelet equations. Generated for the Berkeley lifted flame (section 9.1) conditions: Fuel CH_4-Air (25%-75%) at 323 K and Oxidizer (vitiated co-flow) at 1355 K.

The point of maximum flame temperature at scalar dissipation rate equal to zero corresponds to the state of chemical equilibrium. An increase in the scalar dissipation rate corresponds to an increase in the mixing of the reactants. Thus, on the stable burning branch, the maximum flame temperature decreases with increase in the scalar dissipation rate due to the dilution of the product concentrations with the increased concentration of reactants. As the critical point or when the quenching limit is

reached, the flame temperature drops to a level where Arrhenius rate factors in the chemical kinetics begin to limit the reaction rates. A slight increase in the scalar dissipation rate from thereon will result in the complete extinction of the flamelet. However, there exists a distinct transition from fully burning to fully extinguished state identified by the unstable branch of partially extinguished states (dashed line). Along this branch, dissipation rate decreases with decreasing flame temperature to keep the mixing in balance with the lower reaction rates. On the lower branch of completely extinguished states, the effect of chemical kinetics is negligible and the chemical states are independent of dissipation rate. All the chemical states on the lower branch thus point to pure mixing of the reactants.

In SLFM, the stoichiometric scalar dissipation rate is used to uniquely parameterize the flame states. However, the S-curve clearly shows that multiple solutions can exist for certain values of the scalar dissipation rate. Hence, a unique parameterization of the flame states based on scalar dissipation rate cannot take into account all the flame states along the S-curve. Thus, typically, in SLFM only the flame states along the stable burning branch and extinguished states are considered and the unstable partially extinguished flame states are ignored. This is illustrated by the discontinuous jump (dotted line) in Fig.5.2. On the other hand, the unstable branch has been shown by Pierce (2001) to be important both physically and from modelling point of view since it demarcates the border between ignition and extinction of the flame. Absence of information regarding the unstable partially extinguished states thus makes the steady flamelet model incomplete and inadequate to handle ignition and extinction.

The Flamelet/progress variable approach addresses this concern through the replacement of scalar dissipation rate by a flamelet parameter which is based on reaction progress variable. Introduction of reaction progress variable offers an additional advantage in that the model's applicability can be extended from purely non-premixed to partially premixed combustion. The conserved scalar mixture fraction by itself does not contain any intrinsic information about the chemical reactions and the addition of progress variable which is a non-conserved scalar results in a more comprehensive formulation.

5.5.2 FPV formulation

The FPV approach starts with the introduction of a reactive scalar based flamelet parameter λ which replaces the scalar dissipation rate. The definition of flamelet parameter is dictated by the criterion that the flamelet parameter should uniquely parameterize all the steady flamelet solutions along the S-curve including the unstable partially extinguished states. In the work of Pitsch and Ihme (2005) the flamelet parameter has been defined as the reaction progress variable C at $Z=Z_{st}$ where C has been defined, following Pierce and Moin (2004), as the linear combination of product mass fractions viz. those of CO_2, CO, H_2O and H_2. The $C(Z_{st})$ was found to vary (decrease) monotonically from equilibrium to complete extinction and hence satisfied the flamelet parameter criterion.

In the present study, the FPV has been implemented for CH_4/Air partially premixed flame in vitiated co-flow. For this flame, the vitiated co-flow, which is also the oxidizer, has significant levels of H_2O and H_2. Hence, with a view to keep the progress variable definition simple and avoid any necessity for normalization, a linear combination of only CO_2 and CO mass fractions has been chosen for the present study. The progress variable is thus given by:

$$C = Yco_2 + Yco \tag{5.38}$$

With this definition of progress variable, variation of $C(Z_{st})$ along all the flame states (Fig. 5.3a) has been analysed. It has been found that although the overall variation is monotonic, a careful observation of the region in the near proximity to equilibrium state shows the existence of saddle points (Fig. 5.3b). These saddle points prevent a unique parameterization and hence need to be removed from the solution space if $C(Z_{st})$ were to be used as flamelet parameter. However, this problem vanishes if the maximum value of progress variable C_{max} is used as the definition of flamelet parameter. The variation of C_{max} as shown in Fig 5.3a&b is truly monotonic along the entire solution space. Hence, in the present study, the flamelet parameter λ is defined by C_{max}. An example for a specific maximum progress variable is shown in Fig. 5.4.

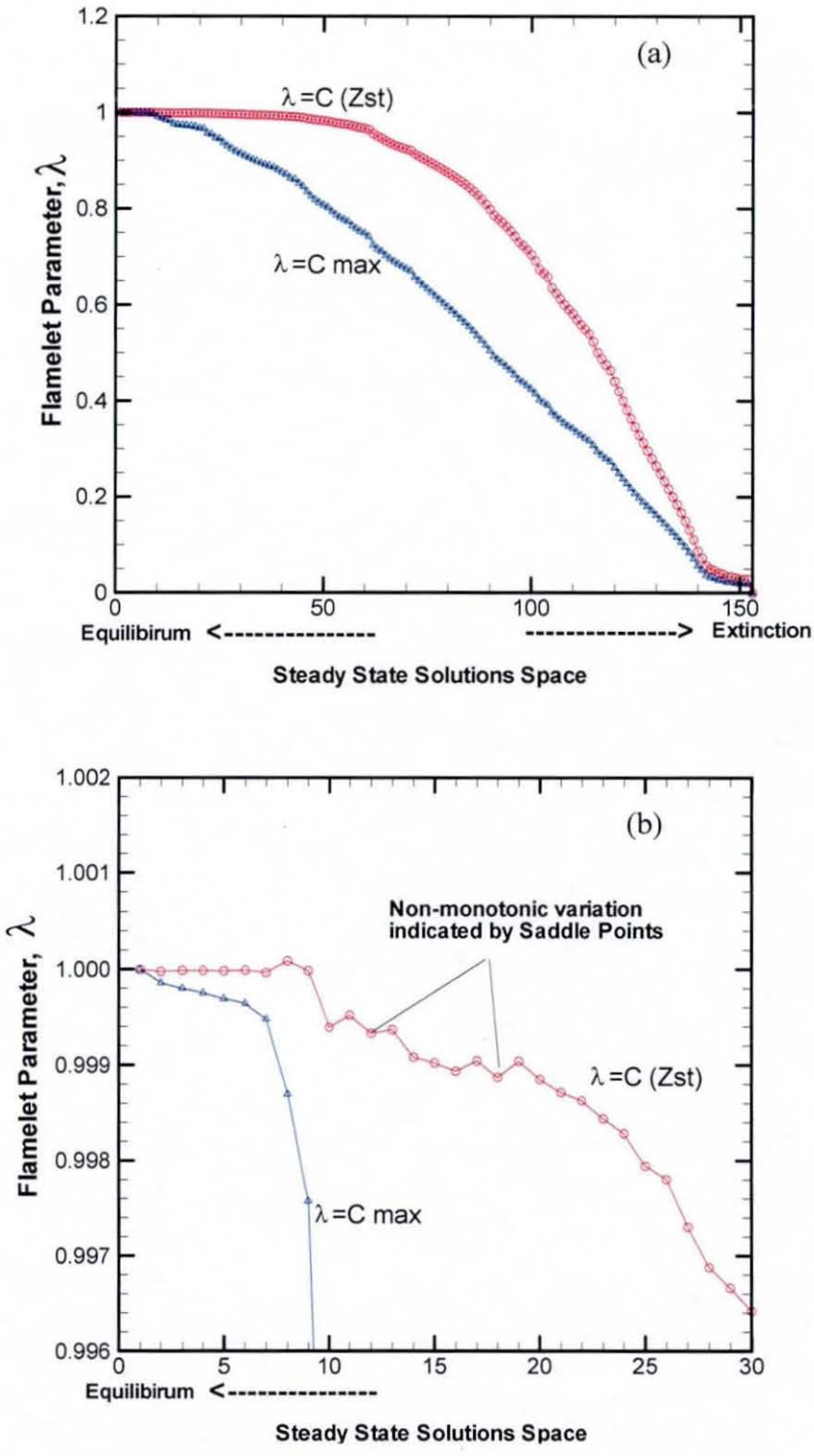

Figure 5.3: Variation in parameterization of flamelets (a) along the entire solution space and (b) close to the equilibrium state with two different definitions of flamelet parameter. Generated for the Berkeley lifted flame (section 9.1) conditions.

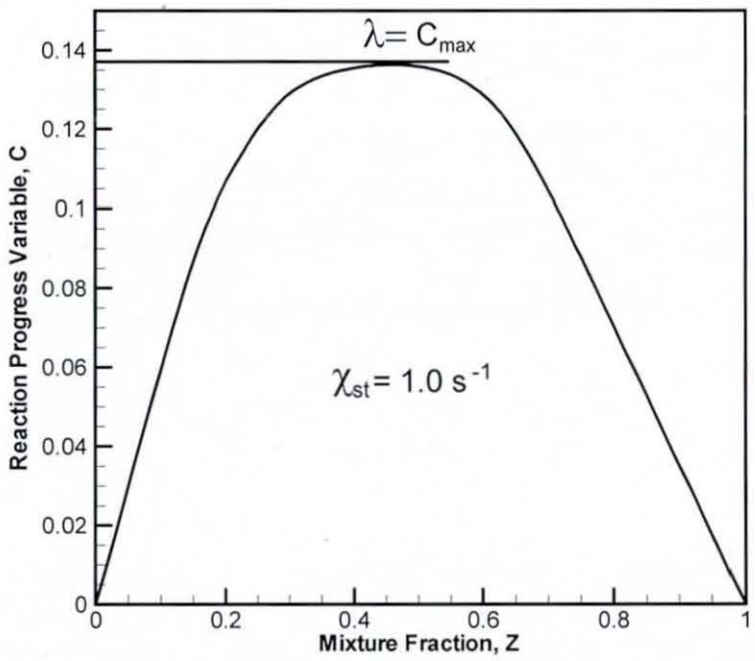

Figure 5.4: Reaction progress variable distribution within a flamelet and the definition of flamelet parameter. Generated for the Berkeley lifted flame (Section 9.1) conditions.

Any local combination of mixture fraction and progress variable corresponding to that flamelet is described by the flamelet parameter indicated in the Fig 5.4. This implies that the value of the flamelet parameter λ is a given value for a given flamelet and therefore independent of the mixture fraction. This is of great advantage in turbulent reacting flows because it simplifies the modelling of joint PDF of Z and λ. The steady flamelet solutions can then be expressed in terms of the flamelet parameter as:

$$\phi = \phi(Z, \lambda) \tag{5.39}$$

Application to LES

Filtered values of the reactive scalars $\tilde{\phi}$ in large eddy simulation can be determined from:

$$\tilde{\phi} = \int_0^1 \int_{\lambda_{min}}^{\lambda_{max}} \phi(Z;\lambda)\, \tilde{P}(Z,\lambda;x,t)\, d\lambda dZ \tag{5.40}$$

Where $\tilde{P}(Z,\lambda;x,t)$ is the Favre filtered joint PDF and the integration limits λ_{min} and λ_{max} correspond to the steady flamelet solution for $\chi_{st}\rightarrow 0$ and $\chi_{st}\rightarrow\infty$, respectively. In the present study, a presumed PDF method has been adopted and the fact that λ is independent of Z augurs well for the modelling as the joint filtered PDF can be expressed as the product of marginal Favre filtered PDF (FPDF) of Z and λ:

$$\tilde{P}(Z,\lambda;x,t)=\tilde{P}(Z)\tilde{P}(\lambda) \tag{5.41}$$

There is enough evidence which suggests that the PDF for a passive scalar such as mixture fraction can be reasonably approximated by a β function (Peters, 1984). However, it is well known that the PDF of a reactive scalar such as the flamelet parameter or reaction progress variable cannot be approximated by presumed distributions. Nevertheless, presumed PDF approach forms the starting point for the development of more complex formulations.

A δ function has been assumed for the marginal FPDF of flamelet parameter in the works of Pierce and Moin (2004) and Pitsch and Ihme (2005). On the other hand, Ihme *et al.* (2005) in an a priori study with DNS data have shown that an FPDF based on β function distribution provides better prediction capability. Also, Bradley *et al.*(1990) achieved successful predictions in a turbulent lifted jet flame using a β function distribution for reaction progress variable in their mixedness-reactedness model.

As will be shown in the sections to follow, the β function based FPDF significantly increases the complexity of the formulation and can lead to appreciable penalties in the computational cost of large eddy simulations. In the present study, both the δ function and β function based FPV formulations have been implemented in LES and the extent of scale up in accuracy of predictions with the rise in computational time has been investigated.

FPV δ function model

In this model, the modelled form of joint FPDF is given by:

$$\tilde{P}(Z,\lambda;x,t)=\beta\left(Z;\tilde{Z},\widetilde{Z''^2}\right)\delta\left(\lambda-\tilde{\lambda}\right) \tag{5.42}$$

Hence, the filtered scalar equation reads:

$$\tilde{\phi} = \int_0^1 \int_{\lambda_{min}}^{\lambda_{max}} \phi(Z;\lambda)\beta\left(Z;\tilde{Z},\widetilde{Z''^2}\right)\delta\left(\lambda-\tilde{\lambda}\right)d\lambda dZ \tag{5.43}$$

The β function can be evaluated from the knowledge of filtered mixture fraction $\tilde{Z}$ and its subgrid variance $\widetilde{Z''^2}$ by following the definition presented in Eqs.5.11-5.13. The filtered mixture fraction $\tilde{Z}$ is known from the solution of its transport equation (Eq.4.58) while the filtered variance $\widetilde{Z''^2}$ is modelled using Eq. 5.20. The $\tilde{\lambda}$ represents the local flamelet parameter in the turbulent reacting flow. Since there is no direct method of determining filtered flamelet parameter in LES, its handling is less straightforward and the suggested approach of Pierce and Moin (2004) and Pitsch and Ihme (2005) is discussed here.

In the FPV approach, an additional transport equation for filtered reaction progress variable $\tilde{C}$ is solved in CFD with the filtered reaction source term $\tilde{\dot{\omega}}_c$ calculated from the chemical states predicted by the steady flamelet equations.

$$\frac{\partial}{\partial t}\left(\bar{\rho}\tilde{C}\right)+\frac{\partial}{\partial x_k}\left(\bar{\rho}\tilde{u}_k\tilde{C}\right)=\frac{\partial}{\partial x_k}\left(\left(\frac{\mu}{Sc}+\frac{\mu_t}{Sc_t}\right)\frac{\partial\tilde{C}}{\partial x_k}\right)+\bar{\rho}\tilde{\dot{\omega}}_c \tag{5.44}$$

$$\tilde{\dot{\omega}}_c = \int_0^1 \int_{\lambda_{min}}^{\lambda_{max}} \dot{\omega}_c(Z;\lambda)\beta\left(Z;\tilde{Z},\widetilde{Z''^2}\right)\delta\left(\lambda-\tilde{\lambda}\right)d\lambda dZ \tag{5.45}$$

Where $\dot{\omega}_c$ is the laminar source term obtained from the solution of flamelet equations by summing the rate of production of the chemical species CO_2 and CO. The laminar and turbulent Schmidt numbers take values of 0.7 and 0.4 respectively.

On the other hand, the solutions $C = C(Z;\lambda)$ of the steady flamelet equations provide additional means of determining the filtered reaction progress variable:

$$\tilde{C}_{sfe} = \int_0^1 \int_{\lambda_{min}}^{\lambda_{max}} C(Z;\lambda)\beta\left(Z;\tilde{Z},\widetilde{Z''^2}\right)\delta\left(\lambda-\tilde{\lambda}\right)d\lambda dZ \tag{5.46}$$

Where the subscript '*sfe*' is used to differentiate the filtered progress variable determined from steady flamelet equations to that obtained from the transport equation (Eq. 5.44).

For the FPV approach to be consistent, it is necessary that Eqs 5.44 and 5.46 are consistent with each other i.e:

$$\tilde{C} = \tilde{C}_{sfe} \tag{5.47}$$

The constraint equation (Eq. 5.47) eliminates the need for direct computation of the filtered flamelet parameter $\tilde{\lambda}$ in LES. In principle, $\tilde{\lambda}$ can be obtained by an iterative procedure by varying its value until the constraint is satisfied. In the present study, FPV is implemented in the numerical code through a look-up-table concept. The filtered scalars determined from Eq.5.43 are first tabulated as a function of $\tilde{Z}$, $\widetilde{Z''^2}$ and $\tilde{\lambda}$. The filtered scalars include the reaction progress variable $\tilde{C}_{sfe}$ as well. This table could then be used in LES. Within each computational cell in LES, $\tilde{\lambda}$ would have to be computed from the constraint equation (Eq. 5.47) through an iterative procedure.

However, for computational efficiency a different approach is followed in the present study. The look-up-table initially generated in λ space is re-interpolated to progress variable space by replacing $\tilde{\lambda}$ with $\tilde{C}$. The re-interpolation process has been discussed in section 7.1.5. The re-interpolated look-up-table then provides the filtered scalars as function of quantities which are readily available from LES (namely, $\tilde{Z}$, $\widetilde{Z''^2}$ and $\tilde{C}$).

$$\tilde{\rho} = \tilde{\rho}\left(\tilde{Z}, \widetilde{Z''^2}, \tilde{C}\right),\ \tilde{T} = \tilde{T}\left(\tilde{Z}, \widetilde{Z''^2}, \tilde{C}\right), \tilde{Y}_i = \tilde{Y}_i\left(\tilde{Z}, \widetilde{Z''^2}, \tilde{C}\right) \text{ and } \tilde{\dot{\omega}}_c = \tilde{\dot{\omega}}_c\left(\tilde{Z}, \widetilde{Z''^2}, \tilde{C}\right) \tag{5.48}$$

FPV β function model

The FPV β function model is an extension of the δ function model. In this model, the modelled form of joint FPDF is given by:

$$\tilde{P}(Z, \lambda; x, t) = \beta\left(Z; \tilde{Z}, \widetilde{Z''^2}\right)\beta\left(\lambda; \tilde{\lambda}, \widetilde{\lambda''^2}\right) \tag{5.49}$$

And the filtered values of the scalars are determined from:

$$\tilde{\phi} = \int_0^1 \int_{\lambda_{min}}^{\lambda_{max}} \phi(Z;\lambda)\beta\left(Z;\tilde{Z},\widetilde{Z''^2}\right)\beta\left(\lambda;\tilde{\lambda},\widetilde{\lambda''^2}\right)d\lambda dZ \tag{5.50}$$

The induction of second moment of flamelet parameter $\widetilde{\lambda''^2}$ brings additional complexity to the FPV β function model. Evaluation of the filtered scalar now requires knowledge of not only the mean but also the variance of flamelet parameter. In the FPV δ function model, it has been shown that a constraint equation can be derived by equating the filtered reaction progress variable $\tilde{C}$ obtained from CFD to that obtained from the solutions of steady flamelet equations $\tilde{C}_{sfe}$. An iterative procedure could then be used to obtain $\tilde{\lambda}$ and thus eliminate the need to model $\tilde{\lambda}$ in CFD. In the present study, this approach has been extended to the variance of flamelet parameter $\widetilde{\lambda''^2}$ and the need to model $\widetilde{\lambda''^2}$ in LES has been circumvented.

With the FPV β function model, the filtered mean and variance of progress variable $\tilde{C}$ and $\widetilde{C''^2}$ are computed in CFD. The filtered mean progress variable $\tilde{C}$ is obtained from the solution of transport equation (Eq. 5.44). Similarly, the sub-grid scale variance $\widetilde{C''^2}$ can be determined from the solution of its transport equation:

$$\begin{aligned}\frac{\partial}{\partial t}\left(\bar{\rho}\widetilde{C''^2}\right)+\frac{\partial}{\partial x_k}\left(\bar{\rho}\tilde{u}_k\widetilde{C''^2}\right) &= \frac{\partial}{\partial x_k}\left(\left(\frac{\mu}{Sc}+\frac{\mu_t}{Sc_t}\right)\frac{\partial\widetilde{C''^2}}{\partial x_k}\right) \\ &\quad +2\frac{\mu_t}{Sc_t}\left(\frac{\partial\tilde{C}}{\partial x_k}\frac{\partial\tilde{C}}{\partial x_k}\right)-2\bar{\rho}\widetilde{C''\dot{\omega}_c''}-\bar{\rho}\widetilde{\chi_c''}\end{aligned} \tag{5.51}$$

In the above equation, the subgrid scalar fluxes have been modelled using the gradient diffusion hypothesis. The turbulent viscosity μ_t can be obtained from the Smagorinsky eddy viscosity model. On the right hand side of the equation, the second and last terms represent the production and dissipation terms respectively. The penultimate term is the filtered covariance term and represents the correlation between progress variable and chemical source term.

However, computing $\widetilde{C''^2}$ from its transport equation would mean further stretching of the LES computational time which is already higher in FPV as compared to the SLFM due to the additional equation for $\tilde{C}$. A computationally efficient alternative similar to that adopted for mixture fraction variance is to model the progress variable variance. The modelling approach has been adopted in the present study as it is best suited for the currently available computational resources. The model for sub-grid scale progress variable variance has been derived (Ihme and Pitsch, 2005) from the variance transport equation by assuming that the production, dissipation and covariance terms are in equilibrium. i.e

$$2\frac{\mu_t}{Sc_{t,c}}\left(\frac{\partial\tilde{C}}{\partial x_k}\frac{\partial\tilde{C}}{\partial x_k}\right)-2\bar{\rho}\widetilde{C''\dot{\omega}_c''}-\bar{\rho}\widetilde{\chi_c''}=0 \tag{5.52}$$

The subgrid dissipation rate of the progress variable $\widetilde{\chi_c''}$ can be written as:

$$\widetilde{\chi_c''}=\widetilde{\chi_c}-\widetilde{\chi_c^{res}}=\widetilde{\chi_c}-2\frac{1}{\bar{\rho}}\frac{\mu_t}{Sc_{t,c}}\left(\frac{\partial\tilde{C}}{\partial x_k}\frac{\partial\tilde{C}}{\partial x_k}\right) \tag{5.53}$$

The dissipation rate of the progress variable $\widetilde{\chi_c}$ is related to the dissipation rate of mixture fraction $\tilde{\chi}$ or $\tilde{\chi}_z$ (for clarity) by the time scale ratio γ.

$$\gamma=\frac{\tau_c}{\tau_z}=\frac{\widetilde{C''^2}}{\widetilde{Z''^2}}\frac{\widetilde{\chi_z}}{\widetilde{\chi_c}} \tag{5.54}$$

Using the relations in Eq.5.53 and Eq. 5.54, the unknown $\widetilde{\chi_c}$ can be replaced from Eq.5.52 thereby resulting in the following model equation for subgrid scale variance:

$$\widetilde{C''^2}=\frac{\gamma\widetilde{Z''^2}}{\tilde{\chi}_z}\left[\frac{2}{\bar{\rho}}\frac{\mu_t}{Sc_{t,c}}\left(\frac{\partial\tilde{C}}{\partial x_k}\frac{\partial\tilde{C}}{\partial x_k}\right)+2\widetilde{C''\dot{\omega}_c''}\right] \tag{5.55}$$

In the present study, the time scale ratio has been set to unity. An advanced method of handling the time scale ratio has been recently proposed by Cha and Trouillet (2006). However, implementation of such a method is beyond the scope of the present study.

The covariance term in the variance model equation is obtained computed from the solutions of the steady flamelet equations:

$$\widetilde{C''\dot{\omega}_c''} = \int_0^1 \int_{\lambda_{min}}^{\lambda_{max}} \left(C(Z;\lambda) - \tilde{C}_{sfe}\right)\left(\dot{\omega}_c(Z;\lambda) - \tilde{\dot{\omega}}_{c,sfe}\right)\beta\left(Z;\tilde{Z},\widetilde{Z''^2}\right)\beta\left(\lambda;\tilde{\lambda},\widetilde{\lambda''^2}\right)d\lambda dZ \quad (5.56)$$

In the above equation, the mean values of the progress variable $\tilde{C}_{sfe}$ and chemical source term $\tilde{\dot{\omega}}_{c,sfe}$ are evaluated from the solutions of the steady flamelet equations using Eq. 5.50. Thus, the subgrid variance of progress variable can be determined in addition to its filtered first moment in LES.

On the other hand, integration of solutions from steady flamelet equations provide different means of computing mean and variance of progress variable:

$$\tilde{C}_{sfe} = \int_0^1 \int_{\lambda_{min}}^{\lambda_{max}} C(Z;\lambda)\beta\left(Z;\tilde{Z},\widetilde{Z''^2}\right)\beta\left(\lambda;\tilde{\lambda},\widetilde{\lambda''^2}\right)d\lambda dZ \quad (5.57)$$

$$\widetilde{C''^2}_{sfe} = \int_0^1 \int_{\lambda_{min}}^{\lambda_{max}} \left(C(Z;\lambda) - \tilde{C}_{sfe}\right)^2 \beta\left(Z;\tilde{Z},\widetilde{Z''^2}\right)\beta\left(\lambda;\tilde{\lambda},\widetilde{\lambda''^2}\right)d\lambda dZ \quad (5.58)$$

For the FPV β function model to be consistent,

$$\tilde{C} = \tilde{C}_{sfe} \quad \text{and} \quad \widetilde{C''^2} = \widetilde{C''^2}_{sfe} \quad (5.59)$$

Here again the subscript '*sfe*' differentiates the values calculated from the steady flamelet equations to those obtained from CFD. The above set of equations define the two constraints which could be used to obtain $\tilde{\lambda}$ and $\widetilde{\lambda''^2}$.

With the FPV β function model, filtered scalars determined from Eq.5.50 are first tabulated as function of $\tilde{Z}$, $\widetilde{Z''^2}$, $\tilde{\lambda}$ and $\widetilde{\lambda''^2}$. Thus generated look-up-table in λ space is re-interpolated to progress variable space by replacing $\tilde{\lambda}$ with $\tilde{C}$ and $\widetilde{\lambda''^2}$ with $\widetilde{C''^2}$. The re-interpolation procedure which has been used is presented in section 7.1.5. The final re-interpolated filtered look-up-table then provides the filtered scalars

as function of quantities which are readily available from LES (namely, $\tilde{Z}$, $\widetilde{Z''^2}$, $\tilde{C}$ and $\widetilde{C''^2}$).

$$\tilde{\rho} = \tilde{\rho}\left(\tilde{Z}, \widetilde{Z''^2}, \tilde{C}, \widetilde{C''^2}\right), \tilde{T} = \tilde{T}\left(\tilde{Z}, \widetilde{Z''^2}, \tilde{C}, \widetilde{C''^2}\right), \tilde{Y}_i = \tilde{Y}_i\left(\tilde{Z}, \widetilde{Z''^2}, \tilde{C}, \widetilde{C''^2}\right),$$

$$\tilde{\dot{\omega}}_c = \tilde{\dot{\omega}}_c\left(\tilde{Z}, \widetilde{Z''^2}, \tilde{C}, \widetilde{C''^2}\right) \text{ and } \widetilde{C''\dot{\omega}_c''} = \widetilde{C''\dot{\omega}_c''}\left(\tilde{Z}, \widetilde{Z''^2}, \tilde{C}, \widetilde{C''^2}\right) \tag{5.60}$$

The FPV β function model in comparison to δ function model is more challenging from both formulation and computational perspectives. From computational point of view, the FPV β function model demands a 4D look-up-table while the δ function model requires only a 3D table. Further with the β function model, re-interpolation of the look-up-table from flamelet parameter space to progress variable space involves handling 2D scattered data which is by no means a trivial task. The δ function model on the other hand requires handling only single dimensional arrays and hence the re-interpolation task is relatively easier.

Application to RANS

Both the FPV-δ function model and β function model have been implemented in the in-house RANS code with the capability of performing calculations using look-up-tables. The formulation of FPV models which has been explained in the context of LES holds good for RANS as well. Infact, a look-up-table generated for a particular FPV model for specific flame conditions could be employed in both LES and RANS for that particular model without any change. In LES, the pre-integrated scalar values in the look-up-table are read as Favre filtered values while the same are read as Favre averaged values in RANS.

For the FPV-δ function model in RANS, similar to LES, a transport equation for mean mixture (Eq. 5.14) is solved. For the variance of mixture fraction, its transport equation (Eq. 5.15) is solved instead of modelling. A transport equation for mean reaction progress variable is solved and its form is identical to Eq. 5.43. Thus, obtained mean values are used to extract mean density and scalar values from the 3D look-up-tables specifically generated for FPV- δ function model.

For the FPV-β function model, similar to the δ function model transport equations are solved for mean mixture fraction, its variance and mean reaction progress variable. Additionally, transport equation is also solved for the variance of reaction progress variable which is modelled in the case of LES. The transport equation for the variance of reaction progress variable is identical to Eq. 5.51 except that the last term which now represents a mean scalar dissipation rate in RANS, is modelled using Eq.5.16.

Chapter 6

Numerical Approach

One of the benefits of the present work is that it facilitated enhancement in the sophistication of the in-house LES and RANS numerical codes through the implementation of the advanced mathematical models describing turbulent combustion and computationally efficient procedures which are required to handle the advanced models. The in-house LES code PUFFIN was originally developed by Kirkpatrick (2002) and Kirkpatrick *et al.* (2003) while the development of the RANS code is due to Malalasekera (1988) and Hossain (1999).

Both these computational codes are very similar as far as their foundation is concerned since in both cases the spatial discretisation is based on a control volume formulation on a staggered, non-uniform, Cartesian grid. However, the LES code handles 3D grids while the current capability and requirement of the RANS code is restricted to 2D grids. In addition, the computations in LES require marching in time while the calculations with RANS are essentially steady. An optimum balance of computational speed, accuracy and numerical stability is thus of paramount importance in LES and hence the discretisation schemes and equation solvers adopted by the LES numerical framework are more advanced in comparison to their RANS counterparts.

In the present chapter, a brief description of the finite-volume method which applies to both the computational codes has been presented in section 6.1. Details of the numerical framework of the LES code has been discussed in section 6.2. Present work contributed to the combustion modelling capability of the LES code through the implementation of steady flamelet model and models based on Flamelet/progress variable approach, both based on look-up-table concept. The working procedure for each of these models has been included in the subsections. In section 6.3, the numerical framework of RANS computational code has been presented. In the RANS computational code, the turbulence modelling capability has been enhanced by the

addition of a Reynolds stress transport model to the existing k-ε model. Combustion models, namely the steady flamelet model, non-adiabatic flamelet model, and models based on flamelet progress variable approach all of which based on look-up-table concept have been implemented. In addition, steady and unsteady flamelets based NO submodels have been integrated with the combustion models. The solution procedure for combustion calculations carried out with these combustion models in conjunction with both the available turbulence models has been presented.

6.1 Finite-volume method

The finite-volume discretisation involves dividing the continuous domain into discrete cells or finite volumes. The governing equations for turbulent reacting flows are the numerically integrated over each volume resulting in a set of simultaneous algebraic equations, whose solution is an approximation to the solution of the continuous equations at a set of discrete points or nodes. Each cell or finite volume constitutes one node and the solution computed for each node is considered representative of the solution within the cell.

Fig.6.1 shows the relative placement of the nodes for scalars, u and v velocity components in the staggered grid. Extension to three dimensions uses the same structure in the z direction with the addition of w velocity component. All the scalar variables including pressure are evaluated at the node of a scalar cell, example P. The velocity components are evaluated on the staggered grid points which lie at the centroid of the scalar cell faces. Staggering of the velocity avoids physically non-realistic predictions for oscillating pressure fields. Also, since the velocities are generated at scalar cell faces, it has the added advantage of avoiding interpolation of velocities for scalar transport computations.

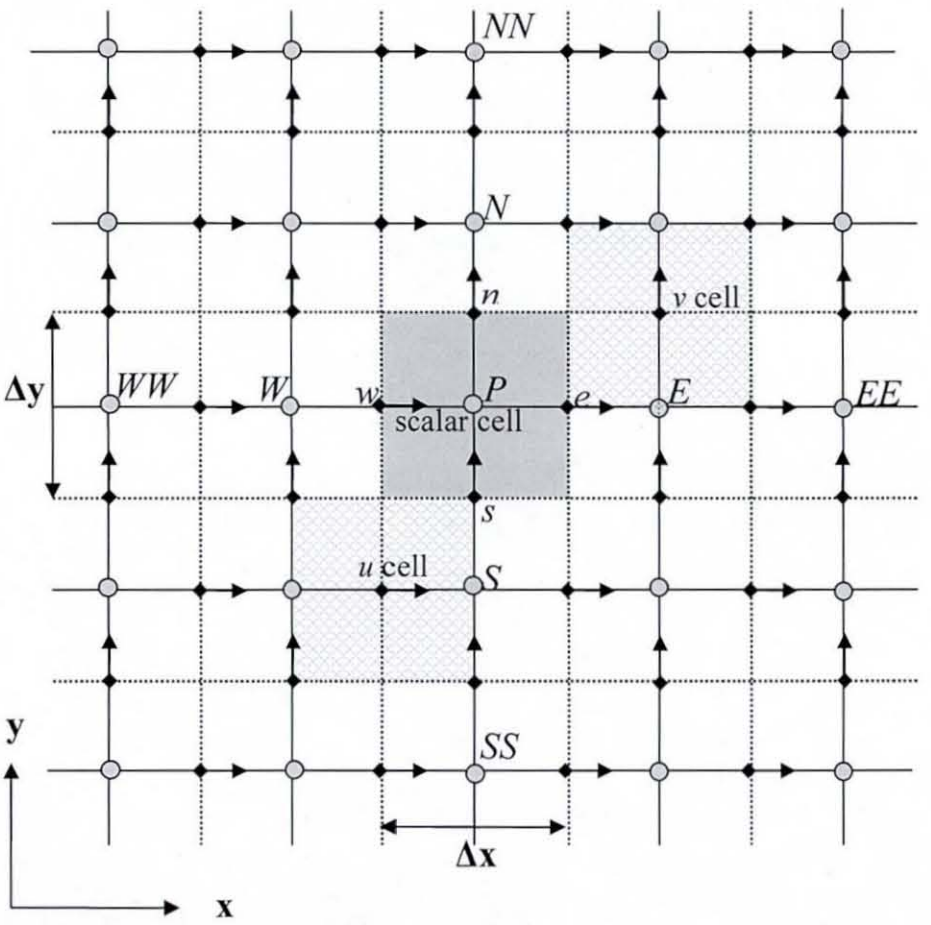

Figure 6.1 Staggered grid and node placement in two dimensions. Circles indicate scalar nodes, horizontal arrows indicate nodes of the *u* velocity component and vertical arrows indicate the *v* velocity component. Examples of a u, v and scalar cell are highlighted.

The Favre averaged or filtered governing equations which have been presented for the turbulent reacting flows in the previous chapters are all in a similar form and hence may be represented by a generic transport equation

$$\frac{\partial}{\partial t}\left(\bar{\rho}\tilde{\phi}\right)+\frac{\partial}{\partial x_k}\left(\bar{\rho}\tilde{u}_k\tilde{\phi}\right)=\frac{\partial}{\partial x_k}\left(\Gamma_\phi\frac{\partial\tilde{\phi}}{\partial x_k}\right)+\tilde{S}_\phi \tag{6.1}$$

Here $\tilde{\phi}$ represents any variable, Γ_ϕ is the diffusion coefficient and $\tilde{S}_\phi$ is a source term.

Integrating the generic equation (Eq. 6.1) over a control volume V bounded by a surface S and employing the Gauss divergence theorem to convert volume integrals into surface integrals yields the following form:

$$\frac{\partial}{\partial t}\int_V \bar{\rho}\tilde{\phi}\,dV + \int_S \bar{\rho}\tilde{u}_k\tilde{\phi}\,dS_k = \int_S \Gamma_\phi \frac{\partial \tilde{\phi}}{\partial x_k}\,dS_k + \int_V \tilde{S}_\phi\,dV \tag{6.2}$$

The differential surface area vector dS has a magnitude equal to the area of the surface element and direction corresponding to the direction of the outward normal to the element. In Eq. 6.2, the time derivative corresponds to the change of a variable within a control volume with respect to time. The second term on the left hand side corresponds to the convective flux and the diffusive flux is given by the first term on right hand side. The last term corresponds to the generation or destruction of the variable ϕ within the control volume. Spatial discretisation involves approximating the volume and surface integrals in this equation and applying the approximation to each cell to obtain a set of simultaneous algebraic equations in ϕ.

In Fig. 6.1, an example of a scalar cell P for which the integrals are to be calculated and its neighbours (indicated by E, W, N, S) and one level away from neighbours (indicated by EE, WW, NN and SS) have been shown in two dimensional space. Extension of this structure to three dimensions has been shown in Fig. 6.2. The labelling of the neighbours uses the following convention: East (E), North (N) and Up (U) correspond to the positive x, y and z directions respectively and West (W), South (S), and Down (D) to the negative x, y and z directions. The small letter e, n, w, s etc refer to the points at the centroid of the respective cell faces. In the following sections, nb is used as a generic subscript for neighbouring cells. To simplify the notation, the formulation of fluxes is given for a particular face such as the east or north face and all results can be applied in a similar manner to other faces.

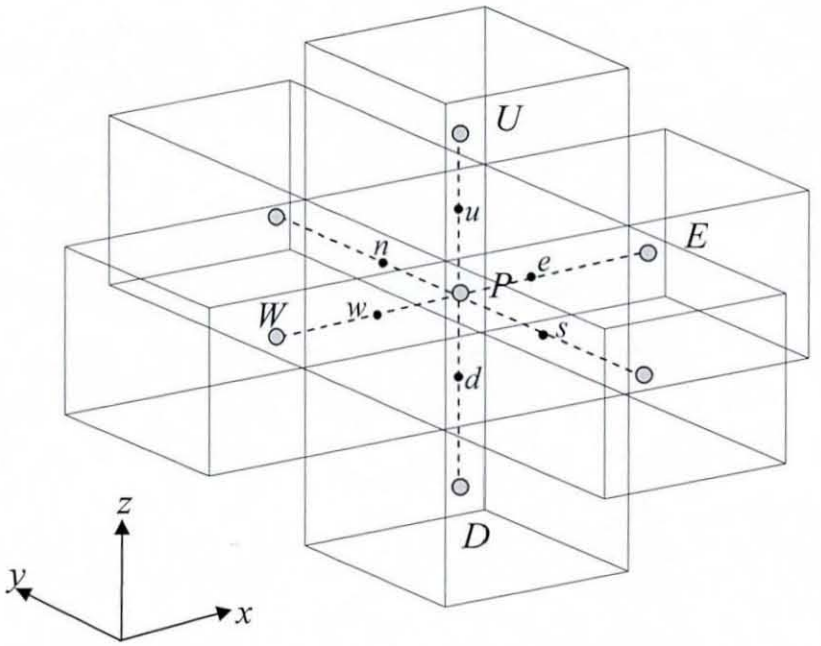

Figure 6.2: A finite volume cell and its neighbours in three dimensions

6.2 Spatial discretisation in LES

6.2.1 Unsteady term

The unsteady term in the governing equation is discretized using a second order accurate central-differencing approximation for the time derivative at $n+\frac{1}{2}$:

$$\frac{\partial}{\partial t}\int_V \bar{\rho}\tilde{\phi}\, dV \approx \frac{(\rho\phi)^{n+1}-(\rho\phi)^{n}}{\Delta t}\Delta V \tag{6.3}$$

Where n is the time level. Superscript n indicates that the value is taken at the start of the current time step, while n+1 indicates the end of the time step.

6.2.2 Convection term

The convective flux across a cell face (example, east face) is given by:

$$F_e = \left(\bar{\rho}\tilde{u}\tilde{\phi}\,\Delta A\right)_e = \left(\bar{\rho}\tilde{u}\,\Delta A\right)_e \tilde{\phi}_e \tag{6.4}$$

Where the velocity component $\tilde{u}$ is normal to the cell face and ΔA is the area of the face. Linear interpolation is adopted to find $\tilde{\phi}_e$ at the centroid of the cell face.

$$\tilde{\phi}_e = (1-\theta)\tilde{\phi}_p + \theta\tilde{\phi}_E \tag{6.5}$$

Where the weighting factor for the interpolation is given by:

$$\theta = \frac{\Delta x_{Pe}}{\Delta x_{PE}} \tag{6.6}$$

Δx_{Pe} and Δx_{PE} are the linear distances between node P to the east face centroid e and the east neighbour node E, as shown in the two dimensional view of the finite volume cell in Fig. 6.1. Due to the staggering of the grid, evaluation of convective velocity u_e and density ρ_e at the face of the cell depend on whether the variable ϕ is a scalar or a velocity component. If the variable is a scalar, the convective velocity u_e is found directly, since a node for the u velocity component is present at the face centroid. However, density must be interpolated using linear interpolation similar to Eq. 6.5:

$$\tilde{\rho}_e = (1-\theta)\tilde{\rho}_P + \theta\tilde{\rho}_E \tag{6.7}$$

When the variable is a velocity component, the situation is exactly opposite in that a node for the scalar is present at the centroid of the face and hence the density can be directly found while convective velocity is obtained through linear interpolation. The resulting formulation is a second-order centred scheme for the convective fluxes,

$$\begin{aligned} F_e &= (\bar{\rho}\tilde{u}\Delta A)_e\left[(1-\theta)\tilde{\phi}_p + \theta\tilde{\phi}_E\right] \\ &= C_e\left[(1-\theta)\tilde{\phi}_p + \theta\tilde{\phi}_E\right] \end{aligned} \tag{6.8}$$

As will be shown later, $C_e = (\bar{\rho}\tilde{u}\Delta A)_e$ represents the contribution of the convective flux across the east face to the co-efficients in the final discretized equation for ϕ (Eq. 6.20).This scheme based on linear interpolation to calculate values of variables at the faces of finite volumes, is equivalent to a second-order central difference scheme in a finite difference formulation. The central difference schemes are relatively free of numerical damping as compared to non-centred schemes. This is highly desirable in LES, as numerical damping acts as an extra unquantified contribution to the eddy viscosity and contaminates the effects of the subgrid scale model. However, the downside of centred schemes is that in convection dominated flows, they fail to recognise the direction of the flow or strength of convection relative to diffusion as under this scheme value at central node of control volume is influenced by all the

neighbouring nodes. Thus, they tend to give solutions containing non-physical oscillations or 'wiggles' in the areas of the flow field containing sharp gradients and can only be rectified through grid refinement . The ratio of the strength of convection to diffusion in a cell is defined as the cell Peclet number, Pe.

$$Pe = \frac{\rho u}{\Gamma / \Delta x} \tag{6.9}$$

It has been found by Patankar (1980) that the central difference scheme provides realistic solutions as long as cell Peclet number $Pe < 2$. However, LES deals with unsteady calculations for which this stability limit is by no means binding and it is possible for the solution to remain oscillation-free over the period of simulation at even $Pe > 2$. In LES, the damping introduced by the model for SGS stresses also helps to reduce the oscillations.

In turbulent reacting flows, the scalars (usually the mixture fraction and/or progress variable) are coupled with the velocity field through density and the wiggles which result from the use of central difference scheme for the scalar convective terms cause problems with the numerical stability of the overall solution scheme. Furthermore, wiggles may result in unphysical results such as mixture fraction outside the physically realistic range of 0 to 1. As mentioned before, grid refinement can help in addressing the problem. However, the structured Cartesian grid system used in the present study does not allow for localized grid refinement and hence an increase in the number of cells Δn_x in one co-ordinate direction means, the total number of cells in the domain is increased to $\Delta n_x \left(n_y n_z \right)$. Computational times with LES rise steeply with the rise in the grid density and hence grid refinement is limited by the available computational resources. For this reason, the convective terms for the scalar equations are discretised using the non-centred schemes of Leonard, QUICK (1979) and SHARP (1987).

QUICK is a third-order upwind scheme which reduces numerical oscillations by introducing fourth-order dissipation. In this scheme, the value of the variable ϕ at cell face is computed through a quadratic interpolation:

$$\tilde{\phi}_e = \left[(1-\theta)\tilde{\phi}_p + \theta \tilde{\phi}_E \right] - \frac{1}{8} CRV \times \Delta x_E{}^2 \tag{6.10}$$

Where the weighting factor θ is calculated using Eq.6.6. The first term in the above equation correspond to the linear interpolation used in the standard second-order central difference scheme. The second term is an upwind- biased curvature term with

$$CRV = \left[\frac{\tilde{\phi}_p - 2\tilde{\phi}_E + \tilde{\phi}_{EE}}{\Delta x_E^{\,2}} \right] \quad u < 0 \tag{6.11}$$

$$CRV = \left[\frac{\tilde{\phi}_E - 2\tilde{\phi}_P + \tilde{\phi}_W}{\Delta x_E^{\,2}} \right] \quad u > 0$$

The curvature term makes the overall interpolation quadratic. Substitution of Eq .6.10 in Eq .6.8 gives the convective flux of a variable ϕ across the east face as:

$$F_e = (\bar{\rho}\tilde{u}\Delta A)_e \left[\left((1-\theta)\tilde{\phi}_p + \theta\tilde{\phi}_E \right) - \frac{1}{8} CRV \times \Delta x_E^{\,2} \right] \tag{6.12}$$

$$= C_e \left[\left((1-\theta)\tilde{\phi}_p + \theta\tilde{\phi}_E \right) + S_{QUICK} \right]$$

As the equation for S_{QUICK} includes values of ϕ at the next level of neighbours (*EE*, *WW* etc in Fig. 6.1), this term is included in the equation as part of the source term S_ϕ. While QUICK reduces wiggles, it may not do so completely and the SHARP scheme is employed to rectify the still existing oscillations. The SHARP scheme is a modification of QUICK which introduces second-order diffusion where local conditions are conducive to oscillations, thereby ensuring that the solution remains monotonic. Finally, summing the convective fluxes over all faces of the control volume gives an expression for the discrete convective operator:

$$\int_S \bar{\rho}\tilde{u}_k\tilde{\phi}\, dS_k \approx \sum C_f \left[\left((1-\theta_f)\tilde{\phi}_p + \theta_f\tilde{\phi}_{nb} \right) + \sum S_{QUICK_f} \right] \tag{6.13}$$

6.2.3 Diffusion term

The diffusive flux for a variable ϕ across a cell face f is given by

$$F_{diff} = \left(\Gamma_\phi \Delta A \frac{\partial \tilde{\phi}}{\partial x_k} \right)_f \tag{6.14}$$

Where x_k is in the direction perpendicular to the face of the cell.

Discretizing the gradient of the variable gives the flux across the east cell face as:

$$F_{diff_e} = \left(\Gamma_\phi \Delta A\right)_e \left(\frac{\partial \tilde{\phi}}{\partial x}\right)_e = \left(\Gamma_\phi \Delta A\right)_e \left(\frac{\tilde{\phi}_E - \tilde{\phi}_P}{\Delta x_E}\right) \tag{6.15}$$

$$F_{diff_e} = D_e\left(\tilde{\phi}_E - \tilde{\phi}_P\right)$$

Where $D_e = \left(\Gamma_\phi \Delta A\right)_e / \Delta x_E$ is the diffusive flux contribution for the east face to the coefficients in the final discretised transport equation (Eq.6.20). The diffusion coefficient at the centre of the face Γ_ϕ is calculated by linear interpolation in the same manner as density in the computation of the convective fluxes. Summing the diffusive fluxes across all the faces of the control volume gives the following expression for the discrete diffusive operator,

$$\int_S \Gamma_\phi \frac{\partial \tilde{\phi}}{\partial x_k} dS_k \approx \sum D_f \left(\tilde{\phi}_{nb} - \tilde{\phi}_P\right) \tag{6.16}$$

Unlike the convective term, the discrete diffusion term does not suffer from numerical stability and hence is used in this form for both momentum and scalars.

6.2.4 Source term

Source terms in the governing equations vary according to the variable that is being transported. For momentum, source terms represent the effects of pressure gradient and body forces if any. A reaction progress variable is associated with a chemical source term. The source term for the second moment of a reaction progress variable includes the contributions of production, dissipation and the correlation between the progress variable and the rate of chemical reaction. For enthalpy in the non-adiabatic flows, radiation heat exchange is treated as a source term. All the source terms encountered in the different transport equations are treated in a similar manner for the purposes of spatial integration. Calculation of the source term involves evaluating the function representing the source term S_ϕ at the node and multiplying by the volume of the cell ΔV :

$$\int_V \tilde{S}_\phi \, dV \approx \tilde{S}_{\phi p} \Delta V \tag{6.17}$$

Gradients in the function are calculated using second-order central difference scheme while interpolations employ a linear profile analogous to that used for convective and

diffusive fluxes. A general source term is written in a linearized form as a combination of an implicit $\tilde{S}_{imp}$ and explicit $\tilde{S}_{exp}$ component:

$$\tilde{S}_{\phi P}\Delta V = \tilde{S}_{imp}\tilde{\phi}_{p} + \tilde{S}_{exp} \tag{6.18}$$

The implicit component is integrated using an implicit time stepping scheme while the explicit component is integrated in time using an explicit scheme. Time advancement schemes are discussed in section 6.3.

6.2.5 Complete discretised equation

The complete discretised transport equation for a generic variable ϕ is given by:

$$\begin{aligned}\frac{(\rho\phi)^{n+1}-(\rho\phi)^{n}}{\Delta t}\Delta V = &\left\{\sum C_f\left[\left(\left(1-\theta_f\right)\tilde{\phi}_p+\theta_f\tilde{\phi}_{nb}\right)\right]\right\}^{(n-2,n-1,n,n+1)}\\ &+\left\{\sum D_f\left[\left(\tilde{\phi}_{nb}-\tilde{\phi}_p\right)\right]\right\}^{(n-1,n,n+1)}\\ &+\left\{\tilde{S}_{imp}\tilde{\phi}_p\right\}^{(n-1,n,n+1)}+\left\{\tilde{S}_{exp}\right\}^{(n-2,n-1,n,n+1)}\end{aligned} \tag{6.19}$$

Here the curly brackets { } with superscripts (n-2, n-1,....) represent the weighted average of the term evaluated at the listed time levels, which gives an estimate of the term at $\left(n+\frac{1}{2}\right)$ level. The weightings for each time level depend upon the time advancement scheme, as discussed in section 6.3. Collecting coefficients, the final form of the complete discretized transport equation is given by:

$$\begin{aligned}a_p^{n+1}\tilde{\phi}_p^{\,n+1} = &\sum_{nb}\left(a_{nb}^{\;n+1}\tilde{\phi}_{nb}^{\;n+1}\right)+S_{imp}\tilde{\phi}_p^{\,n+1}+S_{exp}^{n+1}\\ &+\left[\sum_{nb}\left(a_{nb}^{\;n}\tilde{\phi}_{nb}^{\;n}\right)-a_p^n\tilde{\phi}_p^n+S_{imp}\tilde{\phi}_p^{\,n}+S_{exp}^n\right]\\ &+\left[\sum_{nb}\left(a_{nb}^{n-1}\tilde{\phi}_{nb}^{n-1}\right)-a_P^{n-1}\tilde{\phi}_P^{n-1}+S_{imp}\tilde{\phi}_P^{\,n-1}+S_{exp}^{n-1}\right]\\ &+\left[\sum_{nb}\left(a_{nb}^{n-2}\tilde{\phi}_{nb}^{n-2}\right)-a_P^{n-2}\tilde{\phi}_P^{n-2}+S_{exp}^{n-2}\right]\end{aligned} \tag{6.20}$$

Where the coefficients corresponding to the node of evaluation a_p and its neighbours a_{nb} are formed from the convective and diffusive fluxes C_f's and D_f's respectively.

6.3 Time advancement in LES

In LES, unsteady calculations are adopted for even the statistically steady flows and hence the spatially discretized governing equations need to be integrated in time. In this section, the time integration schemes employed for the momentum and scalar equations are discussed.

6.3.1 Time integration of scalar equations

In the present study, time integration of the scalar equations is accomplished through Crank-Nicolson scheme. The time integrated transport equation for a scalar ϕ reads:

$$\begin{aligned}\frac{\left(\bar{\rho}\tilde{\phi}\right)^{n+1}-\left(\bar{\rho}\tilde{\phi}\right)^{n}}{\Delta t}\Delta V = &-\frac{1}{2}\left[H^{n+1}\left(\tilde{\phi}^{n+1}\right)+H^{n}\left(\tilde{\phi}^{n}\right)\right]\\ &+\frac{1}{2}\left[L^{n+1}\left(\tilde{\phi}^{n+1}\right)+L^{n}\left(\tilde{\phi}^{n}\right)\right]\\ &+\frac{1}{2}\left[S_{imp}^{n+1}\tilde{\phi}^{n+1}+S_{imp}^{n}\left(\tilde{\phi}^{n}\right)\right]\\ &+\frac{1}{2}\left[S_{exp}^{n+1}\tilde{\phi}^{n+1}+S_{exp}^{n}\left(\tilde{\phi}^{n}\right)\right]\end{aligned} \tag{6.21}$$

Here, H represents the discrete convective term

$$H\left(\tilde{\phi}\right)=\sum C_f\left[\left(\left(1-\theta_f\right)\tilde{\phi}_p+\theta_f\tilde{\phi}_{nb}\right)\right], \tag{6.22}$$

L is the discrete diffusive term,

$$L\left(\tilde{\phi}\right)=\sum D_f\left(\tilde{\phi}_{nb}-\tilde{\phi}_p\right) \tag{6.23}$$

and $S_{imp}\tilde{\phi}$ and S_{exp} are the discrete implicit and explicit source terms respectively.

Each term is evaluated at the n and n+1 time levels and a linear interpolation is used to estimate the value of the term at the $n+\frac{1}{2}$ time level. The scheme is thus second order accurate in time. Atleast two iterations of the scalar equations per time step are required due to contributions of terms containing $\tilde{\phi}^{n+1}$ to the explicit source term which result from the use of the QUICK and SHARP spatial discretisation schemes. In turbulent reacting flows, variation in density and diffusivity with respect to time can be quite steep and adequate number of outer iterations of the entire time-advancement scheme per time step is required to ensure second-order accuracy and

stability of the solution. The criterion for the Crank-Nicolson scheme to remain non-oscillatory is given by:

$$\Delta t \le \frac{(\Delta x)^2}{\Gamma} \tag{6.24}$$

While this criterion poses a rather stringent limitation on the improvement that could be achieved on spatial accuracy, it results from an error term in the Taylor series expansion which contains the second derivative in space $\partial^2\tilde{\phi}/(\partial x)^2$. Typically, this term remains relatively small in most flow problems and the scheme remains stable for considerably larger time steps.

6.3.2 Time integration of momentum equations

The momentum equations are advanced in time using either Crank-Nicolson scheme or the second- and third-order hybrid Adams schemes (Kirkpatrick, 2002). In the hybrid schemes, Adams Bashforth methods are used for the convective terms and Adams-Moulton methods are used for the diffusive terms. The discretised momentum equations with Crank-Nicolson scheme based time advancement are given by:

$$\begin{aligned}\frac{\bar{\rho}^{n+1}\tilde{u}^* - (\bar{\rho}\tilde{u})^n}{\Delta t}\Delta V = &-\frac{1}{2}\left[H^{n+1}(\tilde{u}^*) + H^n(\tilde{u}^n)\right] \\ &+ \frac{1}{2}\left[L^{n+1}(\tilde{u}^*) + L^n(\tilde{u}^n)\right] \\ &+ \frac{1}{2}\left[S_{imp}^{n+1}\tilde{u}^* + S_{imp}^n(\tilde{u}^n)\right] \\ &+ \frac{1}{2}\left[S_{exp}^{n+1}\tilde{u}^{n+1} + S_{exp}^n(\tilde{u}^n)\right] \\ &- Gp^{n-1/2}\end{aligned} \tag{6.25}$$

This equation has a form similar to the discretized scalar equation (Eq 6.21) except for the addition of a pressure gradient term $Gp^{n-1/2}$. This term is evaluated at n-1/2 time level as dictated by the pressure correction scheme discussed in section 6.4. The velocities calculated at n+1 time level are written with superscript * to indicate that the values correspond to an approximate solution which is obtained prior to pressure correction step.

The convection terms in the momentum equations are non-linear and hence require an iterative procedure with the Crank-Nicolson scheme to retain second order accuracy. This problem is overcome in the present code by employing second- and third-order hybrid schemes in which the non-linear convective terms are treated explicitly using an Adams-Bashforth Scheme while the diffusion terms are treated implicitly using Adams-Moulton. Explicit contributions of the source terms are as well treated explicitly with Adams-Bashforth.

The discretized momentum equations subjected to the second-order Adams-Bashforth/ Adams-Moulton scheme take the form:

$$\begin{aligned}\frac{\bar{\rho}^{n+1}\tilde{u}^{*}-\left(\bar{\rho}\tilde{u}\right)^{n}}{\Delta t}\Delta V=&-\frac{1}{2}\left[3H^{n+1}\left(\tilde{u}^{n}\right)-H^{n-1}\left(\tilde{u}^{n-1}\right)\right]\\&+\frac{1}{2}\left[L^{n+1}\left(\tilde{u}^{*}\right)+L^{n}\left(\tilde{u}^{n}\right)\right]\\&+\frac{1}{2}\left[S_{imp}^{n+1}\tilde{u}^{*}+S_{imp}^{n}\left(\tilde{u}^{n}\right)\right]\\&+\frac{1}{2}\left[3S_{exp}^{n+1}\tilde{u}^{n}-S_{exp}^{n-1}\left(\tilde{u}^{n-1}\right)\right]\\&-Gp^{n-1/2}\end{aligned}\qquad(6.26)$$

and the application of third-order Adams/Bashforth/Adams-Moulton scheme results in,

$$\begin{aligned}\frac{\bar{\rho}^{n+1}\tilde{u}^{*}-\left(\bar{\rho}\tilde{u}\right)^{n}}{\Delta t}\Delta V=&-\frac{1}{12}\left[23H^{n}\left(\tilde{u}^{n}\right)-16H^{n-1}\left(\tilde{u}^{n-1}\right)+5H^{n-2}\left(\tilde{u}^{n-2}\right)\right]\\&+\frac{1}{12}\left[5L^{n+1}\left(\tilde{u}^{*}\right)+8L^{n}\left(\tilde{u}^{n}\right)-L^{n-1}\left(\tilde{u}^{n-1}\right)\right]\\&+\frac{1}{12}\left[5S_{imp}^{n+1}\tilde{u}^{*}+8S_{imp}^{n}\left(\tilde{u}^{n}\right)-S_{imp}^{n-1}\left(\tilde{u}^{n-1}\right)\right]\\&+\frac{1}{12}\left[23S_{exp}^{n}\tilde{u}^{n}-16S_{exp}^{n-1}\left(\tilde{u}^{n-1}\right)+5S_{exp}^{n-2}\left(\tilde{u}^{n-2}\right)\right]\\&-Gp^{n-1/2}\end{aligned}\qquad(6.27)$$

Since the non-linear convective terms are calculated from the known values at previous time steps, no iteration is required to maintain the accuracy of the scheme for these terms. However, as with the scalars, the variation in density and diffusivity in reacting flows, demand iteration of the overall solution procedure so that the correct value of density $\bar{\rho}^{n+1}$ is included in the unsteady term and the correct value of Γ^{n+1} in the diffusion term.

The fact that the convective terms are calculated from previous time steps means that special treatment is required for initial steps when no information about previous time steps is available. To this end, a 'kick-start' procedure is adopted in which Crank-Nicolson scheme is used for the initial time steps to enable the calculation of the n-1 and n-2 source terms for the Adams schemes.

6.4 Pressure correction in LES

The coupled system for incompressible reacting flow is solved using a fractional step method based on the pressure correction method of Van Kan (1986) and Bell and Colella (1989). This version of the fractional step method was found to be the fastest of the methods tested by Armfield and Street (2002). According to this approach, momentum equations are first integrated to give an approximate solution for the velocity field $\tilde{u}^*$. Mass conservation is then enforced through a pressure correction step in which approximate velocity field is projected onto a subspace of divergence-free velocity fields. The projection is achieved by solving a Poisson equation for the pressure correction p' in which the source term is the mass conservation error in each cell,

$$\Delta t \frac{\delta^2 p'}{\left(\delta x_k\right)^2} = -\left[\frac{\bar{\rho}^{n+1} - \bar{\rho}^n}{\Delta t} + \frac{\delta\left(\bar{\rho}^{n+1} u_k^*\right)}{\delta x_k}\right] \tag{6.28}$$

The pressure correction is then used to correct the velocity field,

$$u_k^{n+1} = u_k^* - \Delta t \frac{\delta p'}{\delta x_k} \tag{6.29}$$

and the pressure field,

$$p^{n+1/2} = p^{n-1/2} + p' \tag{6.30}$$

The pressure correction equation is discretised in a manner analogous to the discretisation of transport equations. Integrating the pressure correction equation over a finite volume cells and applying the Gauss divergence theorem yields,

$$\Delta t \sum\left(\Delta A \frac{\delta p'}{\delta x_k}\right)_f = -\left[\frac{\bar{\rho}^{n+1} - \bar{\rho}^n}{\Delta t}\Delta V + \sum\left(\bar{\rho}^{n+1} u_k^* \Delta A\right)_f\right] \tag{6.31}$$

The pressure gradient term $\frac{\delta p'}{\delta x_k}$ is calculated through a central difference approximation to be consistent with the discretisation of pressure gradient term in the momentum equations. Such a consistency ensures minimum error in projection.

6.5 Solution of LES equations

The discrete governing equations presented in the previous sections are solved using a linear equation solver. A Bi-conjugate Gradient Stabilized (BiCGStab) solver with a Modified Strongly Implicit (MSI) preconditioner has been employed in the present study due to its ability to handle stiff set of equations efficiently. The BiCGStab solver is also employed for the pressure correction equations.

Convergence of the solver is measure using the L_2 norm of the residual. The convergence criterion for the solution of momentum and scalar equations is that the residual be less than 10^{-10}. Typically, one or two sweeps of the solver are required to obtain this level of convergence. At each time step, a number of iterations of the pressure/velocity correction step are carried out to ensure adequate mass conservation. Within each iteration, the pressure correction equation is solved until either the residual is reduced to 10% of its original value or the BiCGStab solver has performed 7 sweeps. Each sweep of the solver includes 2 sweeps of the preconditioner. The solution is then used to correct the pressure and velocity fields and the divergence of the corrected velocity field is calculated. The process is repeated until the L_2 norm of the divergence error is less than pre-set value. Typically, 6 to 8 projections are required to attain the minimum divergence error.

6.5.1 Overall solution procedure for reacting flows

For incompressible reacting flows which are the focus of the present study, the overall solution procedure for each time step follows an approach that has been implemented by Ranga Dinesh (2007) in the context of a single flamelet based steady flamelet combustion model. In the present work, the combustion modelling capability in LES has been enhanced by incorporating a comprehensive steady flamelet model which can handle multiple flamelets or the variation in scalar dissipation rate and advanced

flamelet models, namely the Flamelet/Progress Variable (FPV) approach based FPV δ function model and FPV β function model. Since, both all three models are flamelet based, the overall solution procedure remains unchanged from the approach employed by Ranga Dinesh (2007). However, the exact calculations within each step in the overall solution procedure do vary according to the adopted combustion model and these variations are presented subsequent to the description of the overall procedure.

In the following summary of the solution procedure, superscripts n+1 and n refer to the current and previous time levels, superscript k refers to the iteration cycle within the time step and the superscript 0 indicates the initial guess for the first iteration with a time step i.e. k=0.

Step 1. Choose the initial guesses or predictors for the values of the variables at the next time level. Here a simple choice is adopted by choosing the solution values at the current time level:

$$u_k^0 = u_k^n, \quad \phi_k^0 = \phi_k^n, \quad \text{etc.}$$

Step 2. Solve the scalar transport equation (s) to obtain provisional scalar values. This facilitates better estimation of the density early in the iteration process.

Step 3. Calculate density from the provisional scalar values according to the strategy appropriate to the adopted combustion model.

Step 4. Re-update the scalar (s) from the new density. This is required to preserve primary scalar conservation.

Step 5. Solve the momentum equations

Step 6. Solve the pressure correction equation

Step 7. Correct the pressure and velocity fields

Step 8. Check the mass conservation error and repeat steps 6 and 7 as required.

This completes one iteration cycle within a time step. Typically, 8-10 iterations of this procedure is required to obtain satisfactory convergence at the end of each time step.

At the end of each time step, two more steps need to be executed and these are:

Step 9. Calculate eddy viscosity.

Step 10. Calculate the temperature and species mass fractions

This completes the cycle for a time step. The size of the time step and the number of outer iterations vary according to the flow problem. The time step is varied such that

the Courant number defined as $Cou = \Delta tu_k / \Delta x_k$, remains approximately constant. In general, the solutions are advanced with a time step corresponding to a Courant number in the range Cou=0.2 to 0.8.

With this iterative solution procedure, under-relaxation of density in time is required in order to maintain stability of the solution. Hence, the density computed in **step 3** from the adopted combustion model, $\overline{\rho}^{n+1}$, is not directly used for the remainder of steps but instead use is made of the under-relaxed value $\overline{\rho}_r^{n+1}$ which is given as:

$$\overline{\rho}_r^{n+1} = \alpha\overline{\rho}^{n+1} + (1-\alpha)\overline{\rho}_r^{n+1} \tag{6.32}$$

Here, α is the under-relaxation factor and takes a value of 0.25.

6.5.2 Procedure for steady flamelet model

The exact calculations to be conducted in the **Steps 2, 3, 4** and **10** of the overall solution procedure are dictated by the employed combustion model. For the steady flamelet model (SLFM) implemented in the present study, following is the procedure:

Steps 2&4: Calculate scalar transport equations

2.1: Solve for the filtered mixture fraction equation.

In case filtered NO is to be calculated through a transport equation based approach then additionally perform steps 2.2 to 2.6:

2.2: Compute the sub-grid variance of mixture fraction from its model equation and subsequently calculate the normalized subgrid-variance.

2.3: Compute the filtered scalar dissipation rate from its model equation

2.4: Read the pre-integrated 3D look-up-table specific to SLFM for ordered values of filtered NO source term.

2.5: From the known value of filtered mixture fraction, its normalized variance and filtered scalar dissipation rate, obtain filtered NO source term from the look-up-table using the 3D interpolation technique (Appendix I).

2.6: Solve the transport equation for filtered NO mass fraction using the NO source term obtained from **step 2.5.**

Step 3: Calculate density

3.1: Compute the sub-grid variance of mixture fraction from its model equation and subsequently calculate the normalized subgrid-variance.
3.2: Compute the filtered scalar dissipation rate from its model equation
3.3: Read the pre-integrated 3D look-up-table specific to SLFM for ordered values of filtered density
3.4: From the known value of filtered mixture fraction, its normalized variance and filtered scalar dissipation rate, obtain filtered density from the look-up-table using the 3D interpolation technique.

Step 10: Calculate temperature and species concentrations

10.1: Read the pre-integrated 3D look-up-table specific to SLFM for ordered values of filtered temperature and species mass fractions.
10.2: From the known filtered mixture fraction, its normalized variance and filtered scalar dissipation rate, obtain filtered temperature and species mass fractions from the look-up-table using the 3D interpolation technique.

6.5.3 Procedure for FPV-δ function model

For the FPV-δ function model implemented in the LES code in the present work, the working procedure is as follows:

Steps 2&4: Calculate scalar transport equations

2.1: Solve for the filtered mixture fraction equation
2.2: Compute the sub-grid variance of mixture fraction from its model equation and subsequently calculate the normalized subgrid-variance.
2.3: Read the pre-integrated 3D look-up-table specific to FPV δ function model for ordered values of filtered reaction progress variable source term.
2.4: From the values of filtered mixture fraction and its normalized variance computed from **steps 2.1** and **2.2**, and filtered reaction progress variable obtained

from previous time step or iteration, compute filtered progress variable source term from the look-up-table using the 3D interpolation technique.

2.5: Solve the transport equation for filtered progress variable using the filtered chemical source term obtained from **step 2.4**.

Step 3: Calculate density

3.1: Compute the sub-grid variance of mixture fraction from its model equation and subsequently calculate the normalized subgrid-variance.

3.3: Read the pre-integrated 3D look-up-table specific to FPV δ function for ordered values of filtered density

3.4: From the known values of filtered mixture fraction, its normalized variance and the filtered reaction progress variable obtained from **step 2.5**, obtain filtered density from the look-up-table using the 3D interpolation technique.

Step 10: Calculate temperature and species concentrations

10.1: Read the pre-integrated 3D look-up-table specific to FPV δ function for ordered values of filtered temperature and species mass fractions.

10.2: From the known values of filtered mixture fraction, its normalized variance and the filtered reaction progress variable, obtain filtered temperature and species mass fractions from the look-up-table using the 3D interpolation technique.

6.5.4 Procedure for FPV-β function model

In the FPV-δ function model presented in the previous subsection, the 3D look-up-table is read in every iteration. This provides an advantage in that the 3 dimensional arrays could be allocated before an interpolation operation and deallocated thereafter thereby keeping the RAM requirement to a fairly moderate level (2 GB). This seems an attractive proposition for FPV-β function model as well. However, a major hurdle with FPV-β function model is that the look-up-table is 4 dimensional and reading a 4D table consumes significantly more time.

For instance, a 3D look-up-table used in the present study is typically of size 163x51x151 and the time required for its reading in a 4GB RAM-3.6GHZ Intel Pentium 4 processor is less than 1 sec. For the same processor specifications, a 4D table typically of size 163x51x31x151 takes nearly 30 sec. , a scale up of more than 30 times.

In the FPV-β function model, it is required to read the table for density, progress variable source term, and covariance. Hence, for one outer iteration, the computational time is scaled up more than 90 times. In the LES computations, nearly 8 outer iterations are carried out within a time step and thus, the time for completion of a time step is scaled up by more than 720 times. Given that LES computations with FPV-δ function model take ~30 days, the scale up of 720 times per time step with the FPV-β function model could translate into several months. Furthermore, temperature and species mass fractions are required to be calculated at the end of each time step in LES. For hydrocarbon combustion, typical species of interest are CO_2, CO, H_2O, H_2 and OH. Thus, a calculation involving temperature and 5 species requires reading 6 tables at the end of each time step. While this could be carried out with 3D tables without any concern about the computational speed, it is not so with 4D tables. Reading six 4D tables can slow down the processing at the end of each time step by a significant amount.

In the present work, these problems are circumvented by storing the 4D arrays for the entire length of the LES calculation. The 4D look-up-tables for density, progress variable source term and covariance term are read only once (in **step 2**) and the arrays are saved for the remainder of the LES calculation. However, this stretches the RAM requirements. A 4GB RAM is a minimum requirement while a higher RAM size is highly desirable. With this procedure, 4D look-up-table for temperature too is read only once (in **step 10**) and stored for the entire statistics collection phase of the LES calculation. Tables pertaining to species too can be read and stored along with temperature but considerably higher (>>4GB) amount of RAM must be ensured.

In the present study, FPV-β function model was tested for lifted partially premixed flames with the foremost objective of capturing the experimentally observed temperature distribution. Hence, no account of species mass fractions has been taken.

The working procedure for FPV β function model is thus as follows:

Steps 2&4: Calculate scalar transport equations

2.1: Solve for the filtered mixture fraction equation

2.2: Compute the sub-grid variance of mixture fraction from its model equation and subsequently calculate the normalized subgrid-variance.

2.3: Compute the sub-grid variance of reaction progress variable from its model equation and subsequently calculate its normalized value. The values of filtered reaction progress variable and covariance term are obtained from previous time step or iteration or initial guess.

2.4: If beginning from scratch or resumption from previous run, read the pre-integrated 4D look-up-table specific to FPV β function model for ordered values of the reaction progress variable source term. Save the 4D array to be used for the remainder of the LES calculation.

2.5: Compute filtered progress variable source term from the look-up-tables using the 4D interpolation technique (Appendix I). The inputs needed are the filtered mixture fraction and its normalized variance computed from **steps 2.1** and **2.2**, normalized progress variable variance obtained from **step 2.3** and filtered reaction progress variable obtained from previous time step or iteration or initial guess.

2.6: Solve the transport equation for filtered reaction progress variable using the filtered chemical source term obtained from **step 2.5**.

Step 3: Calculate density

3.1: Compute the sub-grid variance of mixture fraction from its model equation and subsequently calculate the normalized subgrid-variance.

3.2: Compute the sub-grid variance of reaction progress variable from its model equation and subsequently calculate its normalized value. The filtered reaction progress variable is known from **step 2.6** and values of covariance term are obtained from previous time step or iteration or initial guess.

3.3: If beginning from scratch or resumption from previous run, read the pre-integrated 4D look-up-table specific to FPV β function model for ordered values of

filtered density and covariance term. Save the 4D arrays to be used for the remainder of the LES calculation.

3.4: Compute filtered density and covariance term from the look-up-tables using the 4D interpolation technique. The inputs needed are the filtered mixture fraction and its normalized variance obtained from **steps 2.1 and 3.1** respectively, and filtered reaction progress and its normalized variance obtained from **steps 2.6 and 3.2** respectively.

Step 10: Calculate temperature (when collection of statistics is triggered)

10.1: If beginning of the collection of statistics or resumption from a previous collection, read the pre-integrated 4D look-up-table specific to FPV β function model for ordered values of temperature. Save the 4D array to be used for the remainder of the LES calculation.

10.2: From the known values of filtered mixture fraction and its normalized variance and filtered reaction progress variable and its normalized variance, compute filtered temperature using the 4D interpolation technique.

Generation of the look-up-tables for the different models implemented in LES has been discussed in Chapter 7.

6.6 Boundary conditions in LES

Specification of appropriate boundary conditions is of prime importance for an accurate reproduction of the physical geometry and flow conditions. The boundary conditions encountered in the present study include, the solid, inflow and outflow boundaries. The solid boundaries represent walls and obstacles along the borders and within the computational domain. The present LES code has the provision for handling obstacles from a range of basic shapes such as rectangular and trapezoidal prisms, cylinders and spheres (Kirkpatrick, 2002). However, the present study is

restricted to unconfined flames and hence the use of solid boundary condition is made only along the boundaries of the computational domain.

6.6.1 Solid boundaries

The solid wall boundaries which reproduce the physical geometry are treated with impermeable and no-slip conditions. Hence, all the normal and tangential components of velocity at the wall are set to zero. For the turbulent boundary layers in which, it is not feasible to resolve the laminar sublayer, it is necessary to use an approximate boundary condition or wall functions in order to apply the correct shear force to the fluid. The wall function adopted in this study is that of Werner and Wengle (1991) which uses a power-law approximation to the log-law.

For unconfined flows, artificial confinement is usually adopted to avoid the problem of numerical instability due to reverse flow at open boundaries. Thus, artificial wall boundaries which do not exist in practice are placed in the computational domain. The placement of these walls is such that the computational domain is restricted to an affordable size yet the walls are far enough to have any influence on the flame structure. These artificial walls are treated with a free-slip condition which represents a friction less surface. With the free-slip condition, the fluid flow in the direction tangential to the wall exists while the flow in the normal direction is zero. Hence the normal component of velocity and the gradients of tangential components of velocity are set to zero at the wall. For pressure and all the scalars, the gradients in the wall normal direction are set to zero near the wall boundaries in the domain. Additional details on the implementation of wall boundary conditions are available in Kirkpatrick (2002).

6.6.2 Inflow boundary condition

Specification of inflow conditions is less straightforward in LES as compared to RANS due to the need for time dependent turbulent inflow data. In majority of cases, the flow downstream is more or less driven by the conditions at the inlet, making it necessary to provide information on a realistic time series of turbulent fluctuations which are in equilibrium with the mean flow. Experiments rarely provide information in such detail and typically only the time averaged mean and rms of velocity profiles

are made available. A variety of methods to numerically generate turbulent inflow data are currently available in the literature. Simplest of the methods as employed by Branley and Jones (2001) involve superimposing random turbulent fluctuations on mean velocity profiles. Advanced methods which demand additional computational resources include the body-force method of Pierce and Moin (1998) involving auxiliary LES computations on a duct flow to obtain a database of time-varying velocity profiles, digital filter method of Klein *et al.* (2003) and the immersed boundary method of Kempf *et al.* (2005) to name a few. It has been observed by Lund *et al.* (2003) that rather approximate inlet conditions seem to be sufficient for flows with open boundaries such as free-stream turbulence, jets, mixing layer etc. while wall bounded flows, on the other hand, appear to require much more accurate description of inlet turbulence. Thus, for the unconfined flames considered in the present LES calculations, the simple approach of Branley and Jones (2001) seems to be adequate and hence has been adopted.

The instantaneous inflow velocity u_k is hence specified through a mean velocity $\langle U_k \rangle$ perturbed by random fluctuations:

$$u_k(x_k,t) = \langle U_k \rangle + \theta(x_k,t)\langle u_k' \rangle_{rms} \tag{6.33}$$

where $\langle u_k' \rangle_{rms}$ is the rms of turbulent fluctuations and is obtained from experimental measurements and is scaled by the random number $\theta(x_k,t)$ obtained from a Gaussian distribution. For the lifted jet flame configuration studied in the present work (Chapter 9), inflow conditions for fuel jet correspond to a developing turbulent pipe flow that can be approximated by a fully developed flow. Hence, the mean velocity distribution along the inlet has been specified through a $1/7^{th}$ power law profile given by:

$$\langle U \rangle = C_0 U_{bulk}\left(1-\frac{|y|}{\delta}\right)^{1/7} \tag{6.34}$$

where U_{bulk} is the bulk velocity, y is the radial distance from the centreline of the pipe and $\delta = 1.01R_j$, with R_j representing the radius of the pipe. The co-efficient C_o needs to be tuned to ensure experimentally observed mass flow rate. For the lifted jet flame, a value of C_o=1.615 ensured correct mass flow rate. The jet flame configuration involves vitiated co-flow surrounding the fuel jet. The observed velocity distribution

at the co-flow inlet is more or less uniform and hence specification of plug flow was considered sufficient.

In addition to the turbulent velocity data, information regarding all the transported scalars needs to be specified at the inlets. Mixture fraction takes a value of unity in the fuel inlet and zero in the co-flow inlet while the variance of mixture fraction is zero in both the inlets. For the FPV models, the reaction progress variable and its variance are set to zero at both inlets.

6.6.3 Outflow boundary condition

Outflow boundary conditions generally adopt a zero normal gradient condition or a convective outlet boundary condition. The zero normal gradient condition assumes a zero gradient for all flow variables except pressure in a direction normal to the outlet place. Such a condition is appropriate when the flow is fully developed at the outlet and devoid of any flow reversal. Hence, zero normal gradient condition often demands a lengthy computational domain and subsequently more number of grid points which is not desirable from the perspective of LES calculation time.

The convective outlet boundary condition is more suitable for the current LES calculations and hence has been adopted. This boundary condition is mathematically expressed as:

$$\frac{\partial \tilde{\phi}}{\partial t} + U_b \frac{\partial \tilde{\phi}}{\partial n} = 0 \tag{6.35}$$

where U_b is the bulk velocity across the boundary and n is the coordinate in the direction of outward at the outlet boundary.

6.7 Steady RANS numerical framework

The RANS combustion calculations are essentially steady state and have been carried out on a 2D grid. Time varying or unsteady RANS calculations have been carried out only for NO modelling with unsteady flamelets based NO submodels (SLFM-EPFM and NADM-EPFM). However, unlike the time dependent calculations of LES which involve time advancement of all the coupled governing equations of flow, unsteady RANS calculations with EPFM are less complicated in that they require time advancement of a single passive scalar transport equation in a post-processing phase. Details about the unsteady RANS approach are presented in Section 6.8.

For the steady RANS calculations, the generic transport equation integrated over a control volume is given by:

$$\int_S \bar{\rho}\tilde{u}_k\tilde{\phi}\, dS_k = \int_S \Gamma_\phi \frac{\partial\tilde{\phi}}{\partial x_k} dS_k + \int_V \tilde{S}_\phi\, dV \qquad (6.36)$$

Since, this equation is devoid of time derivative term, the solution no longer needs to be advanced in time thus requiring significantly less computational effort as compared to LES. Also, it is now required to account for only the spatial discretisation of the convective, diffusive and source terms in each of the governing equations. Conversion of the Eq.6.36 to a simple linear algebraic form is carried out through an approach similar to the one adopted in LES. However, the exact schemes employed for approximation of the terms in the equations, the solver used for the solution of the linear algebraic equations and the overall solution procedure, are different to LES. Since, all the scales of turbulence are modelled with RANS, additional transport equations as required by the adopted turbulence model, need to be solved. The k-ε model requires solving two additional equations for the turbulent kinetic energy and its dissipation rate. These quantities are stored at the scalar nodes on the staggered grid (Fig. 6.1). For the Reynolds stress transport model, the number of additional equations is much higher and hence the allocation of additional quantities on the staggered grid requires special consideration.

6.7.1 Arrangement of Reynolds stresses on staggered grid

The Reynolds stress transport model implemented in the in-house RANS code requires solving individual transport equations for four non-zero components of the Reynolds stresses, three normal stresses $\widetilde{u''u''}, \widetilde{v''v''}$, and $\widetilde{w''w''}$, and the shear stress $\widetilde{u''v''}$ and an equation each for the turbulent kinetic energy and its dissipation rate.

Both the turbulent kinetic energy and dissipation rate are stored at the scalar node. If shear stresses are stored at the node points and central differences are used for the stress gradients then the mean velocity and shear stress fields may uncouple, i.e. "chequer boarding". One well tested method of overcoming this is to use the stress storage arrangement shown in Fig 6.3 where the shear stresses are stored at the scalar control volume corners with the normal stresses being stored at the scalar node points as is the turbulent kinetic energy and dissipation rate. The mean components of velocity as previously mentioned are stored the centroid of the control volume face.

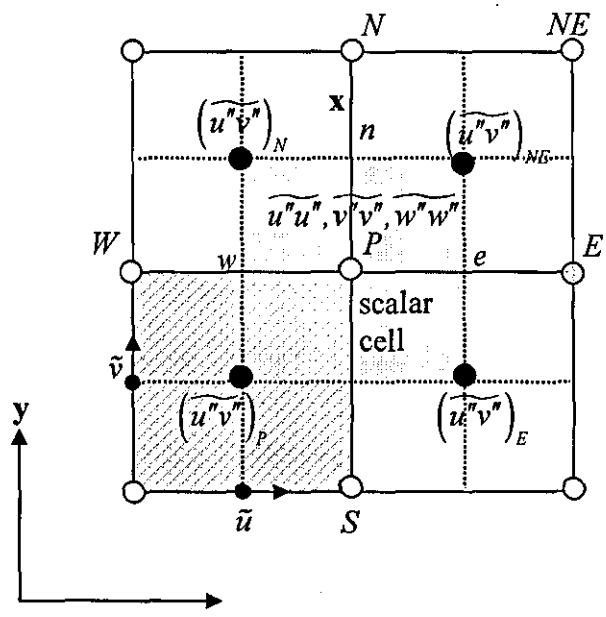

Figure 6.3: Staggered storage arrangement for the Reynolds shear stresses

6.7.2 Spatial discretisation

In LES, a second order central differencing scheme has been adopted for diffusive flux term in all the equations. The convective flux at the face of a control volume is approximated using second order central differencing scheme for momentum equations while higher order QUICK or SHARP scheme has been used for scalar equations to avoid wiggles and unphysical results such as mixture fraction taking values which are negative or more than unity.

The RANS computational code uses the same approach as far as the diffusive fluxes are concerned in that the central differencing scheme has been adopted for the gradient of a variable in the diffusive flux term of all the equations (including those of Reynolds stresses). Discretised diffusive flux across a face (say east) of a control volume is given by:

$$F_{diff_e} = \left(\Gamma_\phi \Delta A\right)_e \left(\frac{\partial \tilde{\phi}}{\partial x}\right)_e = \left(\Gamma_\phi \Delta A\right)_e \left(\frac{\tilde{\phi}_E - \tilde{\phi}_P}{\Delta x_E}\right) = D_e\left(\tilde{\phi}_E - \tilde{\phi}_P\right) \qquad (6.37)$$

Where $D_e = \left(\Gamma_\phi \Delta A\right)_e / \Delta x_E$ is the diffusive flux contribution for the east face to the coefficients in the final discretised transport equation, Eq.6.43. The diffusion coefficient at the centre of the face Γ_ϕ for momentum is known at the scalar node while for the scalars and Reynolds stresses, it is obtained by linear interpolation (Eq. 6.5). Summing the diffusive fluxes across all the faces of the control volume gives the following expression for the discrete diffusive operator,

$$\begin{aligned}\int_S \Gamma_\phi \frac{\partial \tilde{\phi}}{\partial x_k} dS_k &\approx D_e\left(\tilde{\phi}_E - \tilde{\phi}_P\right) + D_w\left(\tilde{\phi}_W - \tilde{\phi}_P\right) + D_n\left(\tilde{\phi}_N - \tilde{\phi}_P\right) + D_s\left(\tilde{\phi}_S - \tilde{\phi}_P\right) \\ &= \sum D_f\left(\tilde{\phi}_{nb} - \tilde{\phi}_P\right)\end{aligned} \qquad (6.38)$$

The convective fluxes in RANS, have been discretised using the hybrid differencing scheme of Spalding (1972). This scheme is based on a combination of second order accurate central differencing scheme and first order accurate upwind scheme. Piecewise formulae based on the local Peclet number which is evaluated at the face of the control volume are used to switch between the central differencing and upwind schemes.

The convective flux across a cell face (example, east face) is given by:

$$F_e = \left(\bar{\rho}\tilde{u}\,\Delta A\right)_e \tilde{\phi}_e = C_e \tilde{\phi}_e \tag{6.39}$$

According to the hybrid differencing scheme based approximation of $\tilde{\phi}_e$,

$$\begin{aligned} F_e &= C_e\left[(1-\theta)\tilde{\phi}_P + \theta\tilde{\phi}_E\right] && \text{for } -2 < Pe_e < 2 \\ F_e &= C_e\tilde{\phi}_P && \text{for } Pe_e \geq 2 \\ F_e &= C_e\tilde{\phi}_E && \text{for } Pe_e \leq -2 \end{aligned} \tag{6.40}$$

The density $\bar{\rho}$ at the face of the control volume is known from the scalar node in case of momentum, while for scalars and Reynolds stresses it is obtained through linear interpolation. The mean velocity $\tilde{u}$ normal to the cell face is known from its value at the scalar node in case of scalars and the Reynolds normal stress while for momentum it is obtained through a linear interpolation. For Reynolds shear stress linear interpolation needs to be pursued thrice to obtain the mean velocity $\tilde{u}_e$ at the centroid of the east face of the $\widetilde{u''v''}$ cell (Fig. 6.3). The first two interpolations result in the mean velocities $\tilde{u}_P$ and $\tilde{u}_S$ at the corners of the east face of the $\widetilde{u''v''}$ cell. The third linear interpolation uses $\tilde{u}_P$ and $\tilde{u}_S$ to obtain the value at the centre of the east face. The hybrid scheme using both central differencing and upwind schemes is only first order accurate but ensures stable and overcomes the problems associated with the use of central differencing scheme in convection dominated flows. The hybrid differencing scheme has found extensive application to practical flows (Versteeg and Malalasekera, 2007) and is relatively simple in regard to numerical implementation when compared to higher order schemes such as QUICK and SHARP.

Treatment of source term follows the same approach as detailed in the context of LES. The source terms arising in all the governing equations are evaluated by computing the function representing the source term S_ϕ at the node and multiplying by the volume of the cell ΔV:

$$\int_V \tilde{S}_\phi \, dV \approx \tilde{S}_{\phi P}\Delta V \tag{6.41}$$

The Gradients in the function are calculated using second-order central difference scheme while interpolations employ a linear profile. In several cases, the source term can be a function of the dependent variable. In such cases the source term is

approximated by means of a linear form which is a combination of the dependent and independent terms. A general source term is thus written as:

$$\tilde{S}_{\phi p}\Delta V = \tilde{S}_p \tilde{\phi}_p + \tilde{S}_u \tag{6.42}$$

Finally, the complete discretised equation is given by:

$$\left(a_P - \tilde{S}_P\right)\tilde{\phi}_P = \sum_{nb}\left(a_{nb}\tilde{\phi}_{nb}\right) + \tilde{S}_u \tag{6.43}$$

With hybrid differencing scheme, the coefficients corresponding to the node of evaluation a_p and its neighbours a_{nb} for 2D problem are given in Table 6.1.

a_E	$max[-C_e,(D_e-C_e/2),0]$
a_W	$max[C_w,(D_w+C_w/2),0]$
a_N	$max[-C_n,(D_n-C_n/2),0]$
a_S	$max[C_s,(D_s+C_s/2),0]$
a_P	$\sum_{nb}(a_{nb})+C_e-C_w+C_n-C_s$

Table 6.1: Co-efficients in the complete discretised equation with hybrid scheme.

6.7.3 Pressure correction

In the coupled momentum equations, pressure gradient appears as an unknown variable. In compressible reacting flows, the continuity equation can be used as a transport equation for density while an energy equation can be used as a transport equation for temperature and pressure may then be obtained from the density and temperature using equation of state. However, in incompressible reacting flow problems there is no equation for pressure as such since the density by definition is independent of pressure and is only a function of temperature. In this case, coupling between pressure and velocity introduces a constraint on the solution of the flow field. Provided a correct pressure field is applied in the momentum equations, the resulting velocity field should satisfy continuity. This problem is usually overcome by adopting an iterative solution strategy.

In the present RANS computational code, calculation of pressure, velocity and other scalars which are coupled to the momentum equations is carried out in a sequential manner using the well known Semi-Implicit Method for Pressure Linked Equations (SIMPLE), introduced by Patankar and Spalding (1972). In this algorithm, the momentum equations are solved using a guessed velocity (u^* and v^*) and pressure (p^*) fields. A pressure correction equation which is deduced from continuity equation is solved to obtain a pressure correction field which is in turn used to update the velocity and pressure fields. The process is iterated until convergence of the pressure and velocity fields is achieved.

The difference between correct pressure field p and guessed pressure field p^* is defined as the pressure correction p':

$$p = p^* + p' \tag{6.44}$$

Discretized form of the pressure correction equation obtained from the continuity equation is given (at a scalar node represented by P in Fig. 6.1) :

$$a_P p'_P = \sum_{nb} \left(a_{nb} p'_{nb} \right) + B'_p \tag{6.45}$$

The source term in this equation B'_p is the continuity imbalance arising from the approximated velocity field. The coefficient at the scalar node is given by,

$$a_P = \sum_{nb} a_{nb} \tag{6.46}$$

and the neighbour coefficients are expressed as :

a_E	aA_W	a_N	a_S	B'_p
$(\bar{\rho}Ad)_e$	$(\bar{\rho}Ad)_w$	$(\bar{\rho}Ad)_n$	$(\bar{\rho}Ad)_s$	$(\bar{\rho}u^*A)_w - (\bar{\rho}u^*A)_e$ $+(\bar{\rho}v^*A)_s - (\bar{\rho}v^*A)_n$

where $d_e = \dfrac{A_e}{a_P \; for \; u \; cell \; on \; east \; face \; of \; the \; scalar \; cell}$

Once the pressure correction field is known, the correct pressure field is obtained from Eq.6.44.

The velocity components are computed at their respective nodes through the correction formulae:

$$u_P = u_P^* + (p_w' - p_e')\frac{A_P}{a_p}$$

$$v_P = v_P^* + (p_s' - p_n')\frac{A_P}{a_p} \tag{6.47}$$

6.7.4 Solution of RANS equations

The discretised linear algebraic equations for velocity, pressure correction, scalars and Reynolds stresses (when using Reynolds stress transport model for turbulence closure) are solved iteratively using a Tri-diagonal matrix algorithm (TDMA). It is computationally inexpensive and has the advantage that it requires minimum amount of storage. It is applied iteratively, in a line-by-line fashion, to solve the two-dimensional problems considered in the present study.

In Fig. 6.4 a schematic of a two dimensional grid for the bluff-body stabilized flames discussed in Chapter 8 is presented. The bluff-body represents solid impermeable region devoid of fluid flow. The ghost cells within the bluff-body act as discontinuities along the lines of calculation. Usually, the TDMA is implemented such that the calculation is swept north to south followed by west to east and the ghost cells are handled like any normal cell by fixing the values of all the variables to zero. However, in the present study, modifications to the TDMA solver have been made such that the line-by-line calculations sense the discontinuity and the ghost cells are completely omitted from the calculation. This resulted in minor savings on computational time. Also, the calculations are swept first from west to east followed by north to south. Such a sequence of sweep direction has been found to improve the stability of the solution for this case. For jet flames without any solid obstacle within the domain, the sequence of sweep direction is less important and a north-south followed by west-east has been used. In all the calculations, 3 to 5 sweeps have been used for each variable within each iteration.

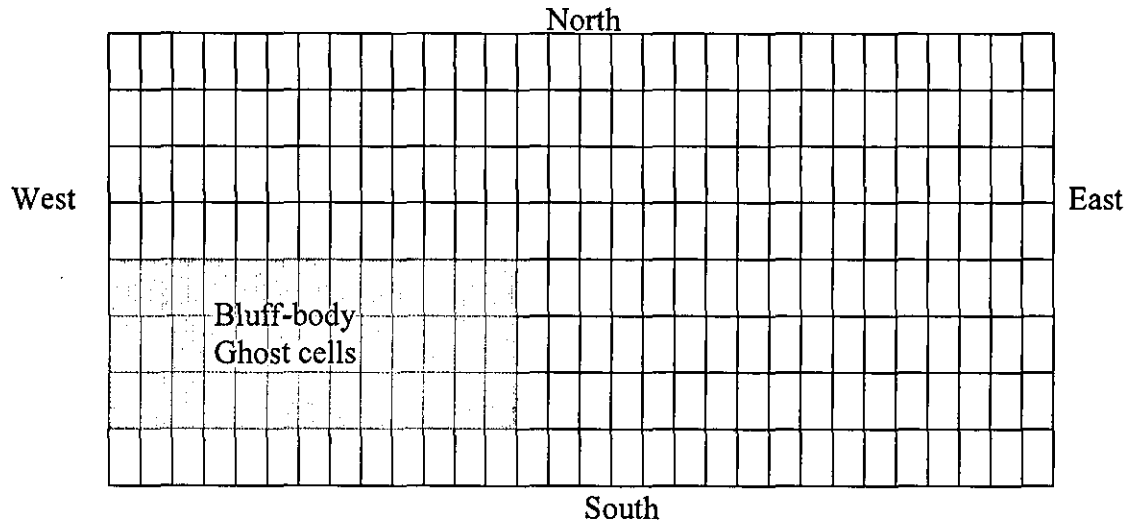

Figure 6.4: Schematic of a 2D grid for a bluff-body flow problem.

The sequence of operations involved in the solution algorithm for a steady reacting flow calculation using Reynolds stress transport model for turbulence closure is as follows.

1. Provide initial guess for all the variables
2. Solve discretized transport equation for Reynolds normal stresses and shear stress
3. Solve discretised momentum equations
4. Solve pressure correction equation and correct the pressure and velocities
5. Solve the discretised transport equations for $\tilde{k}$ and $\tilde{\varepsilon}$
6. Solve other scalar equations (relevant to the adopted combustion model)
7. Calculate density (from equations relevant to the adopted combustion model)
8. Calculate eddy viscosity
9. Reset the initial conditions with new values and repeat steps 2 to 7 till convergence is achieved.

This iterative procedure has been carried out in the present study with a convergence criterion requiring overall residual for mass, momentum and Reynolds stresses to reach a value than less than 10^{-6}. Once the converged flow and mixing fields are obtained, post-processing calculations are carried out.

10. Calculate temperature and mass fraction of species (from equations relevant to the adopted combustion model). Since this requires only the main

combustion model, it can be considered as an integral part of the main combustion model calculations.

11. If NOx modelling is of interest, calculate NO from one of the submodels discussed in Chapter 5.

It is evident from the solution algorithm that combustion modelling fits into the overall solution procedure through steps 6, 7, 10 and 11. The exact calculations to be carried out within these steps depend upon the combustion model and its sub-model. As previously mentioned, a steady flamelet model, non-adiabatic flamelet model and flamelet/progress variable approach based models have been incorporated as the main combustion modelling techniques in RANS. The steady adiabatic and non-adiabatic flamelet models also have the provision of integrated sub-models, using which NO could be modelled. All the main combustion models and their sub-models have been made to work on the look-up-table concept.

6.7.5 RANS procedure for steady flamelet model

The calculations within steps 6, 7 and 10 when employing steady flamelet model are as follows:

Steps 6: Solve scalar transport equations

6.1: Solve the mean mixture fraction transport equation

6.2: Solve the mixture fraction variance transport equation

Step 7: Calculate density

7.1: Compute the mean scalar dissipation rate from its model equation

7.2: Read the pre-integrated 3D look-up-table specific to SLFM for ordered values of mean density

7.3: From the known value of mean mixture fraction, its normalized variance and mean scalar dissipation rate, calculate mean density from the look-up-table using the 3D interpolation technique.

Step 10: Calculate temperature and species concentrations

10.1: Read the pre-integrated 3D look-up-table specific to SLFM for ordered values of mean temperature and species mass fractions.
10.2: From the known mean mixture fraction, its normalized variance and mean scalar dissipation rate, obtain mean temperature and species mass fractions from the look-up-table using the 3D interpolation technique.

Step 11: Calculate NO mass fraction

Both steady and unsteady (EPFM) flamelet based NO submodels can be employed in this step. The required calculations for steady transport equation based NO submodel (**SLFM-NO-TRE**) are as follows:

11.1: Read the converged flow and mixing field solution from the SLFM calculations.
11.2: Read the pre-integrated 3D look-up-table specific to SLFM for ordered values of mean NO source term.
11.3: From the known mean mixture fraction, its normalized variance and mean scalar dissipation rate, obtain mean NO source term from the look-up-table using the 3D interpolation technique.
11.4: Solve the transport equation for mean NO mass fraction using the source term obtained from **step 11.3**

The required calculations for unsteady flamelets (EPFM) based NO sub-model (**SLFM- EPFM**) are as follows:

11.1: Read the converged flow and mixing field solution from the SLFM calculations.
11.2: Solve the unsteady transport equation for the probability of finding a marker particle to store its spatial distribution at every time step. This step requires the use of a time advancing or unsteady RANS calculation which is presented in section 6.8.
11.3: From the known distribution of mean density, scalar dissipation rate and the probability of finding the marker particle, calculate the domain averaged conditional scalar dissipation rate from the model equation at each time step.

11.4: Using the time history of domain averaged condition scalar dissipation rate generate unsteady diffusion flamelets from the FlameMaster code (Pitsch, 1998).

11.4: Finally, calculate the mean NO mass fraction within each cell through a weighted averaged of the time evolution of the instantaneous NO profiles obtained from **step 11.3** with the probability of finding the marker particle.

6.7.6 RANS procedure for non-adiabatic flamelet models

The calculations within steps 6, 7 and 10 when employing the comprehensive non-adiabatic flamelet model, NADM is presented here. Similar procedure without the calculation of scalar dissipation rate is adopted for the NADS model. The procedure for NADM is as follows:

Steps 6: Solve the scalar transport equations

6.1: Solve the mean mixture fraction transport equation

6.2: Solve the mixture fraction variance transport equation

6.3: Read the pre-integrated 4D look-up-table specific to the non-adiabatic flamelet model, NADM, for ordered values of mean temperature and mole fractions of CO_2 and CO.

6.4: Calculate the mean scalar dissipation rate and enthalpy defect. For the first iteration, use the initial guess for actual enthalpy.

6.5: From the known values of mixture fraction, its normalized variance, scalar dissipation rate and enthalpy defect, compute the mean temperature and mole fraction mole fractions of CO_2 and CO using the 4D interpolation technique.

6.6: Using the information obtained from **step 6.5** and the Discrete Transfer Method, calculate the radiation source term in each cell.

6.7: Solve the mean enthalpy equation using the radiation source term obtained from step **6.6.**

Step 7: Calculate density

7.1: Read the pre-integrated 4D look-up-table specific to the NADM model for ordered values of mean density

7.2: Calculate the enthalpy defect from the mean enthalpy obtained from **step 6.7.**
7.3: From the known value of mean mixture fraction, its normalized variance, mean scalar dissipation rate and enthalpy defect, compute mean density from the look-up-table using the 4D interpolation technique.

Step 10: Calculate temperature and species concentrations

10.1: Read the pre-integrated 4D look-up-table specific to steady non-adiabatic flamelet model for ordered values of mean temperature and species mass fractions.
10.2: From the known values of mean mixture fraction, its normalized variance, mean scalar dissipation rate and enthalpy defect, obtain mean temperature and species mass fractions from the look-up-table using the 4D interpolation technique.

Step 11: Calculate NO mass fraction

Both steady and unsteady (EPFM) non-adiabatic flamelet based NO submodels can be employed in this step. The required calculations for steady transport equation based non-adiabatic NO sub-model (**NADM-NO-TRE**) are as follows:

11.1: Read the converged flow and mixing field solution from the NADM model calculations.
11.2: Read the 4 dimensional pre-integrated look-up-table specific to steady non-adiabatic flamelet model for ordered values of NO source term.
11.3: From the known mean mixture fraction, its normalized variance, mean scalar dissipation rate and enthalpy defect, obtain mean NO source term from the look-up-table using the 4D interpolation technique.
11.4: Solve the transport equation for mean NO mass fraction using the source term obtained from **step 11.3.**

The required calculations for unsteady (EPFM) non-adiabatic flamelets based NO sub-model (**NADM-EPFM**) are as follows:

11.1: Read the converged flow and mixing field solution from the steady non-adiabatic flamelet model calculations.

11.2: Using unsteady RANS, solve the unsteady transport equation for the probability of finding a marker particle to store its spatial distribution at every time step.

11.3: From the known distribution of mean density, scalar dissipation rate and the probability of finding the marker particle, calculate the domain averaged conditional scalar dissipation rate from the model equation at each time step.

11.4: Using the time history of domain averaged condition scalar dissipation rate generate unsteady non-adiabatic diffusion flamelets from the FlameMaster code (Pitsch,1998). The unsteady flamelet equations are solved with a radiation source term (assuming optically thin radiation).

11.5: Finally, calculate the mean NO mass fraction within each cell through a weighted averaged of the time evolution of the instantaneous NO profiles obtained from **step 11.4** with the probability of finding the marker particle.

6.7.7 RANS procedure for FPV-δ function model

The calculations within steps 6, 7 and 10 when employing the FPV-δ function model are as follows:

Steps 6: Solve the scalar transport equations

6.1: Solve the mean mixture fraction transport equation

6.2: Solve the mixture fraction variance transport equation

6.3: Read the pre-integrated 3D look-up-table specific to FPV-δ function model for ordered values of mean progress variable source term

6.4: Using the known values of mean mixture fraction and its normalized variance and the mean and reaction progress obtained from initial guess or previous iteration, compute the mean progress variable source term through the 3D interpolation.

6.5: Solve the mean progress variable transport equation using the source term from **step 6.3**

Step 7: Calculate density

7.1: Read the pre-integrated 3D look-up-table specific to FPV-δ function model for ordered values of mean density

7.3: From the known values of mean mixture fraction, its normalized variance and mean progress variable obtained from **step 6.5**, compute mean density from the look-up-table using the 3D interpolation technique.

Step 10: Calculate temperature and species concentrations

10.1: Read the pre-integrated 3D look-up-table specific to FPV-δ function model for ordered values of mean temperature and species mass fractions.

10.2: From the known values of mean mixture fraction, its normalized variance and mean progress variable, compute mean temperature and species mass fractions from the look-up-table using the 3D interpolation technique.

Step 11: Calculate NO mass fraction

In the present study, FPV-δ function model is restricted to mainly calculations of temperature distribution and the NO modelling has not been attempted. However, the approach used in steady flamelet based NO submodel could easily be extended to FPV. Pre-integrated look-up-table for NO source term can be generated using the Pre-PDF FPV δ (Chapter 7) code and stored as a function of mean mixture fraction, its normalized variance and mean reaction progress variable. Steady transport equation for mean NO mass fraction can be then be solved by interpolating the NO source term from look-up-table. Future works can adopt this technique to assess its benefits over SLFM-NO-TRE based calculations.

6.7.8 RANS procedure for FPV-β function model

It has been discussed in detail in the context of LES that the FPV-β function model stretches the RAM requirements because of the need to store the 4D look-up-tables for the entire length of the run. This problem persists with RANS as well. Reading large 4D arrays in each iteration is certainly not desirable as RANS computations

which can otherwise provide a solution in few hours can take few days. While the overall computational time can still be less than that of LES, the very purpose of using RANS (computational efficiency) would then be mitigated. Hence, in the present RANS code, the FPV-β function model is implemented such that the 4D look-up-tables for mean progress variable source term, density and covariance term are read only once in the solution process and stored for the entire length of the run.

The calculations within steps 6, 7 and 10 when employing the FPV- β function model are as follows:

Steps 6: Solve the scalar transport equations

6.1: Solve the mean mixture fraction transport equation

6.2: Solve the mixture fraction variance transport equation

6.3: If beginning of the run or resumption from previous run then, read the pre-integrated 4D look-up-table specific to FPV-β function model for ordered values of mean progress variable source term, covariance term and density.

6.4: Using the known values of mean mixture fraction and its normalized variance and the mean reaction progress variable obtained from initial guess or previous iteration, compute the mean progress variable source term through the 4D interpolation technique

6.5: Solve the mean progress variable transport equation using the source term from **step 6.4**

6.6: Using the known values of mean mixture fraction and its normalized variance, mean reaction progress variable from **step 6.5** and the normalized variance of progress variable obtained from initial guess or previous iteration, compute the mean covariance term through the 4D interpolation technique.

6.7: Solve the mean progress variable variance transport equation with the covariance term obtained from **step 6.6.**

Step 7: Calculate density

7.1: From the known values of mean mixture fraction, its normalized variance and mean progress variable and its variance, compute mean density from the look-up-table using the 4D interpolation technique.

Step 10: Calculate temperature and species concentrations

A significant advantage that RANS provides with the FPV-β function model is in regard to calculation of temperature and species mass fractions. Since in LES, one requires their calculation in every time step, the number of species that could be considered is very limited due to the need for storing the corresponding number of 4D arrays. Infact, present LES computations have been restricted to only filtered temperature. In RANS, temperature and species mass fractions are calculated in the post-processing phase. Hence, the mean mass fraction of each species can be computed sequentially in a one-off calculation. Sequential reading of the 4D look-up-table ensures that RAM requirements are well under control. Thus, with RANS, one is capable of calculating any number of species with the FPV-β function model. The required calculations in this step are as follows:

10.1: Read the pre-integrated 3D look-up-table specific to FPV-δ function model for ordered values of mean temperature and species mass fractions

10.2: From the known values of mean mixture fraction, its normalized variance and mean progress variable, compute mean temperature and species mass fractions from the look-up-table using the 3D interpolation technique.

Step 11: Calculate NO mass fraction

In the present study, NO modelling with FPV-β function model has not been attempted. However, an approach similar to that discussed in the context of FPV-δ function model can be adopted by generating a 4D pre-integrated look-up-table for NO source term from the Pre-PDF FPV β code (Chapter 7).

6.7.9 Boundary conditions

Boundary conditions corresponding to the practical flow configuration are implemented on the nodes along the boundaries of computational domain leading to modifications in the discretised equations along those nodes. Implementation of boundary conditions in the discretised equations is discussed in detail in Versteeg and Malalasekera (2007). Here a brief description of the boundary conditions that have been encountered in the modelling work discussed in Chapters 8 &9 is given.

Inlet boundary

At the inlets to the domain, the spatial distribution of all the flow variables is specified by setting the values of the variables at the nodes. Mean flow properties at the inlet are usually available from measurements. However, for turbulence quantities, in the absence of measured data, turbulent intensity (i=1-10%) and length scale (l = 0.07 x inlet radius) are specified and subsequently $\tilde{k}$ and $\tilde{\varepsilon}$ are calculated from:

$$\tilde{k}_{in} = 1.5\left(i \times U_{in}\right)^2 \text{ and } \tilde{\varepsilon}_{in} = \frac{C_\mu^{3/4} \tilde{k}_{in}^{3/2}}{l} \tag{6.48}$$

where U_{in} the bulk velocity at inlet.

When employing Reynolds stress transport model for the turbulence closure, in addition to $\tilde{k}_{in}$ and $\tilde{\varepsilon}_{in}$, the Reynolds normal and shear stress components' spatial distributions need to be specified. In the absence of measured data, isotropy of turbulence is assumed and the Reynolds normal stresses are obtained from the turbulent kinetic energy:

$$\widetilde{u''u''_{in}} = \widetilde{v''v''_{in}} = \widetilde{w''w''_{in}} = \frac{2}{3}\tilde{k}_{in} \tag{6.49}$$

The shear stress $\widetilde{u''v''_{in}}$ is approximated by: $\widetilde{u''v''_{in}} = 0.5\left(\widetilde{u''u''_{in}}.\widetilde{u''v''_{in}}\right)^{1/2}$

Further details about the inlet conditions are given separately for each of the different turbulent flames studied in the present work in Chapters 8 and 9.

Outlet boundary

At the outlet boundary the gradients of all variables except pressure are considered to be zero in the direction of the flow. For facilitating such an assumption, the outlet boundary is located far from geometrical disturbances to ensure fully developed flow. At the nodes along the outlet plane, values for variables are set equal to those corresponding to immediate interior nodes. However, this treatment is not sufficient for the velocity component normal to boundary as it may lead to problems in overall mass conservation. To correct the difference, total mass flux going out of the domain M_{out} is calculated and the velocities normal to outlet are scaled by a factor M_{out}/M_{in}.

Symmetry boundary

At the symmetry boundary, the conditions of no flow and no scalar flux across the boundary are imposed. In the implementation, the velocities normal to the symmetry boundary and the shear stresses are set to zero while the values of all other properties just outside the solution domain are equated to their values at the nearest node just inside the domain.

Wall boundary

All the walls have been treated as no slip and impermeable. All the components of velocity on the wall have been set to zero. The diffusion of scalar fluxes including the Reynolds stresses normal to the wall boundary are set to zero. At high Reynolds number, the viscous sublayer of a boundary layer is so thin that mesh required in resolving this layer is prohibitively large and hence 'wall functions' are employed. The y^+ (given in Eq. 6.50) is used as criterion for application of wall functions.

$$y^+ = \frac{\Delta y_p}{\nu}\sqrt{\frac{\tau_w}{\bar{\rho}}} \tag{6.50}$$

where Δy_p is the distance of the near wall node P to solid surface (shown in Fig 6.5).

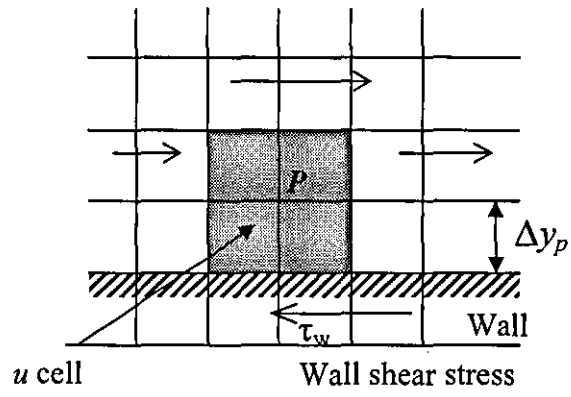

Figure 6.5: u velocity cell at wall boundary

If the value of $y^+ \leq 11.63$, the near wall flow is taken to be laminar and the wall shear stress is obtained by assuming that the velocity varies linearly with distance from the wall:

$$\tau_w = \mu \frac{u_p}{\Delta y_p} \tag{6.51}$$

The wall force which can be obtained from wall shear stress enters as a source term into the momentum equation tangential to the wall. If $y^+ > 11.63$ the near wall node P is considered to be in the log-law region of the turbulent boundary layer and the wall functions are applied. The standard wall functions of Launder and Spalding (1974) have been implemented in the present study. Within the log-law layer,

$$u^+ = \frac{u}{u_\tau} = \frac{1}{\kappa} ln\left(Ey^+\right) \tag{6.52}$$

Where the friction velocity $u_\tau = \left(\tau_w / \bar{\rho}\right)^{1/2}$, κ is the von Karman's constant equal to 0.4187 and E is integration constant and is equal to 9.793. The near wall shear stress is given by:

$$\tau_w = \bar{\rho} C_\mu^{1/4} \tilde{k}_p^{1/2} \tilde{u}_p / u^+ \tag{6.53}$$

In the k-ε model and the RST model implemented in the present work, the k equation is solved in the whole domain including the wall adjacent cells. A zero normal gradient boundary condition has been imposed as the boundary condition at the wall for k. The k equation has the production of kinetic energy its dissipation rate as the source terms. These are computed at the near wall cells on the basis of local

equilibrium hypothesis according to which, the production of k and its dissipation rate are assumed to be equal. Thus, the production of k is computed from,

$$\tilde{P}_{k,p} \approx \tau_w \frac{\partial u}{\partial y} = \frac{\tau_w^2}{\kappa \bar{\rho} C_\mu^{1/4} \tilde{k}_p^{1/2} \Delta y_p} \tag{6.54}$$

and the dissipation rate $\tilde{\varepsilon}_p$ is computed from:

$$\tilde{\varepsilon}_p = \frac{C_\mu^{3/4} \tilde{k}_p^{3/2}}{\kappa \Delta y_p} \tag{6.55}$$

At the near wall nodes, the dissipation rate equation is not solved but instead computed from Eq.6.55. The transport equations for Reynolds normal stresses as well are not solved at the near wall nodes but instead computed from $\tilde{k}_p$ through the functional relationships given in Eq.4.34. The transport equation for Reynolds shear stress however has been solved with the imposed boundary condition of zero normal diffusion to the wall.

6.8 Unsteady RANS procedure

As previously discussed in section 5.4, for NO modelling with SLFM-EPFM and NADM-EPFM, an unsteady equation for marker particle (Eq. 6.56) needs to be solved in CFD during the post processing phase. The solution procedure for solving the unsteady equation is practically the same as for any passive scalar equation in steady RANS except for minor additions driven by the temporal term in the marker particle equation.

$$\frac{\partial}{\partial t}\left(\bar{\rho}\tilde{I}_n\right) + \frac{\partial}{\partial x_k}\left(\bar{\rho}\tilde{u}_k\tilde{I}_n\right) = \frac{\partial}{\partial x_k}\left(\frac{\mu_t}{Sc_{I_n}}\frac{\partial \tilde{I}_n}{\partial x_k}\right) \tag{6.56}$$

The presence of time derivative requires integration of the equation not only over a control volume but also over a time interval from t to $t+\Delta t$:

$$\int_t^{t+\Delta t}\int_V \bar{\rho}\tilde{I}_n \, dV dt + \int_t^{t+\Delta t}\int_S \bar{\rho}\tilde{u}_k\tilde{I}_n \, dS dt = \int_t^{t+\Delta t}\int_S \frac{\mu_T}{Sc_{I_n}}\frac{\partial \tilde{I}_n}{\partial x_k} dS_k dt \tag{6.57}$$

The spatial discretisation for convective and diffusive flux terms follows exactly the same practice in steady RANS. The gradients in diffusion terms are approximated

with central differencing scheme while hybrid differencing is used for convective terms. The time derivative term is approximated with a first order backward differencing scheme. Thus,

$$\int_{t}^{t+\Delta t}\int_{V}\bar{\rho}\tilde{I}_n\,dVdt=\bar{\rho}\left(\tilde{I}_n-\tilde{I}_n^0\right)\Delta V \tag{6.58}$$

where the subscript '*0*' denotes the value at the time level t.

Time discretisation for the convective and diffusive terms is carried out through a first order accurate fully implicit scheme where only the values of the variable at the new time level $t+\Delta t$ are considered. The final discretised equation is given by:

$$a_P\tilde{I}_{n,P}=\sum_{nb}\left(a_{nb}\tilde{I}_{n,nb}\right)+a_P^0\,\tilde{I}_n^0 \tag{6.59}$$

where the central coefficient $a_P=\sum_{nb}\left(a_{nb}\right)+C_e-C_w+C_n-C_s+a_P^0$. The expressions for neighbour co-efficients are the same as presented in Table 6.1. The advantage with fully implicit scheme based temporal discretisation is evident from the discretised equation which is in most regards close to steady state equations. The only additional terms to be accounted are the contribution of a_P^0 to the central coefficient a_P and the contribution of $a_P^0\,\tilde{I}_n^0$ as an additional source term. The coefficient a_P^0 is given by:

$$a_P^0=\frac{\bar{\rho}_P^0\Delta V}{\Delta t} \tag{6.60}$$

A time marching procedure is adopted to obtain the distribution of $\tilde{I}_n$ with respect to space and time The time marching procedure starts from a given initial field of I_n (as discussed in Section 5.4.3). The discretised equation (Eq. 6.59) is solved using a TDMA solver after selecting time step Δt. The fully implicit scheme is unconditionally stable for any size of the time step Δt. However, since it is only first-order accurate in time, smaller time steps are needed to ensure the accuracy of results. In the present study, a time step size of 10^{-5} s has been employed. Next, the solution $\tilde{I}_n$ is assigned to $\tilde{I}_n^0$ and the procedure is repeated to progress the solution by a further time step. The time marching is carried out until $\tilde{I}_n$ is less than 10^{-8} throughout the domain i.e. the marker particle has nearly exited the domain.

Chapter 7

Pre-processing for RANS & LES based Calculations of Turbulent Flames

The RANS and LES based CFD calculations when employing flamelet based combustion models require input in the form of a set of pre-integrated look-up-tables which together hold the information about the mean thermo-chemical structure of the flame under investigation. In the present study, the look-up-tables have been generated from pre-integration tools (referred to as Pre-PDF tools) which have been specifically developed to cater for the different flamelet combustion models used in the current study. Each Pre-PDF tool performs appropriate integrations of flamelet profiles with presumed shape PDFs. The flamelet profiles which form the input to the Pre-PDF tools represent the solutions obtained from flamelet equations. Thus, the first and foremost task in flamelet modelling of turbulent combustion is the generation of flamelets. This along with the subsequent generation of look-up-tables constitutes the pre-processing phase of RANS and LES based turbulent flame calculations.

The steady flamelets generated in the present study can be broadly categorised as adiabatic and non-adiabatic, based on their process of generation. Within each category, flamelets can be classified as non-premixed and partially premixed based on their structure. In the present chapter, details about the variety of flamelets used in the present study and their generation processes have been presented in section 7.1. Based on the combustion model employed for the turbulent flame calculations, flamelets are fed into different Pre-PDF tools for generation of look-up-tables. For steady flamelet model based calculations, a Pre-PDF tool named 'Pre-PDF SLFM' has been developed to generate the necessary look-up-tables and details about this tool are discussed in section 7.2. Subsequently, the 'Pre-PDF NADM' tool, developed to cater for steady non-adiabatic flamelet model based calculations has been presented in section 7.3. The FPV model based calculations require the flamelets to be processed in 'Pre-PDF FPV δ' and 'Pre-PDF FPV β' tools which perform the dual tasks of integration of the flamelets to obtain look-up-tables in flamelet parameter space and

re-interpolation of the look-up-tables to progress variable space. Details about these tools are presented in section 7.4.

7.1 Generation of flamelets

All the flamelet profiles for the different turbulent flame investigations carried out in the present study have been generated using the FlameMaster code of Pitsch (1998). The process of generating flamelets involves obtaining solutions for the flamelet equations (Eq.5.6) after enforcement of appropriate assumptions and inputs. Typical inputs constitute (1) the boundary conditions for fuel and oxidiser streams and (2) chemical kinetic mechanism along with the thermodynamic data. Since the assumption of unity Lewis number and equal diffusivity is made in the derivation of the flamelet equations, the assumption is inherently enforced for all the calculations. However, assumptions regarding the radiation heat loss need to be explicitly specified. All the steady flamelet solutions are obtained without the radiation source term in the flamelet equations. The steady non-adiabatic flamelets too do not consider the radiation source term but employ an enthalpy defect approach which is discussed later in this section.

In the present study, all the investigated flames are based on gaseous hydrocarbon fuels and in particular methane. The GRI 2.11 (Bowman *et al.*, 2007) is the most widely used mechanism for describing the methane-air combustion and provides a detailed account of the elementary reactions participating in the carbon-hydrogen-oxygen chemistry. It also includes NO_x chemistry relevant to natural gas chemistry and reburning. The mechanism comprises of 277 elementary reactions with 49 species out of which 102 reactions and 17 species pertain to the NO_x chemistry. The NO_x chemistry is thus detailed and includes all the possible pathways of NO_x formation viz., thermal, Prompt, nitrous oxide and fuel nitrogen. The use of this mechanism has been accepted as a standard practice in the present study, to describe both the hydrocarbon and NO_x chemistry in all the investigated flames. This has been arrived at after verifying the superiority of the GRI 2.11 mechanism's performance over other detailed mechanisms, the GRI 3.0 (Smith *et al.*, 2007) and SanDiego (Williams, 2007).

7.1.1 Steady adiabatic flamelets

Steady adiabatic flamelets cater for the steady flamelet model and FPV approach based CFD calculations. Generation of steady adiabatic flamelets involves solving for the flamelet equations without the time derivative term and the radiation source term:

$$\rho\frac{\chi}{2}\left(\frac{\partial^2 Y_i}{\partial Z^2}\right)+\dot{\omega}_i=0 \tag{7.1}$$

$$\rho\frac{\chi}{2}\left(\frac{\partial^2 T}{\partial Z^2}\right)+\rho\frac{\chi}{2C_p}\left(\frac{\partial T}{\partial Z}\frac{\partial C_p}{\partial Z}\right)+\sum_{i=1}^{N}\rho\frac{\chi}{2}\frac{C_{pi}}{C_p}\left(\frac{\partial Y_i}{\partial Z}\frac{\partial T}{\partial Z}\right)=\frac{1}{C_p}\sum_{i=1}^{N}h_i\dot{\omega}_i \tag{7.2}$$

The complete set of solutions obtained from these equations for the fuel air conditions corresponding to Berkeley CH_4-Air lifted flame (section 9.1) have been shown by the so called S-curve in Section 5.5, Fig 5.2. There the locus of the stoichiometric temperature for all the solutions have been used to identify three branches of solutions, namely the top stable burning branch, middle unstable branch of partially extinguished states and the bottom branch of completely extinguished states have been identified. The solutions along the fully burning branch are obtained by progressively increasing the stretch rate represented by the stoichiometric scalar dissipation χ_{st} from its value at equilibrium (χ_{st}=0) to the quenching limit $\chi_{st,q}$.

The quenching limit unlike equilibrium limit is not universal and is dictated by the composition and temperature of fuel and oxidiser streams in the turbulent flame. The flamelet structure upon complete extinction corresponds to that of inert mixing of the reactants and remains unaffected for all $\chi_{st} > \chi_{st,q}$. The middle branch of unstable partially extinguished states represents the transition from fully burning to complete extinction. Generation of the middle branch involves choosing a solution corresponding to χ_{st} less than but very close to $\chi_{st,q}$ and then using this as initial solution for a simulation towards smaller values of stoichiometric scalar dissipation rate. The middle branch of solutions are however required only when employing FPV approach for modelling the turbulent flame. With, the steady flamelet model, the flamelets are parameterized by scalar dissipation rate and to ensure a unique parameterization, the unstable middle branch is ignored. Hence, the task of flamelets generation for SLFM based turbulent flame calculations is limited to obtaining solutions for the fully burning branch and completely extinguished state.

The steady flamelet profiles used in SLFM based calculations of the non-premixed Sydney bluff-body flame (HM1, discussed in section 8.1) and partially premixed Sandia D jet flame (discussed in section 8.3) are shown in Fig. 7.1. For the HM1 flame, the fuel stream is composed of a mixture of CH_4 and H_2 in 1:1 ratio by volume while the oxidizer stream consists of pure air. Both the streams are at a temperature of 300 K. For these strictly non-premixed conditions, extinction of a flamelet occurs at $\chi_{st,q}$ approximately equal to 55 s^{-1}. The Sandia D jet flame is a partially premixed flame where the fuel is a mixture of CH_4 and air in 1:3 ratio by volume while the oxidiser consists of pure air and both the streams are at a temperature of 291 K. Flamelet calculations for this flame have shown quenching to take place at $\chi_{st,q} \approx 477\,s^{-1}$.

The contrasting structure of the flamelets in non-premixed and partially premixed conditions can be observed from the temperature profiles at and near equilibrium in Fig 7.1a&b. The flamelet in non-premixed conditions (Fig. 7.1a) consists of a thin diffusive-reaction zone characterised by a high temperature gradient around the stoichiometric mixture fraction Z_{st}. The reactants are consumed (not shown) within this reaction zone and species attain maximum value while density attains lowest due to the maximum heat release. As the stretch on the flamelet increases, the peak temperature drops due to the greater extent of heat loss to the outer regions of the reaction zone in comparison to the amount of heat released. The flamelet finally extinguishes when the stretch rate reaches quenching limit $\chi_{st} = \chi_{st,q}$ resulting in an inert mixing of the reactants.

The partially premixed flamelet (Fig.7.1b) on the other hand exhibits a two-stage flame with distinctly separate premixed-flame and diffusion-flame reaction zones. The overall structure of the flamelet is rather spread out with the diffusive-reaction zone developed around the stoichiometric mixture fraction and the premixed-flame developed near to the premixed fuel end. Consistent with findings of Peters (1984), as the stretch on the partially premixed flamelet increases, the premixed flame merges into the non-equilibrium diffusion flame layer that exists around the maximum temperature.

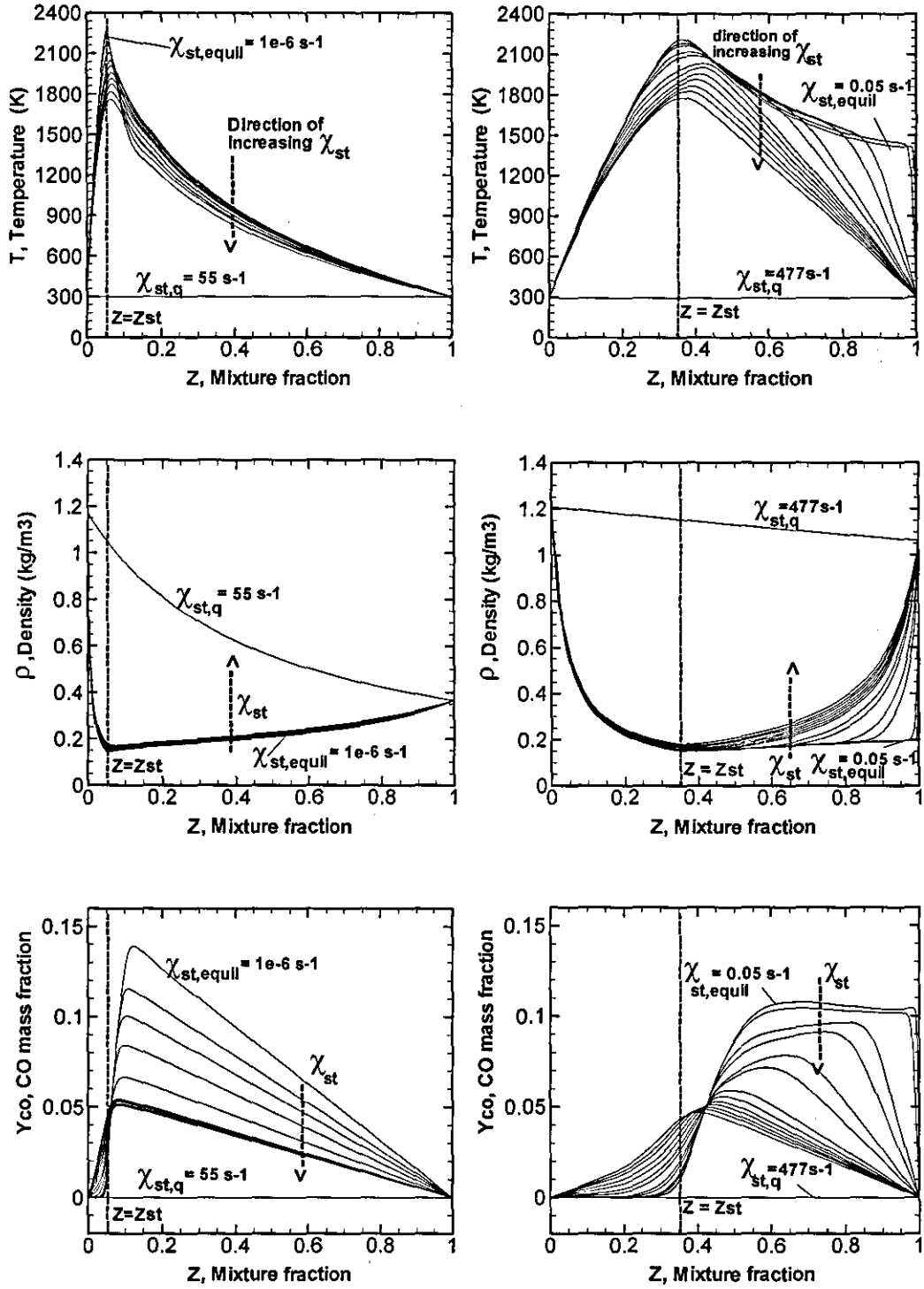

Figure 7.1: Steady flamelet solutions for fully burning and fully extinguished states. Generated for conditions corresponding to (a) HM1 flame and (b) Sandia D flame. These solutions are used for SLFM based turbulent flame calculations.

In each set of profiles shown in Fig 7.1a&b, a discontinuity between the fully burning states and the extinguished (or quenched) state can be observed and this is due to the partially extinguished intermediate states which cannot be accounted in SLFM. The SLFM has been mainly employed for only fully burning turbulent flames in the present study and hence the absence of partially extinguished flame states in the discontinuous region is not of consequence.

An interesting observation that can be made from the HM1 density profiles is that the influence of scalar dissipation rate on the density for the fully burning flamelets is rather weak. This indicates that when simulating turbulent non-premixed flames which are devoid of any local extinction, considering a single representative scalar dissipation rate should yield a mixing field prediction which is more or less similar to that obtained when considering the effect of scalar dissipation rate. This has been used to advantage in the works of Ranga Dinesh (2007) and Hossain (1999) where turbulent non-premixed flames operating far from blow-off have been simulated with a single flamelet based approach using LES and RANS respectively. Employing a single scalar dissipation is particularly useful in LES where the modelled values of scalar dissipation rate fluctuate by large magnitudes often leading to numerical instability.

However, such an approach is not warranted for temperature and species concentrations even for fully burning turbulent flames since the effect of stretch on peak temperatures and species mass fractions is more pronounced as shown in Fig 7.1a&b. Further, if steady flamelets based NO modelling is of interest, then the effect of scalar dissipation rate on NO source term profiles needs to be analysed. In Fig 7.2, the NO source term profiles required in NO modelling of HM1 flame with steady flamelets based NO sub-model (SLFM-NO-TRE), are shown. Positive and negative peaks which correspond to production and destruction of NO show non-monotonic variation in magnitude with change in scalar dissipation rate. Even at moderate non-equilibrium conditions, the variation is significant. This indicates that that, accounting for this variation might be vital for accurate mean NO predictions. Hence, in the present study, SLFM calculations in both RANS and LES consider the effects of scalar dissipation. A total of 14 flamelet profiles (13 fully burning solutions + 1 fully extinguished inert mixing solution) have been provided as input to the Pre-PDF

SLFM code which generates look-up-table of mean scalars for SLFM based turbulent flame calculations.

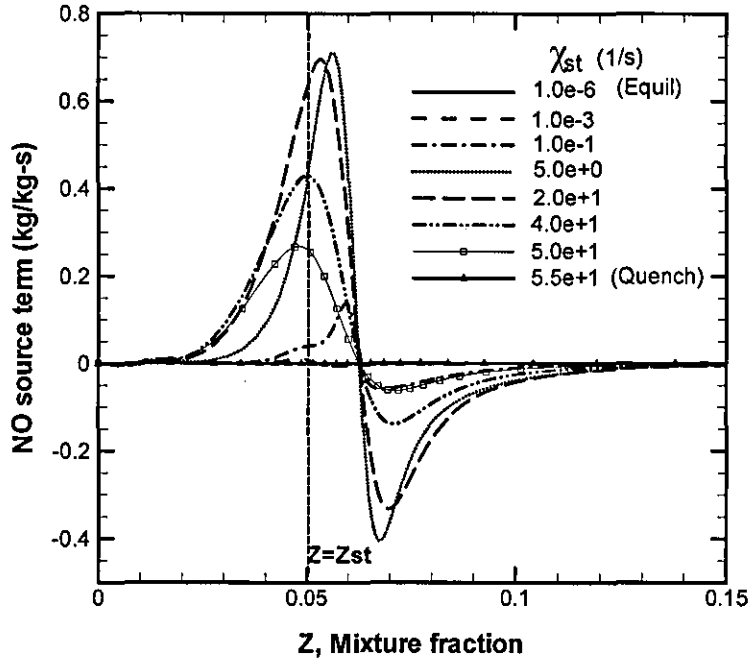

Figure 7.2: NO source term profiles corresponding to fully burning and fully extinguished steady state solutions. Generated for the HM1 flame conditions. These solutions are required in NO modelling with SLFM-NO-TRE.

For the FPV models, the flamelet parameter replaces scalar dissipation rate and it facilitates unique identification of all the steady state solutions including the partially extinguished solutions. Thus, the discontinuity observed with the set of profiles used for SLFM can be bridged with the FPV approach. In Fig 7.3, the flamelet profiles used by FPV models based calculations of Berkeley turbulent lifted jet flame (section 9.1) are shown. The Berkeley flames operate under partially premixed conditions with the fuel consisting of a mixture of CH_4 and air in the ratio of 1:3 by volume and at a temperature of 323 K while the oxidiser consists of vitiated air at 1355 K. At these conditions, near equilibrium flamelets possess a partially premixed structure similar to the ones observed with Sandia D flame. As the stretch rate is increased, the structure tends towards that of a single reaction zone and finally, quenching occurs at $\chi_{st,q} \approx 587 s^{-1}$. The partially extinguished states identified by dotted lines provide a smooth transition from fully burning to complete extinction. In the present study, a total of 153 flamelet profiles (106 fully burning + 52 partially extinguished+1 fully

extinguished) have been provided as input to the Pre-PDF FPV δ and Pre-PDF FPV β codes which generate look-up-tables of mean scalars for FPV δ function and β function based lifted flame calculations.

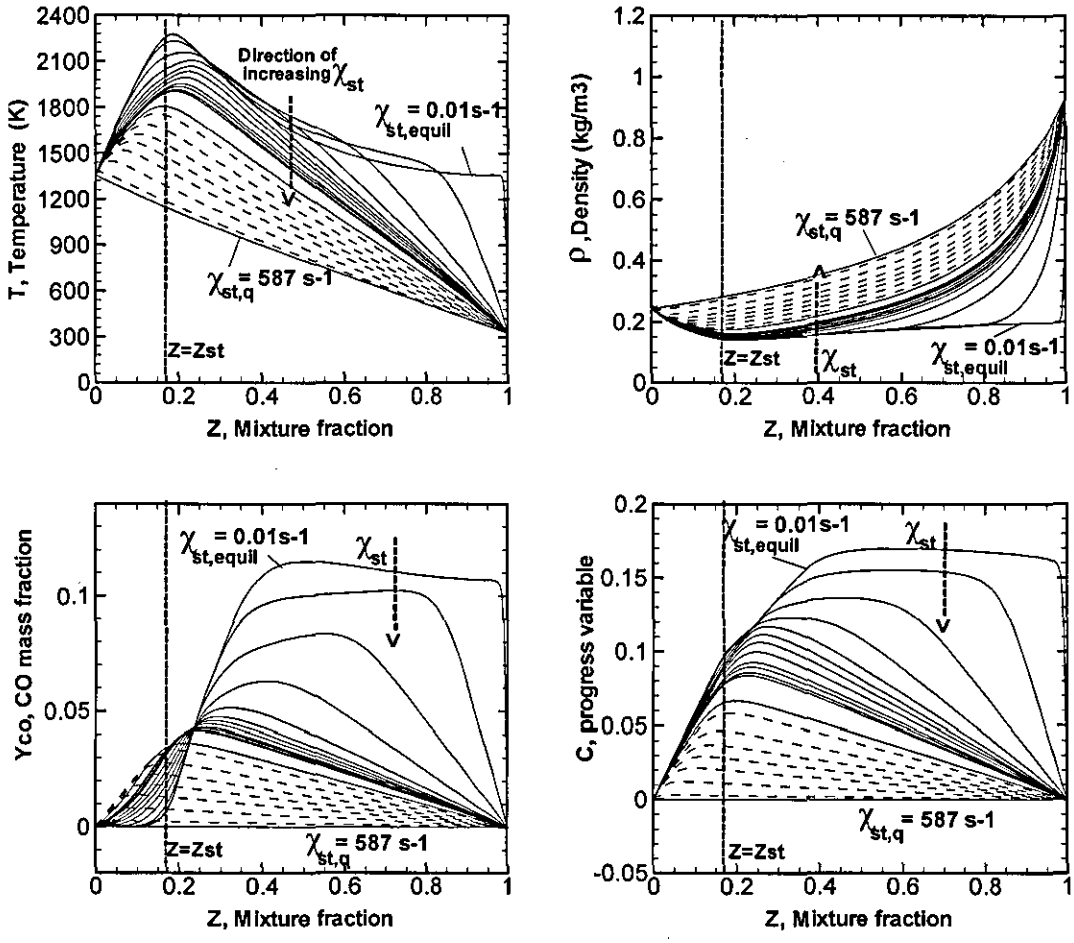

Figure 7.3: Steady flamelet solutions for fully burning, partially extinguished and fully extinguished states. Generated for the Berkeley CH_4-Air lifted jet flame conditions. These solutions are used for FPV based turbulent flame calculations. (——) fully burning and fully extinguished states; (-------) partially extinguished state.

7.1.2 Steady non-adiabatic flamelets

For turbulent flame calculations with the non-adiabatic flamelet model, NADM, steady non-adiabatic flamelet profiles need to be generated for varying levels of non-equilibrium conditions represented by χ_{st} as well as non-adiabatic conditions represented by enthalpy defect ζ. Here again, only fully burning and completely extinguished flamelets need to be generated. Since, radiation heat loss is accounted through the external parameter in the form of enthalpy defect instead of a radiation

source term in the flamelet equations, the equations to be solved are still the same as those used for generating steady adiabatic flamelet profiles (Eqs.7.1 and 7.2). However, unlike scalar dissipation rate, enthalpy defect does not appear as a variable in the flamelet equations and hence coupling enthalpy defect with flamelet equations is a challenging problem that needs to be overcome. To this end, a technique which is based on the ideas of Hossain *et al.* (2001) has been developed in the present study. Generating a steady non-adiabatic flamelet profile with the developed technique requires a two step procedure which is as follows:

1. Steady flamelet equations (Eqs. 7.1 and 7.2) at a given $\chi_{st} < \chi_q$ are solved to obtain steady flamelet profile which is adiabatic. The resulting adiabatic flamelet temperature profile is treated at every point along the mixture fraction space with a temperature defect profile $\Delta T(Z)$ which is computed from a pre-defined enthalpy defect using the formula:

$$\Delta T(Z) = \frac{\zeta}{C_p(Z)} \tag{7.3}$$

Treatment of a temperature profile is aimed at imposing the effect of radiation heat loss on temperature and hence it involves reducing the adiabatic temperature at each location in the mixture fraction space by the temperature defect. The profile after treatment is thus, $T(Z) - |\Delta T(Z)|$ and represents a non-adiabatic temperature profile. Figure 7.4 shows a steady flamelet profile before and after the treatment with $|\Delta T(Z)|$ corresponding to an enthalpy defect of -90.0 kJ/kg. It can be observed from the Fig. 7.4 that the treatment results in a profile which is qualitatively identical to the original adiabatic flamelet but is uniformly of lesser magnitude. It is also evident that the treatment results in temperatures at the boundaries Z=0 and Z=1 i.e. air and fuel streams respectively, which are not only below the adiabatic value of 300 K, but also less than 273 K. To overcome this unrealistic situation, the boundaries of the non-adiabatic temperature profile are truncated so as to restore the adiabatic temperatures at the boundaries. The mixture fraction values at the truncated boundaries thus correspond to a slightly richer oxidizer (Z_o) and slightly leaner fuel (Z_f) as shown in the Fig. 7.4.

2. Imposing the values of temperature and species mass fractions corresponding to the truncated ends Z_o and Z_f as boundary conditions, steady flamelet equations (Eqs. 7.1 and 7.2) are solved for the given χ_{st} to obtain non-adiabatic flamelet profiles.

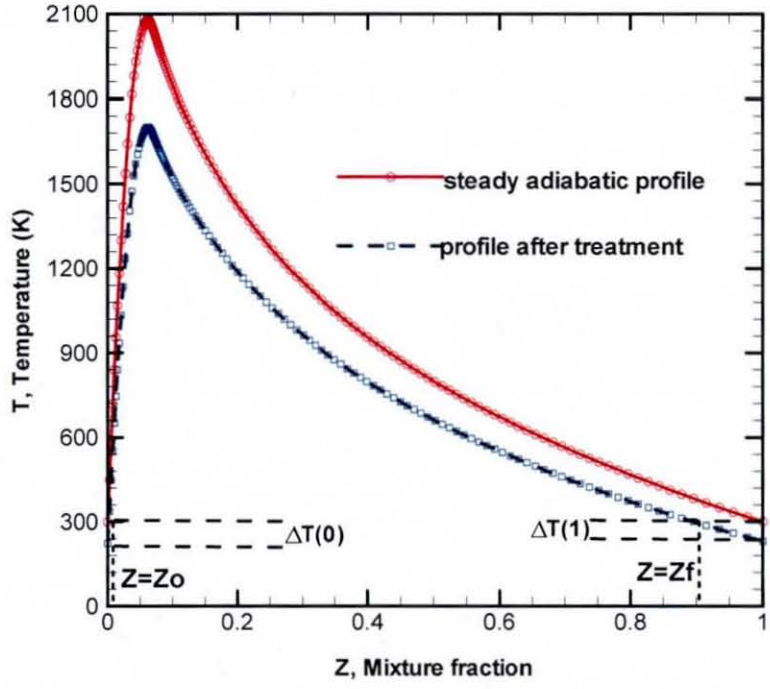

Figure 7.4: Imposing enthalpy defect on a steady adiabatic flamelet generated for HM1 flame conditions

Thus for a given χ_{st} and ζ the non-adiabatic flamelets are generated. Consistent with the boundary conditions, the non-adiabatic flamelets have a slightly truncated mixture fraction span which ranges from Z_o to Z_f instead of Z=0 to Z=1 with the extent of truncation directly proportional to the enthalpy defect. For low enthalpy defects, this truncation is insignificant to raise concerns over the accuracy of the integration with respect to Z (Eq. 5.24) in the mean scalar values calculations. However, it may not be so for higher enthalpy defects. Hence, a thorough investigation into this issue has been carried out and as shown later in Chapter 8, section 8.2.5, the truncation is expected to result in minimal deterioration in accuracy of integrated mean scalars throughout the range of enthalpy defects prevalent in the investigated flames.

The RANS based non-adiabatic flamelet model has been tested for HM1 bluff-body stabilized flame and Sandia D piloted jet flame (both discussed in Chapter 8). For the HM1 flame, enthalpy defects of 0, -15, -45, -60, -75, -90, -105, -120, -150, -180 kJ/kg have been considered to cover adiabatic to an increasing degree of non-adiabatic conditions in the flame. The variation in temperature and NO source term profiles with increasing level of non-adiabatic conditions imposed by enthalpy defect is shown in Fig. 7.5. The effect of radiation heat loss can be observed to be in the direction of simultaneous reduction in both production and destruction of NO. The shift in the peak NO source term towards the fuel rich side can also be observed and this can be considered as an indication of the shift in the dominant NO formation pathway. While thermal NO dominates at the near stoichiometric temperatures, the Prompt mechanism is more influential at fuel rich conditions.

For the Sandia D flame which is relatively more radiating, enthalpy defects of -220 and -250 kJ/kg have been considered in addition to those considered for HM1 flame. For each enthalpy defect, steady non-adiabatic flamelet profiles for $\chi_{st}(\zeta)$ varying from equilibrium to extinction condition have been generated. The series of enthalpy defects can thus be viewed as shelves with each shelf containing a set of fully burning non-adiabatic flamelet profiles. It is to be noted here that the extinction limit of a flamelet varies with enthalpy defect. An increase in enthalpy defect corresponds to an increased heat loss in comparison to the heat generation within a flamelet and hence extinction of a flamelet occurs at a lesser value of χ_{st}. This behaviour can be observed in Fig. 7.6 for the flamelets generated for both HM1 and Sandia D flame conditions.

As previously discussed in Section 5.3, Hossain *et al.* (2001), in their study on HM1 flame with a non-adiabatic model, considered only a single flamelet profile (corresponding to $\chi_{st} = 2.0 s^{-1}$) for each enthalpy defect shelf inorder to reduce the pre-processing time as well as computational time for CFD calculation. With the look-up-table concept, computational time for CFD calculations is no longer affected by the number of flamelets within an enthalpy defect shelf. However, considering only a single flamelet within an enthalpy defect shelf does simplify the pre-processing effort quite significantly.

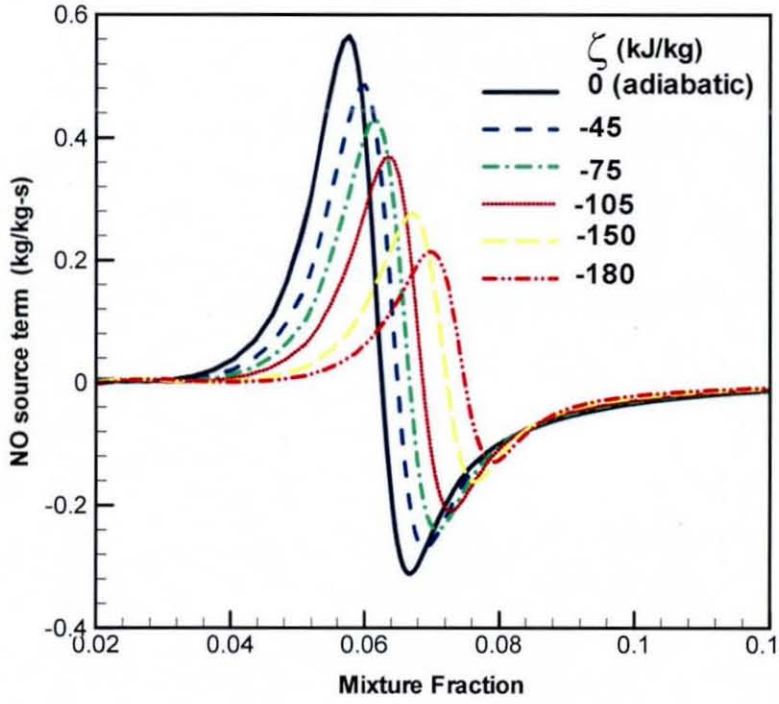

Figure 7.5: Variation of NO source term with enthalpy defect for HM1 flame conditions. The profiles correspond to a stoichiometric scalar dissipation rate of $2.0s^{-1}$.

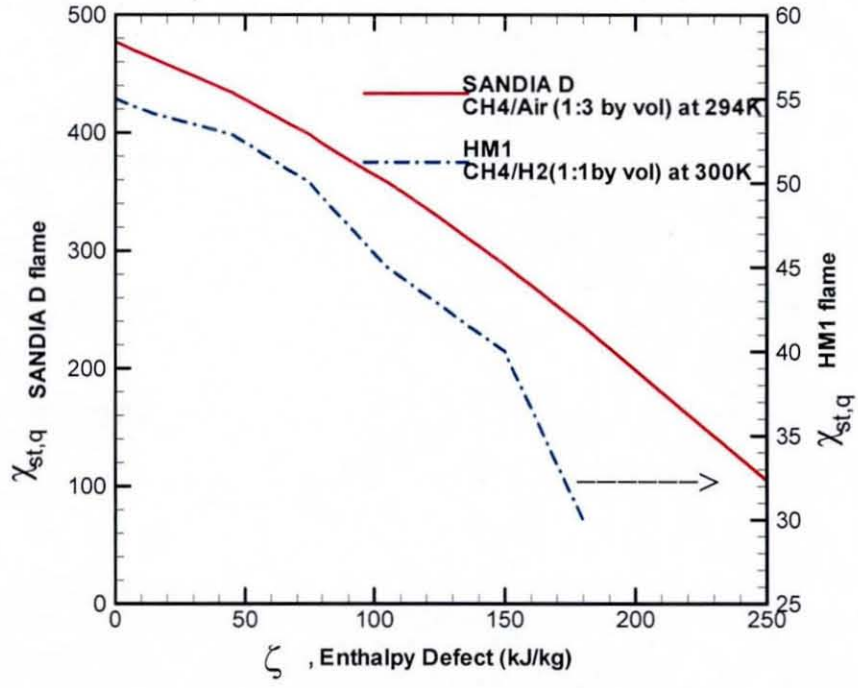

Figure 7.6: Variation of extinction limit with enthalpy defect for HM1 and SANDIA D flame conditions.

Implications of a simplification which discounts the effect of scalar dissipation rate on flamelet structure have not been studied by Hossain *et al.* (2001). Hence in the present work, HM1 flame has been studied with both, the non adiabatic flamelet model, NADM, where multiple flamelets per enthalpy defect shelf are considered, as well as the non-adiabatic flamelet model where only a single flamelet per enthalpy defect is considered (NADS).

7.2 Look-up-tables for SLFM

For SLFM based RANS and LES turbulent combustion calculations, the steady adiabatic laminar flamelets need to be pre-processed to obtain integrated look-up-tables for Favre averaged or filtered thermo-chemical variables $\tilde{\phi}$ (density, temperature, species mass fraction and NO source term) as a function of mean mixture fraction $\tilde{Z}$, its normalized variance $\widetilde{Z''^2_{norm}}$ and scalar dissipation rate $\tilde{\chi}$.

$$\tilde{\phi} = \tilde{\phi}\left(\tilde{Z}, \widetilde{Z''^2_{norm}}, \tilde{\chi}\right)$$

The Pre-PDF SLFM tool has been developed to generate look-up-tables specific to SLFM. Steady adiabatic flamelets obtained from the flamelet calculations are fed into the tool along with ordered values of the look-up-table parameters $\tilde{Z}$, $\widetilde{Z''^2_{norm}}$ and $\tilde{\chi}$. Mean values for each thermo-chemical variable $\tilde{\phi}$ are then obtained at each combination of the three parameters by performing numerical integration of the steady adiabatic flamelets with presumed PDFs for mixture fraction $\tilde{P}(Z)$ and scalar dissipation rate $\tilde{P}(\chi_{st})$ thereby resulting in a 3D look-up-table. The double integral equation which is numerically evaluated is given by:

$$\tilde{\phi} = \int_0^\infty \int_0^1 \phi(Z;\chi_{st})\,\tilde{P}(Z)\,\tilde{P}(\chi_{st})\,dZd\chi \tag{7.4}$$

Specification of table properties

The table properties constitute the range of values for each parameter, the number of discrete points to cover the range and the distribution of the discrete points. For each parameter, specification of the range is guided by the limiting values of the parameter in a turbulent flame. The mixture fraction being a normalized conserved scalar, its mean value $\tilde{Z}$ varies between 0 to 1. For a given $\tilde{Z}$, its variance $\widetilde{Z''^2}$ can take values between 0 to a maximum of $\tilde{Z}\left(1-\tilde{Z}\right)$ in the turbulent flow field. Since, a single range cannot be fixed if absolute variance were to be used as the table parameter it needs to be normalized. In the present Pre-PDF SLFM code, the absolute variance $\widetilde{Z''^2}$ is normalized (Eq. 7.5) by its maximum value for each $\tilde{Z}$ and the normalized variance $\widetilde{Z''^2_{norm}}$ ranges between 0 to 1.

$$\widetilde{Z''^2_{norm}} = \frac{\widetilde{Z''^2}}{\tilde{Z}\left(1-\tilde{Z}\right)} \tag{7.5}$$

The mean scalar dissipation rate $\tilde{\chi}$ is varied such that it covers the equilibrium to extinction conditions which vary from one turbulent flame to another.

Specification of the discrete number of points to cover the range of values for each of the table parameters and the manner in which they are distributed is carried out such that an optimum balance between computational cost and accuracy is achieved. It is ensured that the table has enough resolution to provide accurate results from the interpolations in LES and RANS and at the same time the computational time and memory requirements are kept to a reasonable level. For all the tables generated for SLFM calculations, size of 163 x 51x 31 ($\tilde{Z}$ x $\widetilde{Z''^2_{norm}}$ x $\tilde{\chi}$) has been considered. This preferential allocation allows for accurate capturing of the variation of the mean scalar structure which is particularly steep along the $\tilde{Z}$ axis of the look-up-table.

The distribution of the discrete points along $\tilde{Z}$ axis is directly obtained from the grid (Fig. 7.7) used for the flamelet calculations corresponding to equilibrium condition. While solving for the flamelet equations in the FlameMaster code, the grid on the mixture fraction space is refined automatically using an adaptive gridding technique

according to the steepness of the scalar gradient. The gradients in scalar structure at equilibrium condition are the steepest and hence the grid distribution along mixture fraction is ideal to be emulated for the mean scalar structure. In Fig 7.7, the grid points can be observed to be densely populated around the stoichiometric mixture fraction where high gradients and the density decreases towards the fuel rich side.

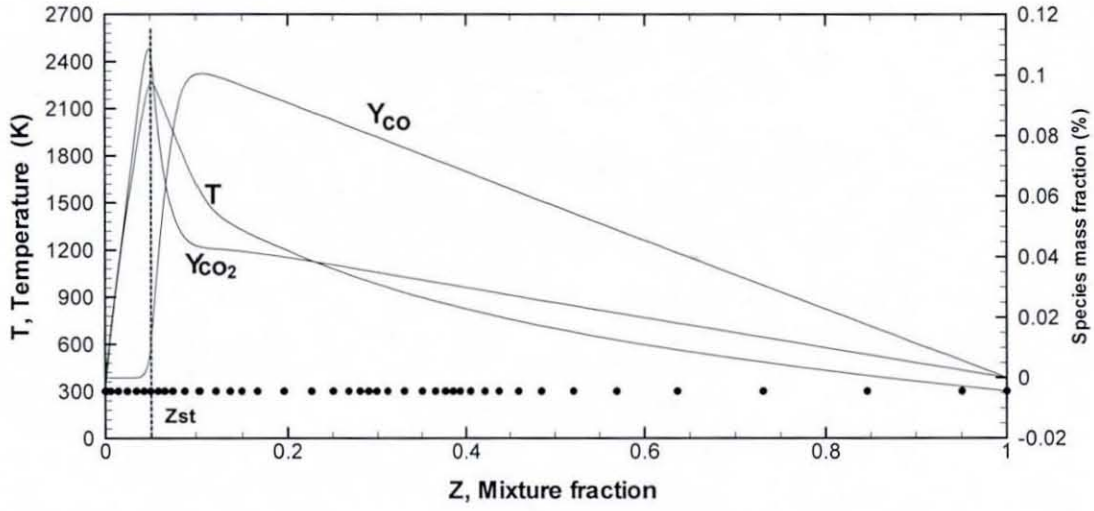

Figure 7.7: Steady adiabatic flamelet solution for equilibrium condition. Generated for HM1 flame conditions. Dots show alternative grid points along Z space.

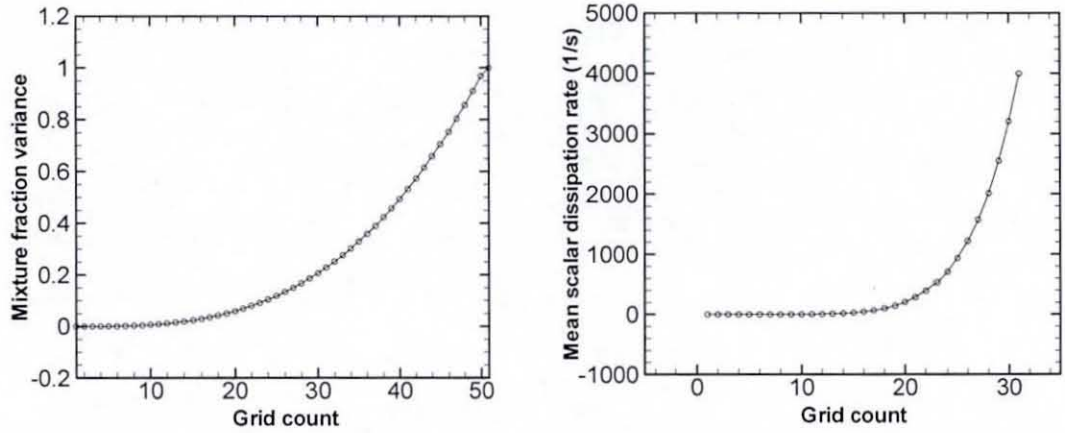

Figure 7.8: The distribution of points along $\widetilde{Z''^2_{norm}}$ and $\tilde{\chi}$ axes of the look-up-table for SLFM based calculations.

The points along the normalised mixture fraction variance and mean scalar dissipation rate axes of the look-up-table are distributed using power-law fit.

$$\Psi(i) = 1e^{-a}(i-1)^{b} \tag{7.6}$$

For $\Psi = \widetilde{Z''^2_{norm}}$ the grid count i varies from 1 to 51 and the constants a and b take the values of 5.0 and 2.95 respectively. For $\Psi = \tilde{\chi}$, the grid count i varies from 1 to 31 and the constants a and b take the values of 6.0 and 6.5 respectively. The distributions for $\widetilde{Z''^2_{norm}}$ and $\tilde{\chi}$ are shown in the Fig. 7.8.

Numerical integration

Once the table properties are specified, the values for $\tilde{Z}$, $\widetilde{Z''^2_{norm}}$ (and hence $\widetilde{Z''^2}$) and $\tilde{\chi}$ are known at every cell in the table. Numerical integrations can then be performed for every cell in the table and for every scalar of interest. Numerical evaluation of Eq. 7.4 is based on the ideas proposed by Lentini (1994) and Hossain (1999). Limited number of flamelets (13 fully burning +1 fully extinguished) are considered and each is represented by χ_l. Integration range in χ_{st} is then split into L subranges $[\chi_{l-1/2}, \chi_{l+1/2}]$, with l=1,2,....L (in particular $\chi_{1/2} = 0$), such that χ_l is a representative value for the corresponding interval. The approximate form of Eq.7.4 then reads:

$$\tilde{\phi} = \sum_{l=1}^{L} \int_{\chi_{l-1/2}}^{\chi_{l+1/2}} \tilde{P}(\chi_{st})\, d\chi_{st} \int_{0}^{1} \phi(Z,\chi_l)\, \tilde{P}(Z)\, dZ \tag{7.7}$$

Evaluation of the two integrals requires the knowledge of $\tilde{P}(\chi_{st})$ and $\tilde{P}(Z)$ and they are presumed to follow log-normal and β function distributions respectively.

Evaluation of the integral $\int_{0}^{1} \phi(Z,\chi_l)\, \tilde{P}(Z)\, dZ$:

The mixture fraction integral with β function distribution is given by:

$$\int_{0}^{1} \phi(Z,\chi_l)\, \tilde{P}(Z)\, dZ = \frac{\Gamma(a+b)}{\Gamma(a)\Gamma(b)} \int_{0}^{1} \phi(Z,\chi_l)\, Z^{a-1}(1-Z)^{b-1}\, dZ \tag{7.8}$$

Where the functional dependence of the constants a and b on $\tilde{Z}$ and $\widetilde{Z''^2}$ is given by:

$$a = \tilde{Z}\left[\frac{\tilde{Z}\left(1-\tilde{Z}\right)}{\widetilde{Z''^2}}-1\right] \tag{7.9}$$

$$b = \left(1-\tilde{Z}\right)\left[\frac{\tilde{Z}\left(1-\tilde{Z}\right)}{Z}-1\right] \tag{7.10}$$

The above integral with respect to mixture fraction is then numerically evaluated by using Romberg's method with mid-point approximation (Press *et al*, 1993). Two numerical difficulties are associated with calculation of the integral in Eq 7.8. The first difficulty arises at the limits of the integral, Z=0 and Z=1, where a or b can take a value less than unity thereby leading to singularity. This problem is overcome by adopting the method suggested by Bray *et al.* (1994) and Chen *et al.* (1994) according to which the integral is split as below:

$$\int_0^1 \phi\left(Z,\chi_l\right) Z^{a-1}\left(1-Z\right)^{b-1} dZ \cong \frac{\xi^a}{a}\phi(0) + \int_{\xi}^{1-\xi} \phi\left(Z,\chi_l\right) Z^{a-1}\left(1-Z\right)^{b-1} dZ + \frac{\xi^b}{b}\phi(1) \tag{7.11}$$

where ξ represents a very small number, taken as 10^{-30}.

The second difficulty which needs to be overcome is the overflow problem caused when the computed values of a and b reach several hundred thousands in magnitude during the iteration process. According to the characteristics of β-function, the distribution is close to a delta function when a or b is adequately large. Hence the overflow problem is tackled by approximating $\tilde{P}(Z)$ to a δ function (Eq. 7.12), when the value of a or b is large. A value of 500 has been set as the limit.

$$\tilde{P}(Z) = \delta\left(Z-\tilde{Z}\right) \tag{7.12}$$

Evaluation of the integral $\int_{\chi_{l-1/2}}^{\chi_{l+1/2}} \tilde{P}(\chi_{st})\, d\chi_{st}$:

Employing log-normal distribution for $\tilde{P}(\chi_{st})$, the integral is given by:

$$\int_{\chi_{l-1/2}}^{\chi_{l+1/2}} \tilde{P}(\chi_{st})\, d\chi_{st} = \int_{\chi_{l-1/2}}^{\chi_{l+1/2}} \frac{1}{\chi_{st}\sigma\sqrt{2\pi}} exp\left[-\frac{1}{2\sigma^2}\left(ln\chi_{st}-\mu\right)^2\right] d\chi_{st} \tag{7.13}$$

where the parameters μ and σ are related to the mean scalar dissipation rate $\tilde{\chi}$ by

$$\tilde{\chi} = exp\left(\mu+\frac{\sigma^2}{2}\right); \sigma = 2.0 \tag{7.14}$$

Introducing variable $\theta = \left(ln\chi_{st} - \mu\right)/\sqrt{2}\sigma$, the integral in Eq. 7.13 is reduced to,

$$\int_{\chi_{l-1/2}}^{\chi_{l+1/2}} \tilde{P}(\chi_{st})\, d\chi_{st} = \frac{1}{\sqrt{\pi}} \int_{\theta_{l-1/2}}^{\theta_{l+1/2}} e^{-\theta^2} d\theta = \frac{1}{2}\left[erf\left(\theta_{l+1/2}\right) - erf\left(\theta_{l-1/2}\right)\right] \quad (7.15)$$

Where *erf* denotes error function and its argument is given by:

$$\theta_{l\mp 1/2} = \frac{1}{\sqrt{2}\sigma} ln\left(\frac{\chi_{l\mp 1/2}}{\tilde{\chi}}\right) - \frac{\sigma}{2\sqrt{2}} \quad (7.16)$$

In the set of flamelet profiles considered for the calculation, one of them corresponds to inert mixing which represents post-quenching state. In order to accurately account for contribution of the inert state, the integration range is divided into subranges in such a way that $\chi_{L-1/2} = \chi_{st,q}$ (flamelet at quenching limit) and $\chi_{L+1/2} = \chi_{\infty}$ (post quenching).

The final forms of the approximated equations for filtered density and Favre averaged (or filtered) scalars $\tilde{\phi}$ are given by:

$$\bar{\rho} = \left[\sum_{l=1}^{L} \frac{1}{2}\left[erf\left(\theta_{l+1/2}\right) - erf\left(\theta_{l-1/2}\right)\right] \int_0^1 \frac{\tilde{P}(Z)}{\rho(Z,\chi_l)} dZ\right]^{-1} \quad (7.17)$$

$$\tilde{\phi} = \sum_{l=1}^{L} \frac{1}{2}\left[erf\left(\theta_{l+1/2}\right) - erf\left(\theta_{l-1/2}\right)\right] \int_0^1 \phi(Z,\chi_l)\, \tilde{P}(Z)\, dZ \quad (7.18)$$

The chosen number of L=14 flamelets have been found to provide adequate accuracy and a reasonably good turn around time. The computational time for generation of 3D, 163x51x31 size look-up-tables for $\bar{\rho}, \tilde{T}$, 6 species and NO source term is kept to less than a day on a 2GB RAM Intel Pentium 4, 3GHZ processor. Figure 7.9 shows examples of 3D look-up-tables for mean temperature generated for HM1 and Sandia D flame conditions. The mean structure can be observed to closely follow the laminar structures in Fig.7.1a&b. The variation in structure with respect to the mean mixture fraction, its normalized variance and the mean scalar dissipation rate can be observed. Similar tables haves been created with Berkeley lifted flame conditions (section 9.1) for SLFM calculations in RANS and LES. In LES, the tables are read as filtered scalar values (e.g. filtered temperature) as a function of filtered mixture fraction, subgrid normalized variance and filtered scalar dissipation rate.

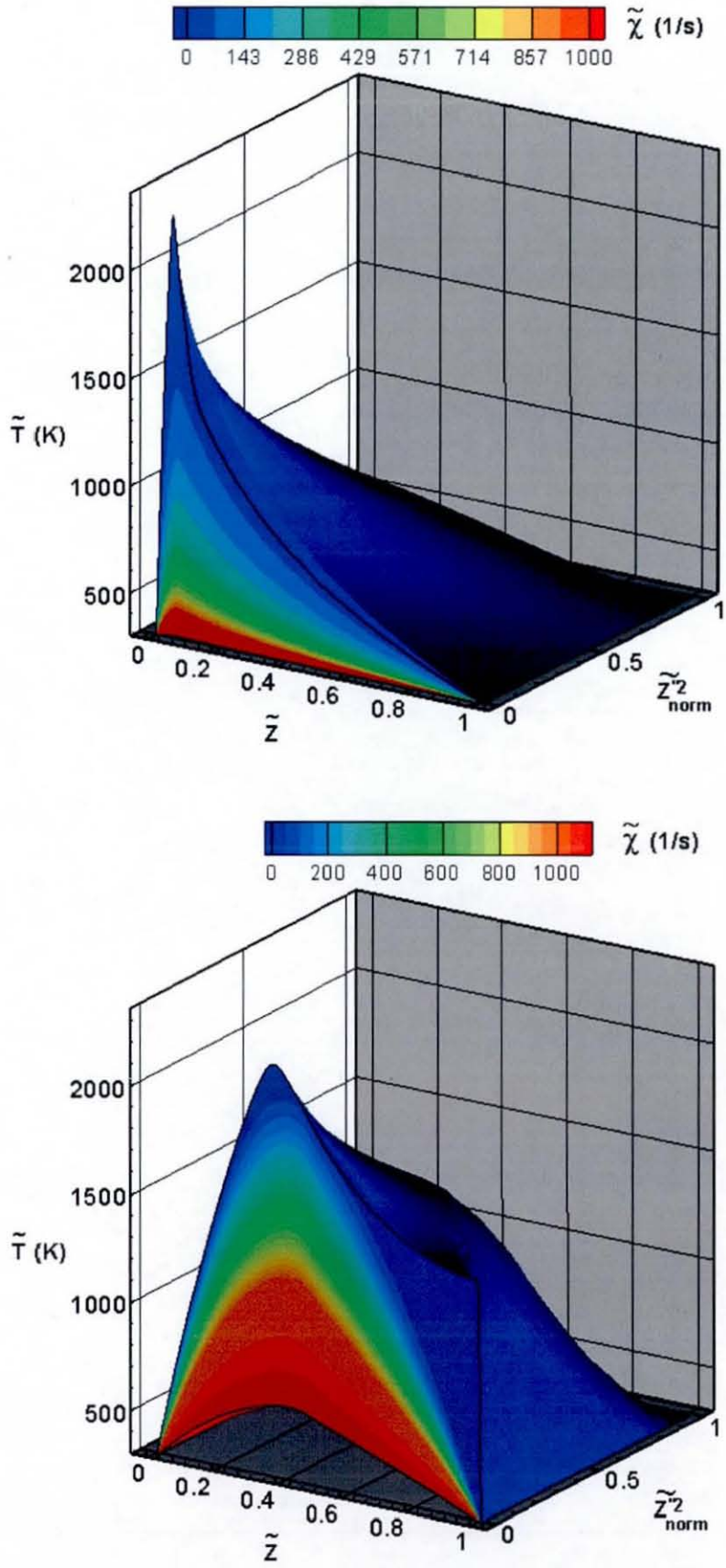

Figure 7.9: Structure of 3D look-up-tables for integrated temperature (K) for SLFM calculations. Generated for HM1flame (top) and Sandia D (bottom) flame conditions.

7.3 Look-up-tables for NADM

In the non-adiabatic flamelet model, NADM, which has been developed for RANS in the present work, the turbulent mean values of the thermo-chemical variables $\tilde{\phi}$ are dependent on $\tilde{Z}, \widetilde{Z''^2}, \tilde{\chi}$ and additionally on the enthalpy defect $\tilde{\zeta}$. Hence for turbulent flame calculations based on this model, 4D look-up-tables of the form given in Eq. 7.19 need to be generated for each mean reactive scalar $\tilde{\phi}$ (density, temperature, species fraction and NO source term). To this end, an extended version of Pre-PDF SLFM called Pre-PDF NADM has been developed.

$$\tilde{\phi} = \tilde{\phi}\left(\tilde{Z}, \widetilde{Z''^2_{norm}}, \tilde{\chi}, \tilde{\zeta}\right) \tag{7.19}$$

The Pre-PDF NADM tool takes the steady non-adiabatic flamelets as input and conducts numerical integration for each reactive scalar of interest for each cell in a 4D table. As part of the specification of table properties, the range and distribution of enthalpy defect $\tilde{\zeta}$ points needs to be specified in addition to those for $\tilde{Z}$, $\widetilde{Z''^2_{norm}}$ and $\tilde{\chi}$ which take the same definitions as with Pre-PDF SLFM. For HM1 flame conditions, a range of 0 (adiabatic) to -180 kJ/kg is specified for the mean enthalpy defect $\tilde{\zeta}$ and this span has been covered by 10 uniformly spaced points. For Sandia D flame conditions, a slightly higher range 0 to -250 kJ/kg has been specified and this has been covered by 12 uniformly spaced points. Thus, the sizes of look-up-tables for HM1 and Sandia D flames for NADM model based calculations are 163x51x31x10 and 163x51x31x12 ($\tilde{Z}, \widetilde{Z''^2_{norm}}, \tilde{\chi}, \tilde{\zeta}$) respectively. The equation for evaluation of mean scalars with NADM model is given by:

$$\tilde{\phi} = \int_0^\infty \int_0^1 \int_{\zeta_{min}}^{\zeta_{max}} \phi(Z;\chi_{st};\zeta)\tilde{P}(Z)\tilde{P}(\chi_{st})\tilde{P}(\zeta)\,d\zeta dZ d\chi_{st} \tag{7.20}$$

Since the flamelet structures are now a function of enthalpy defect as well, a limited number of enthalpy defect shelves are considered for the integrations and within each shelf, a limited number of flamelets corresponding to fully burning and extinguished states are considered. For calculating tables for HM1 flame, a total of 10 enthalpy

defect shelves are considered with the total number of non-adiabatic flamelets equal to 100. For Sandia D flame, a total of 12 enthalpy defect shelves are considered with the total number of non-adiabatic flamelets equal to 120.

The approximations made in Pre-PDF SLFM in regard to the integrations with respect to Z and χ_{st} are enforced here as well. The additional requirement here is to account for $\tilde{P}(\zeta)$ and this is assumed to follow δ function. Thus, the third integral with respect to enthalpy defect can be dropped and the task is reduced to interpolation thereby bringing down the overall computational effort to a tractable level. However, the 4D computations still demand a turn around time which is ~10 times that required for generating 3D look-up-tables for SLFM. The final equations for mean density and scalars take the form:

$$\bar{\rho} = \delta\left(\zeta - \tilde{\zeta}\right)\left[\sum_{l=1}^{L(\zeta)} \frac{1}{2}\left[erf\left(\theta_{l+1/2}\right) - erf\left(\theta_{l-1/2}\right)\right] \int_0^1 \frac{\tilde{P}(Z)}{\rho\left(Z, \chi_l, \zeta\right)} dZ\right]^{-1} \tag{7.21}$$

$$\tilde{\phi} = \delta\left(\zeta - \tilde{\zeta}\right)\left[\sum_{l=1}^{L(\zeta)} \frac{1}{2}\left[erf\left(\theta_{l+1/2}\right) - erf\left(\theta_{l-1/2}\right)\right] \int_0^1 \phi\left(Z, \chi_l, \zeta\right) \tilde{P}(Z) dZ\right] \tag{7.22}$$

The number of sub-ranges into which the integration range of the scalar dissipation rate is split, is now a function of enthalpy defect $L = L(\zeta)$. As previously discussed, extinction limit of a non-adiabatic flamelet increases with the increase in enthalpy defect. Hence the range of χ_{st} for fully burning states reduces. This is exploited to gain computational efficiency by considering a lesser number of flamelets in higher enthalpy defect shelves. The δ function in the above equations is treated by employing a linear interpolation. If m denotes the index of the enthalpy defect shelf, such that the value $\tilde{\zeta}$ for a particular cell in the table lies in the range $\zeta_m \le \tilde{\zeta} < \zeta_{m-1}$, then the interpolation of any mean quantity is carried out as

$$\tilde{\phi} = \frac{\tilde{\zeta} - \zeta_m}{\zeta_{m-1} - \zeta_m} \tilde{\phi}_{m-1} + \frac{\zeta_{m-1} - \tilde{\zeta}_m}{\zeta_{m-1} - \zeta_m} \tilde{\phi}_m \tag{7.23}$$

Where $\tilde{\phi}_m$ stands for:

$$\tilde{\phi}_m = \left[\sum_{l=1}^{L(\zeta_m)} \frac{1}{2}\left[erf\left(\theta_{l+1/2}\right) - erf\left(\theta_{l-1/2}\right)\right] \int_0^1 \phi\left(Z, \chi_l, \zeta_m\right) \tilde{P}(Z) dZ\right] \tag{7.24}$$

7.4 Look-up-tables for FPV models

The 'Pre-PDF FPV δ' and 'Pre-PDF FPV β' tools have been developed to generate look-up-tables for LES or RANS turbulent flame calculations employing FPV δ function and FPV β function combustion models respectively. The Pre-PDF FPV δ generates 3D look-up-tables for mean values of each thermo-chemical variable of interest, parameterized by $\tilde{Z}, \widetilde{Z''^2_{norm}}$ and $\tilde{C}$. The Pre-PDF FPV β generates 4D look-up-tables parameterized by $\tilde{Z}, \widetilde{Z''^2_{norm}}, \widetilde{C''^2_{norm}}$ and $\tilde{C}$.

With the FPV approach, generation of mean values for any thermo-chemical variable ϕ from its flamelet profiles is based on the equation:

$$\tilde{\phi} = \int_0^1 \int_{\lambda_{min}}^{\lambda_{max}} \phi(Z;\lambda)\tilde{P}(Z)\tilde{P}(\lambda)d\lambda dZ \qquad (7.25)$$

This equation has a form identical to that in SLFM with the scalar dissipation rate now replaced by a flamelet parameter λ which parameterizes the flamelets. However, the critical difference here is that $\phi(Z;\lambda)$ now represents a complete set of steady flamelet profiles (fully burning + partially extinguished + fully extinguished) which cover the entire S-curve (Fig. 5.2). The λ for each flamelet corresponds to C_{max} for that particular flamelet. Thus, the flamelet corresponding to equilibrium condition has the maximum λ (λ_{max}) while a completely extinguished flamelet has λ=0. In order to have the integral limits λ_{min} and λ_{max} varying from 0 to 1 in Eq. 7.25, all the flamelets are parameterized by a normalized flamelet parameter λ_n which is equal to λ / λ_{max}. Adopting the standard practice, the PDF for Z is assumed to follow a β function. The PDF for the flamelet parameter $\tilde{P}(\lambda)$ has been tested in the current work with a δ function and a β function which leads to the two different FPV models and hence the two different look-up-table generation tools. Look-up-tables when generated using above equation, are in the flamelet parameter (λ) space and have the following forms depending on whether δ function or β function is used for $\tilde{P}(\lambda)$:

$$\delta \text{ function: } \tilde{\phi} = \tilde{\phi}\left(\tilde{Z}, \widetilde{Z''^2_{norm}}, \tilde{\lambda}\right), \ \beta \text{ function : } \tilde{\phi} = \tilde{\phi}\left(\tilde{Z}, \widetilde{Z''^2_{norm}}, \widetilde{\lambda''^2_{norm}}, \tilde{\lambda}\right) \qquad (7.26)$$

The flamelet parameter λ (defined as C_{max} in the present study) has been introduced in the FPV approach with the only purpose of facilitating consideration of partially extinguished flamelet states along the S-curve (Fig. 5.2) which is not possible with scalar dissipation rate. The flamelet parameter does not hold any meaning in a turbulent flame unlike the scalar dissipation rate. Hence, $\tilde{\lambda}$ and $\widetilde{\lambda''^2_{norm}}$ cannot be computed as part of the solution in LES or RANS. This poses an impediment to the use of look-up-tables generated in λ space for turbulent flame calculations. To overcome this, $\tilde{\lambda}$ and $\widetilde{\lambda''^2_{norm}}$ in the look-up-table are replaced by the quantities $\tilde{C}$ and $\widetilde{C''^2_{norm}}$ which can be readily obtained in LES or RANS.

Thus, additional calculations are needed to convert look-up-table in flamelet parameter or λ space to the progress variable or C space and this is achieved through a re-mapping or re-interpolation procedure. The tools 'Pre-PDF FPV δ' and 'Pre-PDF FPV β' are developed such that they conduct both the tasks of numerical integration of flamelet profiles as well as re-mapping.

7.4.1 Pre-PDF FPV δ

The inputs to be specified to this tool include the complete set of steady flamelets parameterized by the flamelet parameter λ_n and the properties for two tables. The first table is in the λ space and parameterized by $\tilde{Z}, \widetilde{Z''^2_{norm}}$, $\tilde{\lambda}$ while the second is in the C space and parameterized by $\tilde{Z}, \widetilde{Z''^2_{norm}}$ and $\tilde{C}$. For each table, the range, the number of points and their distribution for each table parameter needs to be specified. However, both the tables share the same properties as far as $\tilde{Z}$ and $\widetilde{Z''^2_{norm}}$ are concerned.

Both $\tilde{Z}$ and $\widetilde{Z''^2_{norm}}$ always range from 0 to 1 in a turbulent flame and hence the same has been used for the table. The range for $\tilde{\lambda}$ as well is specified to vary from 0 to 1. However, for $\tilde{C}$, the range is decided based on the maximum value of C within the complete set of steady flamelet profiles. In Fig 7.3, progress variable profiles from a complete set of flamelets generated for the Berkeley CH_4/air flame conditions are shown and the maximum value of C can be seen to be ~ 0.17. Since, the maximum

mean or filtered mean value of a scalar in turbulent flame cannot exceed the maximum value in the flamelet, look-up-tables for Berkeley CH_4/air flame conditions use a range of 0.0 to 0.17 for $\tilde{C}$.

The number of points and the manner of their distribution $\tilde{Z}, \widetilde{Z''^2_{norm}}$ are identical to those used in Pre-PDF SLFM. For both $\tilde{\lambda}$ and $\tilde{C}$, 151 points with uniform distribution has been specified. Thus the size of the final 3D look-up-table is 163x51x151 ($\tilde{Z}, \widetilde{Z''^2_{norm}}, \tilde{C}$).

Numerical integration

Within each cell of the table, approximated form of Eq.7.25 is numerically integrated for each scalar of interest. Adopting δ function for $\tilde{P}(\lambda)$, the Eq. 7.25 takes the form:

$$\tilde{\phi} = \int_0^1 \int_0^1 \phi(Z;\lambda_n)\beta\left(Z;\tilde{Z},\widetilde{Z''^2}\right)\delta\left(\lambda_n - \tilde{\lambda}\right)d\lambda_n dZ \tag{7.27}$$

Numerical integration of mixture fraction integral is carried out using the same procedure as the one described for SLFM in section 7.1.3 and the δ function is treated by linear interpolation similar to the manner it was dealt for NADM (section 7.1.4). The scalars for which the integrations are carried out include the density ρ, temperature T and species mass fractions Y_i, progress variable C and progress variable source term $\tilde{\dot{\omega}}_c$. The mean progress variable calculated here is referred by $\tilde{C}_{sfe}$ to differentiate it from the table parameter $\tilde{C}$ which is representative of the mean progress variable obtained in a turbulent flame calculation through the solution of its transport equation. Look-up-tables resulting from the integrations are in λ space and take the following form:

$$\bar{\rho} = \bar{\rho}\left(\tilde{Z},\widetilde{Z''^2_{norm}},\tilde{\lambda}\right); \tilde{T} = \tilde{T}\left(\tilde{Z},\widetilde{Z''^2_{norm}},\tilde{\lambda}\right); \tilde{Y}_i = \tilde{Y}_i\left(\tilde{Z},\widetilde{Z''^2_{norm}},\tilde{\lambda}\right) \tag{7.28}$$

$$\tilde{C}_{sfe} = \tilde{C}_{sfe}\left(\tilde{Z},\widetilde{Z''^2_{norm}},\tilde{\lambda}\right); \tilde{\dot{\omega}}_c = \tilde{\dot{\omega}}_c\left(\tilde{Z},\widetilde{Z''^2_{norm}},\tilde{\lambda}\right)$$

Re-mapping

In Chapter 5, Section 5.5.2, it has been mentioned that a constraint equation (Eq. 5.43) needs to be satisfied for the FPV δ function model to be consistent and by means of satisfying the constraint, the need to calculate $\tilde{\lambda}$ in LES or RANS can be eliminated. The gist of the constraint is that the $\tilde{C}$ obtained from the transport equation solution in CFD should be equal to that obtained from integration of the flamelets $\tilde{C}_{sfe}$. Thus,

$$\tilde{C} = \tilde{C}_{sfe} \tag{7.29}$$

In the context of look-up-table, $\tilde{C}$ is the table parameter for the look-up-table in C space. Satisfying this constraint forms the basis of the re-mapping procedure which is applied to each of the look-up-tables for temperature, density, species mass fraction and progress variable source term.

The re-mapping procedure developed in the present work is as follows:
For every combination of $\tilde{Z}$ and $\widetilde{Z''^2_{norm}}$ which are common to both λ space and C space tables,

Step: 1 Values of $\tilde{C}_{sfe}$ are extracted for the entire range of $\tilde{\lambda}$ from its look-up-table in λ space. Similarly values of the scalars, temperature, density, species mass fractions and progress variable source term are extracted from their respective look-up-tables in λ space. In Fig 7.10, 3D look-up-tables for $\tilde{C}_{sfe}$ and $\tilde{T}$ are shown. Also, the extraction of values from each look-up-table has been illustrated through dashed lines corresponding to the combination of $\tilde{Z} = 0.6$ and $\widetilde{Z''^2_{norm}} = 0.4$. Both the look-up-table structures have been colored by the contours of $\tilde{\lambda}$ and it can be observed that the lowest point of the dashed line corresponds to the point $\tilde{\lambda} = 0$ while the top most point corresponds to $\tilde{\lambda} = 1$ and thus the dashed line covers the entire range of $\tilde{\lambda}$. The extracted values for $\tilde{C}_{sfe}$ and $\tilde{T}$ are shown in Fig. 7.11.

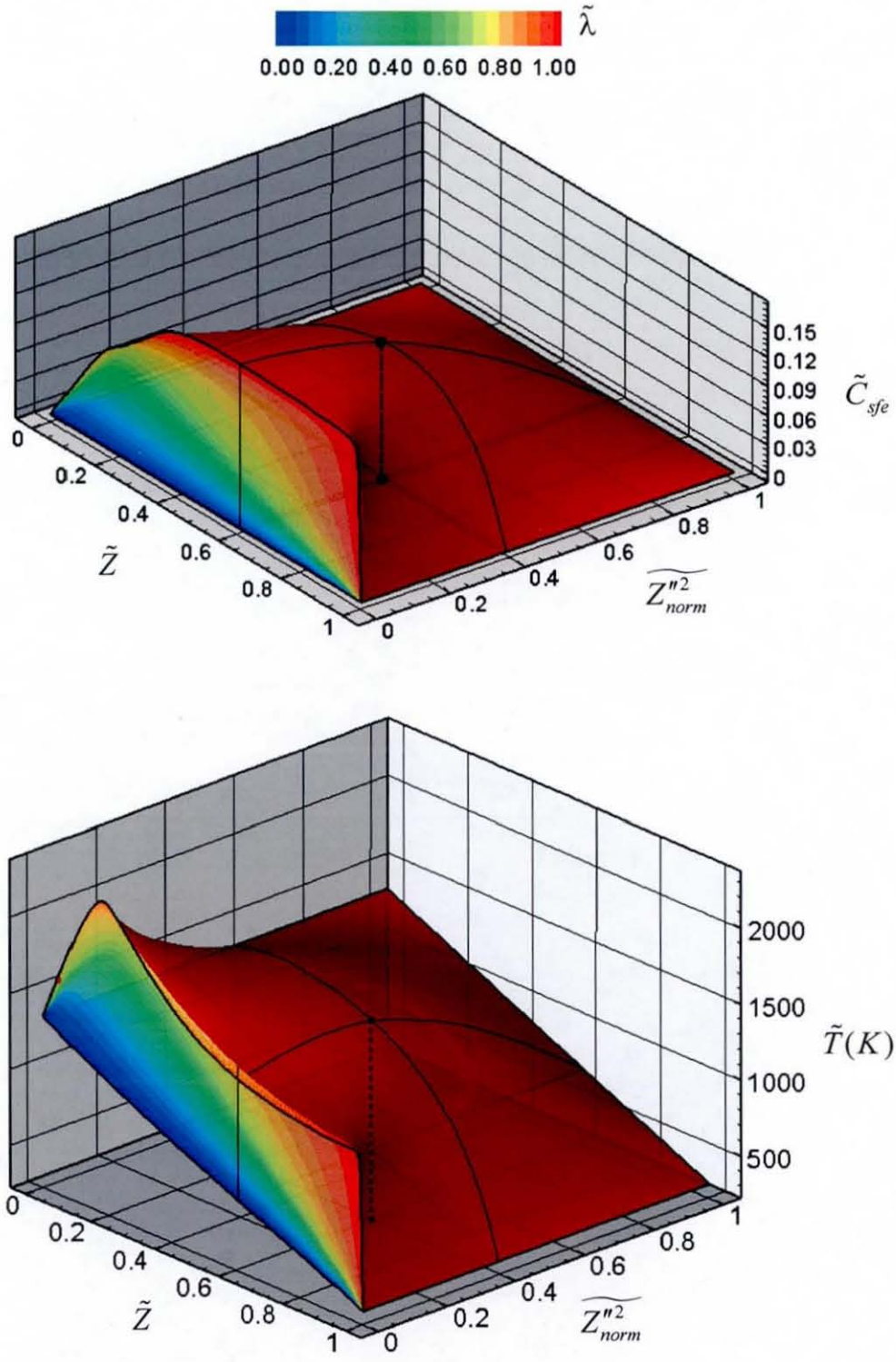

Figure 7.10: The 3D look-up-tables in λ space generated for Berkeley flame conditions. Structures of mean progress variable (top) and temperature (bottom) colored by the mean flamelet parameter.

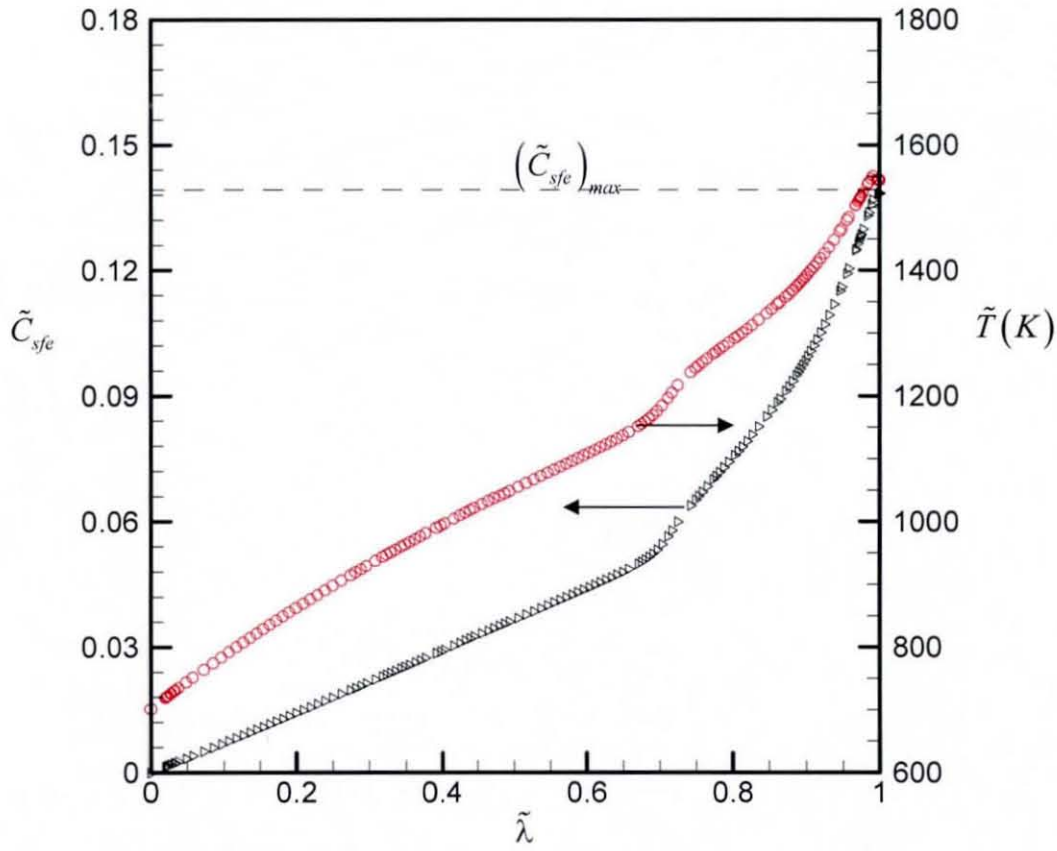

Figure 7.11 Extracted scalar data as a function of $\tilde{\lambda}$ for $\tilde{Z} = 0.6$ and $\widetilde{Z''^2_{norm}} = 0.4$.

Step 2: Satisfying the constraint $\tilde{C} = \tilde{C}_{sfe}$ means that $\tilde{C} = \tilde{C}\left(\tilde{\lambda}\right)$ is now available from the extracted data for $\tilde{C}_{sfe}$. Hence, for every ordered value of the table parameter $\tilde{C}$, the corresponding value of $\tilde{\lambda}$ is obtained by interpolating the extracted data for $\tilde{C}_{sfe}$. Using the interpolated value of $\tilde{\lambda}$, corresponding values of each scalar is obtained by interpolating its extracted data. For example, the extracted data for $\tilde{T}$ (Fig. 7.11) provides $\tilde{T} = \tilde{T}\left(\tilde{\lambda}\right)$ which facilitates interpolation. Thus, for every ordered value of $\tilde{C}$, the scalars $\tilde{T}, \overline{\rho}, \tilde{Y}_i$ and $\tilde{\dot{\omega}}_c$ are known at the given $\tilde{Z}$ and $\widetilde{Z''^2_{norm}}$. In cases where the extracted data for $\tilde{C}_{sfe}$ does not cover the entire range of $\tilde{C}$, all the values of $\tilde{C} > \left(\tilde{C}_{sfe}\right)_{max}$ are made to correspond to $\tilde{\lambda} = 1.0$. The extracted data shown in Fig 7.11 is a typical case where the extracted data for $\tilde{C}_{sfe}$ ranging from 0 to 0.136, does not cover the complete range of $\tilde{C}$ which varies from 0 to 0.17. Hence for each value of

$\tilde{C}$>0.136, the corresponding values of $\tilde{\lambda}$ are set equal to 1.0 and the scalar data corresponding to $\tilde{\lambda}=1.0$ is subsequently obtained.

Thus, by looping over each combination of $\tilde{Z}$ and $\widetilde{Z''^2_{norm}}$ and performing the operations in **steps 1&2**, the look-up-tables for the scalars $\tilde{T}, \overline{\rho}, \tilde{Y}_i$ and $\tilde{\dot{\omega}}_c$ are obtained in C space:

$$\tilde{T}=\tilde{T}\left(\tilde{Z},\widetilde{Z''^2_{norm}},\tilde{C}\right);\ \overline{\rho}=\overline{\rho}\left(\tilde{Z},\widetilde{Z''^2_{norm}},\tilde{C}\right);\ \tilde{Y}_i=\tilde{Y}_i\left(\tilde{Z},\widetilde{Z''^2_{norm}},\tilde{C}\right) \qquad (7.30)$$

$$\tilde{\dot{\omega}}_c=\tilde{\dot{\omega}}_c\left(\tilde{Z},\widetilde{Z''^2_{norm}},\tilde{C}\right)$$

7.4.2 Pre-PDF FPV β

Similar to Pre-PDF FPV δ, the inputs to be specified to this tool include the complete set of steady flamelets parameterized by the normalized flamelet parameter λ_n and the properties for two tables. The table in the λ space is parameterized by 4 variables, $\tilde{Z},\widetilde{Z''^2_{norm}},\tilde{\lambda}$ and additionally $\widetilde{\lambda''^2_{norm}}$ while the table in C space is parameterized by $\tilde{Z},\widetilde{Z''^2_{norm}}$, $\tilde{C}$ and $\widetilde{C''^2_{norm}}$.

The range, number of points and their distribution for $\tilde{Z}$, $\widetilde{Z''^2_{norm}}$, $\tilde{\lambda}$ and $\tilde{C}$ are identical to those specified for Pre-PDF FPV δ. The absolute variance of λ_n is given by $\widetilde{\lambda''^2}$ and it varies from 0 to $\tilde{\lambda}(1-\tilde{\lambda})$ given that the maximum value of $\tilde{\lambda}$ is 1. However, for tabulation purposes a normalized variance $\widetilde{\lambda''^2_{norm}}=\widetilde{\lambda''^2}/\tilde{\lambda}\left(1-\tilde{\lambda}\right)$ which varies from 0 to 1 is used. The absolute variance of progress variable $\widetilde{C''^2}$ is as well normalized by its maximum value which in this case is $\tilde{C}\left(\tilde{C}_{max}-\tilde{C}\right)$ with $\tilde{C}_{max}=0.17$. Thus, the normalized progress variable variance $\widetilde{C''^2_{norm}}=\widetilde{C''^2}/\tilde{C}\left(0.17-\tilde{C}\right)$ varies from 0 to 1.A total of 31 uniformly distributed points have been selected to cover the range for $\widetilde{\lambda''^2_{norm}}$ and $\widetilde{C''^2_{norm}}$. Thus, the calculations are carried out for 4D look-up-tables of size 163x51x151x31 ($\tilde{Z}\times\widetilde{Z''^2_{norm}}\times\tilde{\lambda}\ or\ \tilde{C}\times\widetilde{\lambda''^2_{norm}}\ or\ \widetilde{C''^2_{norm}}$).

Numerical integration

Approximated form of Eq.7.25 is numerically integrated for each scalar of interest within each cell in the 4D table. Adopting β function for $\tilde{P}(\lambda)$, the Eq. 7.25 takes the form:

$$\tilde{\phi} = \int_0^1 \int_0^1 \phi(Z;\lambda_n)\beta\left(Z;\tilde{Z},\widetilde{Z''^2}\right)\beta\left(\lambda_n;\tilde{\lambda},\widetilde{\lambda''^2}\right)d\lambda_n dZ \qquad (7.31)$$

Both the mixture fraction and flamelet parameter integrals carrying the β function are evaluated using the same procedure as the one described for mixture fraction integral in SLFM in section 7.1.3. The numerical integrations are carried out for all the scalars computed in Pre-PDF FPV δ i.e. the density ρ, temperature T and species mass fractions Y_i, progress variable C and its source term $\dot{\omega}_c$. Again, the mean progress variable computed here is referred by $\tilde{C}_{sfe}$ to differentiate it from the table parameter $\tilde{C}$. In addition to these scalars, two more quantities need to be calculated and they are the variance of progress variable $\widetilde{C''^2}_{sfe}$ and the covariance or correlation of the progress variable and its source term $\widetilde{C''\dot{\omega}_c''}$. These quantities are evaluated from the equations:

$$\widetilde{C''^2}_{sfe} = \int_0^1 \int_0^1 \left(C(Z;\lambda_n)-\tilde{C}_{sfe}\right)^2 \beta\left(Z;\tilde{Z},\widetilde{Z''^2}\right)\beta\left(\lambda_n;\tilde{\lambda},\widetilde{\lambda''^2}\right)d\lambda_n dZ \qquad (7.31)$$

$$\widetilde{C''\dot{\omega}_c''} = \int_0^1 \int_0^1 \left(C(Z;\lambda_n)-\tilde{C}_{sfe}\right)\left(\dot{\omega}_c(Z;\lambda_n)-\tilde{\dot{\omega}}_c\right)\beta\left(Z;\tilde{Z},\widetilde{Z''^2}\right)\beta\left(\lambda_n;\tilde{\lambda},\widetilde{\lambda''^2}\right)d\lambda_n dZ \qquad (7.32)$$

Thus, the following 4D look-up-tables are computed in λ space:

$$\bar{\rho} = \bar{\rho}\left(\tilde{Z},\widetilde{Z''^2_{norm}},\tilde{\lambda},\widetilde{\lambda''^2_{norm}}\right);\tilde{T} = \tilde{T}\left(\tilde{Z},\widetilde{Z''^2_{norm}},\tilde{\lambda},\widetilde{\lambda''^2_{norm}}\right);\tilde{Y}_i = \tilde{Y}_i\left(\tilde{Z},\widetilde{Z''^2_{norm}},\tilde{\lambda},\widetilde{\lambda''^2_{norm}}\right) \qquad (7.33)$$

$$\tilde{C}_{sfe} = \tilde{C}_{sfe}\left(\tilde{Z},\widetilde{Z''^2_{norm}},\tilde{\lambda},\widetilde{\lambda''^2_{norm}}\right);\tilde{\dot{\omega}}_c = \tilde{\dot{\omega}}_c\left(\tilde{Z},\widetilde{Z''^2_{norm}},\tilde{\lambda},\widetilde{\lambda''^2_{norm}}\right);$$

$$\widetilde{C''^2}_{sfe} = \widetilde{C''^2}_{sfe}\left(\tilde{Z},\widetilde{Z''^2_{norm}},\tilde{\lambda},\widetilde{\lambda''^2_{norm}}\right);\widetilde{C''\dot{\omega}_c''} = \widetilde{C''\dot{\omega}_c''}\left(\tilde{Z},\widetilde{Z''^2_{norm}},\tilde{\lambda},\widetilde{\lambda''^2_{norm}}\right)$$

Re-Mapping

The re-mapping procedure for 4D tables is developed on a basis similar to that for the 3D look-up-tables in Pre-PDF FPV δ. In Chapter 5, Section 5.5.2, two constraint equations (Eq. 5.54) have been presented and it has been mentioned that that these two equations should be satisfied for the FPV β function model to be consistent and by means of satisfying both the constraints, the need to calculate $\tilde{\lambda}$ and $\widetilde{\lambda''^2}$ in LES or RANS can be eliminated. Thus, with the FPV β function model,

$$\tilde{C} = \tilde{C}_{sfe} \quad \text{and} \quad \widetilde{C''^2} = \widetilde{C''^2}_{sfe} \tag{7.34}$$

In the context of look-up-table, $\tilde{C}$ and $\widetilde{C''^2}$ represent the table parameters for the look-up-table in C space while $\tilde{C}_{sfe}$ and $\widetilde{C''^2}_{sfe}$ represent the values obtained from the integration of the steady flamelets.

The re-mapping procedure for the 4D look-up-tables is as follows:
For every combination of $\tilde{Z}$ and $\widetilde{Z''^2_{norm}}$ which are common to both the λ space and C space tables, the following operations are performed:

Step 1: Values of $\tilde{C}_{sfe}$ and $\widetilde{C''^2}_{sfe}$ are extracted for the entire range of $\tilde{\lambda}$ and $\widetilde{\lambda''^2_{norm}}$ from their respective look-up-tables in λ space. Similarly, data is extracted for all the other scalars as a function of $\tilde{\lambda}$ and $\widetilde{\lambda''^2_{norm}}$. In the present context of the 4D tables, each of the 3D look-up-tables shown in Fig. 7.10 can be regarded as the limiting case where $\widetilde{\lambda''^2_{norm}} = 0$.

Step 2: A schematic of the extracted data for each variable stored as a function of $\tilde{\lambda}$ and $\widetilde{\lambda''^2_{norm}}$ is shown by the 2D array in Fig. 7.12. Satisfying the two constraint equations implies that for every combination of the values of the table parameters $\tilde{C}$ and $\widetilde{C''^2_{norm}}$, corresponding combination of values of $\tilde{\lambda}$ and $\widetilde{\lambda''^2_{norm}}$ can be obtained by performing interpolations on the $\tilde{C}_{sfe}$ and $\widetilde{C''^2}_{sfe}$ data sets. The interpolations for every combination of $\tilde{C}$ and $\widetilde{C''^2_{norm}}$ is further divided into 3 steps.

Step 2.1: Interpolation is first performed for the given value of $\tilde{C}$ in each row of the 2D array shown in Fig 7.13a to obtain corresponding value of $\tilde{\lambda}$. The output (Fig 7.13b) is a one dimensional array of interpolated values of $\tilde{\lambda}$ denoted by $\tilde{\lambda}*$ each of which corresponds to $\tilde{C}$ but at different values of $\widetilde{\lambda_{norm}^{''2}}$.

Step 2.2: Using the $\tilde{\lambda}*$ array, corresponding $\widetilde{C''^2}_{sfe}*$ is obtained by interpolating the $\widetilde{C''^2}_{sfe}$ data. The output of this operation (Fig. 7.13c) is a one dimensional array of $\widetilde{C''^2}_{sfe}*$ stored as a function of $\widetilde{\lambda_{norm}^{''2}}$.

Step 2.3: Interpolation is now performed for the value $\widetilde{C_{norm}^{''2}}$ using $\widetilde{C''^2}_{sfe}*$ data to find the corresponding $\widetilde{\lambda_{norm}^{''2}}$ value denoted by $\widetilde{\lambda_{norm}^{''2}}*$.

Step 2.4: Finally, by back tracking, the value of $\tilde{\lambda}*$ which corresponds to $\widetilde{\lambda_{norm}^{''2}}*$ and denoted by $\tilde{\lambda}**$ is found. The values $\tilde{\lambda}**$ and $\widetilde{\lambda_{norm}^{''2}}*$ are a unique combination obtained for the given $\tilde{C}$ and $\widetilde{C_{norm}^{''2}}$. Thus, the task of obtaining obtained the values of $\tilde{\lambda}$ and $\widetilde{\lambda_{norm}^{''2}}$ corresponding to every combination of $\tilde{C}$ and $\widetilde{C_{norm}^{''2}}$ is accomplished.

Values for the scalars, $\overline{\rho}, \tilde{T}, \widetilde{Y_i}, \widetilde{\dot{\omega}_c}$ and $\widetilde{C''\dot{\omega}_c''}$ are obtained for each combination of $\tilde{C}$ and $\widetilde{C_{norm}^{''2}}$, by performing interpolations of their respective 2D arrays for $\tilde{\lambda}$ corresponding to $\tilde{\lambda}**$ and $\widetilde{\lambda_{norm}^{''2}}$ corresponding to $\widetilde{\lambda_{norm}^{''2}}*$.

Looping over each combination of $\tilde{Z}$ and $\widetilde{Z_{norm}^{''2}}$ and performing the operations in **steps 1&2**, the 4D look-up-tables for the scalars $\overline{\rho}, \tilde{T}, \widetilde{Y_i}, \widetilde{\dot{\omega}_c}$ and $\widetilde{C''\dot{\omega}_c''}$ which are of interest in LES and RANS computations are remapped to C space.

	$\tilde{\lambda}$				
		0	·	·	·	1
$\widetilde{\lambda_{norm}^{''2}}$	0	$\tilde{C}_{sfe}(0,0)$ $\widetilde{C''^2}_{sfe}(0,0)$ $\tilde{\phi}(0,0)$	·	·	·	$\tilde{C}_{sfe}(1,0)$ $\widetilde{C''^2}_{sfe}(1,0)$ $\tilde{\phi}(1,0)$
	·	·	·	·	·	·
	·	·	·	·	·	·
	·	·	·	·	·	·
	1	$\tilde{C}_{sfe}(0,1)$ $\widetilde{C''^2}_{sfe}(0,1)$ $\tilde{\phi}(0,0)$	·	·	·	$\tilde{C}_{sfe}(1,1)$ $\widetilde{C''^2}_{sfe}(1,1)$ $\tilde{\phi}(0,1)$

Figure 7.12: 2D array of data extracted for each variable from their respective look-up-tables in λ space for a given $\tilde{Z}$ and $\widetilde{Z_{norm}^{''2}}$. Scalars represented by $\tilde{\phi} = \left(\overline{\rho}, \tilde{T}, \tilde{Y}_i, \tilde{\dot{\omega}}_c, \widetilde{C''\dot{\omega}_c''}\right)$

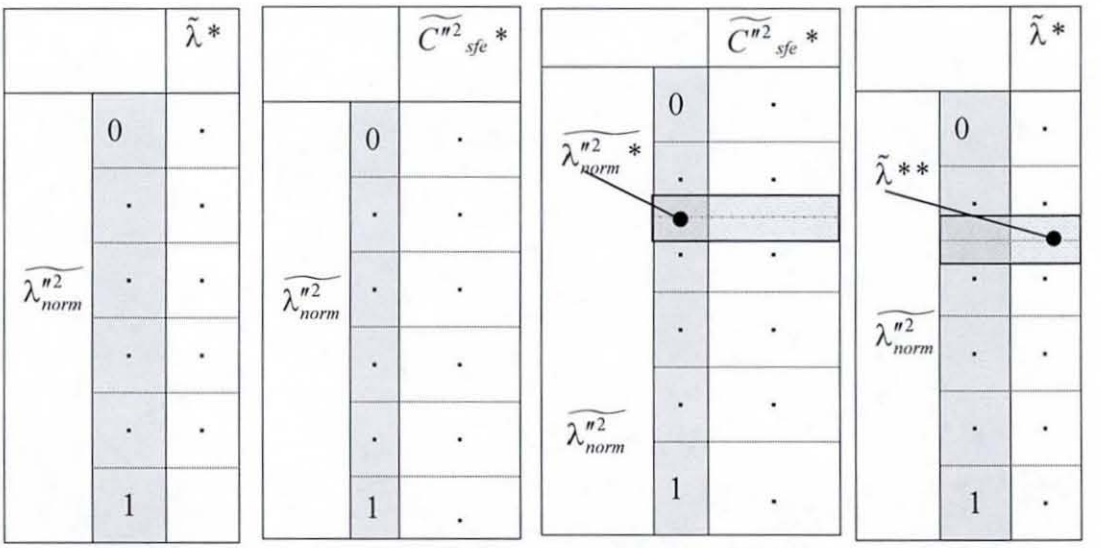

(b) Obtain $\tilde{\lambda}$* array: Values of $\tilde{\lambda}$ corresponding to a given $\tilde{C}$ in each row of the 2D array

(b) Obtain $\widetilde{C''^2}_{sfe}$* array: Values of $\widetilde{C''^2}_{sfe}$ corresponding to each value of $\tilde{\lambda}$* in array

(d) Obtain $\widetilde{\lambda_{norm}^{''2}}$*: Value of $\widetilde{\lambda_{norm}^{''2}}$ corresponding to $\widetilde{C''^2}_{sfe}* = \widetilde{C_{norm}^{''2}}$

(e) Obtain $\tilde{\lambda}$**: Value of $\tilde{\lambda}$* corresponding to $\widetilde{\lambda_{norm}^{''2}} = \widetilde{\lambda_{norm}^{''2}}$*

Figure 7.13: Steps involved in obtaining a unique combination of values for $\tilde{\lambda}$ and $\widetilde{\lambda_{norm}^{''2}}$ corresponding to every combination of $\tilde{C}$ and $\widetilde{C_{norm}^{''2}}$

Chapter 8

Modelling of Turbulent Non-premixed Bluff-body and Jet flames

Turbulent non-premixed flames for which experimental data is readily available, have been modelled in RANS to assess the performance of the non-adiabatic model along with its steady and unsteady NO submodels, implemented in the in-house RANS code. The predictive capability of the non-adiabatic model in conjunction with non-adiabatic steady and unsteady NO submodels has been validated against experiments as well as predictions from its adiabatic counterpart, SLFM. The modelling work also provided a means of verifying the overall accuracy of numerical implementation of the different models (turbulence and combustion) and strategies.

The Sydney CH_4/H_2 bluff-body stabilized flames (Dally *et al.*, 1998a, 2003) and the Sandia D piloted jet flame (Barlow and Frank, 1998; Schneider *et al.*, 2003) have been chosen as test cases. The Sydney bluff-body flames present themselves as ideal model problems for studies on turbulence-chemistry interaction since the complexity of the flow characteristics is close to that found in practical combustors while the geometry is simple and the boundary conditions are well-defined. Since, the fuel is based on the simplest of hydrocarbons, modelling studies are benefited from the availability of accurate chemical mechanisms. Moreover, the experimental data is available for flow, mixing field and compositional structure including the pollutant NO and thus they facilitate a comprehensive validation of the models. The bluff-body flames have thus been selected as target flames for the modelling community in the bi-annual Turbulent Non-Premixed Flames workshop (TNF). Details of the experimental set up for the bluff-body flames, conditions and observations on the general flame structure are first presented in section 8.1 of this chapter. In the current numerical study on bluff-body flames, performance has been assessed for the RST turbulence model using the steady laminar flamelet model which is basically an adiabatic formulation, the non-adiabatic flamelet models and the different NO

submodels (steady/unsteady, adiabatic/non-adiabatic). Results from the study are presented in section 8.2.

While the bluff-body flames did prove useful in evaluating the relative performance of different models, their weakly radiating nature demanded further validation of the non-adiabatic combustion model and its NO submodels on a relatively stronger radiative flame. The Sandia D piloted jet flame which is also one of the target flames in the TNF workshop has been chosen as the second test case as it not only offers all the modelling advantages which are associated with Sydney bluff-body but it is also has much simpler flow characteristics and more importantly exhibits relatively appreciable effects of radiation heat loss. Details of the experimental set up and conditions for the Sandia D flame are presented in section 8.3. The numerical computations were carried out with both adiabatic and non-adiabatic flamelet combustion models and steady and unsteady non-adiabatic NO submodels. Results obtained from the computations are discussed in section 8.4.

8.1 Experimental study of bluff-body stabilized flames

The bluff-body burner used for experimental investigation of the flames by Dally *et al.* (1998a; 2003) has an outer diameter, D, of 50 mm and a concentric jet diameter D_J of 3.6 mm. A wind tunnel with an exit cross section of 254 x 254 mm encloses the burner till the burner exit. Fig. 8.1 shows a schematic of the bluff-body flame along with measurement locations. The distance of these locations from exit of the burner is normalized by bluff-body diameter D. Single point Raman/Rayleigh/LIF technique has been used by Dally *et al.* (1998a) to measure temperature and the concentration of stable species CO_2, CO, H2O, H_2, O_2, N_2 as well as concentration of OH and NO. Comparisons of measurements with predictions from several numerical works (one such work is that of Hossain, 1999) in the past have shown significant disagreement in the CO mass fraction, with the Raman scattering measurements of CO being much higher than predictions from modelling. The Raman scattering measurements of CO in methane flames were found to suffer from laser-excited-interference from higher

hydrocarbons formed on the rich side of the flame. Hence, Dally *et al.* (2003) re-measured the CO mass fractions using two-photon laser induced fluorescence (TPLIF) technique. The updated CO data has been used for validations in the present work.

The bluff-body test cases adopted in the present work are the HM1e and HM1 flames. The fuel used in these flames is a mixture of 50% of CH_4 and 50% of H_2 by volume. Table 8.1 shows the experimental conditions for these two flames. It can be seen that the flames operate far from blow-off which is a pre-requisite for steady flamelets based models which are incapable of reproducing local extinction and re-ignition. The primary test case in the study is the HM1 flame for which experimental measurements in the form of radial profiles mixing field, temperature and compositional structure are available. Although measurements were initially made available for mean and fluctuations of velocity for HM1 conditions, the accuracy of measurements was called into question and hence to provide more reliable mean velocity data, velocity measurements have been repeated although with slightly different velocity conditions resulting in the HM1e flame. However, both HM1 and HM1e correspond to the same blow-off limit and the differences in inlet velocities have negligible effect on the mixing field, temperature and compositional structure. Thus, in the present work, simulations for HM1e conditions were conducted solely for validation of flowfield while the bulk of the validations required the use of HM1 conditions.

Fuel	Flame	U_j(m/s) / U_c(m/s)	Re_j	%Blow off	T_{in} (K)	Z_{st}	T_{ad}(K)
CH_4 (1:1)	HM1	118/40	15800	50	298	0.05	2265
	HM1e	108/35	14461	50			

Table 8.1: Investigated Bluff-body flames and their conditions

8.1.1 Experimentally observed flame structure

The structure of a jet dominant (greater jet momentum) bluff-body stabilized flame is presented in Fig. 8.1. It is characterized by three distinct zones. The first zone consists of recirculation created by flow separation due to presence of bluff body.

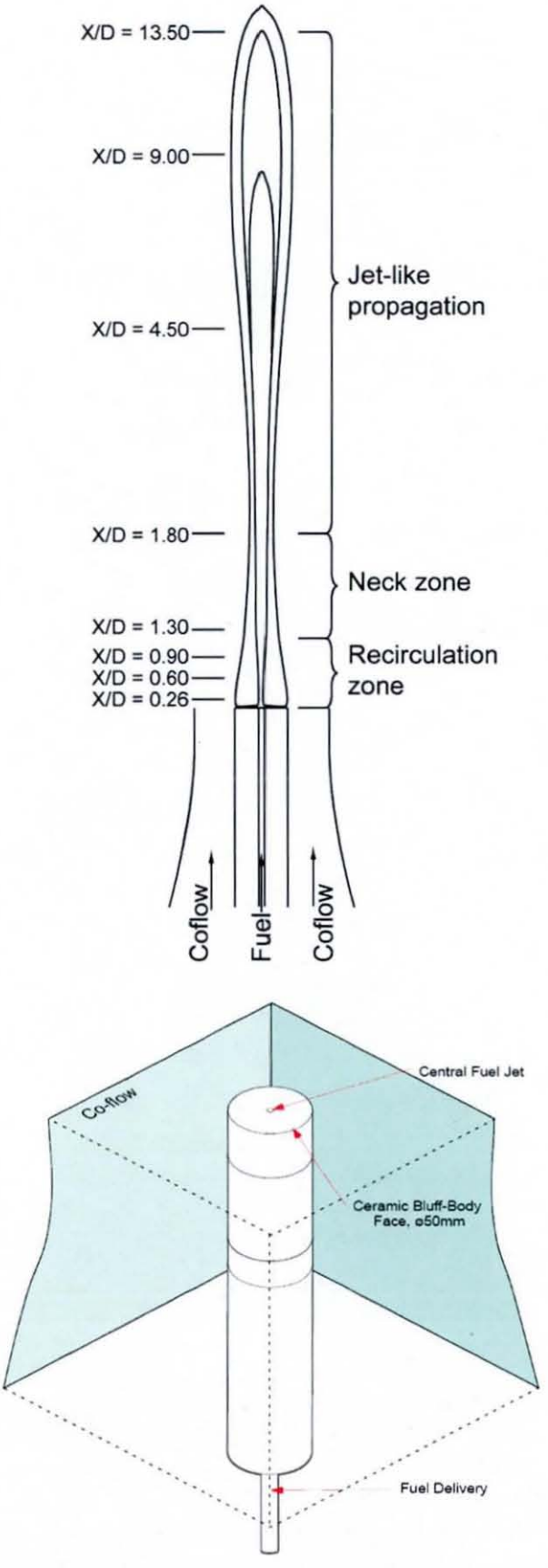

Figure 8.1: Schematic of bluff-body burner, and stabilized flame with measurement locations. (Bottom figure : www.aeromech.usyd.edu.au/thermofluids)

This recirculation zone facilitates stabilization of the flame as the hot products of combustion are made to mix with the reactants. This zone has an outer vortex close to the coflowing air and inner vortex (not shown in the figure) close to central fuel jet. Position of inner vortex is dependent upon the fuel jet velocity. It shifts downstream on increasing the velocity and at sufficiently high velocities it becomes part of the jet. Also, the outer vortex becomes shorter and smaller. Downstream of the recirculation zone is the region of intense mixing where local extinction and blow-off could occur when the fuel jet velocity is increased. This is termed as neck zone and is a region of particular importance for testing a combustion model for its accuracy in predicting extreme non-equilibrium effects like local extinction. The third zone behaves like a jet and at sufficiently high velocities shows re-ignition.

8.2 RANS modelling of HM1e & HM1 flames

The CH_4/H_2 bluff-body flames have been studied using the RANS modelling method by a number of researchers prior to the current work. Dally *et al.* (1998b) conducted numerical investigation of these flames to arrive at a modified k-ε model and Reynolds stress model which predict the spreading rate of the jet better than the standard models. The modification involved replacing the standard value of the constant $C_{\varepsilon 1}$ in dissipation rate equation from 1.4 to 1.6. Merci *et al.* (2001) investigated the bluff-body diffusion flame with a new cubic turbulence model based on non-linear eddy viscosity approach. Li *et al.* (2003) tested Reynolds stress model based turbulence closure on HM1e flame with different pressure-strain models and found that the 'Isotropization of production' model with the modified $C_{\varepsilon 1}$ gives good agreement overall. Adopting the best practices advocated by these studies, the Reynolds stress and k-ε models used in the present work employ the same modification. The above works concentrated mainly on studying the sensitivity of accuracy of predictions to turbulence modelling techniques and hence employed only simple combustion models like fast chemistry and equilibrium chemistry with presumed PDF for mixture fraction. Relatively complex and comprehensive combustion modelling techniques have been adopted for the bluff-body flames by several other researchers.

Liu *et al.* (2005) employed the Joint PDF model with augmented reduced mechanism for the bluff-body flames with varying blow-off limits. They found quite good agreement with experimental data for the flame far from extinction in regard to temperature, major and minor species including CO and OH. However, NO was overpredicted. Kim and Huh (2002) applied the CMC model to study bluff-body methane-hydrogen diffusion flames with three different chemical mechanisms including GRI 2.11 and found overprediction of NO in all the three cases although GRI 2.11 was the best amongst the three. Hossain *et al.* (2001) conducted investigation on the HM1 flame using steady laminar flamelet and a non-adiabatic flamelet model based on enthalpy defect to investigate the effect of radiation heat loss on the thermo-chemical structure. They employed a reduced mechanism of Peters (1993) for hydrocarbon chemistry and the turbulence was modelled by the modified k-ε model. They found that the consideration of radiation heat loss has minimal effects on the compositional structure of flame. However, effects of radiation heat loss on the pollutant NO were not tested and the non-adiabatic flamelet model did not include the effects of scalar dissipation rate on the thermo-chemical structure of the turbulent flame. In a separate study with steady flamelet model in conjunction with modified k-ε model and reduced hydrocarbon chemistry, Hossain and Malalasekera (2003) conducted study on NO with a 3 step thermal NO mechanism and found significant underprediction thereby underlining the need for a detailed account of NO reaction pathways. Another relatively recent work which employed steady laminar flamelet model is that of Yan *et al.* (2004) who assessed the influence of turbulence model on combustion calculations. They found that the explicit algebraic stress model and k-ε model with varied anisotropy parameter perform better than standard k-ε model from comparisons of mixing field, temperature and major species.

Present modelling of the bluff-body flames differs from the reviewed works in that it uses for the first time, the conjunction of flamelet model (adiabatic and non-adiabatic) based on detailed chemistry and Reynolds stress transport (RST) model. A combination which is expected to be of practical interest since it strikes the right balance between accuracy and computational efficiency. It is noteworthy that the RANS predictions from HM1e and HM1 flames simulated in the current study using steady (adiabatic) laminar flamelet model and RST turbulence closure have provided

new contributions (Ravikanti and Malalasekera, 2006) to the modelling database at the TNF 8 workshop (2006).

The set of simulations that have been carried out on HM1e and HM1 flames and the specific models that have been used for each simulation have been listed in Table 8.2. The motive behind these simulations is to not only verify the prediction capability of non-adiabatic flamelet model and its NO submodels against their adiabatic counterparts, but also to study the individual effects of considering radiation heat loss and transient effects on the pollutant NO. In addition, the sensitivity of predictions to the adopted chemical mechanism has also been verified. All the simulations listed in the table have been performed on the same computational domain and grid which has been tested for grid independence and the details are presented in the following subsections.

8.2.1 Computational domain & boundary conditions

Considering the fact that the bluff body flames of interest are axisymmetric, computations have been restricted to 2D axisymmetric domain shown in the Fig 8.2. The domain extends in axial direction by 220mm (~4.5D, D=diameter of bluff-body) and in radial direction by 172mm (~3.5D). The axial domain is split into two regions. A region downstream of the burner exit or face of the bluff-body (x/D>0) where the flame stabilizes and a region upstream of the burner exit (x/D<0) which is specifically meant for generating fully developed flow conditions at the burner exit. Both fuel and co-flow inlets have been extended by a distance of 100mm upstream of the exit of the burner. Although, experimental flow profiles are available at the burner exit, fully developed flow profiles have been preferred in previous studies (Dally *et al.*,1998b; Hossain, 1999) since the experimental profiles seem to under predict mean mass flow rate and momentum of the fuel jet thereby resulting in discrepancy in radial velocity profiles. Infact, the use of fully developed flow profiles is justified since the fuel jet pipe extends 40 diameters upstream of the exit in the experimental configuration. Fully developed flow profiles could be specified at the burner exit using power-law approximations however, the extended inlet has been preferred in the present work to ensure minimum influence of inlet conditions on the predicted results.

Case No.	Flame	Turbulence model	Combustion model	NO submodel	Radiation sub model	Compare	To Evaluate
1	HM1e	**mod. k-ε**	SLFM	not applicable	not applicable		
2	HM1e	**RST**	SLFM	not applicable	not applicable	with 1	1. Performance gain with use of RST. 2. Accuracy of RST implementation.
3	HM1	RST	**SLFM Peters Mec.**	**SLFM-NO-TRE**	not applicable		
4	HM1	RST	**SLFM GRI3.0 Mec.**	**SLFM-NO-TRE**	not applicable		
5	HM1	RST	**SLFM San-Diego Mec.**	**SLFM-NO-TRE**	not applicable		
6	HM1	RST	**SLFM (Default: GRI 2.11)**	**SLFM-NO-TRE**	not applicable	with 3,4&5	Influence of chemical mechanism on the predictions of overall flame structure, particularly NO.
Note: The GRI 2.11 has been used as the standard (default) chemical mechanism							
7	HM1	RST	**NADS**	**NADS-NO-TRE**	DTRM		
8	HM1	RST	**NADM**	**NADM-NO-TRE**	DTRM	with 6&7	1. Performance of the non-adiab. combustion models and NO sub models in comparison to their adiab. counterparts. 2. Impact of radiation heat loss on overall flame structure, particularly NO. 3. Impact of scalar dissipation rate effects.
9	HM1	RST	**NADM**	**NADM-EPFM**	DTRM	with 8	1. Performance difference between steady and unsteady (EPFM) NO submodels. 2.Impact of transient effects on NO.

Table: 8.2: List of RANS Simulations carried for bluff-body stabilized flames using a grid of 162x111 (axial x radial) nodes.

An extended inlet is of particular advantage when dealing with RST model where isotropic turbulence can be imposed along with plug flow at the inlets and fully developed mean flow and Reynolds stresses can be obtained at the burner exit.

At the extended inlet of both fuel jet and co-flow, uniform mean velocities (plug flow) have been specified. Turbulence at inlet has been specified in terms of length scale (0.07x radius of pipe) and intensity, taken as 1%. Turbulent kinetic energy and dissipation rate are subsequently derived. In regard to Reynolds stresses, isotropy has been assumed at inlet for the normal stresses while the shear stress has been considered to be zero. Along the axis of symmetry and co-flow boundary, symmetry conditions have been specified. At the bluff-body walls, no-slip boundary condition has been employed along with log-law based wall-functions. At the cells immediately next to the wall, the Reynolds stresses have been specified as fraction of near wall turbulent kinetic energy (relationships given in Eq .4.34).

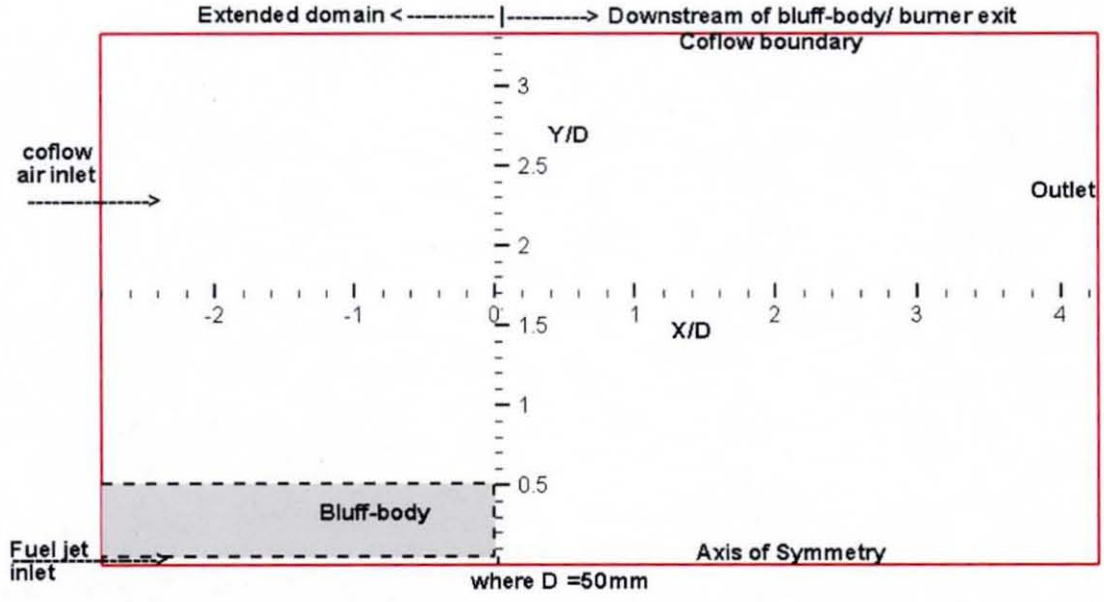

Figure 8.2: Computational domain for RANS modelling of HM1e & HM1 flames.

8.2.2 Computational grid

The grid used for all the computations (listed in Table 8.2) is shown in Fig. 8.3. The grid consists of 162 nodes along axial and 111 nodes in the radial directions with a non-uniform spacing in both directions. In the radial direction, the spacing of the nodes is such that the fuel pipe and the face of the bluff-body are finely resolved by

11 and 55 nodes respectively. In the axial direction as well the nodes are closely spaced near the face of the bluff body and expand towards the exit. Thus, it is ensured that the flame stabilization region where steep gradients in the flame are expected is well resolved. This grid has been tested to produce grid independent results upon comparison of its flow field predictions with those from a coarser and finer grid. The coarser grid consists of 162x89 (axial x radial) nodes while the finer grid consists of 234 x 145 (axial x radial) nodes.

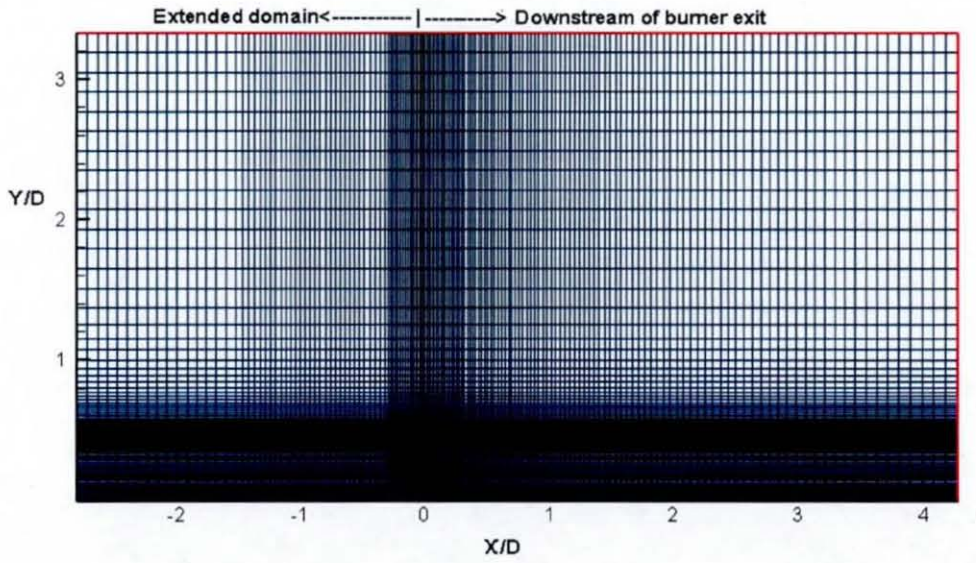

Figure 8.3: Computational grid for RANS modelling of HM1e & HM1 flames. Grid consists of 162 axial nodes and 111 radial nodes.

Results of the grid independence test are shown in Fig 8.4 where the measured radial profiles of mean axial velocity, radial velocity and rms of their fluctuations for HM1e flame have been compared to the predictions from all the three grids. The reacting flow computations have been carried with SLFM in conjunction with RST model for turbulence closure. Predictions from the medium (162x111) and fine (234x145) grids are indistinguishable and are consistently better than the coarser grid (162x89). It is encouraging that a fairly moderate refinement of the coarser grid to medium grid which corresponds to negligible increase in cost of computation, results in notable improvement in the mean radial velocity and the rms distributions. Further refinement of medium grid to the finer grid is certainly not justifiable as the improvements (if any) are negligible. Thus, the use of medium grid for all the calculations is justified.

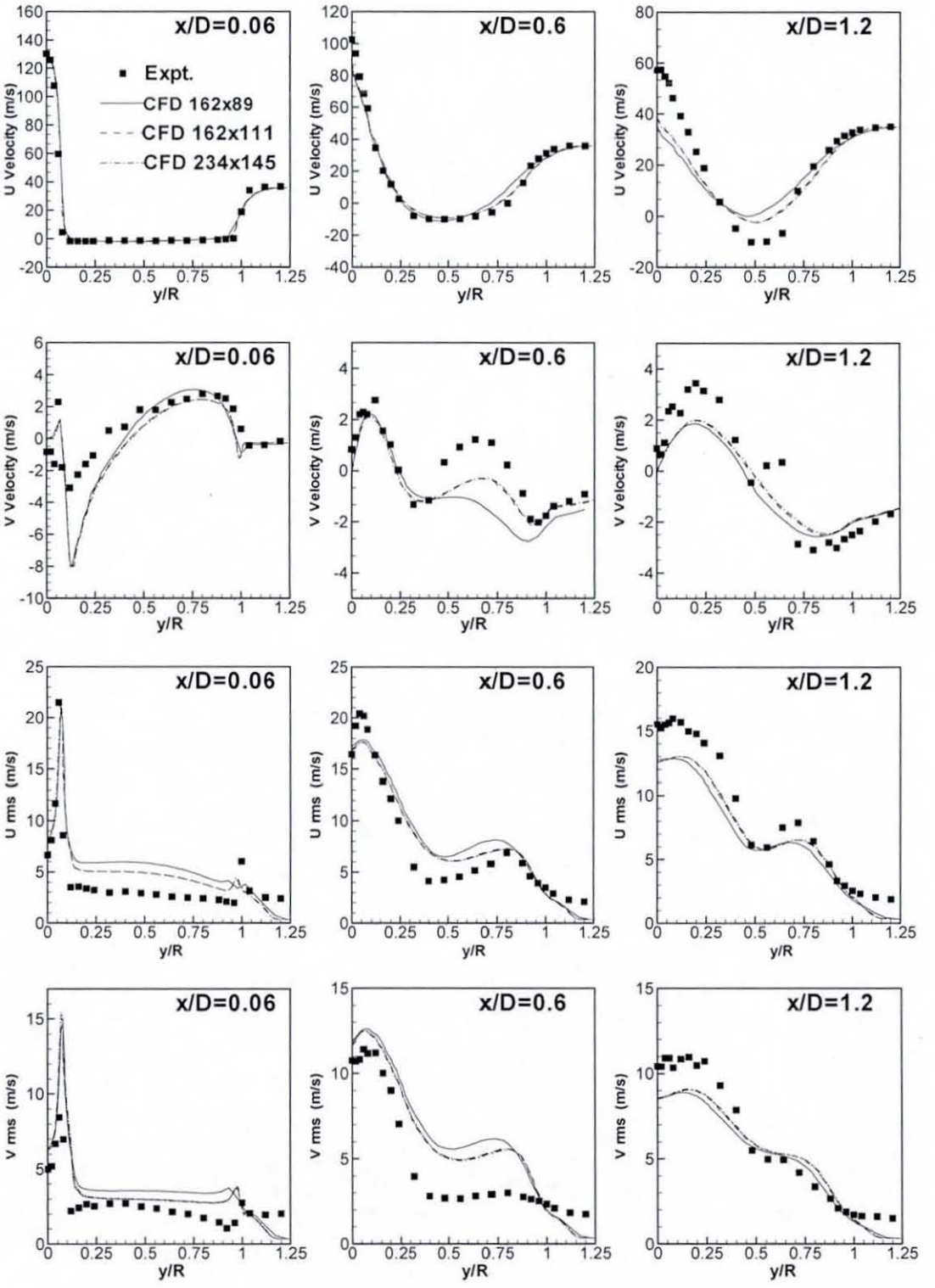

Figure 8.4: HM1e radial profiles of mean and rms fluctuations of axial (U) and radial (V) velocities. Comparison for grid independence test.

8.2.3 Adiabatic flamelet modelling: results & discussion

HM1e flame

Simulations of HM1e flame have been conducted primarily to validate the accuracy with which flow field is predicted by SLFM when used in conjunction with RST model for turbulence closure. In Fig. 8.5a&b, the general characteristics of the bluff-body flame have been presented. The flow comprises of a double-vortex structure within the recirculation zone formed downstream of the bluff-body face. The double vortex comprises of an inner vortex close to the fuel jet and an outer vortex between the inner vortex and co-flow air. The vortex structures result in three distinguishable shear layers. An inner or first shear layer which is a manifestation of the contact between the high velocity fuel jet and the recirculating inner flow of inner vortex. Middle or second shear layer which occurs between the inner portion of the flow in the outer vortex and outer portion of flow in the inner vortex. The third or outer shear layer which occurs between the co-flow stream and the outer part of outer vortex.

The double vortex structure as a whole, controls the flow and mixing patterns. Stabilization of the flame is driven by the recirculation of the hot products of combustion back to the burner exit plane. Thus the recirculation provides a conducive environment with continuous ignition source for the flame. The stabilization of the flame at the face of the bluff-body can be observed from the temperature contours (Fig. 8.5b). Within the recirculation zone, stoichiometric mixture fraction in the recirculation zone lies near to the outer edge of the outer vortex and the flame temperature is maximum here. However, downstream of the recirculation zone, in the neck zone, non-equilibrium effects are expected to be influential and calculations can be observed to capture the effect on temperature. Along the stoichiometric line in the neck region (x/D~1.3 to 2.0) the temperature is significantly reduced compared to that within the recirculation zone. Beyond the recirculation zone, flow can be seen to mimic a simple jet. These predicted characteristics of the flame are inline with the experimental observations of Dally *et al.* (1998a).

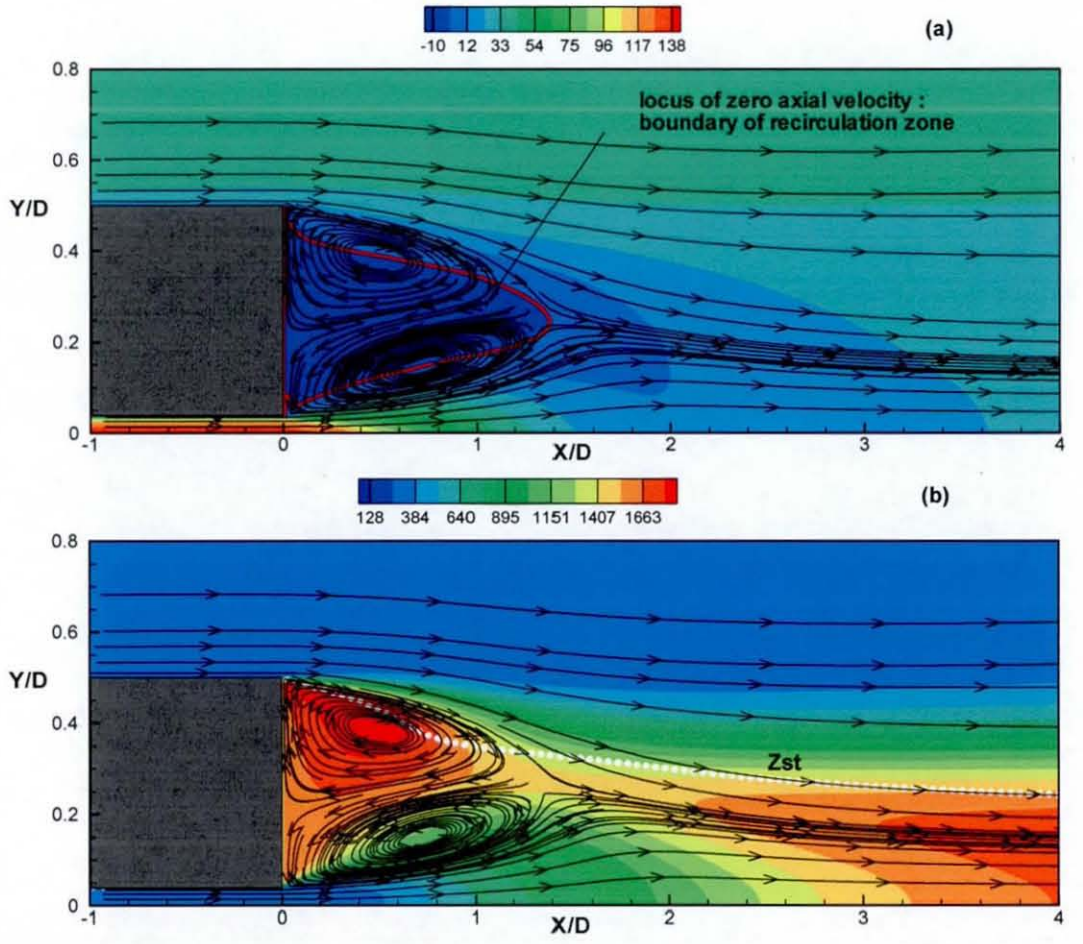

Figure 8.5: HM1e flame (a) axial velocity (m/s) and (b) temperature (k) contours superimposed with streamlines. RANS predictions from SLFM in conjunction with RST model for turbulence closure.

The quantitative match between the predictions and measurements for the flow field is shown in Figs 8.6 and 8.7. Here, the predictions from SLFM simulation using the k-ε model with modified constant ($C_{\varepsilon 1}$=1.6) for turbulence closure is plotted as well, to verify the enhancement in predictive capability with the RST model. In the Fig.8.6, the comparison of radial profiles of mean axial velocity and radial velocity are shown. Predictions of mean axial velocity from both the RST and modified k-ε model are similar at all the axial locations of the flame. Predictions from both the models show good agreement with measurements till x/D =0.6 beyond which they start to deviate along the centerline. This is partly due to the tendency of both the models to overpredict the decay rate of centerline mean axial velocity and partly due to experimental errors induced due to velocity bias as reported by Dally *et al.* (1998b).

The comparisons also show that the length of the recirculation zone is somewhat underpredicted by both the models, the predicted length being ~1.4 bluff-body diameters while measured length is 1.6 bluff-body diameters. Comparisons of mean radial velocity profiles show that the RST model fares slightly better than the modified k-ε model with respect to the radial distribution close to the face of the bluff-body. Dally *et al.* (1998b) reported that the radial velocity component is more prone to experimental inaccuracies and scatter in the experimental data is evident from measurements at x/D=1.4. Predictions with both the turbulence models can thus be considered to be reasonably good.

In Fig. 8.7, the radial profiles of the rms of axial and radial velocity fluctuations are shown. Measurements show a double peaked structure for both the axial and radial fluctuations within the recirculation zone. The inner peak corresponds to the inner shear layer while the outer peak corresponds to the outer shear layer. With the fuel jet velocity almost three times higher than the co-flow velocity, the inner shear layer experiences more production of turbulence and hence greater level of fluctuations than the outer. The anisotropy in the turbulence can be observed from the relative magnitudes of the measured peak fluctuations in axial and radial components. For all the stations within the recirculation zone (X/D < = 1.4) the measured peak axial fluctuations corresponding to the inner shear layer are 1.5 to 2 times higher than the radial fluctuations. The RST model accounts for this anisotropy reasonably well although the axial fluctuations are predominantly underpredicted while radial fluctuations are overpredicted for x/D < 0.6 and underpredicted thereafter. A similar behaviour in radial predictions has also been reported by Li *et al.* (2003) and the reasons are not fully understood yet.

The modified k-ε model's qualitative performance is reasonably good in that the double peaked structure at each axial station with the recirculation zone is captured. However, since the model is based on the assumption of isotropic turbulent fluctuations, it cannot account for the variations in the magnitude of axial and radial fluctuations observed within the recirculation zone. This can be observed clearly at the location x/D=1.0, where the assumption of isotropy means that the peak axial fluctuations in the inner shear layer are severely underpredicted while the radial fluctuations are slightly overpredicted.

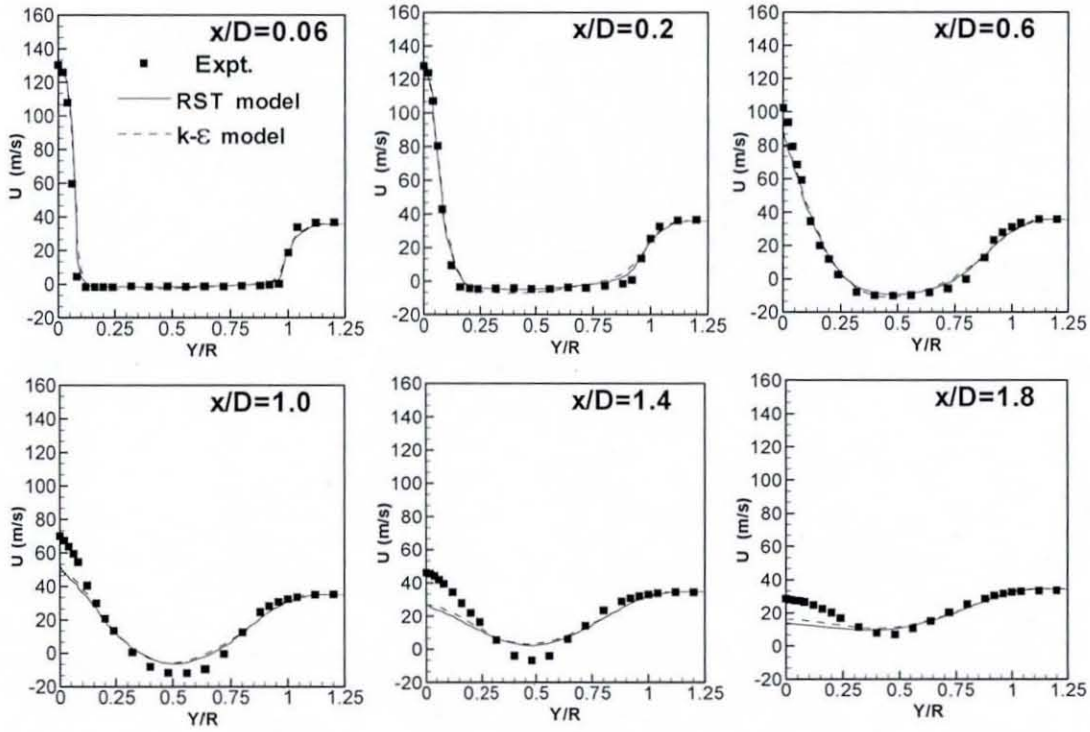

(a)

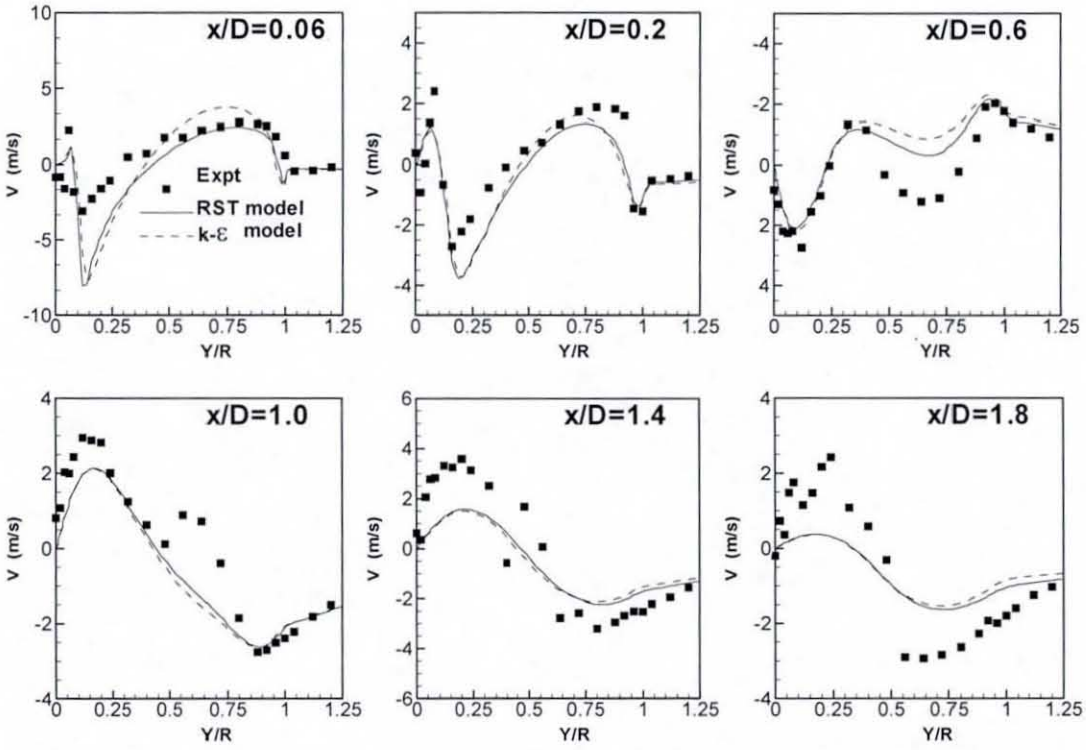

(b)

Figure 8.6: Radial profiles of mean axial velocity (a) and mean radial velocity (b) for at various axial locations in the HM1e flame. Predictions obtained from RANS calculations with SLFM.

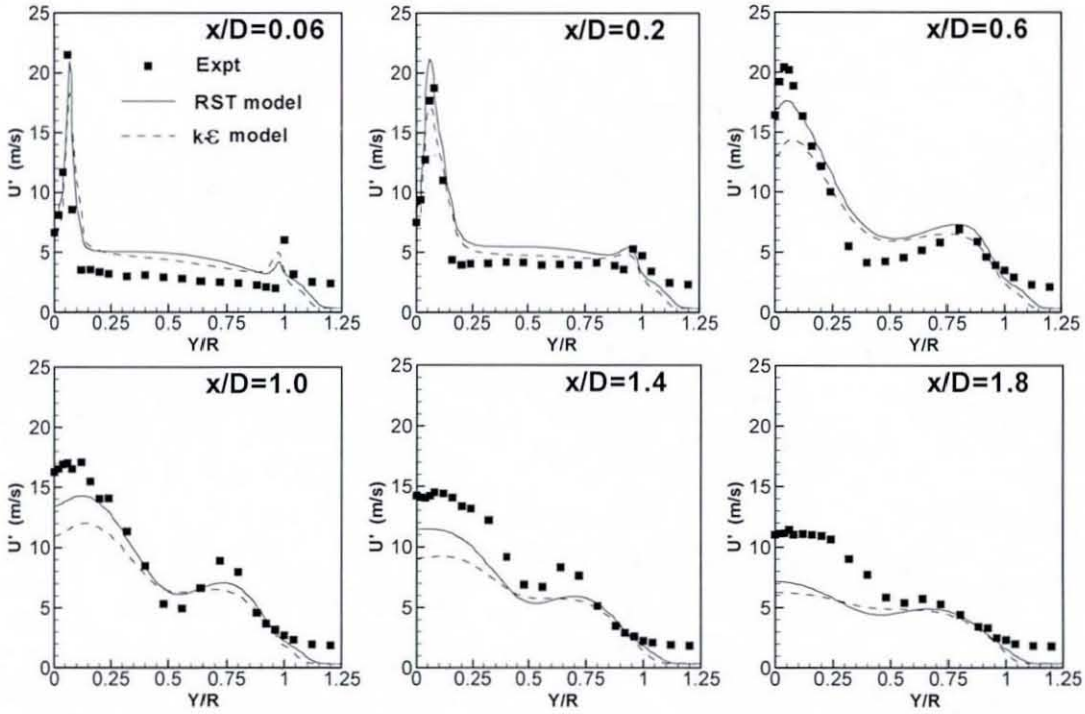

(a)

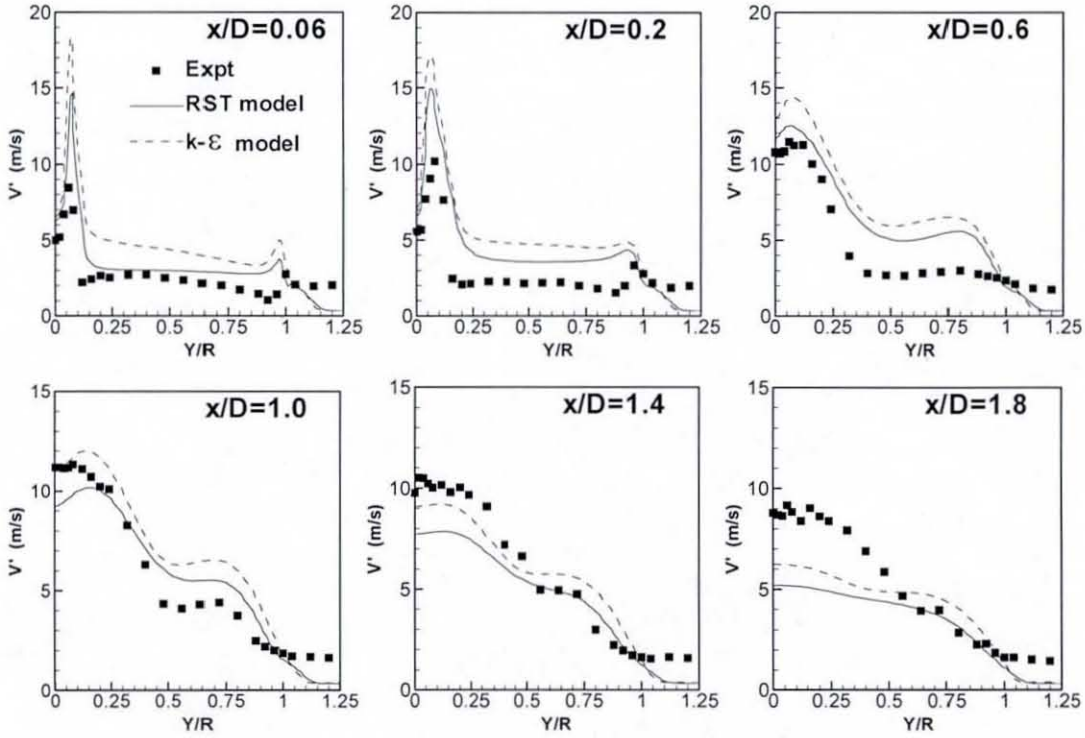

(b)

Figure 8.7: Radial profiles of rms fluctuations of axial (a) and radial (b) components of velocities at various axial locations in the HM1e flame. Predictions obtained from RANS calculations with SLFM.

Thus, although the differences between RST and modified k-ε model are less discernable from the mean velocity fields, the inherent advantage of adopting the RST model is indicated by the predictions of fluctuations. In reacting flow calculations, definitive conclusions about the overall performance of the turbulence models cannot be drawn on the basis of flowfield alone when differences exist in the predictions of fluctuations and given that the coupling between the flow-field and the compositional structure of the flame is non-trivial. Turbulent fluctuations are coupled to turbulence production rate and dissipation rate which in turn drive the scalar (mixture fraction) dissipation rate. The scalar dissipation rate is a vital parameter in the calculation of mean density in SLFM based reacting flow calculations and the mean density in turn is present in the equations for mean and variance of mixture fraction which constitute the mixing field. In SLFM, the accuracy of compositional structure (atleast the temperature and major species) is more or less determined by the accuracy of mixing field. Thus, the mixing field needs to be verified as well.

It should be restated here that no measurement data are available for the HM1e inflow conditions at which the flow field was measured, but rather for the HM1 case. However, it has been checked that, for the radial profiles of mixing field considered here, this is of minor importance. Calculations for HM1e and HM1 conditions result in more or less the same mixing fields at the axial stations where mixing field validations are carried out. Hence, the observed accuracy levels of the models in regard to flowfield in HM1e flame is valid for HM1 flame as well. The predictive capability of SLFM in conjunction with RST and modified k-ε models in capturing the mixing field and compositional structure are analyzed for HM1 flame conditions.

HM1 flame mixing field

The bluff-body flame characteristics discussed for HM1e flame are valid for HM1 flame as well. The comparisons for radial profiles of mixture fraction obtained from measurements and predictions are presented in Fig. 8.8. Predictions are obtained from SLFM based combustion simulations using modified k-ε model and RST model for turbulence closure. Predictions with both the models show good agreement with data for the first two axial locations which fall within the recirculation zone. In the neck zone (x/D =0.9, 1.3) and jet-like flow region (x/D $\geq$ 1.8) the centerline mixture

fraction is considerably underpredicted with the modified k-ε model due to the overprediction of decay rate of mixture fraction. On the other hand, the RST model captures the mixture fraction distribution in the neck region with much higher accuracy. In the jet region too, predictions with the RST model are in better agreement with measurements than k-ε model in that the centerline and radial distribution predictions of mixture fraction are improved by ~ 50%. This is a substantial improvement considering the fact that the present RST model is not a full second moment closure and the mixture fraction fluxes are modelled similar to k-ε model. Hence, the improvements are solely due to the factors discussed earlier viz. better reproduction of turbulence production and dissipation rates. The profiles of rms of mixture fraction fluctuations are shown in Fig. 8.9. Similar to the mean mixture fraction, predictions with both the models are in reasonably good with experimental data. However, unlike mean mixture fraction, the differences between the models are modest.

Overall, the fairly good agreement in predictions with RST model is indicative of a successful numerical implementation of the RST model in the in-house RANS code. It is noteworthy that the current mixing field predictions with SLFM-RST combination are at least comparable or slightly more accurate than the corresponding RST model predictions of Dally *et al.* (1998b). Comparisons at the axial station x/D=1.8 are shown in Fig. 8.10. Although Dally *et al.* (1998) employed simple single step fast chemistry combustion modelling approach as compared to the more elaborate SLFM calculations in the present work, they employed commercial software CFX 4.4 for their RST calculations. Intricate details of the Reynolds stress model implemented in the CFX 4.4 are not available for comparison with the present implementation. However, it is known that use of a generalized gradient diffusion model has been made for the diffusion of Reynolds stresses and this is indeed a more accurate approach than the simple gradient diffusion model implemented in the present RST model (Fletcher, private communication).

While this is one example, there could be few such differences which are expected to provide advantage in accuracy for the Reynolds stress model predictions from commercial software. Hence, it is quite encouraging that the present RST model is able to compete strongly with the more robust and extensively validated

implementations in commercial codes. Another work that was used to establish confidence on the current implementation of RST model is that of Li *et al.* (2003) who employed equilibrium chemistry for combustion modelling and validated a number of pressure-strain term models in the RST model including the linear pressure strain model (section 4.1.4) used in the present work. Similar to the present RST model, they too changed the constant $C_{\varepsilon 1}$ to 1.6 in the dissipation rate equation. Although, the equilibrium chemistry is a less accurate combustion modelling approach than the SLFM used in the present work, their RST model implementation is expected to be more accurate due to the full second moment closure involving transport equations for mixture fraction fluxes. However, mixing field predictions from current RST model have been found to be of better accuracy at all the axial stations in the flame. Comparison plots for the mean and rms of mixture fraction fluctuations at the axial station x/D=1.8 are shown in the Fig 8.10.

Thus, the accuracy of current modelling with RST model for turbulence closure and SLFM for combustion, can be judged to be quite competitive as far as mixing field is concerned.

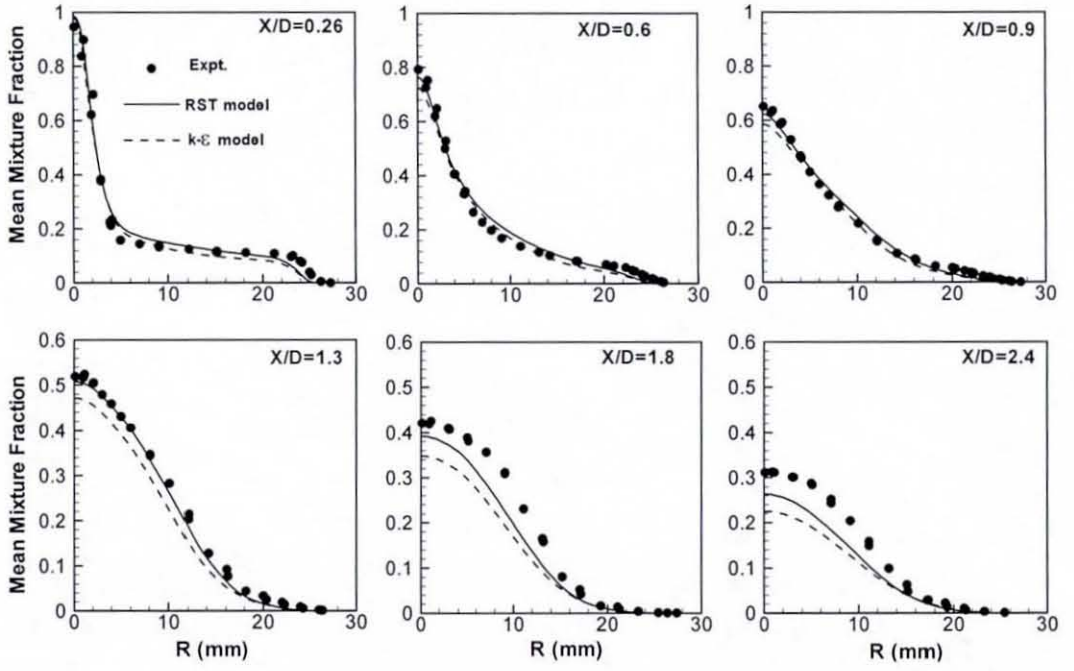

Figure 8.8: Radial profiles of mean mixture fraction at various axial lengths of HM1 flame. Predictions obtained from RANS calculations with SLFM.

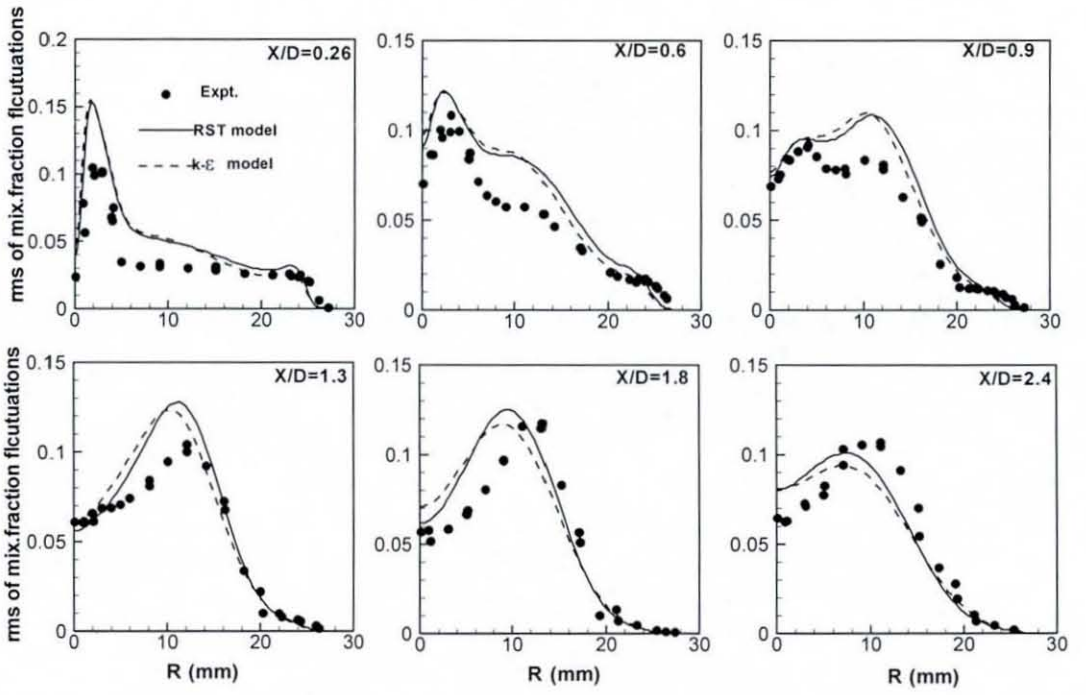

Figure 8.9: Radial profiles of rms of mixture fraction fluctuations at various axial lengths of HM1 flame. Predictions obtained from RANS calculations with SLFM.

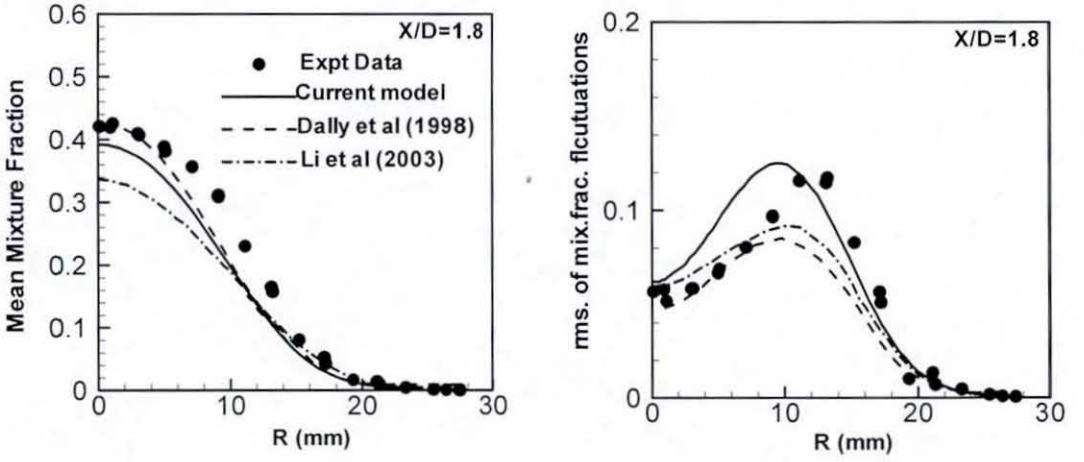

Figure 8.10: Comparison of the in-house RANS code's RST model prediction capability with that of commercial code CFX 4.4 (Dally *et al.*, 1998b) and full second moment closure (Li *et al.*, 2003). All predictions pertain to HM1flame conditions.

HM1 flame temperature & major species

The radial profiles of mean temperature at various axial locations in the flame are shown in Fig. 8.11. It is clear that both RST model and modified k-ε model based SLFM calculations result in fairly good results. The overprediction in temperature with both the models at x/D=0.26 is more a deficiency in the measurements than in simulations. Dally *et al.* (1998b) have reported that the lower levels of measured mean temperatures are due to averaging effects caused by intermittency in the flame at this location. The shift in the structure of the flame with the movement away from the bluff-body face in the downstream direction is well captured by both the models. The steady rise in the centreline mean temperature indicates a shift to jet flame structure. The modified k-ε model can be seen to overpredict the centreline line mean temperature at the last two locations which fall within jet-flame structure. This is primarily due to the overprediction in decay rate of mixture fraction which leads to a mixture closer to fuel rich side of stoichiometry. The fact that SLFM calculations are adiabatic and do not include effects of radiation heat loss and yet the temperature predictions from both the models are fairly good, indicates weakly radiating nature of the flame.

The predictions of mean mass fraction of the major specie CO_2, are shown in Fig. 8.12. Within the recirculation zone, except for the first location right adjacent to bluff-body face, predictions from both the models are fairly good. The underprediction observed with both the models at the first locations is perhaps the manifestation of averaging effects in measured data as previously mentioned. In the far downstream jet flame region, the radial distribution of mean CO_2 mass fraction is overpredicted by both the models. While the underprediction in mixture fraction observed with both the models is certainly a contributor to this deviation, whether or not radiation heat loss has any part to play is observed from non-adiabatic model based calculations discussed in section 8.2.5.

The accuracy of predictions for the other major specie H_2O (Fig. 8.13) follows a similar trend as for CO_2 in that both models result in fairly good results but with the radial distribution underpredicted within the recirculation zone and overpredicted

downstream of it. The predictions with RST model can be observed to be slightly more accurate than the modified k-ε model.

In Fig. 8.14, the predictions of the mean mass fraction of the CO pollutant are shown. Unlike CO_2 and H_2O, the predictions are in better agreement with experiments at the first location which perhaps is not a true indication of the prediction capability as the accuracy of experimental measurements at this location is questionable. However, further downstream the trend is similar to CO_2 and H_2O. Employing the modified k-ε model for turbulence closure leads to severe underprediction in the outer vortex within the recirculation zone while at the downstream neck zone and jet flame regions (x/D=1.3 to 2.4) the CO mass fraction is significantly overpredicted in the fuel rich side of stoichiometry. Employing RST model improves the predictions in the outer vortex to a noticeable extent while bringing slight improvements along the centreline in downstream locations (x/D=1.3 to 2.4). However, there is significant scope for improvement in the predictions of CO mass fractions and the extent consideration of radiation heat loss could help, is discussed in Section 8.2.5.

Finally, the OH radical mass fractions are shown in Fig. 8.15. Experimental observations show steep peaks at the outermost shear layer within the recirculation zone (x/D=0.26 and 0.6). Predictions with the both the models fail to capture the steep slope and instead predict a relatively gradual variation in the OH. Since OH radical is much smaller in concentration, this large discrepancy could be a magnification of error caused due to minor deviations in mixture fraction and variance in the outer vortex. From x/D=0.9 to 2.4, the RST model is shown to agree fairly well with measurements.

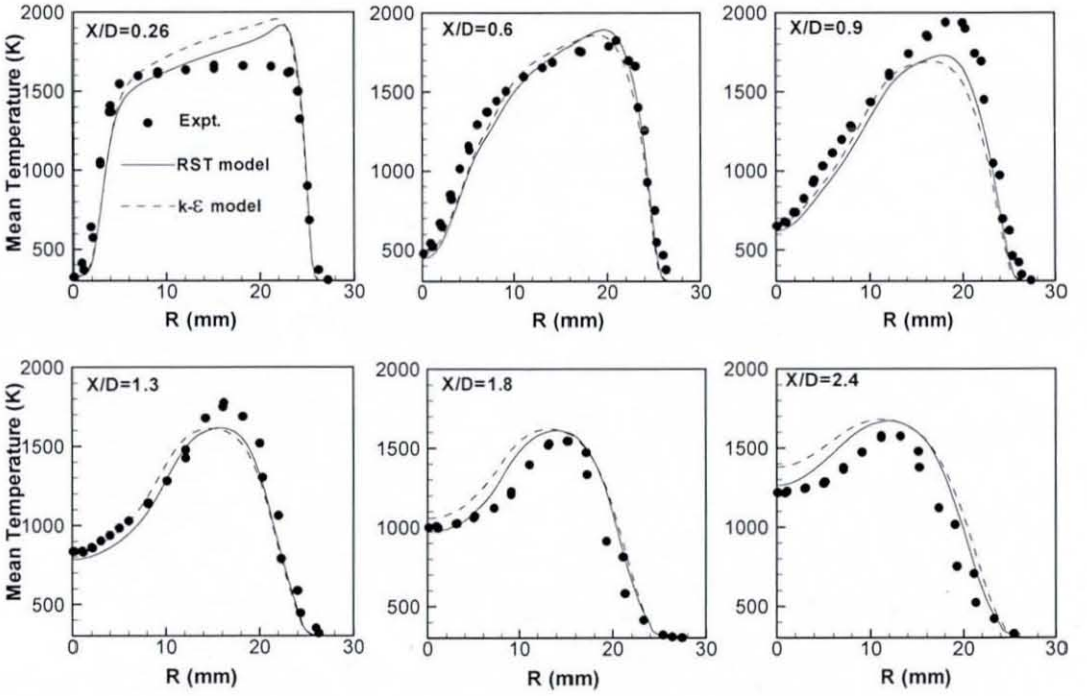

Figure 8.11: Radial profiles of mean temperature at various axial lengths of HM1 flame. Predictions obtained from RANS calculations with SLFM.

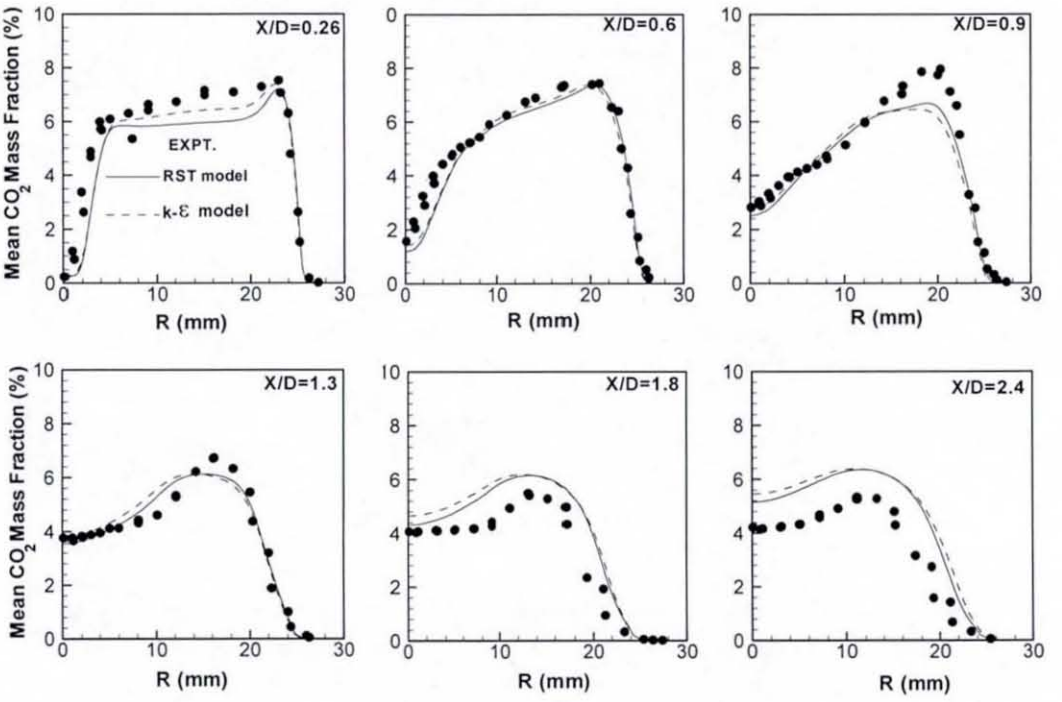

Figure 8.12: Radial profiles of mean CO_2 mass fraction at various axial lengths of HM1 flame. Predictions obtained from RANS calculations with SLFM.

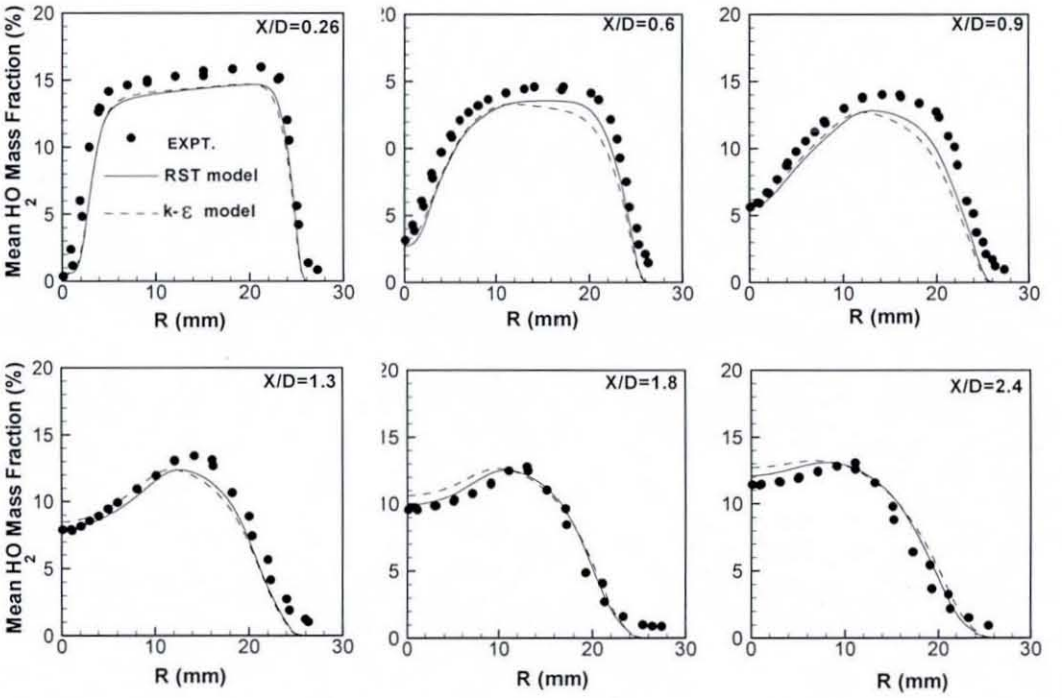

Figure 8.13: Radial profiles of mean H_2O mass fraction at various axial lengths of HM1flame. Predictions obtained from RANS calculations with SLFM.

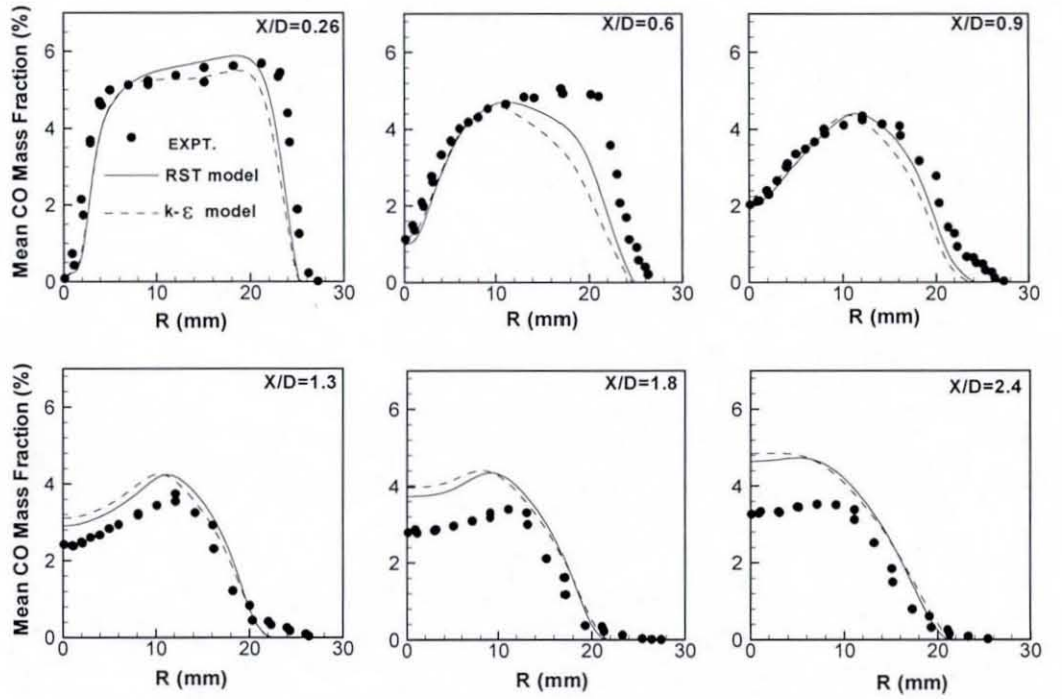

Figure 8.14: Radial profiles of mean CO mass fraction at various axial lengths of HM1 flame. Predictions obtained from RANS calculations with SLFM.

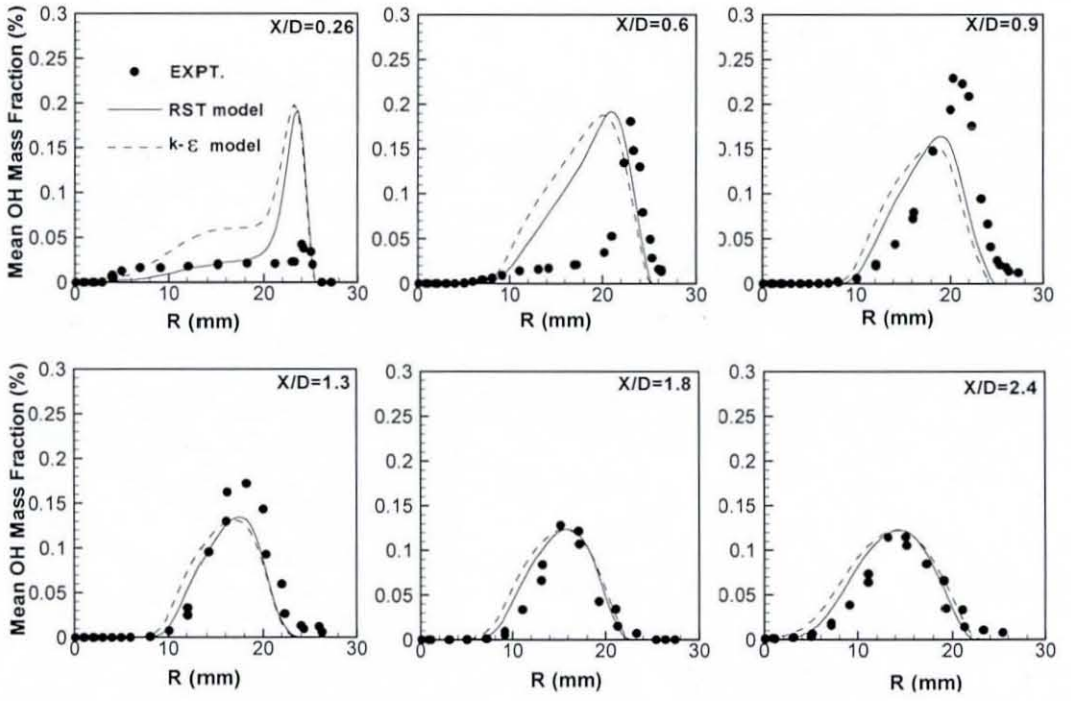

Figure 8.15: Radial profiles of mean OH mass fraction at various axial lengths of HM1flame. Predictions obtained from RANS calculations with SLFM.

HM1 flame pollutant NO

As previously discussed in chapter 5, the mean mass fraction of pollutant NO cannot be directly obtained from flamelet calculations unlike the temperature and major species due to the slow and kinetically controlled chemistry of NO. Submodels which exclusively account for NO have been implemented in the in-house RANS code. Consistent with the use of SLFM for combustion calculations, steady transport equation based NO sub model (SLFM-NO-TRE) has been used for calculating the mean NO mass fraction in post processing phase. The submodel calculations use the converged mixing field obtained from SLFM calculations. In order to illustrate the need for special modelling techniques in the form of submodels for NO, predictions of mean NO mass fraction have also been obtained directly from SLFM by extracting the mean NO mass fractions from flamelet calculations similar to mean temperature and major species.

In Fig. 8.16, the NO mass fraction predictions from the direct SLFM approach and steady transport equation approaches with both the modified k-ε and RST models based turbulence closures are shown. The direct approach overpredicts the peak NO mass fraction by about 4 times the measurements clearly indicating the breakdown of fast chemistry assumption of flamelet concept. Given the simplicity of the steady transport equation based approach (SLFM-NO-TRE), the improvement it promises over the conventional approach is quite significant. Thus, although a notable overprediction throughout the flame still exists, the predictions from both RST and modified k-ε models can be considered to be reasonably good. Between the two turbulence models for the transport equation approach, the RST is clearly the better model with the mean mass fraction of NO along fuel rich region more accurately captured.

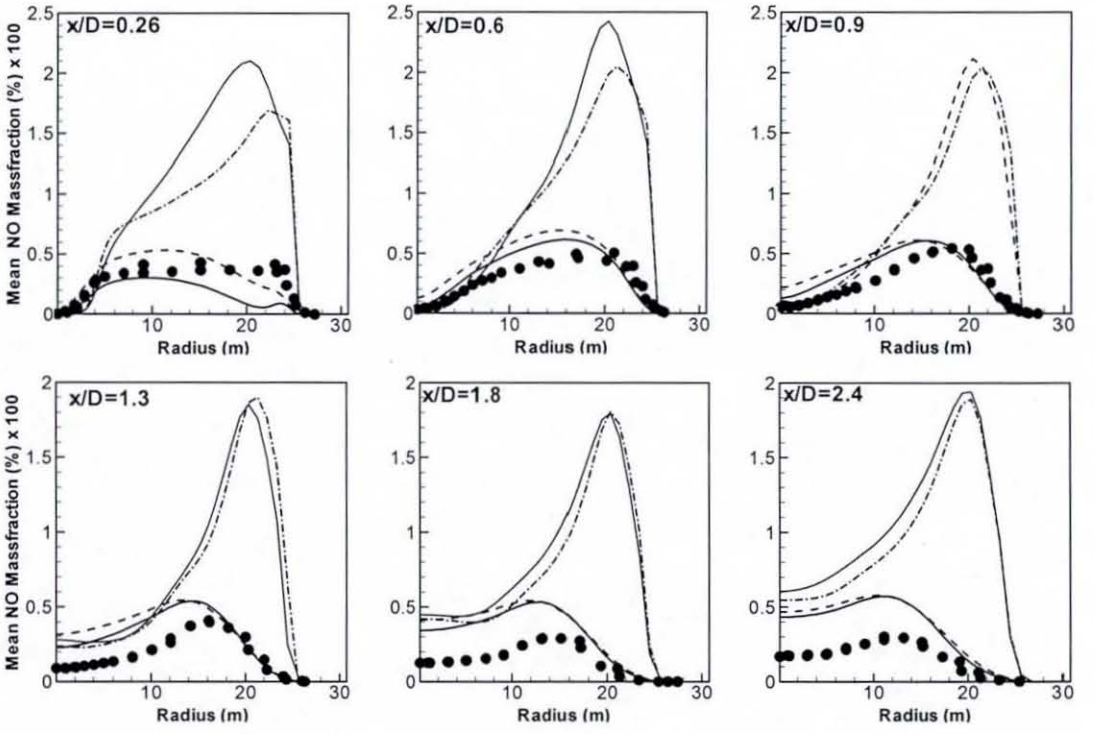

Figure 8.16: Radial profiles of mean NO mass fraction at various axial lengths of HM1 flame. Dots indicate measurements; (——) SLFM-NO-TRE + RST model, (----) SLMF-NO-TRE + mod. k-ε model; (– · – · –) SLFM Direct+ RST model ; (.....) SLFM Direct + mod. k-ε model.

From the comparisons shown so far for the predicted and measured flow, mixing field and compositional structure, it can be concluded that the overall prediction capability of SLFM and its corresponding NO submodel in conjunction with both RST model and modified k-ε models is reasonably good. Predictions with RST model are generally better or at the least comparable to modified k-ε model thus encouraging its use as the standard approach for turbulence closure in the present work. Additional motivation in using RST comes from the fact that with the use of look-up-table concept implemented in the in-house RANS code, the computational time for SLFM calculations with both RST and modified k-ε model is more or less the same.

However, there is scope for improvement in the RST model based turbulence closure and this partly explains for the discrepancies in mixing field and consequently the thermo-chemical structure including NO. Three other factors which are likely to influence the accuracy of predictions are:

- The adopted chemical mechanism
- Non-adiabatic effects due to radiation heat loss
- Transient effects due to the slow chemistry of NO.

While the effects of the first two factors are felt on the entire thermo-chemical structure of the flame, the third factor, transient effects, is known (Pitsch *et al.*, 1998 and Coelho and Peters, 2001a) to be of less influence on temperature and major species (given that the flame is fully burning) and are important only for the slow NO chemistry. Thus, investigations into the influence of chemical mechanism and radiation heat loss have been conducted for temperature and compositional structure of the flame while investigations into the influence of transient effects have been restricted to NO. The results from these investigations are discussed in the subsequent sections.

8.2.4 Influence of chemical mechanism

As previously stated, predictions of SLFM in conjunction with RST model have been obtained with the use of the detailed chemical mechanism, GRI 2.11. In order to verify the extent the predictions from GRI 2.11 (Bowman *et al.*, 2007) could be improved, SLFM based HM1 flame simulations have been conducted with two

different detailed chemical mechanisms the GRI 3.0 (Smith *et al.*, 2007) and SanDiego mechanism (Williams, 2007).

The GRI 3.0 mechanism is a successor to the version 2.11 and comprises of 53 species with 325 elementary chemical reactions (hydrocarbon + nitrogen chemistry) in comparison to the 277 elementary reactions and 49 species with GRI 2.11. Notable modifications include changes in CH kinetics which are important to the Prompt NO formation. A previous study conducted by Kim and Huh (2002) on the HM1 flame has shown that the GRI 3.0 overpredicts NO twice as high as GRI 2.11 while the temperature and major species predictions are more or less similar to those from GRI 2.11. However, these findings were obtained from CMC model based combustion calculations and hence, whether or not they could be generalized was questioned. Hence, performance of GRI 3.0 has been re-investigated with the present SLFM based calculations. The second mechanism used in the investigation, the SanDiego mechanism, is relatively new and it has been developed along the similar lines as the GRI 2.11 and GRI 3.0. This mechanism comprises of 52 species with 454 reactions including detailed nitrogen chemistry which is based on the work of Hewson and Bollig (1996). Performance of this mechanism in turbulent hydrocarbon flames is not yet known and present investigation is expected to contribute to the knowledge in this mechanism's prediction capability.

In addition to the detailed mechanisms, a reduced mechanism of Peters (1993) consisting of 53 elementary reactions for the hydrocarbon chemistry and 3 reactions for nitrogen chemistry has been investigated to verify the need for detailed chemical kinetics in the current bluff-body flames. The 3 step NO chemistry corresponds to the Zeldovich mechanism which accounts for the production of only thermal NO. Thus, SLFM calculations with the reduced chemistry are expected to verify the extent thermal pathway alone contributes to the total NO in the turbulent flame and henceforth the need for detailed nitrogen chemistry.

HM1 flame temperature and major species

The mean temperature predictions of RANS calculations of HM1flame with SLFM combustion model and RST turbulence model for the different chemical mechanisms

are compared to each other and measurements in Fig. 8.17. Similar to the findings of Kim and Huh (2002), no noticeable improvement in predictions are observed with the GRI 3.0 mechanism. The predictions from SanDiego mechanism are more or less similar to GRI 2.11 and GRI 3.0. Discounting the first and the last locations, predictions from the reduced mechanism are close to the predictions from all the three detailed mechanisms. However, the reduced mechanism results in a predominantly overpredicted distribution of mean CO_2 mass fraction and underpredicted mean distribution of CO mass fraction (Fig. 8.18). All the three detailed mechanisms can be observed to result in similar predictions for the mean CO_2 mass fraction. For the mean CO mass fraction both the GRI mechanisms result in similar predictions but the SanDiego mechanism shows deviations from the GRI mechanisms in the first and last location. For the other two major species investigated in the current study, H_2O and OH (both not shown) all the mechanisms have been found to result in similar predictions. Thus, from temperature and major species comparisons, neither of the relatively new detailed mechanisms seem to give better predictions than GRI 2.11. Although reduced mechanism competes well with detailed mechanisms in regard to temperature, its performance is not consistent in regard to species. Detailed hydrocarbon chemistry is thus a necessity for the present study where both temperature and compositional structure are of interest.

HM1 flame pollutant NO

For each mechanism, NO has been post-processed from the steady transport equation based submodel (SLFM-NO-TRE) upon obtaining a converged mixing field from SLFM calculations. The mean NO mass fraction predictions from all the four mechanisms are compared to measurements in Fig. 8.19. From the significant underprediction observed with 3 step Zeldovich's mechanism, it appears that Thermal NO accounts for only ~50% of the total NO predicted by experiments. Hence, for the flame under investigation, it does seem important to account for the Prompt and nitrous oxide pathways of NO formation. Accounting for all the possible NO formation pathways through the different detailed mechanisms has resulted in different levels of overprediction of mean NO mass fraction. The predictions with GRI 3.0 are significantly higher than the corresponding predictions from GRI 2.11 thereby in agreement with the findings of Kim and Huh (2002). With SLFM, the GRI

3.0 predictions are up to 3 times higher than GRI 2.11. Thus, overprediction of NO seems to be the general problem with GRI 3.0 although the exact extent of overprediction can vary according to the combustion model. Since, the temperature and major species predictions do not deteriorate with GRI 3.0 and these are dictated by the hydrocarbon chemistry, the problem seems to be with nitrogen chemistry and in particular with higher rate coefficients in the Prompt mechanism. The nitrogen chemistry with SanDiego mechanism seems to have similar problems as with GRI 3.0 as the predicted mean NO mass fractions are only slightly better than GRI 3.0 while they are still significantly higher than measurements and GRI 2.11.

Overall, the GRI 2.11 stands out as the best amongst the tested mechanisms and hence has been used as the standard mechanism for the hydrocarbon flames in the current work.

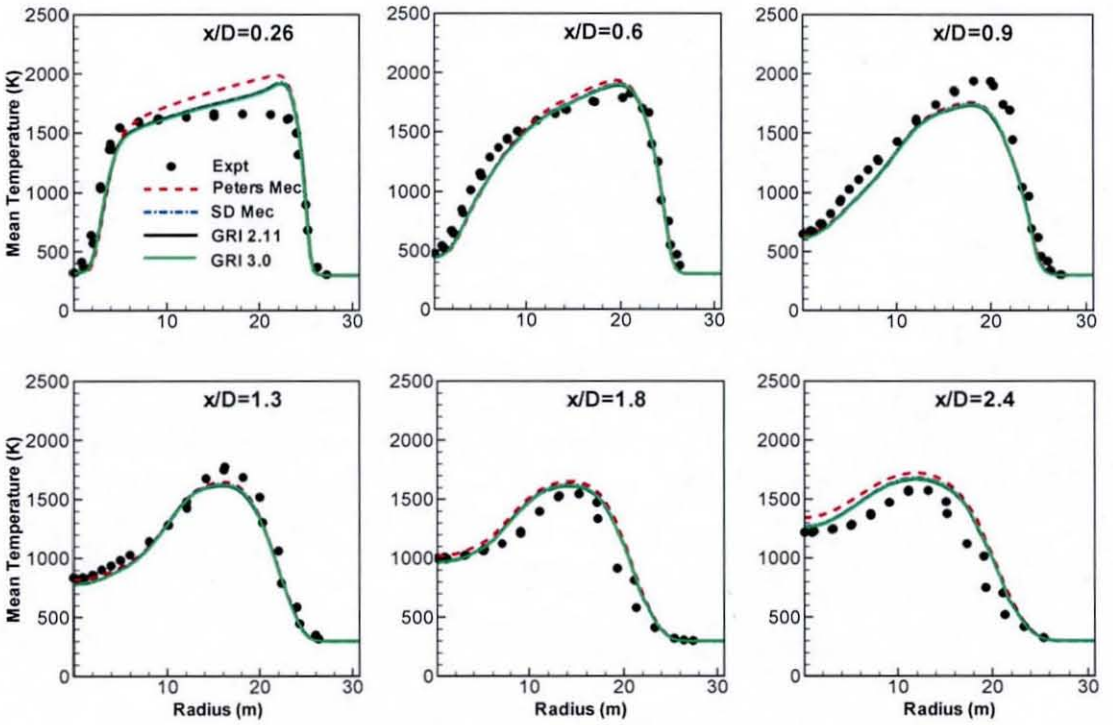

Figure 8.17: Radial profiles of mean temperature: comparison of different mechanisms for hydrocarbon chemistry. Predictions obtained from RANS calculations of SLFM in conjunction with RST model.

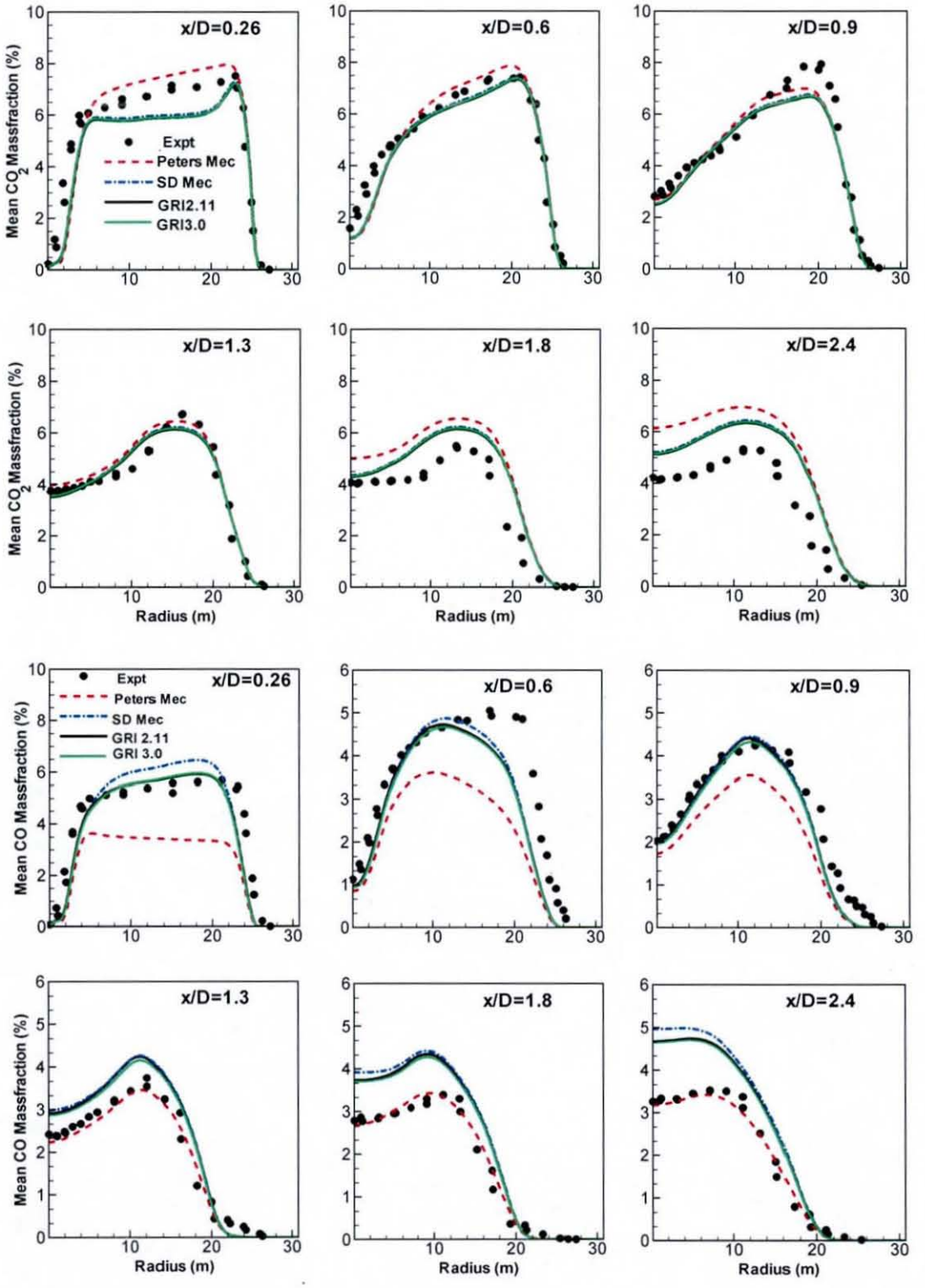

Figure 8.18: Radial profiles of mean CO_2 (top) and CO (bottom) mass fractions. Sensitivity of predictions to mechanisms for hydrocarbon chemistry. Predictions obtained from RANS calculations of SLFM in conjunction with RST model.

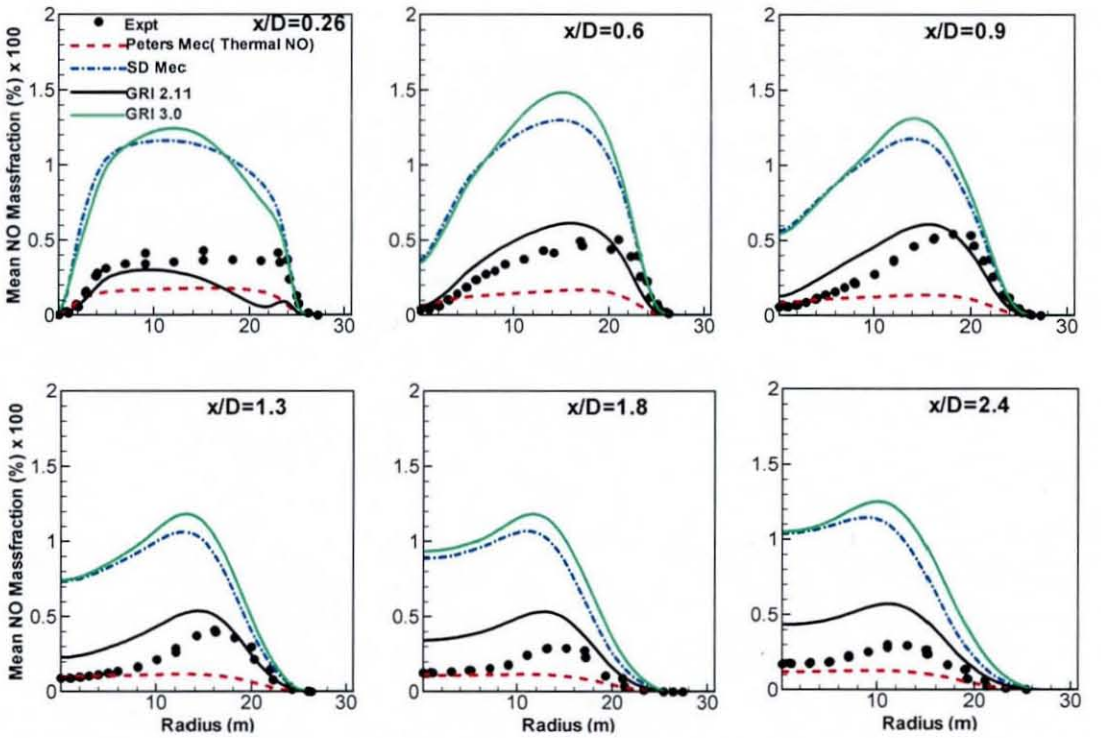

Figure 8.19: Radial profiles of mean NO mass fraction: comparison of different mechanisms for nitrogen chemistry. Predictions obtained from RANS calculations with RST model and SLFM-NO-TRE.

8.2.5 Non-adiabatic flamelet modelling: results & discussion

Here, the HM1flame has been modelled with the RANS based non-adiabatic models (NADM and NADS) and the non-adiabatic NO submodels in conjunction with RST model for turbulence. Predictions from non-adiabatic calculations have been compared with measurements as well as SLFM predictions to study the performance of the non-adiabatic flamelet model and simultaneously asses the extent to which consideration of radiation heat loss could improve the accuracy of predictions observed with SLFM.

Predictions for the mixture fraction from all three models are compared with measurements and shown in Fig 8.20. The NADM model is in good agreement with measurements but shows no notable improvement over SLFM. The overall heat lost due to radiation does not seem to be significant enough for the net heat released to be

adequately far from adiabatic conditions. Hence the effect on density and consequently the mixing field is not notable. The simplified model NADS, even without considering the effects of scalar dissipation rate, is able to produce similar predictions as NADM. However, this is expected for the mixture fraction since density has weak dependence on scalar dissipation rate in the non-premixed flamelets considered in the present study as previously observed from Fig 7.1 in Section 7.1.1.

Similarity between the SLFM and NADM models can be observed for the rms of mixture fraction fluctuations as well in Fig. 8.21. However, here the NADS model shows deterioration in performance with respect to NADM model in that it overpredicts the magnitude of peak fluctuations in mixture fraction along the inner shear layer within the recirculation zone and the radial distribution along the fuel rich zone of stoichiometry.

Fig. 8.22 shows radial profiles of mean temperature. Here again, no signs of the effect of radiation heat loss are evident. Hence, the distribution of radiation heat loss within the flame from NADM calculations has been examined from the contours of mean enthalpy defect as shown in Fig. 8.23. The mean enthalpy defect contours show a certain presence of radiation loss. The maximum loss could be seen taking place right adjacent to the bluff-body wall where the flame stabilizes. In the immediate proximity of the wall ($x/D < 0.25$) the heat loss is fairly high varying between -150 to -100 kJ/kg with steep gradients. However, for the majority of the flame further downstream where measurements have been obtained, the heat loss is far less and more uniform with an average of ~ -60 kJ/kg. This predicted level of heat loss does not translate into notable change in temperature and hence corresponds to weak radiation. However, its impact on major species and pollutant NO, still needs verification.

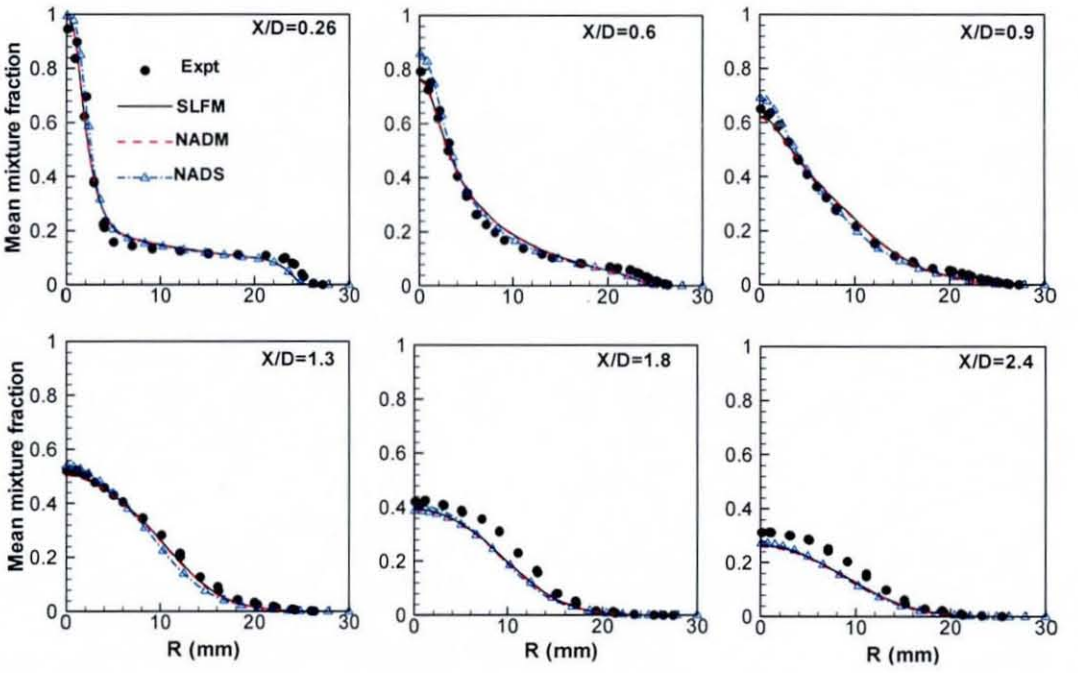

Figure 8.20: Radial profiles of mean mixture fraction along various axial stations in HM1 flame. Predictions obtained from adiabatic and non-adiabatic RANS simulations using RST model for turbulence closure.

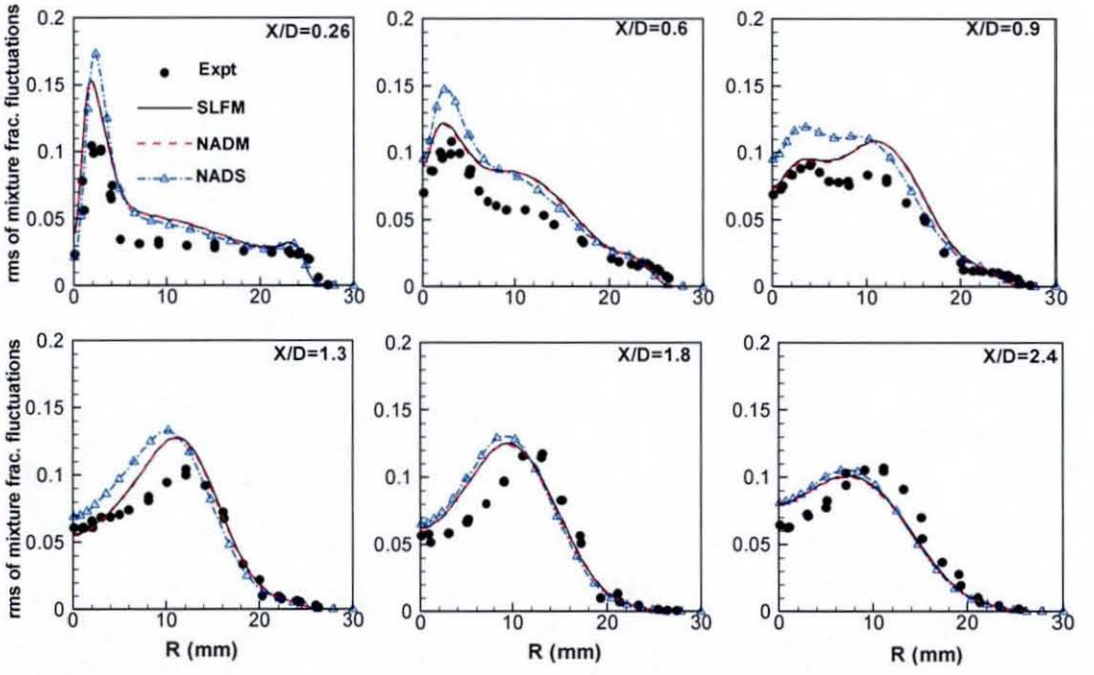

Figure 8.21: Radial profiles of rms of mixture fraction fluctuations along various axial stations in HM1 flame. Predictions obtained from adiabatic and non-adiabatic RANS simulations using RST model for turbulence closure.

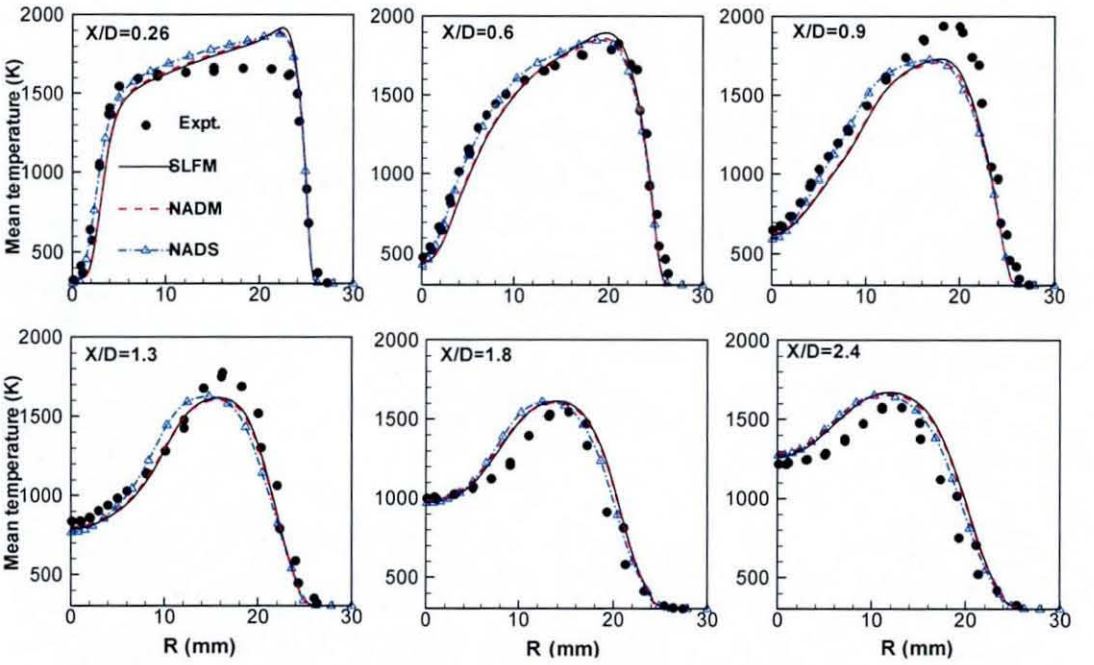

Figure 8.22: Radial profiles of mean temperature (K) along various axial stations in HM1 flame. Predictions obtained from adiabatic and non-adiabatic RANS simulations using RST model for turbulence closure.

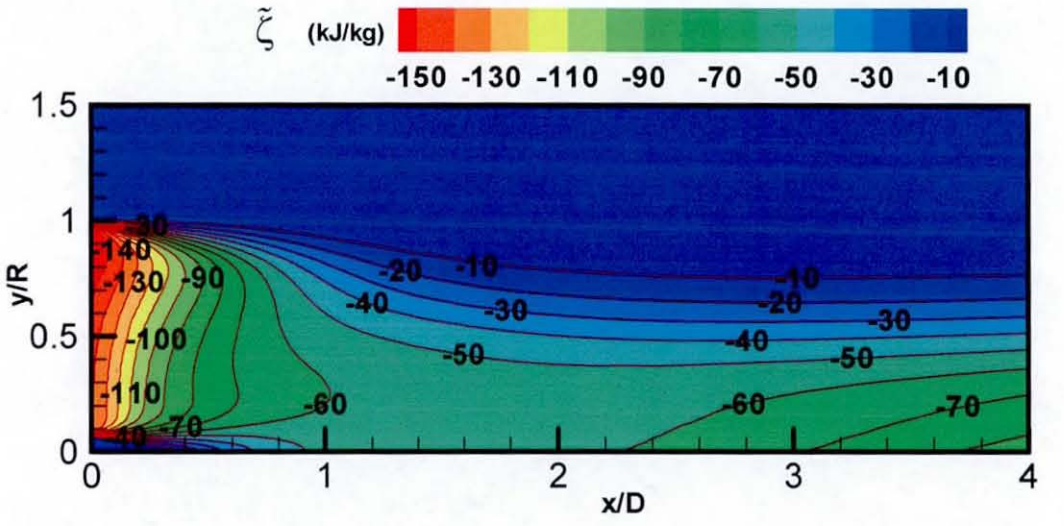

Figure 8.23: Contours of mean enthalpy defect (kJ/kg) in HM1 flame. Predictions obtained from simulation with NADM model using RST model for turbulence closure.

The CO_2 mass fraction profiles are shown in Fig. 8.24. NADM model shows a marked improvement over SLFM at the first location where the radiation heat loss has been observed to be more pronounced. Further downstream locations, the NADM model predicts slightly higher CO_2 levels than SLFM in the region close to the centreline where the mixture fraction levels are on the fuel rich side of stoichiometry. This behaviour of CO_2 is a direct consequence of the effect of enthalpy defect on the flamelet CO_2 structure which is shown in Fig 8.25. As the imposed enthalpy defect on a flamelet increases, it can be seen that the CO_2 levels increase along the fuel rich side of the stoichiometry and decrease along the fuel lean side. Since, the mean mixture fraction along the fuel rich zone of the flame is slightly underpredicted, the predicted mean CO_2 mass fraction by SLFM is higher than the measurements. Adding the radiation heat loss correction through enthalpy defect with NADM model then further increases the deviation. Hence, the deviation cannot be regarded as a deficiency of the non-adiabatic model, atleast the NADM model.

The problem with simplifications in the non-adiabatic formulation is made discernable by the CO_2 predictions from NADS model. The simplified non-adiabatic model, unlike for temperature, shows significant deviation from measurements and predictions from NADM model. This confirms the observation made in section 7.1.1, where the effect of scalar dissipation rate on flamelet structure for species mass fractions was found to be relatively stronger than on temperature and density. Figure 8.26 shows comparisons for mean CO mass fraction. Contrary to the improvement observed with CO_2, the NADM model results in an underprediction compared to the SLFM model within the recirculation zone. Such an adverse effect on CO mass fractions has been observed by Marracino and Lentini (1997) as well in their non-adiabatic modelling of jet flames and the causes behind this behaviour are yet to be understood. However, the NADM model still does better than the NADS model within the recirculation zones. Improvement in predictions with the NADS model at the last two locations is misleading as the mean CO predictions with non-adiabatic formulation do not seem to show the overall correct trend.

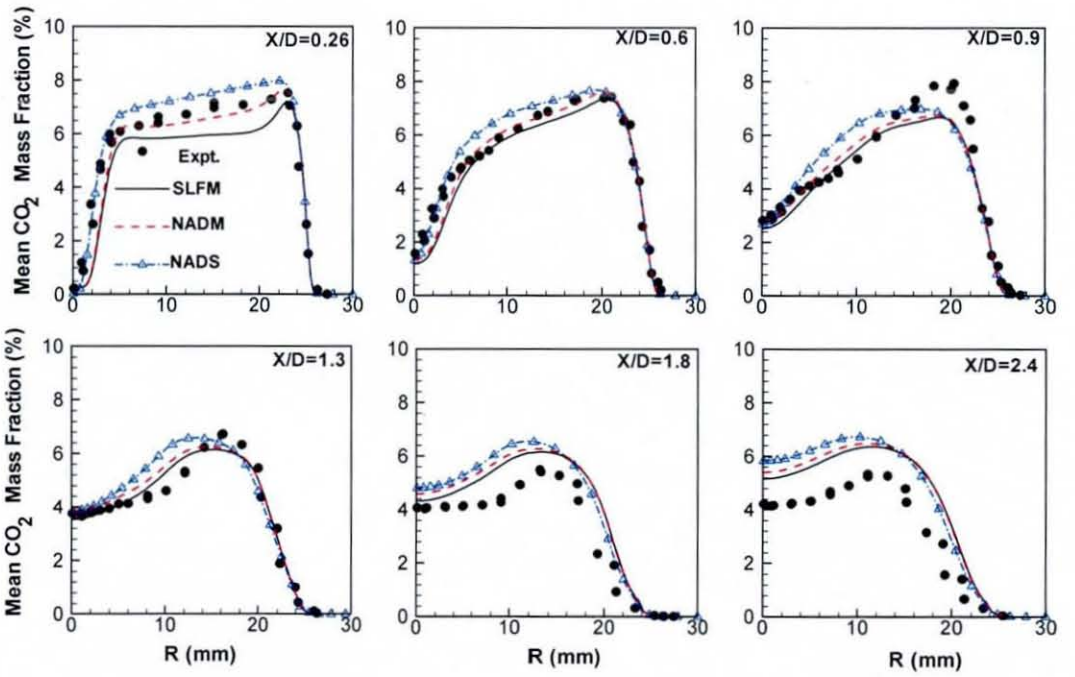

Figure 8.24: Radial profiles of mean CO_2 mass fraction along various axial stations in HM1 flame. Predictions obtained from adiabatic and non-adiabatic simulations using RST model for turbulence closure.

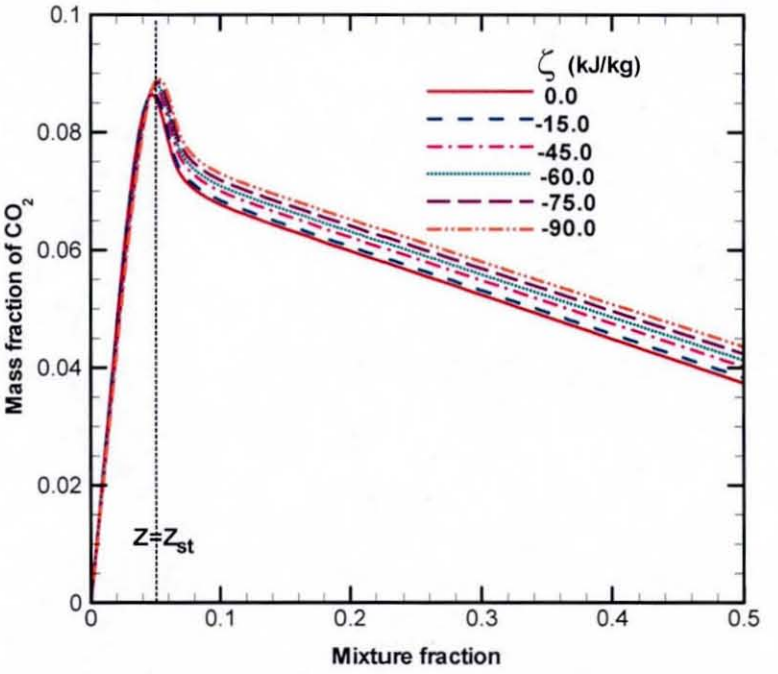

Figure 8.25: Flamelet CO_2 structure at various enthalpy defects. Generated for HM1 flame conditions using GRI 2.11 mechanism.

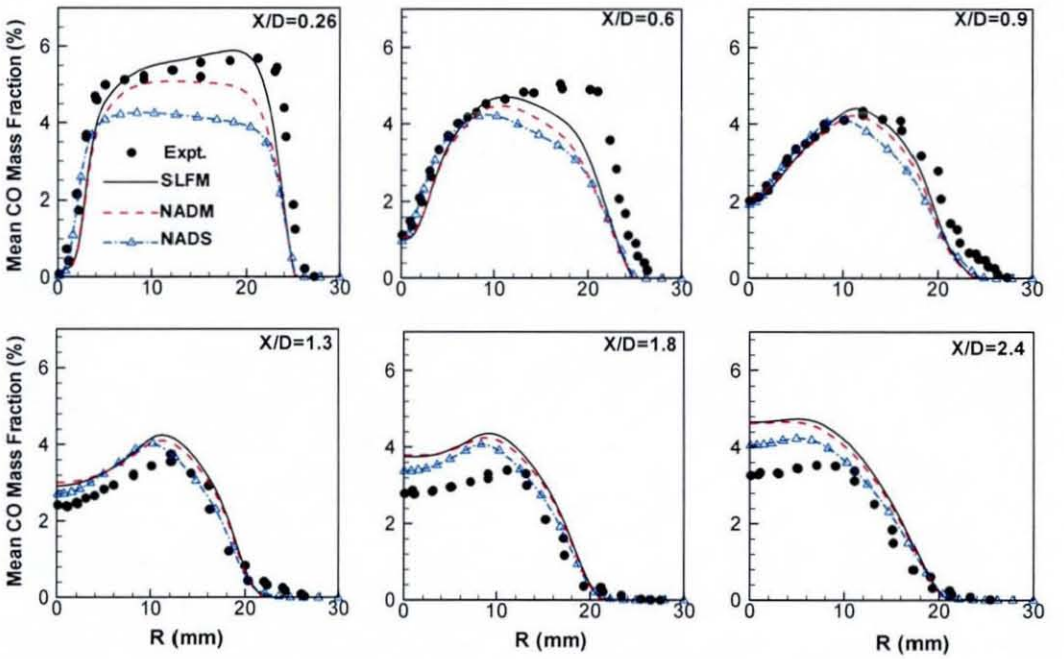

Figure 8.26: Radial profiles of mean CO mass fraction along various axial stations in HM1 flame. Predictions obtained from adiabatic and non-adiabatic simulations using RST model for turbulence closure.

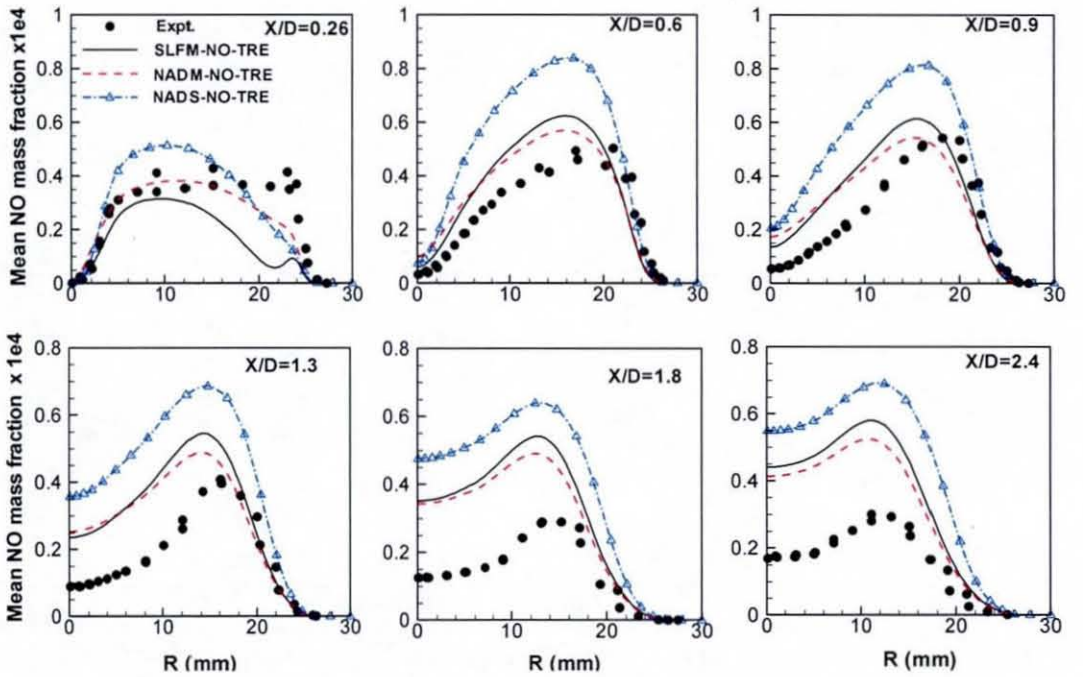

Figure 8.27: Radial profiles of mean NO mass fraction along various axial stations in HM1 flame. Predictions obtained from adiabatic and non-adiabatic simulations using RST model for turbulence closure.

Pollutant NO from steady non-adiabatic NO sub models

Finally, the performance of steady non-adiabatic NO submodels, integrated with the non-adiabatic models, in predicting NO mass fractions is analysed. Upon obtaining converged mixing field from the NADM and NADS calculations, post-processing of NO has been carried out with the NADM-NO-TRE and NADS-NO-TRE respectively. The predicted radial profiles of mean NO from these steady non-adiabatic transport equation based submodels are compared to predictions from adiabatic calculations (SLFM-NO-TRE) and measurements in Fig. 8.27.

The extent of overprediction observed with the adiabatic sub-model is expected to be reduced with the non-adiabatic models where consideration of radiation heat loss through enthalpy defect lowers the magnitude of peak NO source terms (as observed from Fig 7.5, Chapter 7) which enter into the NO transport equation. However, the effect produced by employing NADS model is contrary to the expectation. The predictions further deviate from SLFM in that the peak NO mass fractions are scaled up by approximately 1.5 times. It has been observed from Fig. 7.2 (Chapter 7) that the NO source term is highly sensitive to even small variations in scalar dissipation rate and hence neglecting the effect of scalar dissipation rate seems to have marred the effect of considering radiation heat loss. This is further confirmed from the performance of NADM model which produces the correct effect of incorporating radiation heat loss in that the extent of overprediction observed with adiabatic model is consistently reduced. Although the improvement achieved with NADM is modest, the overall trend is quite promising especially when the flame under study is of weakly radiating nature.

The existing discrepancy between the predictions from NADM model and measurements are considered to be manifestation of the inaccuracies in mixing field and the transient effects which are not accounted by the steady NO submodels. In addition, the extent the truncation (discussed in Section 7.1.2) in non-adiabatic flamelets may have compromised the accuracy of NADM model predictions has been called into question. Hence, an investigation into this issue has been carried out and the results are discussed in the following section. Subsequently, the influence of transient effects is discussed.

Impact of truncation in flamelets on accuracy of mean scalars

As mentioned in Chapter 7, section 7.1.2, due to modified inlet conditions, the non-adiabatic flamelets are subjected to truncation in Z space. Hence the usual limits of Z which vary from Z = 0 to1, are curtailed to Z = Z_o to Z_f, where Z_o= Z(ζ) > 0 and Z_f = Z(ζ) < 1. For the non-adiabatic flamelets, integration for mean scalars is split according to Eq. 8.1 and the first and third parts are neglected.

$$\widetilde{\phi} = \int_0^\infty \int_{z=0}^{z=z_o} \phi(Z;\chi_{st};\zeta)P(Z)P(\chi_{st})dZd\chi_{st} + \int_0^\infty \int_{z=z_o}^{z=z_f} \phi(Z;\chi_{st};\zeta)P(Z)P(\chi_{st})dZd\chi_{st} +$$

$$\int_0^\infty \int_{z=z_f}^{z=1} \phi(Z;\chi_{st};\zeta)P(Z)P(\chi_{st})dZd\chi_{st} \qquad (8.1)$$

For low enthalpy defects, Z_o and Z_f are close to 0 and 1 respectively and hence neglecting the contribution of first and last terms does not affect the accuracy of numerical integration. However, for higher enthalpy defects there is a concern that the first and last terms might have sizeable contribution and hence neglecting the terms might result in errors in the mean quantities viz. the mean temperature, major species and the mean NO source term.

In order to verify this issue, a 'high enthalpy defect' (HED) zone as shown in Fig. 8.28, has been identified within the HM1 flame computed from NADM model. The HED zone encloses the region of the flame where the enthalpy defect varies between the domain maximum of -150 kJ/kg and a cut-off limit of -105 kJ/kg. For enthalpy defects less than the cut-off limit, truncation in flamelets has been found to be insignificant enough to avoid any concerns over accuracy of integration. Hence the investigation can be focused solely on the HED zone to which the issue is confined.

From each cell that is lying within the HED zone, the shape of the Favre averaged presumed PDF for mixture fraction $\tilde{P}(Z)$ which corresponds to β PDF, has been extracted. Thus obtained comprehensive collection of PDF shapes are shown in Fig 8.29 (a). From the plot, it can be readily inferred that for Z greater than 0.8 the value of $\tilde{P}(Z)$ is nearly zero for the entire range of PDF shapes. In other words, the truncation at the fuel end which is a maximum of -1% (for ζ = -150 kJ/kg) for the

flamelets in the present study should have no affect on the accuracy of integration. The second inference that can be drawn from the plot is that the bulk of the PDF shapes have peaks clustered at or around the stoichiometric mixture fraction (Z_{st} = 0.05) with the $\tilde{P}(Z)$ values dropping steeply as one moves towards oxidizer end. Thus indicating a weak influence of $\tilde{P}(Z)$ near oxidizer end on the integrated mean values.

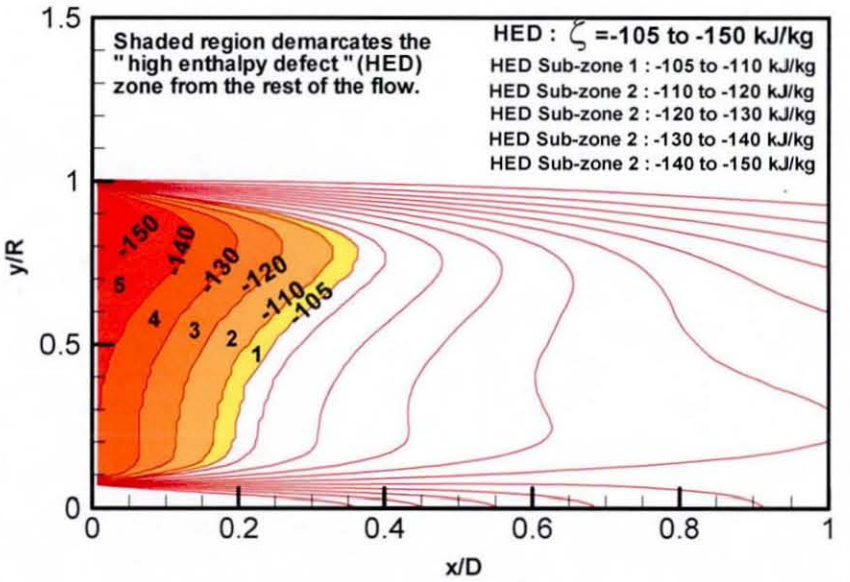

Figure 8.28: Predicted 'High Enthalpy Defect' zone and its sub-zone within HM1 flame from RANS simulation carried out with NADM model in conjunction with RST model for turbulence closure.

For a closer investigation, the HED zone has been split into 5 sub-zones (Fig. 8.28) and the PDF shapes within each sub-zone are separately plotted as shown in Figs 8.29 (b) to (f). These plots help in discerning the influence of enthalpy defect on β PDF shapes. It can be observed that as the enthalpy defect increases, the profiles become narrower and the peaks shift further away from stoichiometric mixture fraction in the direction of richer Z. For the highest enthalpy defect range of -140 to -150 kJ/kg, all the extracted PDF shapes are clearly far from the oxidizer end.

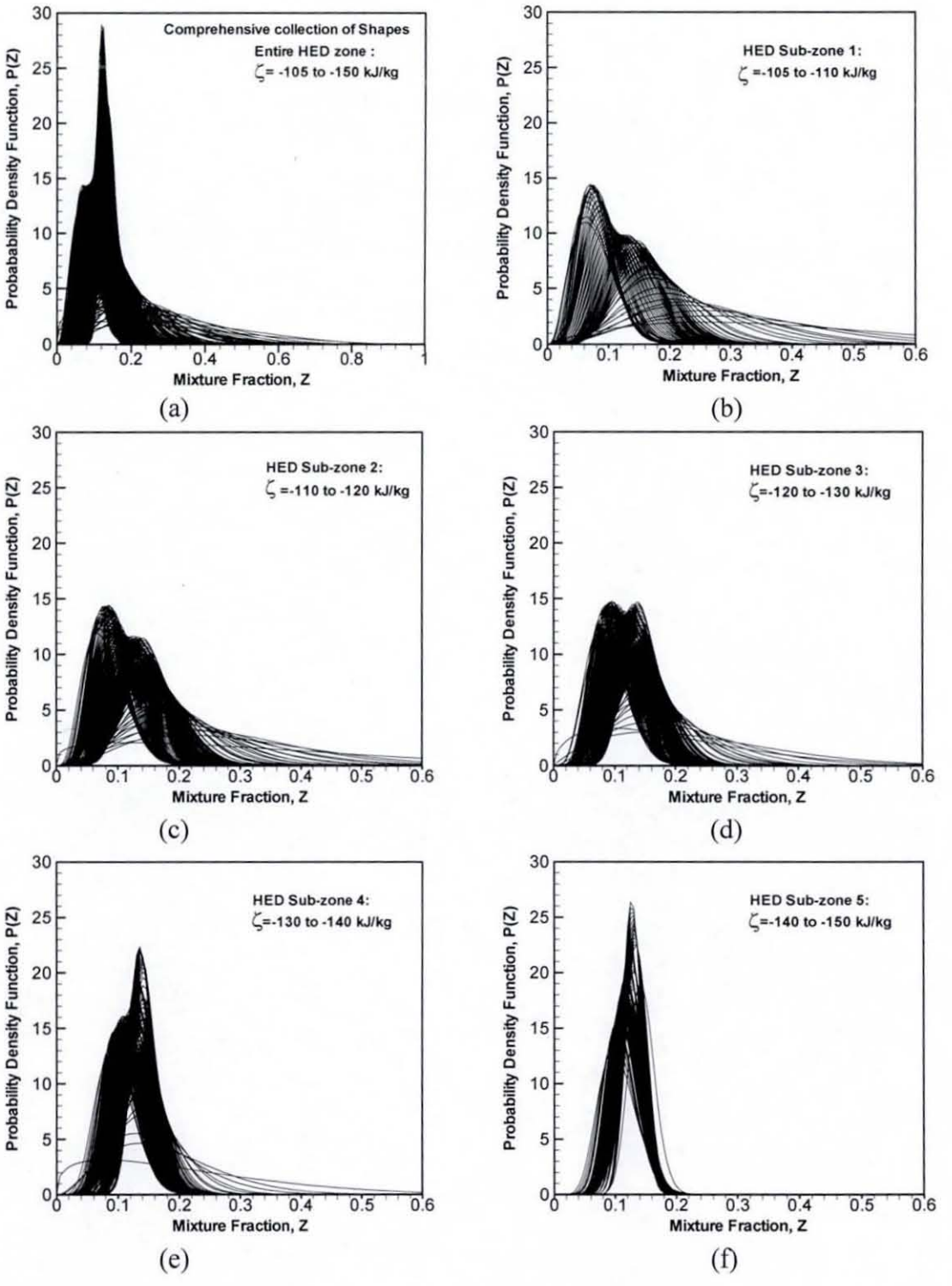

Figure 8.29: The β PDF shapes extracted from the entire HED zone (a) and within each HED sub-zone (b)-(f) in HM1 flame. RANS Simulation carried out with NADM model in conjunction with RST model for turbulence closure.

This finding is interesting as it means that any influence of the increase in truncation on integration is negated by the shift of PDF away from the ends. In the computed non-adiabatic flamelets, the maximum truncation at oxidizer end is about +0.3% (for ζ = -150 kJ/kg). Hence the maximum truncation on oxidizer end would still result in a Z_o which is safely lesser than the value at which $\tilde{P}(Z)$ starts to contribute to the integration.

Thus, it is confirmed that the Z truncation in the non-adiabatic flamelets is expected to have minimal or no impact on the integrated mean density and reactive scalars for the entire range of enthalpy defects encountered in the computed flame. The differences between the NADM predictions and measured data for radial profiles of temperature and major species are thus primarily due to the deviations in mixing field and hence a problem to be addressed by turbulence closure method. For mean NO mass fraction, transient effects may additionally contribute to the deviation and this is verified in the following section.

8.2.6 Influence of transient effects on NO

Transient effects in globally steady flames are a result of the finite time required by the flamelet structure to adapt to the changes in scalar (mixture fraction) dissipation rate. However, the distribution of temperature and major species within a fully burning flamelet tends to adjust to the changes in the scalar dissipation adequately fast for the process to be assumed as steady. Hence, it is sufficient to represent the thermal and chemical (only the major species) structure of a fully burning turbulent flame with steady flamelets.

However, the slow chemistry of NO does not allow for rapid changes in its structure with scalar dissipation rate. Assuming the process to be steady henceforth results in significant overprediction as previously shown in Fig. 8.16. The steady transport equation based adiabatic and non-adiabatic NO submodels (SLFM-NO-TRE and NADM-NO-TRE) provide simple work around to the problem. However, these models are not completely accurate as they still assume the process to be steady with the NO source term which enters the transport equation essentially obtained from steady flamelets. An unsteady flamelet modelling has been found (Pitsch *et al.* 1998,

Coelho and Peters, 2001a) essential to address the slow chemistry of NO in a more complete manner. Thus, the in-house RANS code has been equipped with unsteady NO submodels, SLFM-EPFM and NADM-EPFM to be used in conjunction with adiabatic (SLFM) and non-adiabatic (NADM) combustion simulations respectively.

The mean NO distribution in HM1 flame has been post-processed with each of these submodels by using the converged mixing field obtained from the CFD simulations with SLFM and NADM models. The post-processing with the unsteady models requires a greater effort than with the steady transport equation based submodels. An unsteady marker particle equation is solved until the particle completely exits the domain. Domain averaged conditional scalar dissipation rate $\tilde{\chi}_{st}$ is calculated at each time step thereby obtaining the variation of an average scalar dissipation rate with respect to time. The time evolution of $\tilde{\chi}_{st}$ obtained from calculations with NADM-EPFM submodel and the corresponding NO evolution obtained from solution of unsteady non-adiabatic flamelet equations (Eqs 7.1 and 7.2) are shown in Fig. 8.30

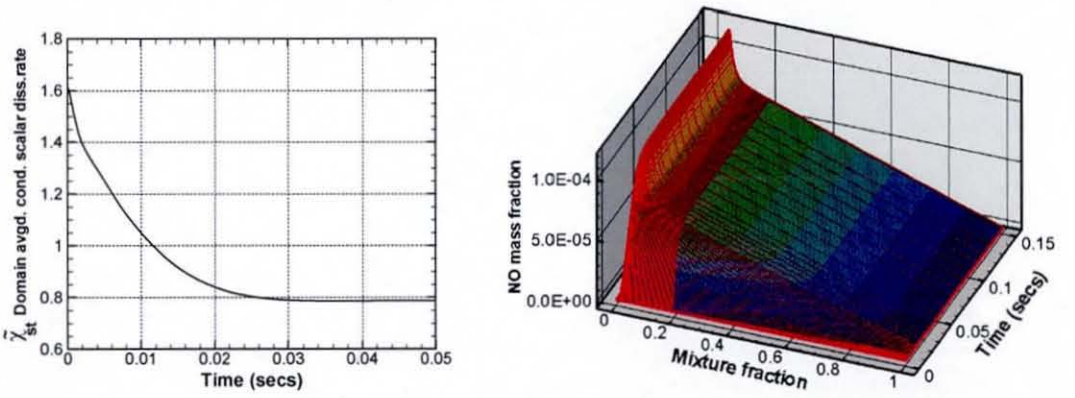

Figure 8.30: Time evolution of domain averaged conditional scalar dissipation rate (a) and the corresponding evolution of flamelet NO distribution (b).

The average scalar dissipation rate can be observed to vary rather steeply till 0.03 sec. after which it reaches more or less a steady state. The effect of this variation on the laminar structure of NO is evident in Fig 8.30 (b). The peak NO mass fraction as well as its distribution in mixture fraction space rise steeply till 0.03 sec and reach a steady state thereafter. Thus, if only the steady state flamelet NO mass fraction distribution is

considered in a turbulent flame calculation (as is done with SLFM direct approach Fig. 8.16), the obvious result would be an overprediction in the mean NO mass fraction. In EPFM, the entire evolution of NO is taken into account and it is weighted with the probability of finding the marker particle (Eq .5.36) to evaluate the mean NO mass fraction at each location in the domain. The effect of this detailed accounting of the behaviour of flamelet NO distribution can be observed from Fig. 8.31 where predictions obtained from the unsteady NO submodels are compared to measurements as well as predictions obtained from steady transport equation based submodels.

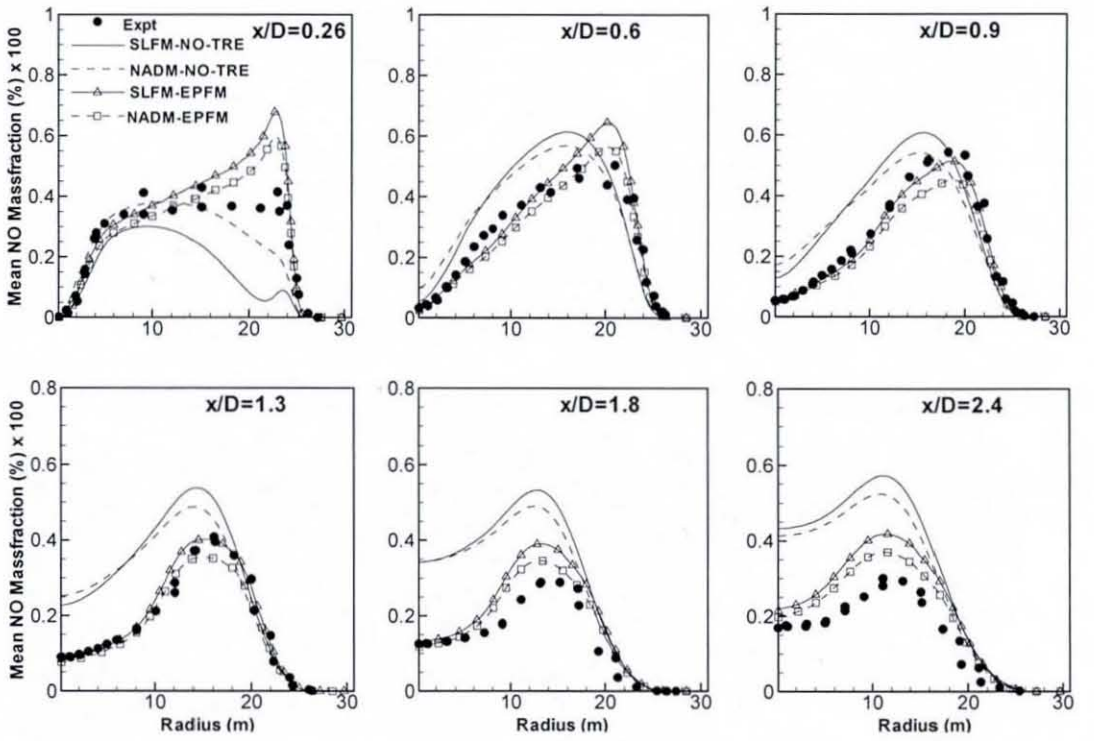

Figure 8.31: Steady vs. Unsteady NO submodels in RANS calculations of HM1flame with RST model for turbulence closure.

The importance of transient effects on mean NO mass fraction is evident from the comparisons. By employing the unsteady NO submodels, SLFM-EPFM and NADM-EPFM, the NO distribution predictions are remarkably improved over the corresponding steady submodels throughout the length of the flame. The fact that the influence of transient effects is felt not only in the flame stabilization region but also in the neck and further downstream jet flame region projects the complexity of the bluff-body stabilized flame and in a way justifies the selection of this flame for testing

the advanced models. Also, evident from the comparisons is that the transient effects have a greater influence on the mean NO predictions than the non-adiabatic effects for this weakly radiating flame. Consideration of heat loss with the unsteady models can be observed to result in a similar level of improvement as with the steady models. However, the strategy of non-adiabatic flamelet model in conjunction with unsteady NO submodel NADM-EPFM certainly provides a more complete approach to modelling NO.

Since, the effects of radiation heat loss are not prominent in the modelled HM1 flame, the predictive capability of non-adiabatic model NADM to account for the effects of radiation heat loss has not been made clear. Hence, the NADM model and its NO submodels have been tested in a relatively higher radiation heat loss conditions and the details are discussed in the following section.

8.3 Experimental study of Sandia D jet flame

Similar to the Sydney bluff-body flames, the Sandia D jet flame has been promoted by the TNF workshop community as a target flame for validation of turbulent non-premixed combustion models. This flame has been experimentally studied by Barlow and Frank (1998) and Schneider *et al.* (2003). While the former conducted scalar measurements, the latter conducted measurements of the flow field. The burner consists of an axisymmetric jet centered in an annulus in which a number of premixed flames are stabilised on a flame holder (Fig. 8.32). The burner is centered in an unconfined stream of co-flowing air. The premixed flames provide the heat source for stabilizing the main jet to the burner's exit plane. The main jet inner diameter D=7.2 mm with a pipe length exceeding 40D. The pilot's inner and outer diameters are 7.7 mm and 18.2 mm respectively and the diameter of the outer wall of the burner is 18.9 mm. The exit of the wind tunnel which hosts the co-flowing air stream is 30 cm by 30 cm. The fuel jet consists of a 25% CH_4 and 75% air by volume. The partially premixed fuel helps in reducing the length of the flame and provides a more stable flame than pure CH_4. Hence, the flame can be operated at reasonably high Reynolds number (Re = 22,400) with little or no local extinction even with a modest pilot.

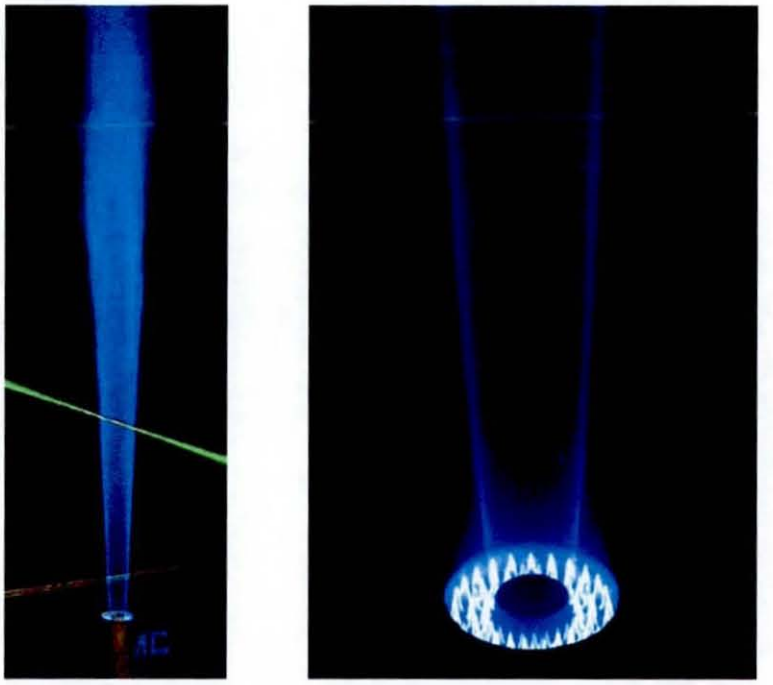

Figure 8.32: Experimentally observed image of Flame D (left) and close-up of the pilot flame (right). (Courtesy: Barlow and Frank (2007))

The mixing rates for this flame are high enough for the flame to burn as diffusion flame with a single reaction zone near the stoichiometric mixture fraction without any indication of premixed reaction in the fuel rich mixture (Barlow and Frank, 2007). Hence although, the fuel is partially premixed, the flame can be categorised under non-premixed and the non-premixed combustion models could be tested. The pilot consists of a lean mixture of C_2H_2, H_2, air, CO_2 and N_2 with the same nominal enthalpy and equilibrium composition as methane/air at 0.77 equivalence ratio. The temperatures of fuel jet, pilot and co-flow are 294 K, 1880 K and 291 K respectively while the bulk velocities are 49.6, 11.9 and 0.9 m/s respectively.

8.4 RANS modelling of Sandia D jet flame

The RANS based modelling of Sandia D has been conducted by several researchers in the past with the aim of studying the influence of thermal radiation in turbulent combustion processes. Coelho *et al.* (2003) employed full second moment closure for turbulence, laminar flamelet model for combustion and the discrete ordinates method

(DOM) for radiative transfer calculations. They studied the importance of considering spectral effects and turbulence-radiation interaction (TRI). The performance of different methods of accounting the turbulence-radiation was studied for the same flame by Coelho (2004). Recently, Xu *et al* (2006) studied the effect of considering TRI in Sandia D by employing a multiple-time scale k-ε turbulence model for turbulence, combination of PDF transport and Lagrangian flamelet model for combustion and a finite volume/ correlated-k method for radiation heat transfer.

These works have shown that consideration of turbulence-radiation interactions can improve the predicted level of radiation heat loss and interactions are caused mostly by the fluctuations in temperature than in major species. It has also been observed that consideration of radiation heat loss results in notable improvements in temperature and NO predictions but the effect on major species is rather weak. Noticeable radiation effects on the entire thermo-chemical structure would have been ideal for studying the all-round performance of the non-adiabatic model in the present study. However, given the limited availability of experimental data for radiating flames of simple hydrocarbon fuels which provide NO measurements, it is encouraging that the level of radiation loss in Sandia D flame is adequate enough to result in notable variation in atleast temperature and the pollutant NO which is crucial for testing non-adiabatic NO submodels.

The non-adiabatic flamelet model (NADM) employed in simulating the Sandia D flame in the current study excludes turbulence-radiation interactions. The radiative transfer calculations for mixing field, temperature and major species concentrations employ Discrete Transfer Method which falls under the class of detailed methods for accounting radiation heat transfer. For the NADM-EPFM submodel calculations, the unsteady flamelets assume radiation heat loss through an optically thin limit approximation.

Simulations of Sandia D flame in the current study have been carried out with RST model for turbulence closure while combustion has been modelled using both adiabatic (SLFM) and non-adiabatic (NADM) flamelet models. Pollutant NO for the adiabatic calculations has been modelled using the steady NO submodel, SLFM-NO-

TRE. For the non-adiabatic calculations, both steady and unsteady non-adiabatic NO submodels NADM-NO-TRE and NADM-EPFM have been employed.

8.4.1 Computational set up

The RANS simulations for Sandia D flame employ a 2D axi-symmetric computational domain (Fig. 8.33) which starts from the burner exit plane in experimental configuration and extends in the axial direction by 80 jet diameters. Along the radial direction, the domain extends by 40 jet diameters. This domain has been discretized by non-uniformly spaced 141 nodes along axial direction and 104 nodes along radial direction and this grid has been verified to produce grid independent results.

In regard to the boundary conditions, zero normal gradient conditions have been specified along the axis symmetry and co-flow boundary. Although not identified in the figure, the wall thickness of the main jet burner which separates main jet from the pilot has been considered and no slip condition with log-law based standard wall functions have been applied along the wall. The near wall Reynolds normal stresses are computed from turbulent kinetic energy using Eq. 4.34 while shear stress has been solved after imposing zero diffusion to the wall condition. At fuel, pilot and co-flow inlets, radial profiles of mean axial velocity obtained from experiments (Schneider *et al.*, 2003) have been mapped. Turbulence at the inlets has been specified by mapping the experimental profiles for the mean Reynolds normal stresses $\widetilde{u''u''}$, $\widetilde{v''v''}$ and the shear stress $\widetilde{u''v''}$. The distribution of the mean normal stress component $\widetilde{w''w''}$ has been assumed to be equal to $\widetilde{v''v''}$. In addition to the mean Reynolds stresses, mean turbulent kinetic energy $\tilde{k}$ which is derived from the normal stresses and the mean dissipation rate $\tilde{\varepsilon}$ which is obtained from Eq. 6.48 have been specified.

For the fuel inlet, the mixture fraction Z is set to 1, while in the co-flow air stream it is set to 0. The pilot stream has a mixture fraction equal to 0.27 (Barlow and Frank, 2007). The mixture fraction variance has been set equal to zero at all the inlets. For the NADM model, the enthalpies of various streams need to be specified. The enthalpy at each inlet is given by the summation of gross calorific value and sensible enthalpy. The enthalpy for fuel stream h_{fuel}=9.0E+06 J/kg, co-flow stream $h_{co\text{-}flow}$ = 2.9 E+05 J/kg and the pilot stream $h_{pilot}= h_{fuel} . Z + h_{coflow}.(1-Z)$.

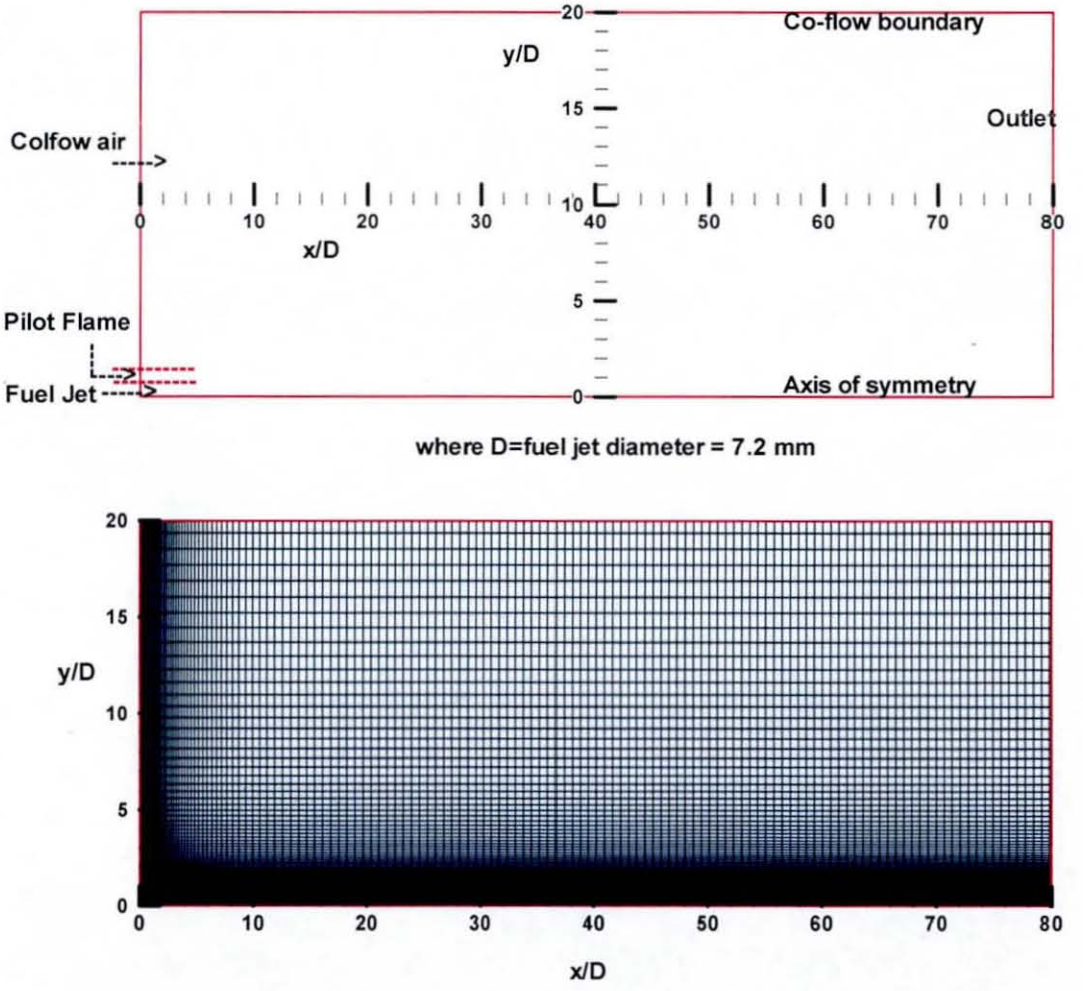

Figure 8.33: Computational domain (top) and grid (bottom) used for RANS based modelling of Sandia D flame. Grid consists of 141 axial nodes by 104 radial nodes.

8.4.2 Non-adiabatic flamelet modelling: results & discussion

The temperature and enthalpy defect distribution obtained from the calculations conducted with NADM model in conjunction with RST model for turbulence closure are shown in Fig.8.34. Flame stabilisation at the burner exit plane (x/D=0) due to the pilot flame can be observed in the predictions. Measurements show that the flame has a visible length of 67 D and a stoichiometric length of 47 D. Since, the cut-off temperature for visible length has not been reported, the latter has been used to compare the accuracy of predictions. The locus of the predicted stoichiometric mean mixture fraction has been plotted over the temperature distribution in Fig. 8.34. It can be observed that, the predicted stoichiometric length given by the location at which

the locus cuts the centreline, is approximately 45 D and hence in good agreement with measurements. From the distribution of enthalpy defect, it can be observed that the maximum enthalpy defect is ~-160 kJ/kg which is of the same order as the maximum defect observed in the HM1 flame. However, focusing on the region bounded by x/D=40-75 and y/D=0-3, it can be observed that enthalpy defect varies approximately from -160 kJ/kg to -80 kJ/kg. The average heat loss is thus higher than that observed in HM1 flame (~-60 kJ/kg) and the loss occurs over a much wider region. This is expected to translate into a notable effect on reactive scalars.

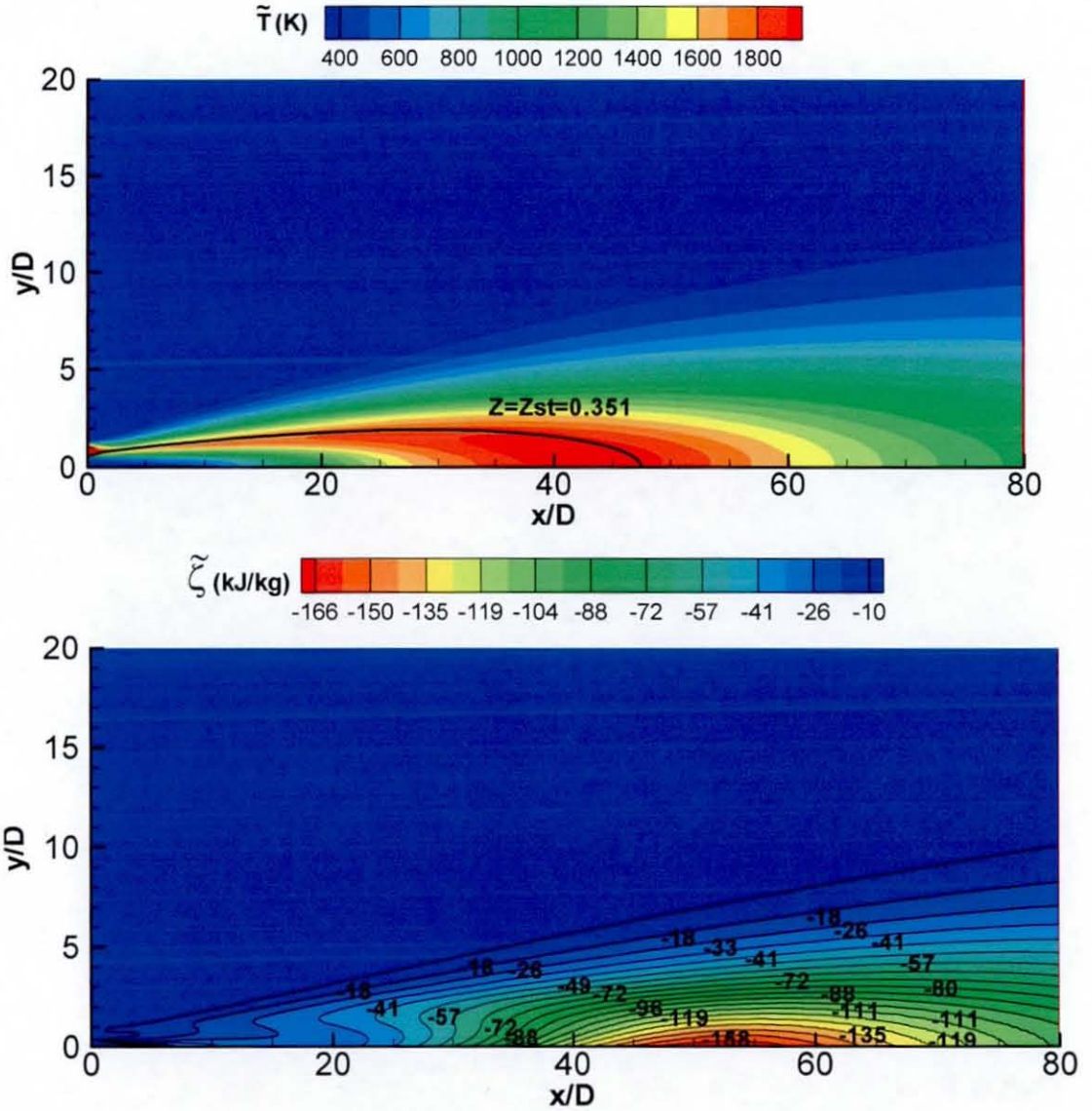

Figure 8.34: Mean temperature (K) (top) and enthalpy defect (kJ/kg) (bottom) contours of Sandia D flame predicted by RANS simulation with NADM model.

In Fig. 8.35, mixing field predictions from NADM model are compared with its adiabatic counterpart SLFM and measurements. Similar to the behaviour observed in HM1 flame, the density field and hence the mixture fraction and its variance seem to be less influenced by the predicted level of heat loss. The overprediction in mixture fraction at locations x/D =60 and 75 is a manifestation of the discrepancy in spreading rate and centreline decay rate of the fuel jet which is underpredicted here. This discrepancy occurs despite reducing the Schmidt number for the scalars viz., the mean and variance of mixture fraction and mean enthalpy, to a value of 0.7 from the original 0.9 employed for HM1 flame calculations. Hence, further tuning of the models constants in the pressure-strain term of the RST turbulence model and/or the $C_{\varepsilon 1}$ constant in the turbulent dissipation rate equation is necessary. However, the existing level of accuracy for the mixing predictions was found to be adequate to study the effects of radiation heat loss on mean temperature and NO mass fraction distribution.

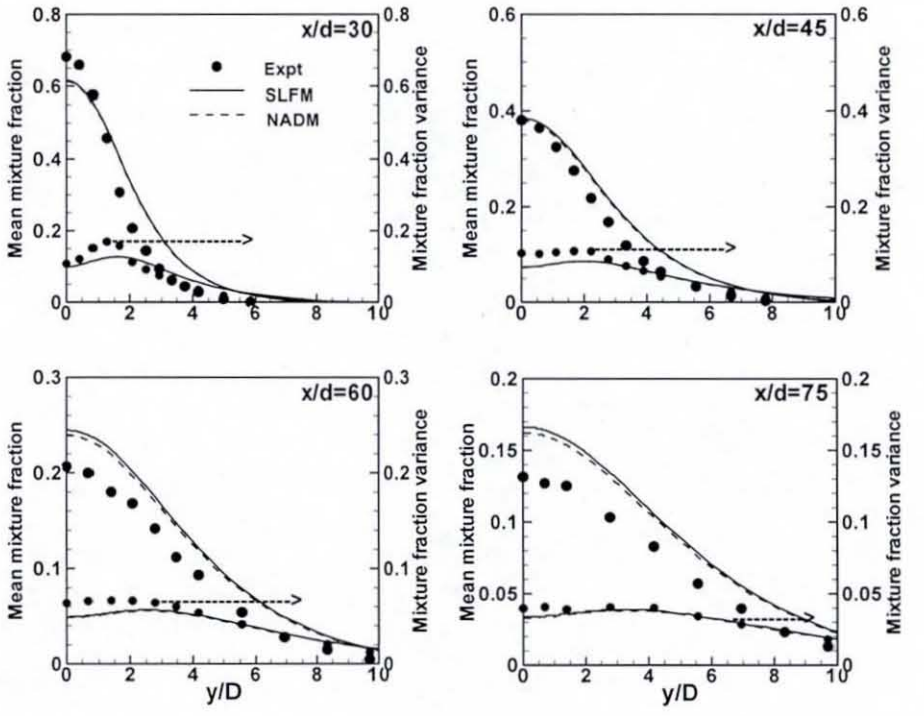

Figure 8.35: Radial profiles of mean and variance of mixture fraction at various axial locations in the Sandia D flame. Predictions from adiabatic and non-adiabatic RANS simulations with RST model for turbulent closure.

The radial profiles of mean temperature shown in Fig. 8.36. The location x/D =30.0 is less influenced by radiation heat loss as already shown by enthalpy defect distribution (Fig. 8.34) and hence both NADM and SLFM result in similar predictions for mean temperature. However the locations x/D=45, 60 and 75 fall within the zone where enthalpy defects reach maximum levels. Consequently, the mean temperature predictions are appreciably improved with NADM model at these locations. The maximum reduction in temperature is achieved at x/D =60 where the difference in centreline mean temperature predicted by NADM and SLFM models can be observed to be ~200 K. Further downstream at x/D=75, the extent of reduction is ~ 150 K and this is consistent with the enthalpy defect distribution. It is noteworthy that the predicted levels of improvement with the NADM model are close to those observed by Coelho *et al.* (2003) and similar to his findings, the major species were found to be less influenced by the consideration of radiation heat loss. This is illustrated in the Fig. 8.37 where the radial profile comparisons for mean CO_2 mass fraction are plotted. Signs of improvement at x/D=60 and 75 can be seen but the improvement is at best, modest.

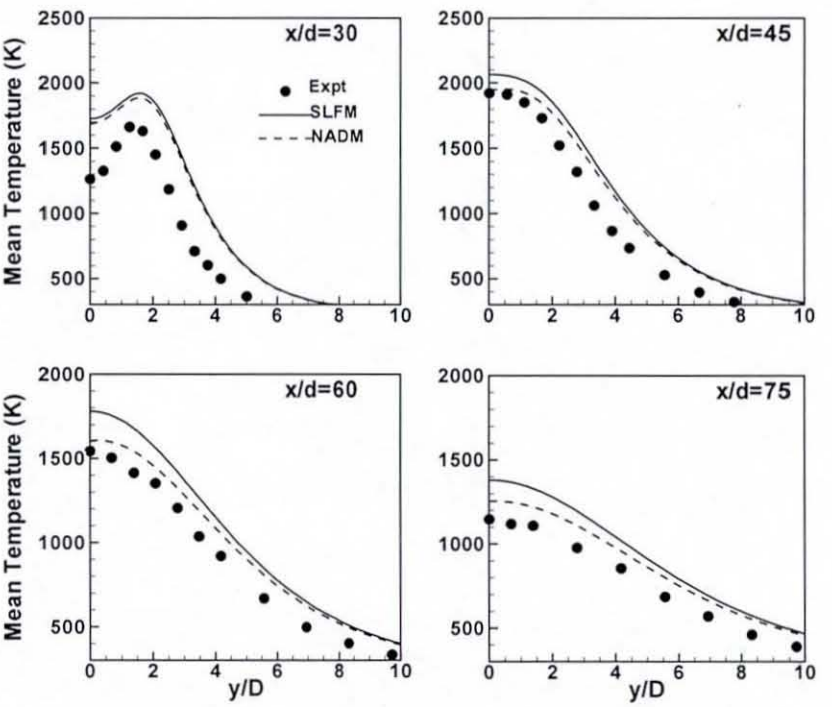

Figure 8.36: Radial profiles of mean temperature (K) at various axial locations in the Sandia D flame. Predictions from adiabatic and non-adiabatic RANS simulations with RST model for turbulent closure.

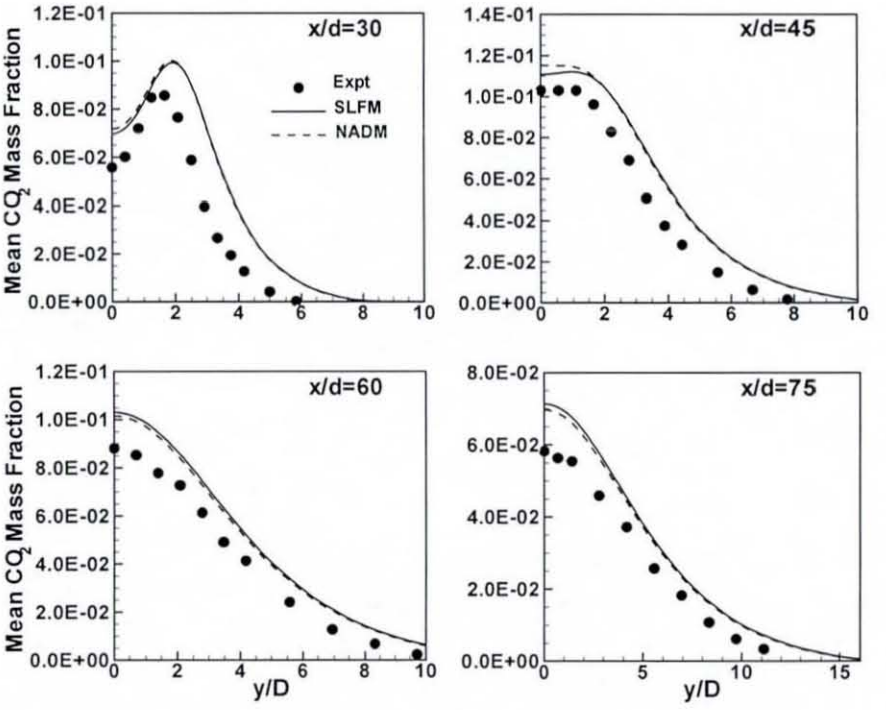

Figure 8.37: Radial profiles of mean CO_2 mass fraction at various axial locations in the Sandia D flame. Predictions from adiabatic and non-adiabatic RANS simulations with RST model for turbulent closure.

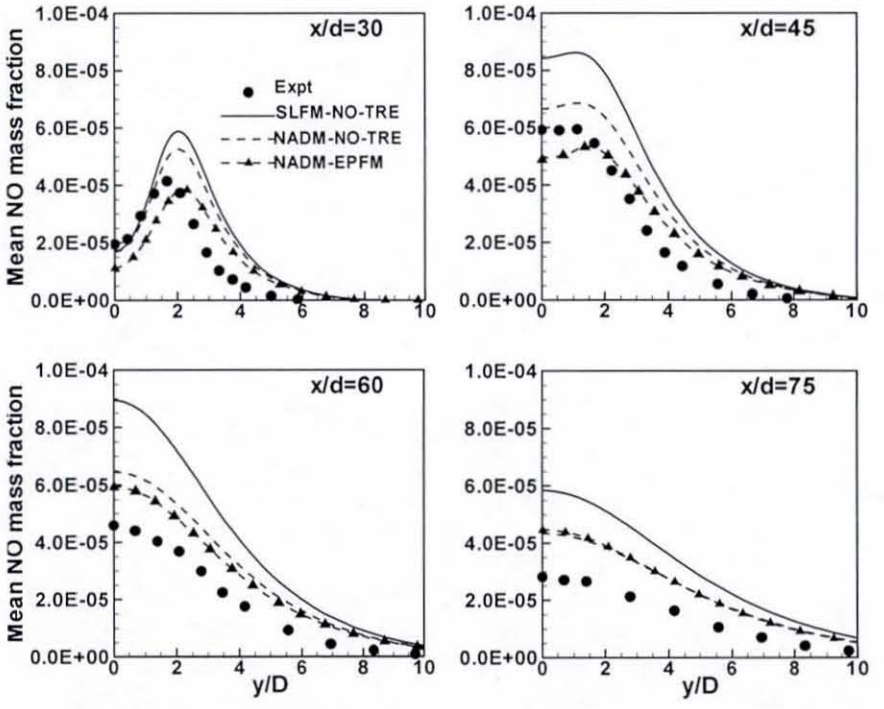

Figure 8.38: Radial profiles of mean NO mass fraction at various axial locations in the Sandia D flame. Predictions from adiabatic and non-adiabatic RANS simulations with RST model for turbulent closure.

Finally, the mean NO mass fractions are compared in Fig 8.38. Unlike the HM1flame where the transient effects dominate the radiation effects, the Sandia D flame shows dominant radiation effects. Comparing the steady non-adiabatic submodel NADM-NO-TRE predictions to its adiabatic counterpart SLFM-NO-TRE, remarkable improvements can be noticed at the locations x/D=45 to 75 which are also the locations where improvements in temperature have been obtained. Considering the complexity of NO chemistry, it is quite encouraging that a simple steady transport equation based approach could produce reasonably accurate results by considering the radiation heat loss.

Inclusion of transient effects in addition to radiation effects through the NADM-EPFM submodel helps in reducing the overprediction. However, transient effects are not as pronounced as they are in HM1 flame. This perhaps could be explained by the relative lengths of the flames. The location x/D =75 in Sandia D flame corresponds to 540 mm from burner exit while the last location of experimental measurements x/D =2.4 in HM1 flame corresponds to 120mm from burner exit. Thus, the residence time for the flamelets in Sandia D flame especially in the last two measurement locations must be much higher than in HM1 flame which brings their chemical structure closer to steady state and henceforth decreases the transient effects.

Overall, the strategy of turbulent flame calculations with NADM model and NO modelling with NADM-EPFM submodel provides a promising approach of modelling the detailed structure of turbulent non-premixed flames. By accounting for both the effects of radiation heat loss and transient nature of NO evolution, the strategy provides reasonable level of improvement over SLFM based modelling in accuracy as well as robustness. Additionally, for flames where transient effects are not pronounced, the strategy of NADM in conjunction with a much simpler NADM-NO-TRE submodel provides a valuable alternative. Future works can help in further corroboration of the predictive capability of the NADM model by employing the model in highly radiating flames where the effect of radiation heat loss on major species mass fractions is significant.

Chapter 9

Modelling of Turbulent Partially-premixed Lifted Jet Flame

In this chapter, results of the investigation carried into the capability of the Flamelet/Progress Variable (FPV) approach based combustion models, namely the FPV-δ function model and FPV-β function model, to account for turbulent partially premixed combustion occurring in a partially premixed lifted jet flame has been presented. Both the FPV models have been incorporated in LES as well as RANS frameworks thereby facilitating investigation of their predictive capabilities in both the simulation techniques. Additionally, RANS and LES based modelling has been carried out with SLFM to confirm its limitations.

The test case selected for modelling is the Berkeley CH_4/air lifted jet flame in vitiated co-flow, experimentally studied by Cabra *et al.* (2005). The vitiated co-flow results in conditions similar to those encountered in gas turbine combustors and furnaces when a partially premixed fuel interacts with recirculating hot combustion products. In addition, the vitiated co-flow introduces auto-ignition as a possible mechanism for flame stabilization in addition to premixed flamelet front propagation (Cabra *et al.*, 2005).

Description of the experimental set up and conditions for the test case have been presented in section 9.1. Computational set up for the RANS simulations is presented in section 9.2 while the set up for LES is presented in 9.3. A total of six simulations, three each in RANS and LES have been carried out using the SLFM, FPV-δ function model and FPV-β function model for the baseline line case conditions reported by Cabra *et al.* (2005). Results obtained from these simulations have been discussed in the final section, 9.4.

9.1 Experimental study of Berkeley lifted jet flame in vitiated co-flow

A schematic of the burner used for the experimental investigation of the partially premixed lifted jet flame by Cabra *et al.* (2005) is shown in Fig. 9.1 (a). It consists of a central nozzle with inner diameter of 4.57 mm and outer diameter of 6.35 mm. Fuel jet consisting of a mixture of 33% CH_4 and 66% air at a temperature of 320 K is issued from the central nozzle with a bulk velocity V_{jet}=100 m/s. Surrounded by the central nozzle is a perforated plate of 210 mm diameter through which vitiated co-flow air is issued at a velocity V_{coflow}=5.4 m/s. The surface of the perforated plate is located such that it is at a distance of 70 mm below the exit plane of the fuel nozzle. The vitiated co-flow consists of products of lean premixed H_2/air flame (equivalence ratio = 0.4) at 1355 K. The entrainment of ambient air into the co-flow has been delayed by incorporating an exit collar which surrounds the perforated plate. This and the significantly larger diameter of coflow compared to the fuel jet, make the flow-field of interest unaffected by the ambient air. Hence the flame can be treated computationally as a two-stream problem. The conditions presented above correspond to the baseline case studied by Cabra *et al.* (2005).

Experimentally captured image of the lifted flame is shown in Fig 9.1 (b). The lift-off height H, nominally corresponds to an average stabilization position of the flame. The absolute lift-off height H has been determined in the measurements by considering the lowest point where the luminosity of the flame has been detected. For the baseline conditions, the measured mean lift-off height normalized over fuel jet diameter has been reported to be H/D ~ 35. It has also been observed in the experiments that the lifted flame base is highly unstable and fluctuates by several times the jet diameter thereby resulting in extinction and re-ignition. The current lifted jet flame thus tests the capability of FPV models to predict the extinction and re-ignition phenomena as well.

The sensitivity of the lift-off height with respect to velocities of the jet and coflow and the coflow temperature has been studied through experimentation as well as Joint

PDF calculations with modified-curl mixing model by Cabra *et al.* (2005) and the results showed that the co-flow temperature was most influential. A 5 % drop in coflow temperature was found to roughly double the lift-off height. An important result from the parametric study was that auto-ignition of very lean mixtures which have the shortest ignition delay might be the controlling mechanism. This was based on the argument that the modified-curl mixing model which relies entirely on auto-ignition for initial flame stabilization was able to capture the measured sensitivity of lift-of height to coflow temperature. However, the experimental scattered data although limited with respect to number of measured locations, did not show such a preference for reactivity at very lean mixtures and hence the relative importance of auto-ignition and turbulent edge flame propagation in stabilizing these flames is still under investigation.

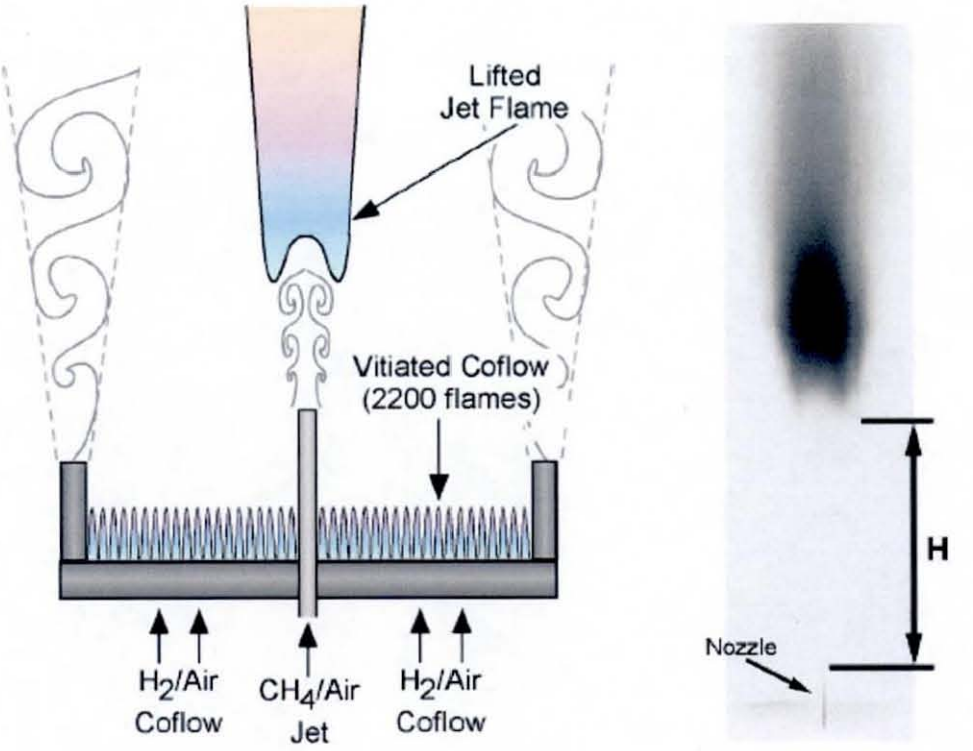

Figure 9.1: (a) Burner schematic and (b) measured image of a turbulent CH_4/air lifted jet flame in vitiated coflow. (Cabra *et al.* 2005).

9.2 Computational set up for RANS

The RANS calculations of the lifted flames have been carried out in a 2D axi-symmetric computational domain. Fig. 9.2 shows the computational domain which has been aligned vertically. Calculations are started from downstream (~15 D, where D =jet diameters) of the burner exit plane. This allows for fully developed flow at the burner exit plane. The burner wall thickness has been modelled and this separates the fuel jet and coflow until the burner exit plane. The computational domain extends by ~110 D from the burner exit plane in the axial direction and by ~22D in the radial direction. These lengths were selected to ensure that the predictions in the region of interest are not influenced by the boundary conditions on outlet plane and the co-flow boundary. At the outlet boundary, outflow conditions have been specified while symmetry conditions have been specified along the axis of symmetry and the co-flow boundary. Along the wall boundaries, no-slip conditions have been imposed along with log-law based standard wall functions.

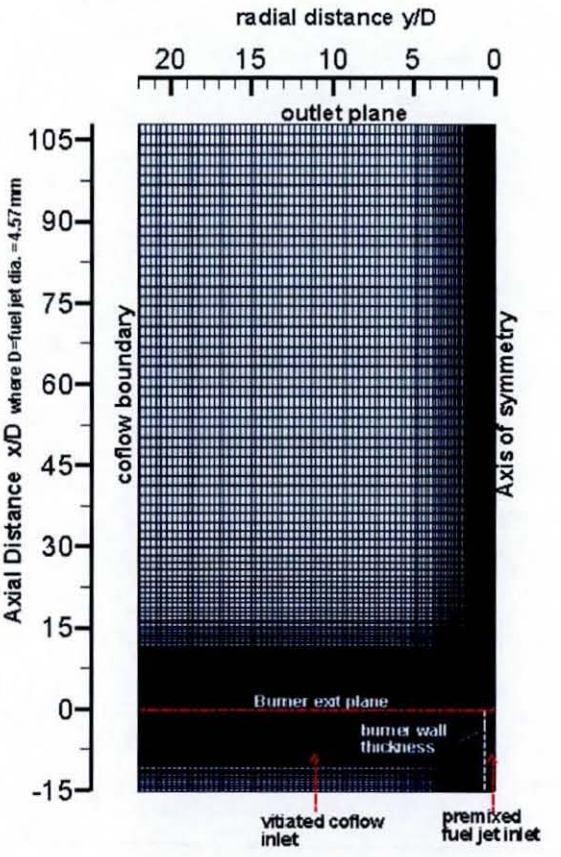

Figure 9.2: Computational domain and grid for RANS based simulations of Berkeley CH_4/air lifted flame. The grid consists of 198x110 nodes.

Near wall Reynolds stresses have been computed from turbulent kinetic energy using the algebraic functions (Eq. 4.34) while the shear stress has been solved with the condition of zero diffusion to the wall. At the inlets to the domain, bulk velocities, turbulent intensity (1%) and length scale (0.07 x inlet diameter) have been specified. The inlet Reynolds normal stresses have been derived from turbulent kinetic energy by assuming isotropic turbulence. The mean mixture fraction at the inlet of the premixed fuel stream has been specified as unity while for the vitiated coflow it is specified as zero. The variance of mixture fraction has been specified as zero at both the inlets. These conditions are sufficient for carrying out SLFM based calculations.

Calculations with FPV δ function model require specification of mean reaction progress variable $\tilde{C}$. This has been given as zero at both the inlets. For FPV β function model the variance of reaction progress variable $\widetilde{C''^2}$ needs to be additionally specified and this has been given as zero at both the inlets. The progress variable based FPV calculations require a source of ignition to start the calculations. This has been provided by patching a small region along the axis of symmetry with a value of $\tilde{C}$ which corresponds to burnt mixture. It is to be noted here that the choice of the location of ignition did not prove to be of any consequence to the mean flame stabilization height obtained after convergence of the calculations.

In the Fig 9.2, the grid used for the computations has also been shown. This grid has been tested to produce grid independent results and it consists of 198 non-uniformly spaced nodes along the axial direction and 110 non-uniformly spaced nodes along the radial direction.

9.3 Computational set up for LES

The LES simulations employ a three dimensional computational domain which is shown in Fig 9.3a. It extends axially (Z direction) 410 mm downstream from fuel jet inlet (~90 D) and has a square cross section with dimensions along X and Y extending up to 200mm (~44D). Unlike the RANS computations, the LES computations start right at the exit of the burner. Hence, as previously mentioned in section 6.6, mean

velocity distribution at the fuel inlet is specified through a $1/7^{th}$ power law profile (Eq. 6.34). Measured co-flow mean velocity profiles at the burner exit plane were found to be more or less uniform (Cabra *et al.*, 2005) and hence, plug flow has been specified along the coflow inlet in the computations. At both fuel and co-flow inlet, turbulent fluctuations have been superimposed on the mean velocity by scaling the measured rms values of turbulent fluctuations with random numbers obtained from a Gaussian distribution. At the fuel inlet, filtered mixture fraction has been set to unity while it has been specified as zero at the coflow. For the FPV models, the filtered progress variable and its subgrid variance have been set to zero at both the inlets.

All the walls have been treated as adiabatic and impermeable. Along the burner wall thickness which separates the fuel and co-flow inlets no-slip and zero normal gradient conditions have been assumed and the near wall flow has been modelled using log-law based wall functions. The co-flow boundaries were assumed to be artificial friction less walls and hence free-slip and zero normal gradient conditions have been imposed. At the outlet plane, convective outlet boundary conditions have been imposed.

Similar to RANS, computations with FPV model in LES too require a computational source of ignition at the start (t =0 sec.) of the time dependent calculations. This has been provided by patching a small region along the centerline (Z axis) with a value of $\tilde{C}$ corresponding to burnt mixture. Here again, the location and size of the patched region has been found to be of no consequence to the time averaged flame characteristics obtained at the end of the calculations. To nullify the effect of initial conditions on the final results, calculations with both SLFM and FPV models were run for a sufficiently long time (about 30 ms for the FPV models) before the collection of statistics for evaluation of the time averaged structure of the flame. Adequate samples have been collected in the statistics collection phase of the run by allowing for a minimum of 7 flow passes. The calculations have been advanced in time with a time step such that the variation in Courant number was limited to the range, 0.2 to 0.8.

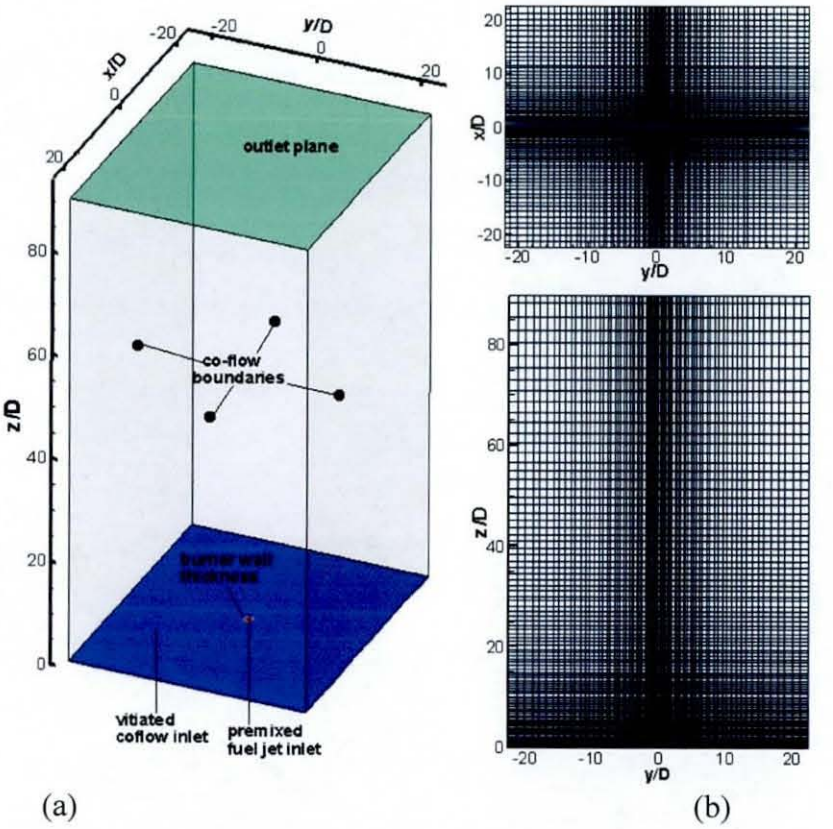

Figure 9.3: (a) Computational domain and (b) grid used for LES based modelling of Berkeley CH_4/air lifted jet flame

For the simulation with SLFM model, the modelled scalar dissipation rate (Eq .5.21) has been found to result in instability in the beginning of the calculations due to significant fluctuations in density. To overcome this problem, LES calculation with SLFM has been carried out initially with a constant scalar dissipation rate corresponding to equilibrium conditions for a minimum of two flow-passes (~10 ms). The instantaneous solution at the end of this calculation has then been used as initial conditions for the main calculation where variation in scalar dissipation was accounted. For the simulations with FPV models, no instability issues have been encountered either due to the chemical source term or the progress variable variance source terms.

The grid used for the computations is shown in Fig. 9.3 (b). The rectangular grids in z-y and x-y planes correspond to hexahedral cells in their three dimensional form. The distribution of grid points was not determined by any systematic rules, but rather by

experience and trail-and-error, although general requirements are that the grid should be smooth and refined along the axial direction at the fuel jet. The size of the grid is 85 x 85 x 150 cells in the X, Y and Z directions, respectively, and has been determined by cost considerations as the largest grid on which the simulations could be completed in a reasonable span of time. All the simulations have been serially processed on the in-house Linux High Performance Computing facility, Husky. The SLFM model based calculation required a total processing time of about 40 days while both the FPV models required nearly 30 days. The calculation with FPV-β function model however demanded significantly higher amount of RAM than that with the FPV-δ function model.

9.4 Results and discussion

In this section, predictions from RANS and LES based modelling with the three chemistry models, the SLFM, FPV-δ function model and FPV-β function model are compared to one another as well as with experimental measurements. The aim of these comparisons is to verify the accuracy with which the FPV models are able to capture the gross characteristics and behavior of the flame, such as flame lift-off, ignition and extinction associated with fluctuating flame base. Calculations of mean distributions of major species concentrations and pollutant NO are not the target of the current work. The results obtained from the three models with RANS calculations are presented first.

9.4.1 Performance of SLFM & FPV models in RANS

Mean mixing field and temperature distribution

The mean mixture fraction contours are shown in Fig 9.4. In each of the plots, the stoichiometric mixture fraction (Z_{st}=0.17) contour has been identified. For the SLFM, the shape of the contour and gradual spreading of the jet resemble the mixing characteristics in a typical diffusion flame. For the FPV-δ function model, careful observation of the Z_{st} contour and its fuel lean surroundings at x/D ~ 15 reveal a sudden expansion. This expansion is more pronounced with the FPV-β function

model and is observed to take place further downstream, x/D ~ 40. This expansion suggests a sudden rise in the heat release due to chemical reaction. Another noticeable difference between the models is in the level of fuel jet penetration. The level of penetration is highest with SLFM and lowest with the FPV β function model which, indicates that the level of entrainment of the vitiated co-flow air into the fuel jet is more in case in SLFM. The effect of these differences in mixing field on the temperature distribution can be observed in Fig 9.5. The higher level of jet penetration with SLFM is in fact an indication of an attached flame. The presence of a flame attached to the rim of the burner inhibits the entrainment of the vitiated coflow. The attached flame is illustrative of the inability of SLFM to handle partially premixed combustion typical in turbulent lifted flames. With quenching of partially premixed flamelets as the only possible means to a detached flame and no account of the degree of completeness of a chemical reaction, the SLFM is inadequate to predict flame lift-off.

On the other hand, both the FPV models are quite successful in predicting the lift-off phenomenon. The sudden expansion in mixture fraction distribution observed with the FPV models at a particular location above the burner corresponds to the stabilization of the flame at that location. Upstream of the base of the flame corresponds to an inert mixing zone where the premixed fuel jet mixes with the hotter vitiated coflow which not only increases the temperature of the fuel prior to ignition but also makes the fuel leaner. Stabilization of the flame with both the FPV models can be observed to take place along the stoichiometric contour.

However, the height at which the flame stabilizes above the burner seems to be influenced significantly by the form of the PDF for reaction progress variable. The δ function model ignores the fluctuations in progress variable which, although simplifies the FPV formulation, is a gross treatment especially when used with RANS. As a consequence, the flame stabilizes at almost half the height at which flame stabilization is predicted by the β function model. In the β function model, the chemical source term is influenced by both the mean and variance of reaction progress variable and this can be observed to result, not only in a greater lift-off height but also a wider flame base. Given the measured lift-off height H/D ~ 35, the flame structure predicted by FPV-β function model seems to be in better agreement.

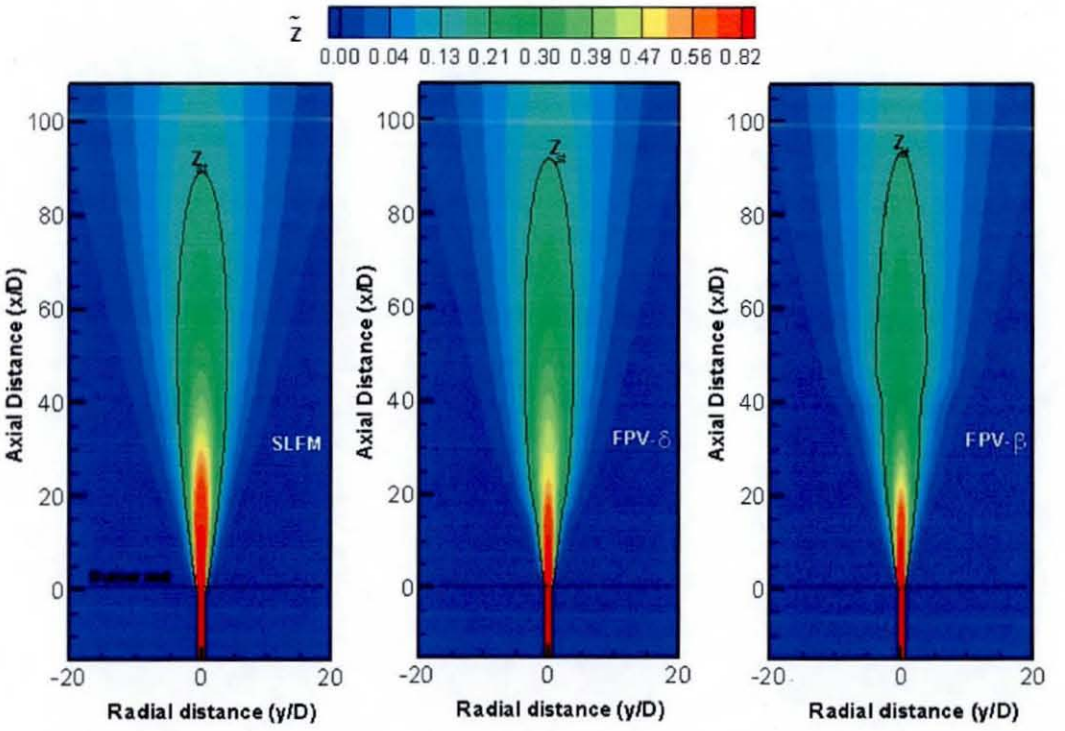

Figure 9.4: Predictions of mean mixture fraction contours from RANS simulations of Berkeley CH_4/air lifted jet flame at baseline conditions.

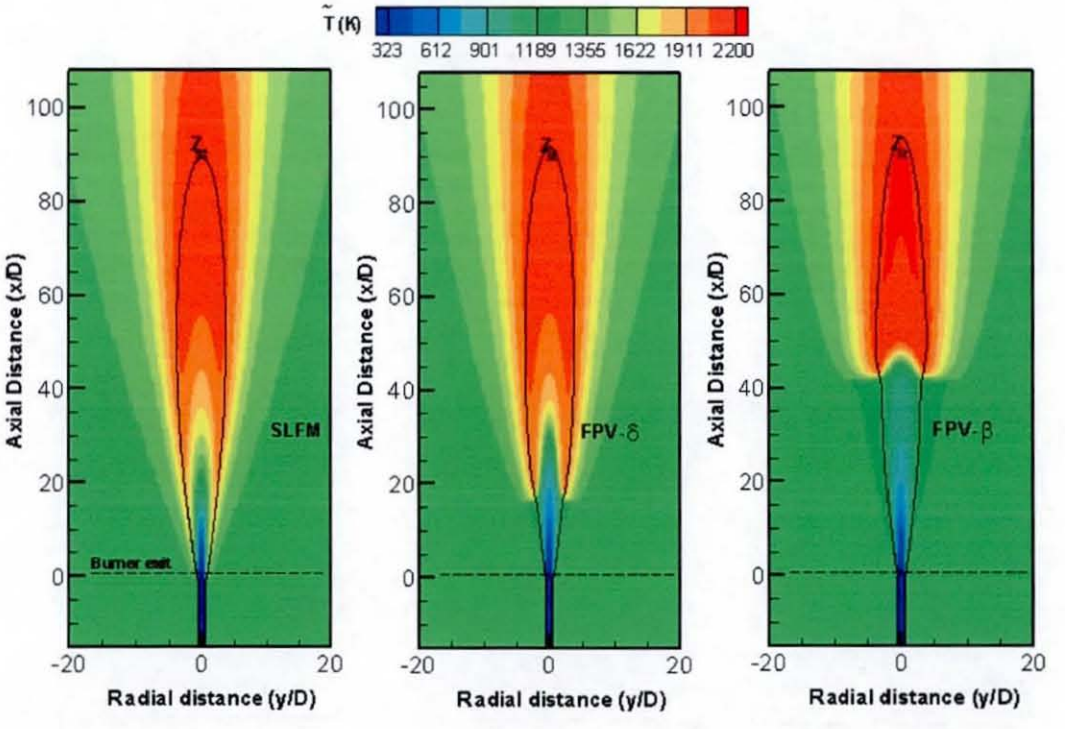

Figure 9.5: Predictions of mean temperature contours from RANS simulations of Berkeley CH_4/air lifted jet flame at baseline conditions.

For a quantitative comparison with the measured lift-off height, a definition has to be in place for estimating the lift-off height from predictions. As previously mentioned, the definition of lift-off height as per the measurements relies on the lowest location where luminosity in the flame is detected. Measurements also indicate that the peak of the light emitting species occurs at nearly the same location as the peak of the maximum heat release. Cabra *et al.* (2005), for their predictions from Joint PDF calculations, employed a definition based on the average of the axial locations where peaks of C_2H_4 and C_2H_2 occur. These intermediate species have been observed to bracket the maximum heat release according to their results from auto-ignition calculations. For the current computations with FPV models, use of the above definition is prohibited by computational cost considerations. Hence, the axial location, at which peak chemical source term which is representative of peak heat release, has been used to estimate the lift-off height.

Mean chemical source term distribution

The distributions of mean chemical source term as predicted by each of the FPV models are shown in Fig 9.6. A distinct thin zone where the chemical source term is subjected to steep variation can be observed in both the plots. This zone corresponds to the mean lifted flame base and it can be seen that the FPV-δ function model predicts a narrower flame base as compared to β function model. Within this zone, the peak values of the chemical source term are found to occur at or around the vicinity of stoichiometric mixture fraction. For a model which does not consider the variance in progress variable, it is expected that the chemical source term be higher than when variance is considered. The peak value of chemical source term as predicted by FPV-δ function model is ~ 600 (kg/kg-s) although the maximum level in the contours has been curtailed for the sake of clarity. And this occurs at the axial location x/D ~ 17.2 which is in comparison to the measurements is nearly 50% shorter. In comparison to this, FPV-β function model predicts a peak value of chemical source ~350 (kg/kg-s) at the axial location x/D ~ 43. Thus, although the lift-off height is overpredicted by about 27%, the FPV-β function model clearly has better physics incorporated. For further investigation into the performance of the FPV models, comparisons have been made between the predicted and measured radial profiles of mean mixing field and mean temperature.

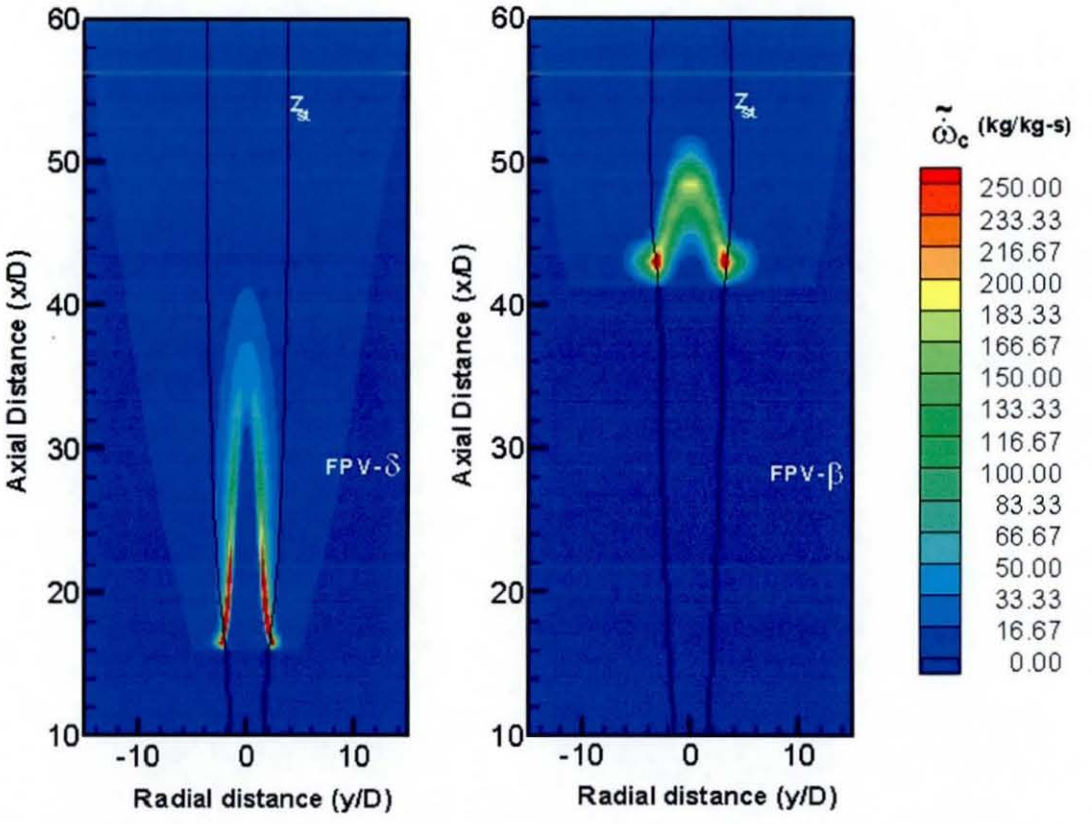

Figure 9.6: Predicted distribution of mean chemical source term from RANS simulations of Berkeley CH_4/air lifted jet flame at baseline conditions.

Radial profiles of mean temperature

Figure 9.7 compares the measured radial profiles of mean and rms fluctuations of mixture fraction with predictions from RANS–FPV calculations at various axial locations in the flame. At x/D=1.0, which is the location right adjacent to burner exit, measurements indicate steep variation in the mean mixture fraction which corresponds to inert mixing while the rms fluctuations indicate a sharp peak corresponding to the shear layer between the jet and coflow. At this location (x/D=1.0), the mean mixture fraction predictions from both the FPV models are in good agreement with measurements while the predictions from SLFM show a slightly broader profile that suggests an attached flame. The peak value of rms fluctuations at this location is overpredicted by all the models while the SLFM predicts a broader profile. The presence of chemical reaction and hence an attached flame with SLFM is

apparent from the radial profiles of mean temperature shown Fig 9.8. At x/D=1.0, the SLFM predictions show a sudden rise in the temperature above the coflow temperature of 1355 K while both the FPV models capture the measured behavior.

At x/D =15.0, the measured mean and rms fluctuations of mixture fraction and temperature profiles are slightly broader as compared to the first location however no sign of chemical reaction is indicated as the maximum temperature corresponds to that of coflow. The broadening is hence entirely due to the entrainment of the vitiated air into the jet which also raises the temperature of the fuel jet. The SLFM results in significant overprediction in the mean and rms fluctuations of mixture fraction as well as the temperature which corresponds to the unrealistic chemical reaction at this location. The mean mixture fraction predictions from both the FPV models at this location are in good agreement with the measurements although the predicted radial distribution is somewhat broader. Since, the conditions at this location are of pure inert mixing, the discrepancy in mean mixture fraction seems to be entirely due to the overprediction of jet spreading rate by the RST turbulence model. This also seems to be cause for the overprediction in the rms of mixture fraction fluctuations and the slight underprediction observed in the mean temperature at this location.

At x/D =30.0, the measured mean temperature profile still shows no indication of chemical reaction. However, both SLFM and FPV-δ function model indicate the presence of a flame. The predicted mean temperature profiles provide an indirect indication of the location of flame stabilization. As already mentioned, the FPV-δ function model underpredicts the mean lift-off height and results in flame stabilization at x/D ~17.2. The presence of flame increases the extent of penetration of the jet and the radial spread and this explains for the significant overprediction in the mean and rms fluctuations with the FPV-δ function model as well as SLFM. The FPV-β function model however predicts an inert mixing zone inline with the measurements at this location.

At x/D =40.0, the measured mean temperature profile indicates the existence of chemical reaction with the peak value of mean temperature (1500 K) exceeding the coflow temperature. This corroborates the measured observation that the flame stabilizes at x/D ~35. Both SLFM and FPV-δ function models result in appreciable

overprediction of the mean temperature as well as the mean and rms fluctuations of mixture fraction due to the early occurrence of the flame. On the other hand, the mean temperature profile predicted by the FPV-β function model still shows no signs of chemical reaction with the maximum mean temperature still equal to that of coflow (1355 K). This corroborates the finding that the FPV-β function model overpredicts the lift-off height and hence even at x/D=40.0, the model predicts inert mixing condition. The overprediction in mean stabilization height with FPV-β function model explains for the discrepancy in its predictions of mean temperature and the mean and rms fluctuations of mixture fraction. The predicted mean temperature and mixture fraction at the centerline however can be observed to be in good agreement with measurements. This is because, in practice, although the flame stabilizes at x/D =35.0, its fuel core extends by more than 5D before a substantial change in mixture fraction or temperature due to entrainment could be felt. Hence, at x/D=40.0, the measured centerline mean temperature is only a 100 K higher than that at x/D=30.0.

From the distribution of chemical source term (Fig 9.6) it was found that the FPV-β function model predicts flame stabilization at x/D ~ 43. This finding is validated by the prediction of chemical reaction by FPV-β function model at x/D=50.0. The FPV-β function model along with SLFM and FPV-δ function models, predicts peak mean temperatures close to 2000 K. However, the measured centerline and peak temperatures are much lesser (by 500 K) than the predictions from all the three models at this location (x/D=50.0).

The overprediction in mean temperature with both the FPV models at this location seems to be a manifestation of the discrepancies observed in the predicted mean stabilization heights. Also, Cabra *et al.* (2005) reported from their measurements that the flame base was found to fluctuate along the vertical distance by several jet diameters (x/D=30 to 50 or more). Fluctuation of the flame base is associated with extinction and re-ignition phenomena which consequently result in mean temperatures than are lower than those observed with a stable flame base. Thus, it seems that the RANS calculations with FPV models are unable to account for fluctuation in the flame base.

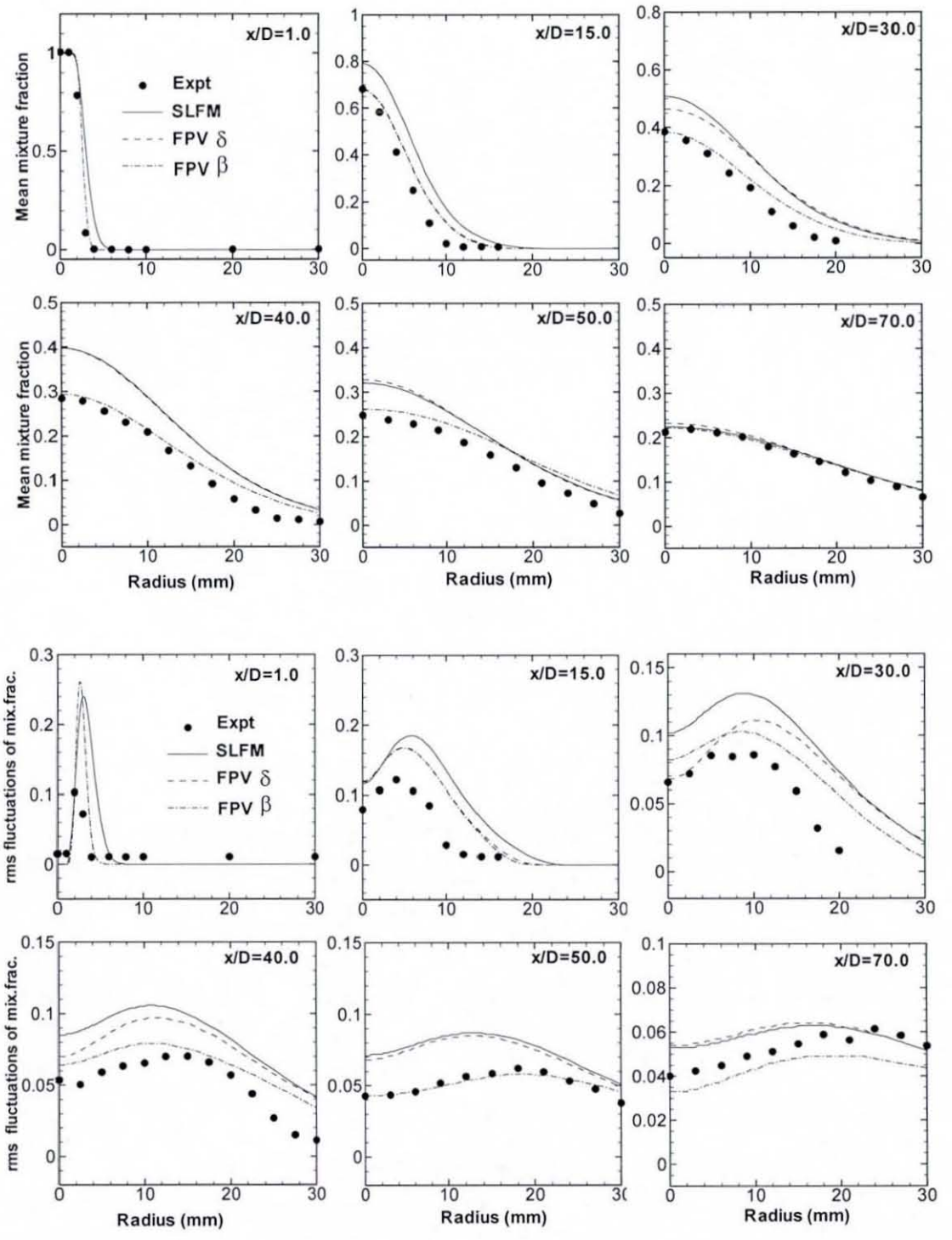

Figure 9.7: Radial profiles of mean and rms fluctuations of mixture fraction at various axial locations in Berkeley CH_4/air lifted jet flame. Predictions correspond to RANS calculations at baseline conditions.

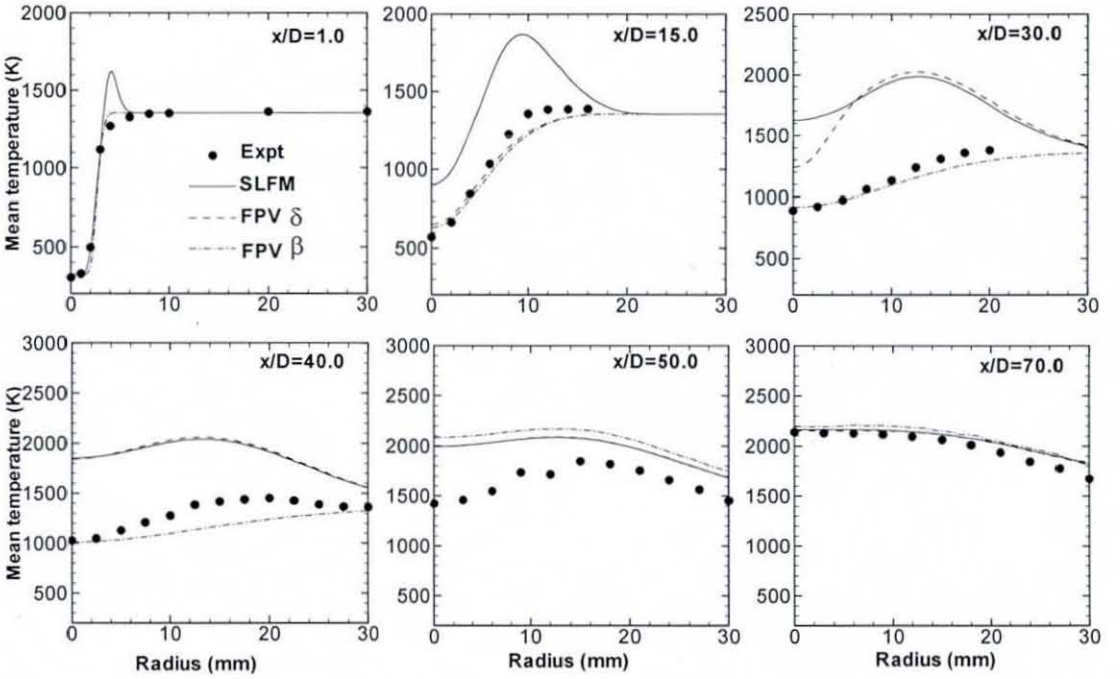

Figure 9.8: Radial profiles of mean temperature (K) at various axial locations in the Berkeley CH_4/air lifted jet flame. Predictions correspond to RANS calculations at baseline conditions.

Also, present calculations have not considered the effects of radiation heat loss which may be important given the high temperatures prevalent at this location. (x/D =50.0). Thus, it is not clear as yet whether the overprediction in mean temperature observed at this location (x/D=50.0) is due to (1) omission of radiation heat loss or (2) limitations in steady RANS modelling approach or (3) limitations in the FPV formulation. The results obtained from LES based modelling with FPV models (discussed in section 9.4.2), provide a fair idea on the extent factors 2&3 contribute the discrepancy.

Finally, at x/D =70.0 which is sufficiently far from the flame stabilization region, the measured and predicted mean and rms fluctuations of mixture fraction and the mean temperature are in good agreement for all the three models. The fact that the predictions from SLFM are similar to those from FPV models indicates that the flame at this location burns essentially as a diffusion flame and the reaction has reached its completion which corresponds to the condition of maximum progress variable in the

FPV calculations. Also, the fluctuations in reaction progress variable are negligible as indicated by the similarity in the predictions of both the FPV models.

9.4.2 Performance of SLFM & FPV models in LES

In LES of reacting flows, all the chemical scales are unresolved and hence, similar to RANS, combustion is entirely modelled. Thus, the combustion models, SLFM, the FPV-δ function model and the FPV-β function model, are common to both RANS and LES expect for the few differences discussed in Chapter 5. However, in LES, the large scales of turbulence which contain the majority of the turbulent kinetic energy and have significant influence on mixing characteristics, are resolved unlike in RANS where all the scales of turbulence are modelled. Since turbulence and chemistry are coupled in reactive flows through the variable density, elaborate accounting of unsteady large scale turbulent motion, in principle, is expected to improve the thermo-chemical structure predictions of the turbulent flame in comparison to RANS. Thus, it is of interest to verify the predictive capability of the combustion models, particularly the FPV-δ function and β function models in LES. Also, since LES involves time marching calculations, it is of particular interest to verify the ability of the FPV models to capture the unsteady phenomenon of fluctuating flame base.

Mean temperature distribution

The mean temperature distributions predicted by SLFM, FPV-δ function model and FPV-β function model when employed in LES are shown in Fig 9.9. The mean temperatures have been obtained from LES by time averaging the instantaneous filtered temperatures collected for a time period of 30 ms during the statistics collection phase of the LES run. From the mean temperature contours, it is clear that the trend observed with RANS simulations has been reproduced by LES. The SLFM results in an attached flame while both the FPV models are able to predict flame lift-off with the FPV-δ function model predicting a shorter lift as compared to the FPV-β function model.

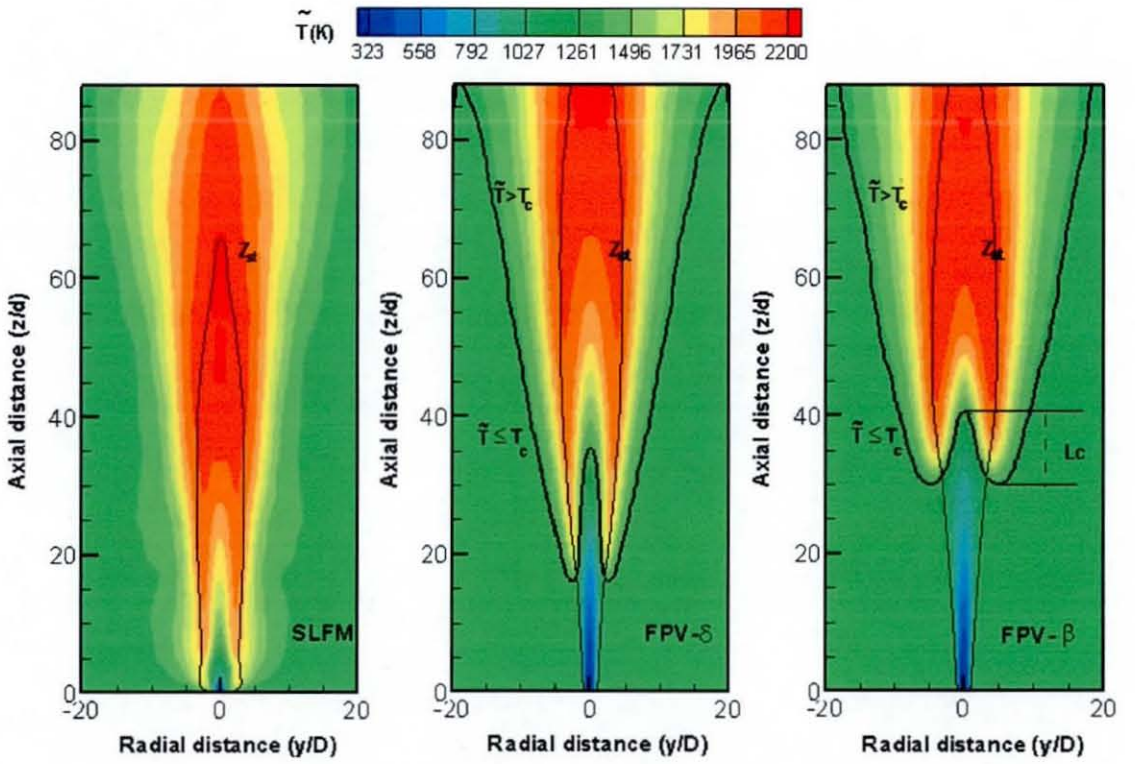

Figure 9.9: LES predictions of mean temperature (K) contours for Berkeley CH_4/air lifted jet flame at baseline conditions. Contours plotted along the mid-plane (X=0) of the LES computational domain.

For the FPV-β function model, the mean temperature predictions from LES show a noticeable difference in comparison to RANS (Fig 9.5). The lowest axial location where the mean temperature crosses the co-flow temperature (Tc = 1355 K) is lowered by more than 10 jet diameters with LES in comparison to RANS where the crossover occurs only after x/D ~ 40. This is expected to correspond to a stabilization height lower than that predicted with RANS (x/D ~ 43). Infact, using the peak chemical source term as the indicator for the location of flame stabilization, the stabilization height with FPV-β function model in LES has been found to occur at the axial location z/D ~ 35.4. This is in excellent agreement with the measured lift-off height of H/D ~ 35 thereby indicating a remarkable improvement in the predictive capability of the FPV-β function model.

Another noticeable difference in the LES and RANS mean temperature predictions with the FPV-β function model is in the axial length of the fuel rich core region that is

surrounded by the flame base or the flame stabilization region. The axial length of the fuel core region has been identified by Lc in Fig 9.9. For convenience of studying the differences between LES and RANS predictions, Lc is defined here as the distance between the upstream and downstream ends of the flame stabilization region where the mean temperature equals the coflow temperature. The boundary which demarcates the region of the flame which has a mean temperature less than equal to coflow and the region with a mean temperature above coflow has been identified by Tc in the Fig 9.9. The LES predictions show the core extending by roughly 10D (z/d ~ 30 to 40) while the RANS FPV-β function model predictions (Fig 9.5) indicate a core of roughly half the length (x/D~41 to 45).

Similar differences between LES and RANS could be observed with mean temperature predictions from FPV-δ function as well. The RANS predictions (Fig 9.5) indicate that the fuel core region surrounded by flame stabilization region extends by ~ 15D (x/D ~16 to 31) while LES predictions show the core region extending by ~20D (x/D ~15 to 35). The stabilization height with FPV-δ function model in LES has been found to occur at the axial location z/D ~ 24.4 based on the peak chemical source term. This is an encouraging improvement in comparison to RANS where the predicted height with the FPV-δ function model was x/D ~17.2. However, in comparison to the measured lift-off height, the LES FPV-δ function model predictions are still 30% lower.

An increase in the length of the core observed with both the FPV models could be an indirect indication that the LES calculations are able to predict extinction and re-ignition associated with the unsteady behavior of the flame base. This is based on the argument that if the flame base were to fluctuate by several diameters along the axial length, the length of the central core too should extend by similar magnitude and eventually the mean length of the core should be longer than that for a stable flame base. In order to verify if there is any merit in this argument, instantaneous snapshots of filtered temperature distribution have been studied.

Instantaneous temperature distribution

In Fig 9.10, the instantaneous filtered temperature distributions predicted by LES FPV-β function calculations have been shown for 6 different times. In all the contour plots, the boundary Tc serves as a guide for locating the flame base and consequently the fuel core region that it surrounds. The instantaneous shape of the flame base can be observed to be highly asymmetric and corrugated and varies significantly with respect to time.

At time t = 0.0 ms, the fuel core region has an axial length of roughly 10 D (z/D~ 30 to 40) and its width is rather uniform. At time t =2.5 ms, the downstream end of the flame stabilization zone can be observed to have extended till x/D ~ 53. This corresponds to a fuel core region of length ~23 D which is double that observed at t=0.0 ms. The width of the fuel core region is no longer uniform and its reduces from the upstream end of flame stabilization to the downstream end. At time t =5.0 ms, it is evident that the waning of the downstream end of flame stabilization zone has already begun. The length of the fuel core can be observed to have decreased by approximately 5D while the fuel core has partly regained uniformity in its width. As the location of the downstream end of the flame stabilization zone decreases to z/D < 40 at time t=11.5 ms, the length of the fuel core too can be observed to have decreased to less than 10 D. And this decrease in the length is associated with an increase in the width of the fuel core which is now more uniform than at time t = 0.0 ms. Thus, the fluctuation in the downstream end of the flame stabilization zone has a direct influence on the characteristics of the fuel core region.

Therefore, it is confirmed that the increase in the mean length of the core observed in the LES predictions (Fig. 9.9) of both the FPV models is indeed an indication of the ability of the models to predict the fluctuation in the flame base and hence the phenomenon of extinction and re-ignition. The instantaneous plots in Fig 9.10 indicate that the predicted fluctuation is mainly that of the downstream end of the flame stabilization zone and it occurs in both axial and lateral directions. The extent of fluctuation in the height of the upstream end of the flame stabilization zone which lies more or less on the Z_{st} contour is not appreciable. Hence the predicted extinction and re-ignition is essentially on the fuel rich side of the stoichiometric mixture fraction.

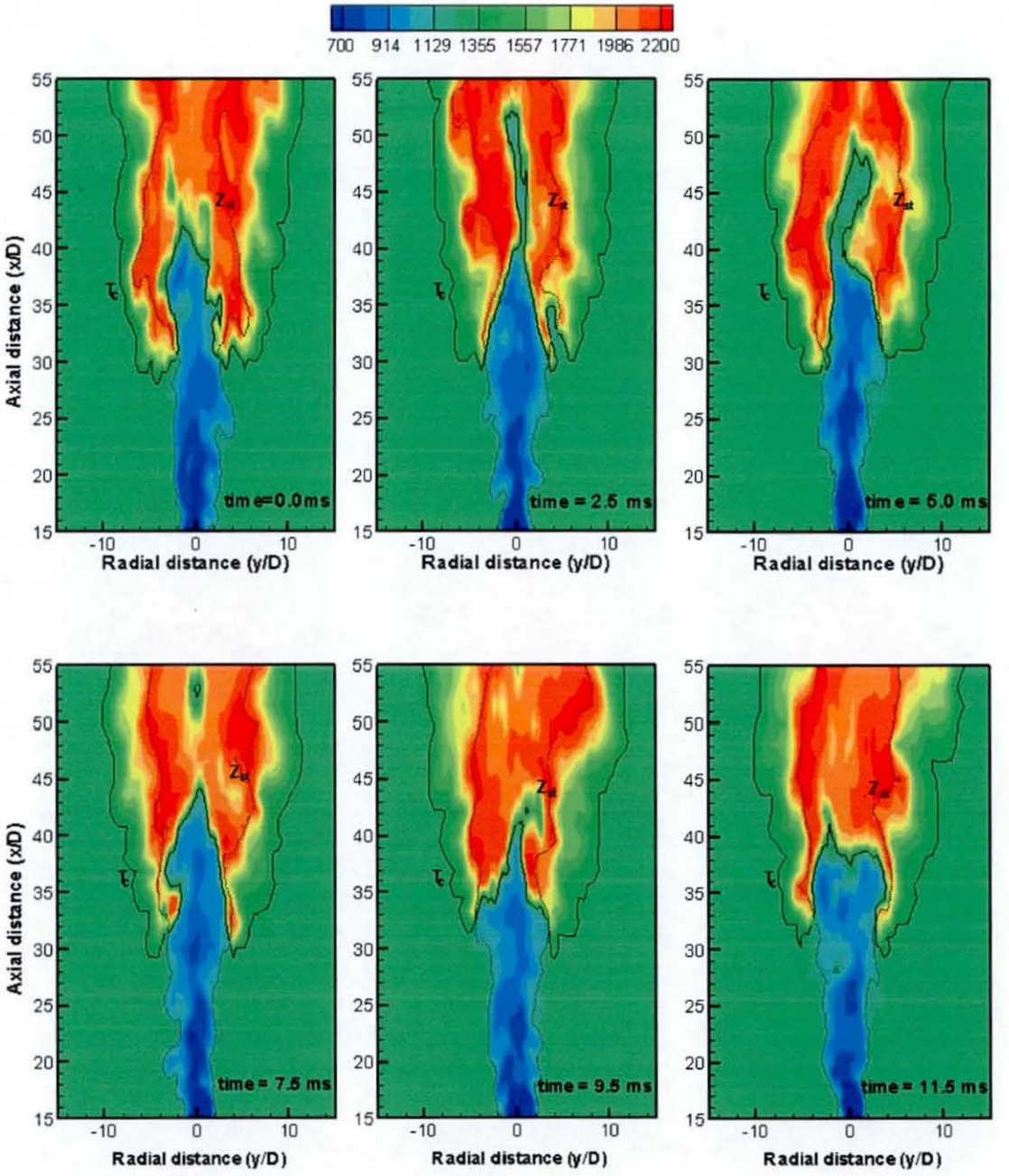

Figure 9.10: Variation in the instantaneous filtered temperature (K) distribution with respect to time. LES FPV-β function model predictions of Berkeley CH_4/air lifted jet flame at baseline conditions. All contours plotted along the mid-plane (X=0) of the LES computational domain.

Similar findings have been found from the instantaneous filtered temperature distributions of FPV-δ function model and hence not shown here. The quantitative accuracy of these findings has been verified by means of scattered temperature data comparisons which are discussed next.

Scattered temperature data

In addition to the radial profiles of mean mixing field and reactive scalars, Cabra *et al.* (2005) have provided the scattered data of temperature for the CH_4/air lifted jet flame for the baseline conditions. In the LES calculations with FPV models, the instantaneous filtered temperature distributions across the domain have been stored over a period of 30ms during the statistics collection phase of the run. These distributions were used to extract the predicted scattered data for temperature.

In Fig 9.11, the experimental and measured scattered data for temperature has been plotted for various axial locations in the flame along the mixture fraction space. The experimental data at the first (z/D=30.0) and the last (z/D=70.0) locations correspond to the two limiting states of the turbulent flame. The majority of the experimental samples at location z/D=30.0 represent the inert mixing state while those at z/D=70.0 are fully reacted and represent equilibrium limit. Between these two locations, the measured behavior of the flame is essentially bimodal. The majority of the samples lie close to mixing or equilibrium limits with relatively lesser number of partially reacted samples in between. These partially reacted samples are greater in number in the conditions prevailing on the fuel rich side of the stoichiometric mixture fraction than on the fuel lean and at the stoichiometric conditions. From the measured samples at z/D=30.0 there is already evidence of chemical reaction while at z/D=50.0 there are still numerous samples which are in inert mixing state. Hence, the lifted flame base fluctuates over a vertical distance of about 20 D.

Focusing attention on the FPV-δ function model predictions at the axial location, z/D = 30.0, it can be seen that the majority of the samples have already reached the equilibrium limit. This corroborates the finding that the model underpredicts the lift-off height even with LES. Between the conditions of Z=0 to 0.4, few partially reacted

samples can be observed but none of them reach the inert mixing condition. Presence of samples in the inert mixing state can only be observed for the conditions of $Z > 0.4$ which prevail within the fuel rich core region. The significant amount of extinction and re-ignition occurring within this region indicate that the fluctuations in the flame base are mainly in its downstream end. Such an observation has also been made from the contours of instantaneous filtered temperature distributions (although shown only for FPV β function model in Fig 9.10).

In contrast to the FPV-δ function model, the FPV-β function model predictions at z/D =30.0 are in good agreement with the measured behaviour of the flame. The FPV-β function model predictions show the existence of samples corresponding to pure mixing along the entire range of mixture fraction conditions with partially reacted states restricted to conditions of $Z < 0.4$. Similar to experiments, the majority of samples are in the inert mixing state thereby indicating that flame stabilization has occurred further downstream. The broad distribution of the samples predicted by FPV-β function model are quite consistent with the measurements and also are similar to the predictions reported by Cabra *et al.* (2005) from their RANS joint PDF calculations with the M-Curl and EMST mixing models.

At z/D=40.0, the FPV-δ function model predictions fail to capture the measured bimodal behavior. Majority of the predicted samples are fully reacted and are in the equilibrium state. Due to the shorter flame stabilization height with the δ function model, the jet penetration is overpredicted and this results in conditions of $Z > 0.4$ which are non-existent in the measurements. However, for the fuel rich conditions of $Z > 0.4$, the δ function model does predict a fair amount of samples in inert mixing and partially reacted states thereby showing that the predicted fluctuation in the downstream end of the flame base extends till z/D =40.

Studying the FPV-β function model predictions at z/D =40.0, the predicted conditions of the mixture fraction (Z=0 to 0.4) can be found to be in excellent agreement with measurements. This suggests that the predicted extent of fuel jet penetration and hence the height of flame stabilization, are inline with the measurements.

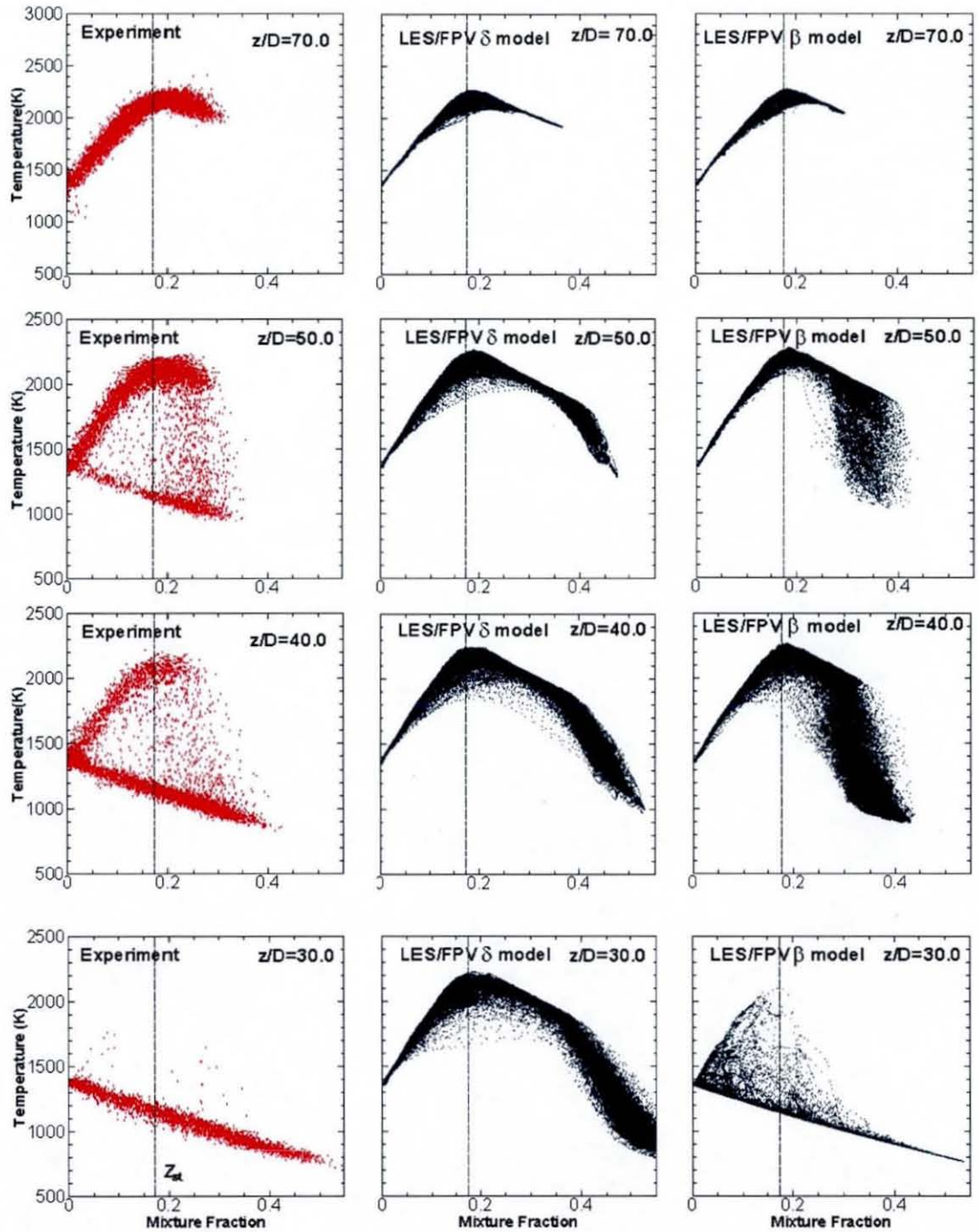

Figure 9.11: Predicted and measured distributions (scattered data) of instantaneous temperature (K) at four axial stations in the Berkeley CH4/air lifted jet flame at baseline conditions.

A significant amount of fully reacted samples can be observed from the predictions and hence the flame stabilization can be confirmed to have occurred between the axial locations, z/D=30.0 and 40.0. This corroborates the finding that, the lift-off height predicted by FPV-β function model with LES is around z/D~35.4 Unlike the δ function model, the β function model is able to successfully predict significant amount of inert mixing and partially reacted states between Z=0.3 to 0.4.

However, similar to the δ function model, the β function model is also unable to predict the inert mixing states for conditions at or on the fuel lean side of the stoichiometric mixture fraction. This is consistent with the previous observation from the instantaneous temperature plots in Fig 9.10, that the fluctuations in the upstream end of flame base are rather modest in comparison to its fuel rich downstream end.

At z/D=50.0, the FPV-δ function model predictions show no trace of inert mixing along the entire range of the mixture fraction conditions. Due to the underprediction in the lift-off height, the fluctuations in the flame base do not reach as far z/D=50.0. Discrepancy in the predicted mixing conditions due to shorter lift-off height is evident at this location as well. While the measured conditions are limited to Z=0.35, the predicted conditions with FPV-δ function model exist beyond Z=0.4. The mixture fraction conditions predicted by FPV-β function model on the other hand are relatively in better agreement with measurements although the conditions are slightly richer. This discrepancy can be attributed to the fact that although the β function model is able to predict the correct mean lift-off height, it is unable to predict the measured extent of fluctuations in the upstream end of the flame base. Hence the extent of entrainment of the coflow air is underpredicted which leads to fuel conditions in the core richer than measured. Fluctuations in the downstream end of the flame stabilization zone are however well predicted by the β function model as indicated by the presence of inert mixing states between Z=0.3 to 0.4.

Further downstream at z/D=70.0, both the FPV models result in fully reacted samples and the predictions are inline with the measurements. The form of the PDF for the reaction progress variable can be observed to be of less consequence at this location. The flame is fully reacted and the fluctuations in the progress variable are negligible. Hence the shape of the β PDF tends towards a δ function.

From the scattered data comparisons, it is clear that the accuracy of FPV-β function model in predicting the fluctuation in the fuel rich downstream end of the flame base is superior to that of δ function model. The FPV-β function does exceedingly well in capturing the broad flame base of the lifted flame. However, neither the FPV-β function model nor the δ function model are able to completely predict the measured level of fluctuations in the upstream end of the flame base which prevails in conditions at or on the fuel lean side of the stoichiometric mixture fraction. The reasons behind this discrepancy are not clear.

Radial profiles of mean temperature

It is now clear that both the FPV models predict, with LES, certain degree of extinction and re-ignition associated with the flame base fluctuation and the mean lift-off heights are significantly improved in comparison to RANS. The underprediction in mean lift-off height with FPV-δ function model is reduced from 50% (in RANS) to 30% (in LES) while the overprediction in mean lift-off height with FPV-β function model is completely addressed with LES. The extent these improvements affect the mean temperature distribution predictions within the flame has been verified by comparing the radial profiles of temperature shown in Fig 9.12.

At z/D=1.0, the RANS predictions show slightly better accuracy than LES predictions. This may be due to the better flow conditions at the burner exit. With RANS, the extended inlet allows for simulation of flow conditions at the burner exit while for LES the computational domain starts at the burner exit plane and approximate mean velocity profiles have been mapped at the inlets. However, the effect of inlet conditions is only short lived and infact at z/D=15.0, the LES predictions with both the FPV models are better than those of RANS.

At z/D=30.0, the LES predictions with FPV-δ function show improvement over RANS although the deviation with respect to measurements is still substantial. This is due to the fact that with LES, the FPV-δ function model predicts a mean lift-off height of z/D~24.4 in comparison to x/D~17.2 with RANS. Thus although the mean lift-off

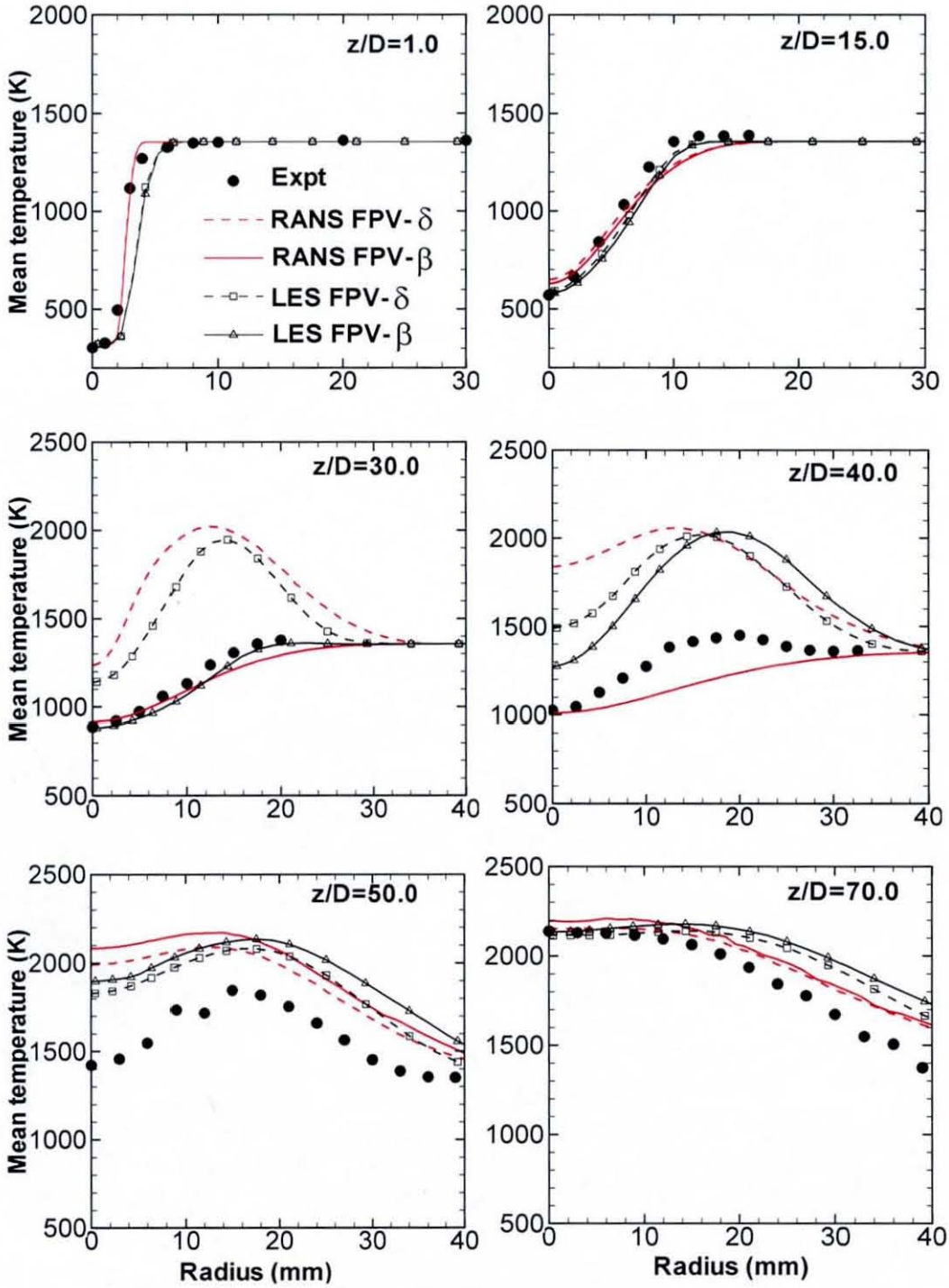

Figure 9.12: Radial profiles of mean temperature at various axial locations in Berkeley CH_4/air lifted jet flame at baseline conditions.

height is improved with LES, it is still 30% lower than the measured height. Comparison of the LES and RANS predictions with FPV-β function model at z/D=30.0, shows minor improvements with LES predictions in the fuel lean conditions (radius=20mm). This can be attributed to the model's ability in LES to predict both partially reacted and inert mixing samples at this location (Fig 9.11).

Downstream at z/D =40.0, the FPV-δ function model with both RANS and LES can be observed to result in overprediction due to the shorter flame stabilization height. However, the overprediction observed with FPV δ function model in RANS, is significantly reduced (up to ~500K) near the centerline by its use in LES. This seems to be the effect of FPV-δ function model's ability in LES to predict notable amount of fluctuation in the downstream end of the flame base which lies in fuel rich conditions but not quite in the upstream end where the conditions are at or on the leaner side of stoichiometric mixture fraction Thus, the deviation observed with RANS FPV-δ function model predictions at this location can be attributed to both the model's limitation to predict shorter lift-off height as well as the inability of RANS modelling approach to facilitate accounting of large scale fluctuations.

At the same location (z/D=40.0), the FPV-β function model predictions with LES show a qualitative improvement over RANS in that the occurrence of chemical reaction is captured at this location. Since the β function model in LES is not able to capture the same level of extinction as measurements indicate at this location (Fig 9.11), the mean temperature distribution is overpredicted. Still, the mean temperatures near centerline are better predicted by LES FPV-β function model than LES δ function model. This is consistent with the FPV-β function model's prediction of greater number of partially reacted samples on the fuel rich side of stoichiometric mixture fraction (z/D=40.0 in Fig. 9.11).

At z/D=50.0, the improvements with LES are rather modest since neither of the models is able to predict the same level of bimodality as observed in measurements. (Fig. 9.11). With either of the models, the overprediction observed with RANS, is improved near the centerline (up to 200K) with LES. However, away from the centerline RANS predictions seem to fare better with either of the models. Such a trend could be observed for z/D=70.0 as well. While the exact reasons behind the

better accuracy with RANS are not clear from the present level of investigation, it seems that the tendency of the models, in LES, to predict extinction only in the fuel rich region close to centerline seems to have rather complicated effects on the mixing characteristics and consequently the temperature.

Thus, the current LES methodology does seem to assist in improving the overall predictive capability of the FPV models in comparison to RANS. However, the extent of improvement is limited by the accuracy of the subgrid scale combustion model. The FPV models are not yet able to capture the extinction associated with the fluctuation in the upstream end of the flame base in fuel lean conditions which seems to contribute to the overprediction of mean temperature. Also, since the models are currently based on an adiabatic formulation, radiation heat loss effects are not accounted and this may partly explain for the overprediction in mean temperature.

It is, however, quite encouraging that the FPV models provide major advantages over SLFM. Unlike SLFM, both the models are able to predict the phenomenon of flame lift-off even with steady RANS approach. When extended to LES, the FPV models are also able to predict certain degree of flame base fluctuation which is indeed promising. Adopting LES seems to be useful especially with FPV-β function model, as the predicted lifted flame base characteristics (Fig. 9.11, z/D=30.0) and the mean lift-off height are in excellent agreement with measurements. With further refinements to this model, LES could be employed with greater benefit to accurately capture the structure of turbulent partially premixed flames. The observed scale up in accuracy with FPV-β function model in comparison to the δ function model (in LES) justifies the additional pre-processing effort and computational memory requirements required by the β function model. The model thus presents in itself an interesting prospect for further research.

Chapter 10

Conclusions and Future Recommendations

The classical steady laminar flamelet model (SLFM) is a popular choice for RANS based modelling of turbulent non-premixed combustion in several practical applications and its extension to LES of turbulent non-premixed combustion has gained significant interest in the recent years. However, the model's accuracy in regard to slow chemical processes like pollutant NO formation, non-adiabatic effects due to radiation heat loss and local extinction and re-ignition phenomena is an area of concern and there is practical interest in enhancing its formulation to address the issues. Additionally, it is also seen as an added advantage to extend the model's ability to account for turbulent partially premixed combustion which is increasingly being adopted in practical combustion equipment. Advancements in the model's predictive capability are considered to be essential for not only enhancing the predictive capability of RANS modelling approach which is currently the main predictive tool in industry but also for benefiting from the sophistication of LES. This provides the motivation for the current work.

The present work has been undertaken with two main objectives. Firstly, a RANS based turbulent non-premixed combustion modelling strategy, which while using the flamelet concept is able to account for the slow chemistry of NO and the effects of radiation heat loss on detailed structure of the turbulent non-premixed flame, has been developed and its performance in turbulent bluff-body stabilized and piloted jet flames has been investigated. The developed combustion modelling strategy has been based on a non-adiabatic flamelet model (NADM) integrated with either steady or unsteady non-adiabatic flamelets based NO submodels.

Secondly, combustion models based on flamelet/progress variable (FPV) approach, primarily developed (by Pierce and Moin, 2004) for turbulent non-premixed combustion, have been employed in RANS and LES frameworks and their capability

to account for turbulent partially premixed combustion in a lifted jet flame in vitiated coflow has been investigated. Numerical investigations have been carried out using in-house finite volume based RANS and LES codes into which the advanced models have been incorporated.

The non-adiabatic flamelet model uses an enthalpy defect concept to couple the radiation heat loss in the turbulent flow with the flamelet structure while the radiation heat loss itself is calculated through a radiation submodel in the form of Discrete Transfer Method. The steady non-adiabatic flamelets based NO submodel (NADM-NO-TRE) involves a simple technique of solving for mean NO mass fraction within the turbulent flow with a NO production term obtained from enthalpy defect imposed steady non-adiabatic flamelets. The unsteady non-adiabatic flamelets based NO submodel (NADM-EPFM) is based on Eulerian Particle Flamelet Model (EPFM). Additionally, adiabatic counterparts of the above NO submodels which can be integrated with SLFM, have been incorporated in RANS framework for facilitating comparisons. Simulations with non-adiabatic combustion modelling strategies as well as SLFM have been conducted for CH_4/H_2 bluff-stabilized flames of Dally *et al.* (1998a, 2003) and the piloted Sandia D jet flame (Barlow and Frank, 1998, Schneider *et al.*, 2003) with Reynolds stress transport based turbulence closure.

The FPV approach is based on a two scalars, mixture fraction and reaction progress variable, formulation. According to the FPV approach, the diffusion flamelet structure is no longer parameterized with respect to the conventional scalar dissipation rate. Instead, a flamelet parameter which is represented by the maximum reaction progress variable in a flamelet is used to parameterize the flamelets and this provides the advantage of considering the partially extinguished flamelet structure which is not possible with the scalar dissipation rate employed in SLFM and NADM. Depending on the marginal PDF for reaction progress variable, two model formulations of the FPV approach, FPV-δ function model and FPV-β function model, have been derived. Both the models have been incorporated in the in-house RANS and LES codes. The turbulent partially premixed Berkeley CH_4/air lifted jet flame in vitiated coflow (Cabra *et al.*, 2005) has been used as the test case and modelling has been carried out with FPV models as well as SLFM in RANS and LES.

10.1 Conclusions

The key conclusions from the RANS based modelling of turbulent non-premixed flames are as follows:

- For the **HM1 bluff-body stabilized flame**, the predicted mixing field, temperature and major species with both SLFM and NADM are in reasonably good agreement with measurements and they are similar to each other thereby showing the weakly radiating nature of the flame. The mixing field predictions with Reynolds stress transport (RST) model have a better accuracy than those with modified k-ε model in that the overprediction in centreline decay rate and the spreading rate of the jet are fairly reduced (up to 50%) with RST model.

- For the pollutant NO in HM1 flame, predictions with the steady adiabatic submodel SLFM-NO-TRE and steady non-adiabatic submodel NADM-NO-TRE are in similar agreement with measurements and the agreement is reasonably good considering the simplicity of the submodels. However, minor but encouraging improvements are visible. The steady non-adiabatic submodel results in the right trend of reducing the overprediction observed by its adiabatic counterpart.

- The minor improvements in pollutant NO with consideration of radiation heat loss in steady flamelets, are however subject to the condition that the effect of scalar dissipation rate on the mean NO source term is taken into account. Simplifications to non-adiabatic modelling in the form of single representative scalar dissipation rate (NADS model in conjunction with NADS-NO-TRE), further increase the overprediction observed with steady adiabatic NO submodel.

- For the HM1 flame, inclusion of transient effects through unsteady NO submodels remarkably improves the predictions throughout the flame. While the differences between the predictions obtained with unsteady adiabatic (SLFM-EPFM) and non-adiabatic submodels (NADM-EPFM) are fairly small

due to modest heat loss effects, the unsteady non-adiabatic submodel provides the best match with the measurements.

- The **Sandia D jet flame** exhibits relatively notable effects of radiation heat loss on the mean temperature and pollutant NO mass fraction although the effects on major species are rather modest. The SLFM has been observed to significantly overpredict the mean temperature distribution especially in the far downstream measurement locations of the flame where the residence time is high enough for the radiation effects to be notable. Accounting for radiation heat loss through NADM model reduces the overprediction to appreciable levels thereby showing that the current non-adiabatic model is indeed effective. The still existing overprediction seems to be partly due to the underprediction of jet decay rate by the RST model and partly due to the turbulence radiation interactions which are neglected in the present study.

- Comparisons of predicted and measured mean NO mass fractions in Sandia D jet flame show that the effects of radiation heat loss are more dominant than transient effects, unlike in HM1 flame. This is especially true in the far downstream of the jet where the residence times are higher. Inclusion of only radiation heat loss through steady non-adiabatic model (NADM-NO-TRE) significantly reduces the overprediction observed with steady adiabatic submodel (SLFM-NO-TRE). Inclusion of transient effects along with radiation heat loss through the unsteady non-adiabatic submodel (NADM-EPFM) results in relatively lesser improvement over the NADM-NO-TRE predictions.

- Thus, the developed strategy of employing the non-adiabatic flamelet model, NADM, for calculating the mixing field, temperature and major species and subsequently employing NADM-EPFM for pollutant NO calculations has been found to be an effective alternative to SLFM based modelling in turbulent non-premixed combustion.

The key conclusions from the RANS and LES based modelling of the **Berkeley CH_4/air partially premixed turbulent lifted jet flame**, are as follows:

- Even with RANS based modelling, both the FPV-δ function and β function models are able to successfully predict the lift-off phenomenon while the incompleteness of SLFM formulation is confirmed by its prediction of an attached flame. The FPV-δ function model, due to omission of the effect of progress variable fluctuations on the chemical source term, overpredicts the peak chemical source term and thereby results in a shorter stabilization height which is about 50% less than the measured height. The FPV-β function model which models the fluctuations in the reaction progress variable through a variance transport equation, overpredicts the lift-off height by ~27%.

- The shorter lift-off height predicted by FPV-δ function model results in significant overprediction in the fuel jet penetration along centreline. consequently, the radial profiles of mixing field and mean temperature distribution within the flame are overpredicted. Although the FPV-β function model improves the mixing field predictions, mean temperature distribution downstream of the measured flame stabilization height is appreciably overpredicted.

- From LES based modelling it is confirmed that the discrepancy in the mean temperature predictions observed with both the FPV models in RANS, is partly due to the limitation of steady RANS based modelling in resolving large scale turbulent fluctuations as well as the limitation of FPV models in capturing extinction and re-ignition in conditions at or on the fuel lean side of stoichiometric mixture fraction.

- Adopting LES significantly improves the predicted mean lift-off heights with both the models. For the FPV-δ function model, the underprediction in mean lift-off height, which was observed to be ~ 50% with RANS, is reduced to 30% with LES. For the FPV-β function model, the improvement is quite

remarkable in that the overprediction in mean lift-off height, which was ~ 27% in RANS, is completely resolved with LES.

- Adopting LES also helps in realizing the ability of the FPV models (the FPV-β function model in particular) to predict the fluctuation of the flame base with an encouraging level of accuracy. This is confirmed from scattered temperature data. Consistent with the improvement in mean lift-off height, the scattered data predicted by FPV-β function model shows excellent agreement with measurements at the lifted flame base. The β function model is able to predict the broad flame base with inert mixing and partially reacted samples, remarkably well. The model is also able to predict the extinction and re-ignition phenomena occurring in fuel rich zone of the flame base (or downstream end). However, in mixing conditions at or on the fuel lean side of stoichiometry (upstream end of flame base), the model is not yet able to predict extinction. Still, the predicted levels of flame base fluctuations with the β function model are more favourable than with δ function model.

- The improvement in mean lift-off heights and ability of the models to predict certain degree of extinction and re-ignition prediction in LES, translates into an encouraging level of improvement in mean temperature. However, a fair degree of overprediction still exits with either of the FPV models in LES as the models are not yet able to capture the extinction in fuel lean conditions. Also, radiation heat loss has not been considered in the present study and this may have contributed to the discrepancy to an extent.

- Overall, the FPV models provide major advantage over SLFM in that they are able to predict the gross characteristics of turbulent partially premixed flames satisfactorily. The FPV-β function model provides more realistic description of the structure of lifted flame and it highlights the vital role played by the form of the PDF for reaction progress variable in FPV approach. With further refinements to the FPV-β function model, LES could be employed with greater benefit to provide an accurate description of partially premixed combustion.

10.2 Recommendations for future work

- Although the current implementation of RST model in the in-house RANS code provides reasonably good mixing field predictions, discrepancies have been observed with respect to centerline decay rate and jet spreading rate. Future works can attempt full second moment closure and generalized gradient diffusion models to improve the model's prediction capability.

- The unsteady non-adiabatic NO submodel (NADM-EPFM) currently uses an optically thin limit approximation with a radiation source term in the flamelet equations for generating unsteady non-adiabatic flamelets. A strategy to generate these flamelets by imposing enthalpy defect instead of the radiation source term will be helpful in making the model more consistent with the NADM model.

- Current implementation of the NADM model discounts turbulence-radiation interactions (TRI). Accounting for TRI should help in enhancing the sophistication of the non-adiabatic flamelet modelling.

- The causes for the discrepancies observed with the predicted levels of extinction with FPV models in LES can be investigated in the directions of:
    - The definition of progress variable
    - Influence of assumptions in the model equation for progress variable variance
    - Numerical accuracy of the procedure adopted to remap the look-up-tables from flamelet parameter space to progress variable space.
    - Form of the PDF for reaction progress variable

- It is also worthwhile to include radiation heat loss effects in the FPV models through an optically thin limit approximation and study the extent to which the mean temperature predictions of the lifted flame could be improved.

10.3 Present contribution

The key contributions from the current work are:

1. Enhancement in the accuracy of turbulence modelling capability of the in-house RANS code through the implementation of a Reynolds stress transport model

2. Development of a RANS based turbulent non-premixed combustion modelling strategy using a non-adiabatic flamelet model integrated with steady or unsteady (EPFM) non-adiabatic flamelets based NO submodels.

3. Enhancement in the sophistication of the in-house RANS combustion modelling capability through the incorporation of look-up-table concept based steady laminar flamelet model, non-adiabatic flamelet model, steady and unsteady flamelets based NO submodels and flamelet/progress variable (FPV) approach based models.

4. Enhancement in the sophistication of subgrid scale combustion modelling capability in the in-house large eddy simulation (LES) code through incorporation of look-up-table concept based steady flamelet model and flamelet/progress variable approach based models. The LES code is now capable of simulating both turbulent non-premixed and partially premixed combustion.

5. Development of FORTRAN 90 based pre-processing tools for generation of 3D and 4D pre-integrated look-up-tables for SLFM, NADM, FPV-δ function and FPV-β function model based CFD calculations.

6. Validation of non-adiabatic flamelet modelling strategy through modelling of detailed structure including pollutant NO in turbulent bluff-body stabilized flames as well as piloted jet flames.

7. First ever evaluation of the performance of FPV models in describing the thermal structure of lifted partially premixed jet flames using LES and RANS based modelling.

Appendix I

Interpolation Schemes

Depending on the employed combustion model and the number of dictating parameters in look-up-table, 3D or 4D interpolation is carried out in CFD calculations for obtaining Favre filtered or averaged density, temperature, species mass fraction and source terms. In order to obtain a smooth distribution of the interpolated scalars, a 4^{th} order interpolation scheme which accounts for discretisation along each dictating parameter is employed and is presented below.

I.1 3D Interpolation

A 3D interpolation is employed in SLFM and FPV-δ function based calculations in RANS and LES. The interpolation methodology is illustrated by considering its application in SLFM where the look-up-tables are parameterized by mixture fraction $\widetilde{Z}$, mixture fraction variance $\widetilde{Z}''^2$ and scalar dissipation rate $\widetilde{\chi}$.

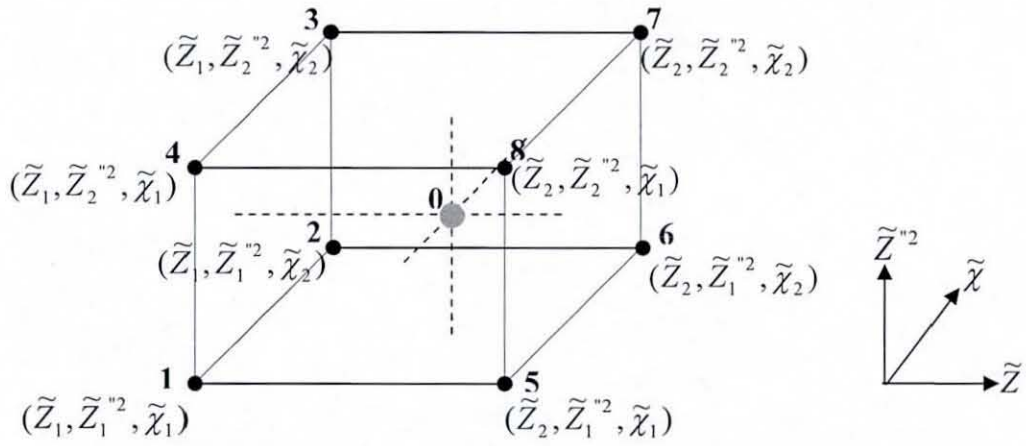

Figure I.1: Scenario of 4^{th} order interpolation in 3D space

Let $\widetilde{Z}_0, \widetilde{Z}_0^{"2}, \widetilde{\chi}_0$ be the known values of the look-up-table parameters in a CFD control volume and $\widetilde{\phi}_0$ be the value of the scalar to be evaluated in that control volume. First, $\widetilde{Z}_0, \widetilde{Z}_0^{"2}, \widetilde{\chi}_0$ are located within individual 1D ordered matrices for $\widetilde{Z}$, $\widetilde{Z}^{"2}$ and $\widetilde{\chi}$ respectively in the look-up-table for scalar ϕ. Subsequently, the bracketing points $(\widetilde{Z}_1, \widetilde{Z}_2)$, $(\widetilde{Z}_1^{"2}, \widetilde{Z}_2^{"2})$ and $(\widetilde{\chi}_1, \widetilde{\chi}_2)$ are identified. Combinations of these bracketing points correspond to locations in the 3D look-up-table which enclose the point where the unknown, the scalar $\widetilde{\phi}_0$, is to be evaluated. Figure 1 depicts a hexahedron enclosing the point '0' at which the value of the scalar is to be evaluated and its vertices corresponding to the locations in the look-up-table where the scalar values $(\widetilde{\phi}_1, \widetilde{\phi}_2 ..... \widetilde{\phi}_8)$ are known. The unknown value of the scalar $\widetilde{\phi}_0$ is then calculated by employing a volume weighted averaging procedure as given below:

$$V1 = (\widetilde{Z}_0 - \widetilde{Z}_1).(\widetilde{Z}_0^{"2} - \widetilde{Z}_1^{"2}).(\widetilde{\chi}_0 - \widetilde{\chi}_1)$$

$$V2 = (\widetilde{Z}_0 - \widetilde{Z}_1).(\widetilde{Z}_0^{"2} - \widetilde{Z}_1^{"2}).(\widetilde{\chi}_2 - \widetilde{\chi}_0)$$

$$V3 = (\widetilde{Z}_0 - \widetilde{Z}_1).(\widetilde{Z}_2^{"2} - \widetilde{Z}_0^{"2}).(\widetilde{\chi}_2 - \widetilde{\chi}_0)$$

$$V4 = (\widetilde{Z}_0 - \widetilde{Z}_1).(\widetilde{Z}_2^{"2} - \widetilde{Z}_0^{"2}).(\widetilde{\chi}_1 - \widetilde{\chi}_0)$$

$$V5 = (\widetilde{Z}_2 - \widetilde{Z}_0).(\widetilde{Z}_0^{"2} - \widetilde{Z}_1^{"2}).(\widetilde{\chi}_0 - \widetilde{\chi}_1)$$

$$V6 = (\widetilde{Z}_2 - \widetilde{Z}_0).(\widetilde{Z}_0^{"2} - \widetilde{Z}_1^{"2}).(\widetilde{\chi}_2 - \widetilde{\chi}_0)$$

$$V7 = (\widetilde{Z}_2 - \widetilde{Z}_0).(\widetilde{Z}_2^{"2} - \widetilde{Z}_0^{"2}).(\widetilde{\chi}_2 - \widetilde{\chi}_0)$$

$$V8 = (\widetilde{Z}_2 - \widetilde{Z}_0).(\widetilde{Z}_2^{"2} - \widetilde{Z}_0^{"2}).(\widetilde{\chi}_1 - \widetilde{\chi}_0)$$

Total volume $TV = (\widetilde{Z}_2 - \widetilde{Z}_1).(\widetilde{Z}_2^{"2} - \widetilde{Z}_1^{"2}).(\widetilde{\chi}_2 - \widetilde{\chi}_1)$

The Favre filtered or averaged value of the scalar is then evaluated from:

$$\widetilde{\phi}_0 = \frac{\widetilde{\phi}_1.V7 + \widetilde{\phi}_2.V8 + \widetilde{\phi}_3.V5 + \widetilde{\phi}_4.V6 + \widetilde{\phi}_5.V3 + \widetilde{\phi}_6.V4 + \widetilde{\phi}_7.V1 + \widetilde{\phi}_8.V2}{TV}$$

I.2 4D Interpolation

A 4D interpolation is required when the CFD calculations employ FPV-β function model or NADM model. The look-up-tables for FPV-β function model are parameterized by mixture fraction $\widetilde{Z}$, mixture fraction variance $\widetilde{Z}^{"2}$, reaction progress variable $\widetilde{C}$ and its variance $\widetilde{C}^{"2}$. The methodology adopted for interpolation is similar to that in 3D except that the number of points enclosing the point of evaluation is now raised to 16.

$$V1 = (\widetilde{Z}_0 - \widetilde{Z}_1).(\widetilde{Z}_0^{"2} - \widetilde{Z}_1^{"2}).(\widetilde{C}_0 - \widetilde{C}_1).(\widetilde{C}_0^{"2} - \widetilde{C}_1^{"2})$$

$$V2 = (\widetilde{Z}_0 - \widetilde{Z}_1).(\widetilde{Z}_0^{"2} - \widetilde{Z}_1^{"2}).(\widetilde{C}_2 - \widetilde{C}_0).(\widetilde{C}_0^{"2} - \widetilde{C}_1^{"2})$$

$$V3 = (\widetilde{Z}_0 - \widetilde{Z}_1).(\widetilde{Z}_2^{"2} - \widetilde{Z}_0^{"2}).(\widetilde{C}_2 - \widetilde{C}_0).(\widetilde{C}_0^{"2} - \widetilde{C}_1^{"2})$$

$$V4 = (\widetilde{Z}_0 - \widetilde{Z}_1).(\widetilde{Z}_2^{"2} - \widetilde{Z}_0^{"2}).(\widetilde{C}_1 - \widetilde{C}_0).(\widetilde{C}_0^{"2} - \widetilde{C}_1^{"2})$$

$$V5 = (\widetilde{Z}_2 - \widetilde{Z}_0).(\widetilde{Z}_0^{"2} - \widetilde{Z}_1^{"2}).(\widetilde{C}_0 - \widetilde{C}_1).(\widetilde{C}_0^{"2} - \widetilde{C}_1^{"2})$$

$$V6 = (\widetilde{Z}_2 - \widetilde{Z}_0).(\widetilde{Z}_0^{"2} - \widetilde{Z}_1^{"2}).(\widetilde{C}_2 - \widetilde{C}_0).(\widetilde{C}_0^{"2} - \widetilde{C}_1^{"2})$$

$$V7 = (\widetilde{Z}_2 - \widetilde{Z}_0).(\widetilde{Z}_2^{"2} - \widetilde{Z}_0^{"2}).(\widetilde{C}_2 - \widetilde{C}_0).(\widetilde{C}_0^{"2} - \widetilde{C}_1^{"2})$$

$$V8 = (\widetilde{Z}_2 - \widetilde{Z}_0).(\widetilde{Z}_2^{"2} - \widetilde{Z}_0^{"2}).(\widetilde{C}_1 - \widetilde{C}_0).(\widetilde{C}_0^{"2} - \widetilde{C}_1^{"2})$$

$$V9 = (\widetilde{Z}_0 - \widetilde{Z}_1).(\widetilde{Z}_0^{"2} - \widetilde{Z}_1^{"2}).(\widetilde{C}_0 - \widetilde{C}_1).(\widetilde{C}_2^{"2} - \widetilde{C}_0^{"2})$$

$$V10 = (\widetilde{Z}_0 - \widetilde{Z}_1).(\widetilde{Z}_0^{"2} - \widetilde{Z}_1^{"2}).(\widetilde{C}_2 - \widetilde{C}_0).(\widetilde{C}_2^{"2} - \widetilde{C}_0^{"2})$$

$$V11 = (\widetilde{Z}_0 - \widetilde{Z}_1).(\widetilde{Z}_2^{"2} - \widetilde{Z}_0^{"2}).(\widetilde{C}_2 - \widetilde{C}_0).(\widetilde{C}_2^{"2} - \widetilde{C}_0^{"2})$$

$$V12 = (\widetilde{Z}_0 - \widetilde{Z}_1).(\widetilde{Z}_2^{"2} - \widetilde{Z}_0^{"2}).(\widetilde{C}_1 - \widetilde{C}_0).(\widetilde{C}_2^{"2} - \widetilde{C}_0^{"2})$$

$$V13 = (\widetilde{Z}_2 - \widetilde{Z}_0).(\widetilde{Z}_0^{"2} - \widetilde{Z}_1^{"2}).(\widetilde{C}_0 - \widetilde{C}_1).(\widetilde{C}_2^{"2} - \widetilde{C}_0^{"2})$$

$$V14 = (\widetilde{Z}_2 - \widetilde{Z}_0).(\widetilde{Z}_0^{"2} - \widetilde{Z}_1^{"2}).(\widetilde{C}_2 - \widetilde{C}_0).(\widetilde{C}_2^{"2} - \widetilde{C}_0^{"2})$$

$$V15 = (\widetilde{Z}_2 - \widetilde{Z}_0).(\widetilde{Z}_2^{"2} - \widetilde{Z}_0^{"2}).(\widetilde{C}_2 - \widetilde{C}_0).(\widetilde{C}_2^{"2} - \widetilde{C}_0^{"2})$$

$$V16 = (\widetilde{Z}_2 - \widetilde{Z}_0).(\widetilde{Z}_2^{"2} - \widetilde{Z}_0^{"2}).(\widetilde{C}_1 - \widetilde{C}_0).(\widetilde{C}_2^{"2} - \widetilde{C}_0^{"2})$$

Total volume $TV = (\widetilde{Z}_2 - \widetilde{Z}_1).(\widetilde{Z}_2^{"2} - \widetilde{Z}_1^{"2}).(\widetilde{C}_2 - \widetilde{C}_1).(\widetilde{C}_2^{"2} - \widetilde{C}_1^{"2})$

The Favre filtered or averaged value of the scalar is then evaluated from:

$$\widetilde{\phi}_0 = \frac{\widetilde{\phi}_1.V7 + \widetilde{\phi}_2.V8 + \widetilde{\phi}_3.V5 + \widetilde{\phi}_4.V6 + \widetilde{\phi}_5.V3 + \widetilde{\phi}_6.V4 + \widetilde{\phi}_7.V1 + \widetilde{\phi}_8.V2}{TV} +$$
$$\frac{\widetilde{\phi}_1.V7 + \widetilde{\phi}_2.V8 + \widetilde{\phi}_3.V5 + \widetilde{\phi}_4.V6 + \widetilde{\phi}_5.V3 + \widetilde{\phi}_6.V4 + \widetilde{\phi}_7.V1 + \widetilde{\phi}_8.V2}{TV}$$

References

Armfield, S., Street, R. (2002), "An Analysis and Comparison of the Time Accuracy of Fractional-Step Methods for the Navier–Stokes Equations on Staggered Grids", *International Journal for Numerical Methods in Fluids* 38, 255–282.

Barlow, R. S. and Frank, J. H. (1998), "Effects of Turbulence on Species Mass Fractions in Methane-Air Jet Flames", *Twenty Seventh Symposium (International) on Combustion/The Combustion Institute*, 1087-1095.

Barlow, R.S. and Frank, J. (2007), "Piloted CH4/Air Flames C, D, E, and F – Release 2.1", *SandiaPilotDoc21.pdf.*

Barlow, R.S., and Frank, J.H. (1998), "Effects of Turbulence on Species Mass Fractions in Methane/Air Jet Flames", *Twenty-seventh Symposium (International) on Combustion/The Combustion Institute*,1087-1095.

Barlow, R.S., Fiechtner, G.J., Carter, C.D. and Chen, J.Y. (2000), "Experiments on the Scalar Structure of Turbulent CO/H2/N2 Jet Flames", *Combustion and Flame 120*,549-569.

Barths, H., Antoni, C., and Peters, N. (1998b), "Three-Dimensional Simulation of Pollutant Formation in a DI Diesel Engines Using Multiple Interactive Flamelets", *SAE Paper* 982459.

Barths, H., Hasse, C. and Peters, N., (2000),"Computational Fluid Dynamics Modelling of Non-Premixed Combustion in Direct Injection Diesel Engines", *International Journal of Engine Research 1,* 249-267.

Barths, H., Peters, N., Brehm, N., Mack, A., Pfitzner, M., and Smiljanovski, V. (1998a), "Simulation of Pollutant Formation in a Gas-Turbine Combustor Using Unsteady Flamelets", *Twenty-seventh Symposium (International) on Combustion/The Combustion Institute*, 1841-1847.

Bell, J.B. and Colella, P. (1989), "A Second Order Projection Method for the Incompressible Navier-Stokes Equations", *Journal of Computational Physics 85*, 257–283.

Bergmann, V., Meier, W., Wolff, D., Stricker, W. (1998), "Application of Spontaneous Raman and Rayleigh Scattering and 2D LIF for the Characterization of a Turbulent CH4/H2/N2 Jet Diffusion Flame", *Applied Physics B 66,* 489-502.

Bilger, R.W. (1976), "Turbulent Jet Diffusion Flames", *Progress in Energy and Combustion Science 1*, 87-109.

Bilger, R.W. (1980), "Turbulent Jet Diffusion Flames", *Combustion Science and Technology 22*, 251-261.

Bilger, R.W. (1988), "The Structure of Turbulent NonPremixed flames", *Twenty-second Symposium (International) on Combustion/The Combustion Institute*, 475-488.

Bilger, R.W. (1993), "Conditional Moment Closure for Turbulent Reactive Flows", *Physics of Fluids A 52*, 436-444.

Bowman, C. T., Hanson, R. K., Davidson, D.F., Gardiner, W.C., Lassianski, V., Smith, G. P., Golden, D. M., Frenklach, M., Wang, H. and Goldenberg, M. (2007) in http://www.me.berkeley.edu/gri-mech/releases.html

Bradley, D., Gaskell, P.H. and Gu, X.J. (1998a), "The Modeling of Aerodynamic Strain Rate and Flame Curvature Effects in Premixed Turbulent Combustion", *Twenty Seventh Symposium (International) on Combustion/The Combustion Institute*, 849-856.

Bradley, D., Gaskell, P.H. and Gu, X.J. (1998b), "The Mathematical Modelling of Liftoff and Blowoff of Turbulent Non-premixed Methane Jet Flames at High Strain Rates", *Twenty Seventh Symposium (International) on Combustion/The Combustion Institute*, 915-922.

Bradley, D., Gaskell, P.H. and Lau, A.K.C. (1990), "A Mixedness-Reactedness Flamelet Model for Turbulent Diffusion Flames", *Twenty Third Symposium (International) on Combustion/The Combustion Institute*, 685-692.

Branley, N. and Jones, W.P. (1999), "Large Eddy Simulation of a Nonpremixed Turbulent Swirling Flame", In W. Rodi and D.Laurence (Eds.), *Engineering Turbulence Modelling and Experiments 4*, pp.861-870, Amsterdam: Elsevier Science.

Branley, N. and Jones, W.P. (2001), "Large Eddy Simulation of a Turbulent Non-premixed Flame", *Combustion and Flame 127*, 1914–1934.

Bray, K. N. C., Champion, M. and Libby, P. A. (1994), "Flames in Stagnating Turbulence", In P. A. Libby and F. A. Williams (Eds.), *Turbulent reacting flows*, Chapter 9, 573–638. London: Academic Press.

Bray, K.N.C., and Moss. J.B., (1977), "A Unified Statistical Model of the Premixed Turbulent Flame". *Acta Astronautica 4*, 291-319.

Bray, K.N.C., and Peters, N. (1994), "Laminar Flamelets in Turbulent Flames", In P.A. Libby and F.A. Williams (Eds.), *Turbulent Reacting Flows*, Chapter 2,pp.63-94, London : Academic Press.

Breuer, M. and Rodi W. (1994), "Large Eddy Simulation of Turbulent Flow Through a Straight Square Duct and a 180° Bend", In P.R.Voke, R. Kleiser and J.P. Chollet (Eds.), *Fluid Mechanics and its Applications 26*, Kluwer Academic.

Broadwell, J.E., Dahm, W.J.A. and Mungal, M.G. (1984), "Blowout of turbulent diffusion flames", *Twentieth Symposium (International) on Combustion/The Combustion Institute*, 303-310.

Bushe, W.K. and Steiner, H. (1999), "Conditional Moment Closure for Large Eddy Simulation of Nonpremixed Turbulent Reacting Flows", *Physics of Fluids 11*, 1896–1906.

Cabra, R., Chen, J.-Y., Dibble, R.W., Karpetis, A.N. and Barlow, R.S. (2005), "Lifted Methane-Air Jet Flames in a Vitiated Coflow", *Combustion and Flame 143*, 491-506.

Carpentier, S., Meunier, P. and Aguile, F. (2005), "A Non Adiabatic Flamelet Model to Simulate Turbulent Natural Gas Flames", Eccomas Thematic Conference on Computational Combustion, paper number 30.

Cha, C. M. and Trouillet, P. (2003), "A Subgrid-Scale Mixing Model for Large-Eddy Simulations of Turbulent Reacting Flows using the Filtered Density Function," *Physics of Fluids 15 (6)*, 1496–1504.

Chen, C.-S., Chang, K.-C. and Chen, J.-Y. (1994), "Application of a Robust β-PDF Treatment for Analysis of Thermal NO Formation in Nonpremixed Hydrogen-Air Flame", *Combustion and Flame 98*, 375–390.

Chen, J.-Y., and Chang, W.C. (1996), "Flamelet and PDF Modeling of CO and NOx Emissions from a Turbulent, Methane Hydrogen Jet Nonpremixed Flame", *Twenty-sixth Symposium (International) on Combustion/The Combustion Institute*, 2207-2214.

Chen, M., Hermann, M. and Peters, N. (2000), "Flamelet Modeling of Lifted Turbulent Methane/Air and Propane/Air Jet Diffusion Flames", *Twenty Eigth Symposium (International) on Combustion/The Combustion Institute*, 167-174.

Coelho, P.J. (2004), "Detailed Numerical Simulation of Radiative Transfer in a Non-Luminous Turbulent Jet Diffusion Flame", *Combustion and Flame 136,* 481-492.

Coelho, P.J., and Peters, N. (2001a), "Unsteady Modelling of Piloted Methane/Air Jet Flame Based on the Eulerian Particle Flamelet Model", *Combustion and Flame 124,* 444-465.

Coelho, P.J., and Peters, N. (2001b), "Numerical Simulation of a Mild Combustion Burner", *Combustion and Flame 124,* 503-518.

Coelho, P.J., Teerling, O.J., Roekaerts, D. (2003), "Spectral Radiative Effects and Turbulence/Radiation Interaction in a Non-Luminous Turbulent Jet Diffusion Flame", *Combustion and Flame 133,* 75-91.

Cook, A.W. and Riley, J.J. (1994), "A Subgrid Model for Equilibrium Chemistry in Turbulent Flows", *Physics of Fluids 6*,2868–2870.

Cook, A.W. and Riley, J.J. (1998), "Subgrid-Scale Modeling for Turbulent Reactive Flows", *Combustion and Flame 112*, 593–606.

Cook, A.W. and Riley, J.J. and Kosaly, G. (1997), "A Laminar Flamelet Approach to Subgrid Scale Chemistry in Turbulent Flows", *Combustion and Flame 109*, 332-341.

Correa, S.M., and Gulati, A. (1992), "Measurements and Modeling of a Bluff Body Stabilized Flame", *Combustion and Flame 89*,195-213.

Dally, B.B., Fletcher, D.F., Masri, A.R. (1998b), "Flow and Mixing Fields of Turbulent Bluff-Body Jets and Flames", *Combustion Theory and Modelling 2*, 193-219.

Dally, B.B., Masri, A.R., Barlow, R.S., Fiechtner, G.J. (1998a), "Instantaneous and Mean Compositional Structure of a Bluff-Body Stabilized Nonpremixed Flames", *Combustion and Flame 114*, 119-148.

Dally, B.B., Masri, A.R., Barlow, R.S., Fiechtner, G.J. (2003), "Two Photon Laser-Induced Fluorescence Measurement of CO in Turbulent Non-Premixed Bluff-Body Flames", *Combustion and Flame 132*, 272-274.

Daly, B.J. and Harlow, F.H. (1970), "Transport Equations of Turbulence", *Physics of Fluids 13*, 2634-2649.

De Bruyn Kops, S.M., Riley, J.J., Kosaly, G., Cook, A.W. (1998), "Investigation of Modeling for Non-premixed Turbulent Combustion", *Flow Turbulence and Combustion 60*,105–122.

Deardorff, J.W. (1970), "A Numerical Study of Three-Dimensional Turbulent Channel Flow at Large Reynolds Numbers", *Journal of Fluid Mechanics 41*, 453-480.

Di Mare, F., Jones, W., Menzies, K. (2004), "Large Eddy Simulation of a Model Gas Turbine Combustor", *Combustion and Flame 137*, 278–294.

Domingo, P. and Vervisch, L. (1996), "Triple Flames and Partially-premixed Combustion in Auto-ignition of Non-premixed Turbulent Mixtures", *Twenty Sixth Symposium (International) on Combustion/The Combustion Institute*, 233-240.

Donnerhack, S., and Peters, N. (1984), "Stabilization Heights in Lifted Methane-Air Jet Diffusion Flames Diluted with Nitrogen", *Combustion Science and Technology 41*, 101-108.

Drake, C (1986), "Stretched Laminar Flamelet Analysis of Turbulent H_2 and $CO/H_2/N_2$ Diffusion Flames", *Twenty-first Symposium (International) on Combustion/The Combustion Institute*, 1579-1589.

Drake, M.C., and Blint, R.J. (1988), "Structure of Laminar Opposed-Flow Diffusion Flames with $CO/H_2/N_2$ Fuel", *Combustion Science and Technology 61*, 187-224.

Duchamp de Lageneste, L. and Pitsch, H. (2001), "Progress in Large-Eddy Simulation of Premixed and Partially-premixed Turbulent Combustion", *Annual Research Briefs*, Center for Turbulence Research, NASA Ames/Stanford University.97–107.

Effelsberg, E., and Peters, N. (1988), "Scalar Dissipation Rates in Turbulent Jets and Jet Diffusion Flames", *Twenty-second Symposium (International) on Combustion/The Combustion Institute*, 693-700.

Eickhoff, H., Lenze, B. and Leuckel, W. (1984), "Experimental Investigation on the Stabilization Mechanism of Jet Diffusion Flames", *Twentieth Symposium (International) on Combustion/The Combustion Institute*, 311-318.

Ferreira, J.C. (1996), "Flamelet Modelling of Stabilization in Turbulent Non-Premixed Combustion", PhD Thesis, ETH Nr.1184.

Ferreira, J.C. (2001), "Steady and Transient Flamelet Modelling of Turbulent Non-Premixed Combustion", *Progress in Computational Fluid Dynamics 1, 29-42.*

Forkel, H. and Janicka, J. (1999), "Large Eddy Simulation of a Turbulent Hydrogen Diffusion Flame", *Proceedings of the 1st International Symposium on Turbulence and Shear Flow Phenomena*, pp. 65-70.

Germano, M., Piomelli, U., Moin, P., and Cabot, W. H. (1991), "A Dynamic Sub-grid Scale Eddy Viscosity Model", *Physics of Fluids A (3)*, 1760-1765.

Giordano, P. and Lentini, D. (2001), "Combustion-Radiation-Turbulence Interaction Modelling in Absorbing/Emitting Nonpremixed flames", *Combustion Science and Technology 172*, 1-22.

Girimaji, S.S. and Zhou, Y. (1996), "Analysis and Modeling of Subgrid Scalar Mixing using Numerical Data", *Physics of Fluids 8*, 1224-1236.

Hanjalic, K., and Jakirlic, S. (2002), "Second-Moment Turbulence Closure Modelling", In Brian Launder and Neil Sandham (Eds.), *Closure Strategies for turbulent and transitional flows*, 47-101, Cambridge: University Press.

Haworth, D.C., Drake, M.C., and Blint, R.J. (1988a), "Stretched Laminar Flamelet Modeling of a Turbulent Jet Diffusion Flame", *Combustion Science and Technology 60,* 287-318.

Haworth, D.C., Drake, M.C., Pope, S.B., and Blint, R.J. (1988b), "The Importance of Time Dependent Flame Structure In Stretched Laminar Flamelet Models For Turbulent Jet Diffusion Flames", *Twenty-Second Symposium (International) on Combustion/The Combustion Institute*, 589-597.

Held, T. J., and Mongia, H. C. (1998b), "Emissions Modeling of Gas Turbine Combustors using a Partially-Premixed Laminar Flamelet Model", *AIAA Paper* 98-3950.

Held, T. J., Mueller, M.A., Li, S.-C., and Mongia, H.C. (2001), "A Data-Driven Emissions Submodel for Laminar Flamelet Modeling of DLE Combustors", AIAA 2001-3425.

Held, T.J., and Mongia, H.C. (1998a), "Application of a Partially Premixed Laminar Flamelet Model to a Low Emissions Gas Turbine Combustor", *ASME Paper* 98-GT-217.

Heyl, A., and Bockhorn, H. (2001), "Flamelet Modelling of NO Formation in Laminar and Turbulent Diffusion Flames", *Chemosphere 42,* 449-462.

Hossain, M. (1999), "CFD Modelling of Turbulent Non-Premixed Combustion", *Ph.D Thesis*, Loughborough University, UK.

Hossain, M., and Malalasekera, W. (2003), "Modelling of a Bluff Body Stabilized CH4/H2 Flame Based on a Laminar Flamelet Model with Emphasis on NO Prediction", *Journal of Power and Energy 217*, 201-210.

Hossain, M., Jones, J.C. and Malalasekera, W. (2001), "Modelling of a Bluff-Body Nonpremixed Flame Using a Coupled Radiation/Flamelet Combustion Model", *Flow Turbulence and Combustion 67*, 217-234.

Ihme, M. and Pitsch, H. (2005), "LES of a Non-premixed Flame using an Extended Flamelet/Progress Variable Model", *AIAA Paper* 2005-0558.

Ihme, M., Cha, C.M. and Pitsch, H. (2005), "Prediction of Local Extinction and Re-ignition Effects in Non-premixed Turbulent Combustion by a Flamelet/Progress Variable Approach", *Thirtieth Symposium (International) on Combustion/The Combustion Institute*, 793-800.

Janicka, J. and Peters, N. (1983), "Prediction of Turbulent Jet Diffusion Flame Lift-off using a PDF Transport Equation", *Nineteenth Symposium (International) on Combustion/The Combustion Institute*, 367-374.

Jiménez, J., Liñán, A., Rogers, M.M., and Higuera, F.J. (1997), "A Priori Testing of Subgrid Models for Chemically Reacting Non-premixed Turbulent Shear Flows", *Journal of Fluid Mechanics 349*, 149-171.

Jones, W.P. (1994), "Turbulence Modelling and Numerical Solution Methods for Variable Density and Combusting Flows", In P.A. Libby and F.A. Williams (Eds.), *Turbulent Reacting Flows*, Chapter 6, pp.309-368, London: Academic Press.

Jones, W.P., and Launder, B.E. (1972), "The prediction of Laminarization with a Two-Equation Model of Turbulence", *International Journal of Heat Mass Transfer 15*,301-314.

Jones, W.P., and Whitelaw, J.H. (1982), "Calculation Methods for Reacting Turbulent Flows: A Review", *Combustion and Flame 48*,1-26.

Kalghatgi, G.T. (1981), "Blow-out Stability of Gaseous Jet Diffusion Flames. Part I: In Still Air", *Combustion Science and Technology 26*, 233-239.

Kalghatgi, G.T. (1984), "Lift-off Heights and Visible Lengths of Vertical Turbulent Jet Diffusion Flames in Still Air", *Combustion Science and Technology 41*, 17-29.

Kalghatgi, G.T. (1984), "Lift-off Heights and Visible Lengths of Vertical Turbulent Jet Diffusion Flames in Still Air", *Combustion Science and Technology 41*, 17-29.

Kempf, A., Flemming, F. and Janicka, J. (2005), "Investigation of Lengthscales, Scalar Dissipation and Flame Orientation in a Piloted Diffusion Flame by LES", *Thirteeth Symposium (International) on Combustion/The Combustion Institute*, 557-565.

Kempf, A., Lindstedt, R.P. and Janicka, J. (2006), "Large-eddy Simulation of a Bluff-body Stabilized Non-premixed Flame", *Combustion and Flame 144*, 170-189.

Kerstein, A.R. (1992), "Linear Eddy Modelling of Turbulent Transport: part 4: structure of diffusion flames", *Combustion Science and Technology 81*, 75-86.

Kim, H.S., Huh, Y.K. (2002), "Use of the Conditional Moment Closure Model to Predict NO formation in a Turbulent CH4/H2 flame over a Bluff-Body", *Combustion and Flame 130*, 94-111.

Kirkpatrick, M.P. (2002), "A Large Eddy Simulation Code for Industrial and Enviromental Flows", *Ph.D. Thesis*, University of Sydney, Australia.

Kirkpatrick, M.P., Armfield, S.W. and Kent, J.H. (2003), "A Representation of Curved Boundaries for the Solution of the Navier-Stokes Equations on a Staggered Three Dimensional Cartesian Grid", *Journal of Computational Physics 184*, 1–36.

Klein, M., Sadiki, A. and Janicka, J. (2003), "A Digital Filter Based Generation of Inflow Data for Spatially Developing Direct Numerical or Large Eddy Simulation", *Journal of Computational Physics 186*, 652–665.

Klimenko, A.Y. (1990), "Multicomponent Diffusion of Various Admixtures in Turbulent Flows, *Fluid Dynamics 25*, 327-334.

Kuo, K.K. (1986), "*Principles of Combustion*", New York: Wiley International.

Launder, B.E. and Spalding, D.B. (1974), "The Numerical Computation of Turbulent Flows", *Computer Methods in Applied Mechanics and Engineering 3*, 269–289.

Launder, B.E., Reece, G.J. and Rodi, W. (1975), "Progress in the Development of a Reynolds-Stress Turbulence Closure", *Journal of Fluid Mechanics 68*, 537-566.

Lentini, D. (1994), "Assessment of the Stretched Laminar Flamelet Approach for NonPremixed Turbulent Combustion", *Combustion Science and Technology 100*, 95-122.

Lentini, D. and Puri, I.K. (1995), "Stretched Laminar Flamelet Modeling of Turbulent Chloromethane-Air Nonpremixed Jet Flames", *Combustion and Flame 103*, 328-338.

Leonard, B.P. (1979), "A Stable and Accurate Convective Modeling Procedure Based on Quadratic Upstream Interpolation", *Journal of Computational Methods in Applied Mechanical Engineering 19*,59-98.

Leonard, B.P. (1987), "SHARP Simulation of Discontinuities in Highly Convective Steady Flow", *NASA Technical Report* 100240.

Leonard., A. (1974), "Energy Cascade in Large Eddy Simulations of Turbulent Fluid Flows", *Advances in Geophysics*, 18A:237.

Leschziner, M.A., and Lien, F.S. (1994), "Numerical Aspects of Applying Second-Moment Closure to Complex Flows", In Brian Launder and Neil Sandham (Eds.), *Closure Strategies for turbulent and transitional flows*, 153-187, Cambridge: University Press.

Li, G., Bertrand, N., Roakaerts, D. (2003), "Numerical Investigation of a Bluff-Body Stabilised Nonpremixed Flame with Differential Reynolds-Stress Models", Flow *Turbulence and Combustion 70*, 211-240.

Libby, P.A., and Bray. K.N.C., (1981), "Counter-Gradient Diffusion in Premixed Turbulent Flames". *AIAA Journal 19*, 205-213.

Libby, P.A., and, Williams, F.A. (1994), "Fundamental aspects and review", In P.A. Libby and F.A. Williams (Eds.), *Turbulent Reacting Flows*, Chapter 1, pp.1-61, London: Academic Press.

Lien, F.S., and Leschziner, M.A. (1994), "Assessment of Turbulence-Transport Models Including Non-Linear RNG Eddy-Viscosity Formulation And Second-Moment Closure For Flow Over a Backward-Facing Step", *Computers and Fluids 8*, 983-1004.

Liew, S.K, Bray, K.N.C., and Moss, J.B. (1984), "A Stretched Laminar Flamelet Model of Turbulent Nonpremixed Combustion", *Combustion and Flame 56,*199-213.

Lilly, D. K. (1991), "A Proposed Modification of the Germano Subgrid-Scale Closure Method", *Physics of Fluids A (4)*, 633-635.

Lilly, D.K. (1966), "On the Application of the Eddy Viscosity Concept in the Inertial Subrange of Turbulence", *NCAR Manuscript 123*.

Liñán, A. (1994), "Ignition and Flame Spread in Laminar Mixing Layers", In J.Buckmaster, T.L. Jackson, and A. Kumar (Eds.), *Combustion in High-Speed Flows*, pp.461-476, Dordrecht: Kluwer Academic.

Liu, K., Pope, S.B., Caughey, D.A. (2005), "Calculations of Bluff-Body Stabilized Flames Using a Joint Probability Density Function Model with Detailed Chemistry", *Combustion and Flame 141*, 89-117.

Liu, K., Pope, S.B., Caughey, D.A. (2005), "Calculations of Bluff-Body Stabilized Flames Using a Joint Probability Density Function Model with Detailed Chemistry", *Combustion and Flame 141,* 89-117.

Lockwood, F.C. and Shah, N.G. (1981), "A New Radiation Solution for Incorporation in General Combustion Prediction Procedures", *Eighteenth Symposium (International) on Combustion/The Combustion Institute*, 1405-1413.

Lund, T.S., Squires, K.D. and Wu, X. (2003), "Turbulent Inflow Boundary Conditions for LES", *AIAA Paper* 2003-0067.

Ma, C.Y., Mahmud, T., Fairweather, M., Hampartsoumian, E. and Gaskell, P.H. (2002), "Prediction of Lifted Non-premixed Turbulent Flames using a Mixedness-Reactedness Flamelet Model with Radiation Heat Loss", *Combustion and Flame 128*, pp.60-73.

Maas, U. and Pope, S. (1992), "Simplifying Chemical Kinetics: Intrinsic low-Dimensional Manifolds in Composition Space", *Combustion and Flame 88*, 239–264.

Mahesh, K., Constantinescu, G. and Moin, P. (2004), "A Numerical Method for Large-Eddy Simulation in Complex Geometries", *Journal of Computational Physics 197*, 215–240.

Malalasekera, W.M.G. (1988), "Mathematical Modelling of Fires and Related Processess", *Ph.D Thesis*, Imperial College, London, UK.

Marracino, B. and Lentini, D. (1997), "Radiation Modelling in Non-Luminous NonPremixed Turbulent Flames", *Combustion Science and Technology 128*, 23-48.

Masri, A.R., Bilger, R.W., and Dibble, R.W. (1988), "Turbulent NonPremixed Flames of Methane Near Extinction: Probability Density Functions", *Combustion and Flame 73*,261-285.

Mauss, F, Keller, D., and Peters, N. (1990), "A Lagrangian Simulation of Flamelet Extinction and Re-Ignition In Turbulent Jet Diffusion Flames", *Twenty-third Symposium (International) on Combustion/The Combustion Institute*, 693- 698.

Merci, B., Dick, E., Vierendeels, J., Roekaerts, .D, and Peeters, T.W.J., (2001), "Application of a New Cubic Turbulence Model to Piloted and Bluff-Body Diffusion Flames", *Combustion and Flame 126*, 1533-1556.

Moin, P. and Kim, J. (1982), "Numerical Investigation of Turbulent Channel Flow", *Journal of Fluid Mechanics 118*, 341-377.

Moin. P. (2002), "Advances in Large Eddy Simulation Methodology For Complex Flows", *International Journal of Heat and Fluid Flow 23*, 710-720.

Mongia, H.C. (2002), "Development of Combustion Chamber Design Tools", IIT Madras 2002 Turbulent Reacting Flows Workshop.

Müller, C. M., Breitbach, H. and Peters, N. (1994), "Partially Premixed Turbulent Flame Propagation in Jet Flames", *Twenty fifth Symposium (International) on Combustion/The Combustion Institute*, 1099-1106.

Naot, D., Shavit, A. and Wolfshtein, M. (1970), " Interaction between Components of the Turbulent Velocity Correlation Tensor", *Israel Journal of Technology 8*, 259-269.

Patankar, S.V. (1980), "*Numerical Heat Transfer and Fluid Flow*", New York: McGraw Hill.

Patankar, S.V., and Spalding, D.B. (1972), "A Calculation Procedure for Heat, Mass and Momentum Transfer in Three-Dimensional Parabolic Flows", *International Journal of Heat Mass Transfer 15*, 1787-1806.

Peters, N. (1983), "Local Quenching Due to Flame Stretch and Non-Premixed Turbulent Combustion", *Combustion Science and Technology 30,* 1-17.

Peters, N. (1984), "Laminar Diffusion Flamelet Models in Non-Premixed Turbulent Combustion", *Progress in Energy and Combustion Science 10*,319-339.

Peters, N. (1986), "Laminar Flamelet Concepts in Turbulent Combustion", *Twenty-first Symposium (International) on Combustion/The Combustion Institute*, 1231-1250.

Peters, N. (1993), "Flame Calculations with Reduced Mechanism-an Outline", In N. Peters and B. Rogg (Eds.), *Reduced kinetic mechanisms for applications in combustion systems*, Chapter 1, pp.3-14, Berlin: Springer-Verlag.

Peters, N. (1999), "The Turbulent Burning Velocity for Large Scale and Small Scale Turbulence", *Journal of Fluid Mechanics 384*, 107-132.

Peters, N. and Williams, F.A. (1983), "Lift-off Characteristics of Turbulent Jet Diffusion Flames", *AIAA Journal 21*, 423-429.

Pierce, C.D. (2001), "Progress-Variable Approach for Large-Eddy Simulation of Turbulent Combustion", *Ph.D Thesis*, Stanford University, USA.

Pierce, C.D. and Moin, P. (1998), "A Dynamic Model for Subgrid-Scale Variance and Dissipation Rate of a Conserved Scalar", *Physics of Fluids 10*, 3041–3044.

Pierce, C.D. and Moin, P. (2004), "Progress-Variable Approach for Large Eddy Simulation of Non-premixed Turbulent Combustion", *Journal of Fluid Mechanics 504*, 73-97.

Piomelli, U. and Liu, J. (1995), "Large Eddy Simulation of Rotating Channel Flows using a Localized Dynamic Model", *Physics of Fluids 7*, 839-848.

Piomelli, U., Moin, P. and Ferziger, J. H. (1988), "Model Consistency in Large Eddy Simulation of Turbulent Channel Flows", *Physics of Fluids 31*, 1884–1891.

Piomelli, U., Yu, Y. and Adrian, R. J. (1996), "Subgrid-scale Energy Transfer and Near-Wall Turbulence Structure", *Physics of Fluids 8*, 215–224.

Pitsch, H. (1998), A C++ Computer Program for 0-D and 1-D Laminar Flame Calculations, RWTH Aachen.

Pitsch, H. (2000), "Unsteady Flamelet Modelling of Differential Diffusion in Turbulent Jet Diffusion Flames", *Combustion and Flame 123,* 358-374.

Pitsch, H. (2002), "Improved Pollutant Predictions in Large-Eddy Simulations of Turbulent Non-premixed Combustion by Considering Scalar Dissipation rate Fluctuations", *Twenty Ninth Symposium (International) on Combustion/The Combustion Institute*,1971–1978.

Pitsch, H. (2006), "Large Eddy Simulation of Turbulent Combustion", *Annual Review of Fluid Mechanics 38*, 453-482.

Pitsch, H. and Duchamp de Lageneste, L. (2001), "Large-Eddy Simulation of Premixed and Partially Premixed Turbulent Combustion Using a Level Set Method", *Fifty Fourth Annual Meeting of the Division of Fluid Dynamics, Session KP -Turbulent Reacting Flows II*, KP002.

Pitsch, H. and Ihme, M. (2005), "An Unsteady/Flamelet Progress Variable Method for LES of Nonpremixed Turbulent Combustion", *AIAA Paper* 2004-557.

Pitsch, H., and Peters, N. (1998), "A Consistent Flamelet Formulation for Non-Premixed Combustion Considering Differential Diffusion Effects", *Combustion and Flame 114*, 26-40.

Pitsch, H., Barths, H., and Peters, N. (1996), "Three Dimensional Modelling of NOx and Soot Formation in DI-Diesel Engines Using Detailed Chemistry Based on the Interactive Flamelet Approach", *SAE Paper* 962057.

Pitsch, H., Chen, M., and Peters, N. (1998), "Unsteady Flamelet Modeling of Turbulent Hydrogen-Air Diffusion Flames", *Twenty-Seventh Symposium (International) on Combustion/The Combustion Institute*, 1057-1064.

Pitsch, H., Steiner, H. (2000). "Large-Eddy Simulation of a Turbulent Piloted Methane/Air Diffusion flame (Sandia Flame D)", *Physics of Fluids 12*, 2541–2554.

Pope, S.B.(1985), "PDF methods for Turbulent Reactive Flows", *Progress in Energy and Combustion Science 11*,119-192.

Press, W.H., Flannery, B.P., Teukolsky, S.A., and Vetterling, W.T. (1993), *Numerical Recipes in FORTRAN, The Art of Computing Science*. Cambridge: Cambridge University Press.

Raman, V. and Pitsch, H. (2005), "Large-Eddy Simulation of a Bluff-body Stabilized Non-premixed Flame using a Recursive-refinement Procedure", *Combustion and Flame 142*,329–347.

Raman, V., Pitsch, H. (2005), "Large-Eddy Simulation of a Bluff-body Stabilized Nonpremixed Flame using a Recursive-Refinement Procedure", *Combustion and Flame 142*, 329–347.

Ranga-Dinesh, K.K.J. (2007), "Large Eddy Simulation of Turbulent Swirling Flames", *Ph.D Thesis*, Loughborough University, UK.

Ranga-Dinesh, K.K.J., Malalasekera, W., Ibrahim, S.S. and Kirkpatrick, M.P. (2006), "Large Eddy Simulation of Turbulent Non-Premixed Swirling Flames",

Proceedings of the 5th International Symposium on Turbulence, Heat and Mass Transfer, pp 1-7.

Ravikanti, M. and Malalasekera, W. (2006), "Computational Predictions for Sydney/Sandia Bluff-body Flames", *Proceedings of Eighth Turbulent Non-premixed Flames Workshop, Germany*, pp.19-31.

Riesmeier, E., Honnet, S., and Peters, N. (2004), "Flamelet Modeling of Pollutant Formation in a Gas Turbine Combustion Chamber Using Detailed Chemistry for a Kerosene Model Fuel", *Journal of Engineering for Gas Turbines and Power 126,* 899-905.

Roberts, P.T and Moss, J.B. (1981), "A Wrinkled Flame Interpretation of The Open Turbulent Diffusion Flame", *Eighteenth Symposium (International) on Combustion/The Combustion Institute*, 941.

Rotta, J.C. (1951), "Statistiche Theorie Nichthomogener Turbulenz", *Zeitschrift für Physik 129*, 547-572.

Sanders, J.P.H, Chen, J.-Y., and Gökalp (1997), "Flamelet based Modeling of NO formation in Turbulent Hydrogen Jet Diffusion Flames", *Combustion and Flame 111,* 1-15.

Sanders, J.P.H. and Lamers, A.P.G.G. (1994), "Modelling and Calculation of Turbulent Lifted Diffusion Flames", *Combustion and Flame 96*, 22-33.

Schlatter, M., Ferreira, J.C., Flury, M., and Gass, J. (1996) "Analysis of Turbulence-Chemistry Interaction With Respect to NO Formation in Turbulent Nonpremixed Hydrogen-Air Flames", *Twenty-sixth Symposium (International) on Combustion/The Combustion Institute*, 2215-2222.

Schneider, Ch., Dreizler, A. and Janicka, J. (2003), "Flow Field Measurements of Stable and Locally Extinguishing Hydrocarbon-Fuelled Jet Flames", *Combustion and Flame 135*, 185-190.

Smagorinsky, J. (1963), "General Circulation Experiments with the Primitive Equations, Part I: The Basic Experiment", *Monthly Weather Review 91*, 99-164.

Smith, P.G, Golden, D.M., Frenklach, M., Moriarty, N.W., Eiteneer, B., Goldenberg, M., Bowman, C.T., Hanson, R.K., Song, S., Gardiner, W.C., Lissianski, V. and Qin, Z. (2007), in http://www.me.berkeley.edu/gri-mech/releases.html

Smooke, M.D., Crump, J., Seshadri, K. and Giovangigli, V. (1990), "Comparison between Experimental Measurements and Numerical Calculations of the Structure of Counterflow, Diluted Methane-Air, Premixed Flames", *Twenty Third Symposium (International) on Combustion/The Combustion Institute*, 463-470.

Spalding, D.B. (1972), "A Novel Finite-Difference Formulation for Differential Expressions Involving both First and Second Derivatives", *International Journal for Numerical Methods in Fluids 4*, 551-559.

Sreenivasan, K. R., Antonia, R. A. and Danh, H. Q. (1977), "Temperature Dissipation Fluctuations in a Turbulent Boundary Layer", *Physics of Fluids 20*, 1238-1249.

Stone, C., Menon, S. (2003), "Open-Loop Control of Combustion Instabilities in a Model Gas Turbine Combustor", *Journal of Turbulence 4*, 20-20.

Tennekes, H. and Lumley, J.L. (1972), "*A First Course in Turbulence*", MIT Press.

VanKan, J. (1986), "A Second Order Accurate Pressure Correction Scheme for Viscous Incompressible Flow", SIAM *Journal of Scientific and Statistical Computing 7*, 870-891.

Vanquickenborne, L. and Van Tiggelen, A. (1966), "The Stabilization Mechanism of Lifted Diffusion Flames", *Combustion and Flame 10*,pp. 59-69.

Versteeg, H.K., and Malalasekera, W. (2007), "*An Introduction to Computational Fluid Dynamics*: *The Finite Volume Method*", Harlow, England; New York: Pearson Education Ltd.

Veynante, D., Vervisch, L., Poinsot, T., Liñán, A., Ruetsch, G. (1994), "Triple Flame Structure and Diffusion Flame Stabilization". *Summer Proceedings of Center for Turbulence Research*, NASA Ames/Stanford University, 55-73.

Vranos, A., Knight, B.A., Proscia, W.M., Chiappetta, L., and Smooke, M.D. (1992), "Nitric Oxide Formation and Differential Diffusion in a Turbulent Methane-Hydrogen Diffusion Flame", *Twenty Fourth Symposium (International) on Combustion/The Combustion Institute*, 377-384.

Werner, H. and Wengle, H. (1991), "Large Eddy Simulation of Turbulent Flow Over and Around a Cube in a Plane Channel", Eighth *Symposium on Turbulent Shear Flows*, 155-168.

Williams, F.A. (1975), "Recent Advances in Theoretical Descriptions of Turbulent Diffusion Flames", In S.N.B. Murthy (Ed.), *Turbulent Mixing in Nonreactive and Reactive Flows*, pp.189-208, New York: Plenum Press.

Williams, F.A. (2007) in http://www-mae.ucsd.edu/~combustion/cermech/

Xu, X., Chen, Y., Wang, H. (2006), "Detailed Numerical Simulation of Thermal Radiation Influence in Sandia flame D", *International Journal of Heat and Mass Transfer 49*, 2347-2335.

Yan, J., Thiele, F., and Buffat, M. (2004), "A Turbulence Model Sensitivity Study for CH_4/H_2 Bluff-Body Stabilized Flames", *Flow Turbulence and Combustion 73*, 1-24.

Young, K. J. and Moss, J.B. (1995), "Modelling Sooting Turbulent Jet flames using an Extended Flamelet Technique", *Combustion Science and Technology 105*, 33-53.